Lifetimes, level energies and light shifts in a single trapped Ba+ Ion

Mohanty, Amita

Lifetimes, Level Energies and Light Shifts in a Single Trapped Ba^+ Ion

To my parents

Cover: Photograph of the fluorescence collected from a crystal of laser cooled Ba^+ ions in a Paul trap.

This work is part of a research program funded in part by the Stichting voor Fundamenteel Onderzoek der Materie (FOM), which is financially supported by the Nederlandse Organisatie voor Wetenschappelijk Onderzoek (NWO).

ISBN: 978-90-367-9062-8 (printed version)
ISBN: 978-90-367-9060-4 (electronic version)

Printed By: Ipskamp Printers, Enschede, 2016

university of groningen

Lifetimes, Level Energies and Light Shifts in a Single Trapped Ba^+ Ion

PhD thesis

to obtain the degree of PhD at the
University of Groningen
on the authority of the
Rector Magnificus Prof. E. Sterken
and in accordance with
the decision by the College of Deans.

This thesis will be defended in public on

Friday 9 September 2016 at 16:15 hours

by

Amita Mohanty

born on 18 January 1985
in Orissa, India

Supervisor
Prof. K. H. K. J. Jungmann

Co-supervisor
Dr. L. Willmann

Assessment committee
Prof. R. A. Hoekstra
Prof. W. Nörthershäuser
Prof. N. Severijns

Abstract

A precise measurement of Atomic Parity Violation (APV) in atomic systems aims at the determination of electroweak mixing Weinberg angle ($\sin^2\theta_W$) at low momentum transfer. The precision to which $\sin^2\theta_W$ can be determined depends on the accuracy of the knowledge of the atomic structure of the trapped and laser cooled simple alkaline earth ionic systems like Ba^+ and Ra^+ and their intrinsic sensitivity to high precision measurements. Available information on the atomic system Ba^+ and Ra^+ and experimental inputs for verification of recent improved calculations for Ba^+ wavefunctions is within the scope of this thesis. The information on the lifetime of the long lived $5d\,^2D_{5/2}$ state, level energies and light shifts in the presence of the additional laser field in single Ba^+ ion is provided with a focus on the experimental conditions and their influence on the measurements. This information will be further implemented in a single Ra^+ ion towards APV. A single ion localized to better than one optical wavelength is a necessary prerequisite for such a precise APV measurement. With the localized ion, a measurement of light shifts of order a few Hz of Zeeman sublevels of the $7s\,^2S_{1/2}$ ground state forms the crucial step towards determination of APV in a single trapped ion. A single Ba^+ ion experiment has been constructed and the frequency stabilization techniques for the employed laser systems have been implemented. The lifetime $\tau_{D_{5/2}}$ of the metastable $5d\,^2D_{5/2}$ state is extensively studied both in single and multiple ions in this setup. These measurements provide for detailed and precise understanding of the intrinsic atomic structure and enables extraction of atomic wavefunctions of the involved states. High resolution frequency spectroscopy of the laser cooling transitions $6s\,^2S_{1/2}$–$6p\,^2P_{1/2}$ and $5d\,^2D_{3/2}$–$6p\,^2P_{1/2}$ in Ba^+ with single and multiple trapped and laser cooled ions permits the determination of absolute frequencies of the relevant transitions to 100 kHz accuracy which is more than 100 times better than earlier measurements. This gives an excellent understanding of the complex spectra of Ba^+ with an Optical Bloch Equation (OBE) 8-level system. The spectra are exploited towards observation of light shifts in the $6p\,^2P_{1/2}$–$5d\,^2D_{3/2}$ transition in a single Ba^+ ion for the first time and the systematic effects have been investigated. The vector and tensor light shifts of the individual Zeeman components for different $6s\,^2S_{1/2}$–$5d\,^2D_{3/2}$ transitions in Ba^+ are observed. Further, extensive studies of these vector and tensor light shifts have been initiated and are currently in progress. This is an excellent step towards light shift determinations in the Zeeman sublevels of the ground state of a single ion which is crucial for the precise determination of APV.

Contents

1 Introduction **1**
- 1.1 Standard Model and its limitations . . . 1
- 1.2 Electroweak interaction . . . 2
- 1.3 APV measurement: determination of weak charge and Weinberg angle . . . 5
- 1.4 Single ion: trapping, laser cooling and spectroscopy . . . 8

2 Parity violation in heavy alkaline earth ions: Ba^+ and Ra^+ **11**
- 2.1 Properties of Ba^+ and Ra^+ . . . 11
- 2.2 Parity violation in Ba^+ and Ra^+ . . . 15
- 2.3 Ra^+: suitable candidate for APV measurements . . . 17
- 2.4 Sensitivity to APV . . . 20
  - 2.4.1 Lifetime of the metastable $5d\,^2D_{5/2}$ state . . . 20
  - 2.4.2 Absolute transition frequencies . . . 21
  - 2.4.3 Light shifts in atoms . . . 21
  - 2.4.4 On resonance light shifts in Ra^+ and Ba^+. . . . 24
- 2.5 Ba^+: predecessor to Ra^+ in APV measurements . . . 25
  - 2.5.1 Concept of the experimental setup . . . 26
- 2.6 Section Summary . . . 31

3 Experimental tools for single ion spectroscopy **33**
- 3.1 Ultra-High Vacuum (UHV) system . . . 33
  - 3.1.1 Maintaining good vacuum conditions . . . 35
- 3.2 Hyperbolic Paul trap for optical spectroscopy . . . 37
  - 3.2.1 Electric fields in a hyperbolic Paul trap . . . 38
    - 3.2.1.1 Rf trapping with resonators . . . 38
    - 3.2.1.2 Adjusting the rf amplitude . . . 41
  - 3.2.2 Compensation of stray electric fields . . . 42
- 3.3 Fluorescence detection system . . . 43
  - 3.3.1 Cooled photomultiplier . . . 44
  - 3.3.2 EMCCD . . . 45
- 3.4 UHV compatible effusive beam of Ba atoms . . . 46
  - 3.4.1 Optical detection of Ba atomic beam . . . 46
- 3.5 Formation of Ba^+ ions . . . 50
  - 3.5.1 Photoionization using on-resonant diode laser at λ_{413} . . . 51
- 3.6 Magnetic field . . . 53

3.7 Section Summary 53

4 Single Ba^+ spectroscopy and laser control system 55
4.1 Optical frequency comb 57
4.2 Ti:Sapphire laser 58
4.2.1 Beat note signal between the Ti:Sapphire laser and frequency comb 58
4.3 Diode laser stabilized to iodine 59
4.3.1 Saturated absorption spectroscopy in iodine 60
4.3.2 Beat note signal between the diode laser and frequency comb 62
4.4 Dye laser stabilized to diode laser 63
4.5 Frequency-offset locking between iodine-stabilized diode laser and dye laser 65
4.6 Beam diagnostics and manipulation 68
4.6.1 Frequency doubling of Ti:Sapphire laser light 68
4.6.2 Dye laser light through the trap 69
4.6.3 Frequency switching of dye laser for cooling and spectroscopy 70
4.6.4 Delivery of light to the center of trap 70
4.7 Shelving and deshelving LEDs 72
4.8 Light shift laser 73
4.9 Section Summary 75

5 Precise determination of lifetime of $5d\,^2D_{5/2}$ state in Ba^+ 77
5.1 Introduction 77
5.2 Electron shelving technique 78
5.2.1 Application to single trapped ion 78
5.2.2 Application to multiple trapped ions 81
5.3 Quantum jumps analysis 84
5.4 Sensitivity of lifetime to experimental parameters 85
5.5 Lifetime of $5d\,^2D_{5/2}$ state with multiple ions 88
5.6 Results 89
5.7 Section Summary 90

6 Single ion dynamics and determination of transition frequencies[1] 93
6.1 Line shape as result of laser cooling 93
6.2 Experimental determination 97
6.2.1 Effects of micromotion 97
6.2.2 Duty cycle and frequency switching 99
6.3 Systematic study of Raman spectrum 100
6.4 Results 102
6.5 Section Summary 103

7 Light shifts in Ba^+ 105
7.1 Measuring light induced frequency shift 105

[1]The main contents of this chapter is also published under E. A. Dijck et al. (A. Mohanty) [88] and provides additional material.

7.2 Shelving caused by light at wavelength 590 nm 109
7.3 Light shift caused by near resonant light 112
7.3.1 Procedure to overlap laser beam with ion 112
7.3.2 Specific light shift measurement 114
7.3.3 Increased optical resolution of spectral features 116
7.4 Section Summary 120

8 Conclusion and Outlook **121**

9 Nederlandse Samenvatting **125**

A Abbreviations **129**

B Alternate method of rf-switching **131**

C DC voltages to the endcaps **133**

D Atomic spectroscopy of the $6s^2\ {}^1S_0$–$6s\,6p\ {}^1P_1$ transition in barium **137**

E Laboratory Parameters **141**

F Lifetime vs parameters **145**

G Jumps vs parameters **147**

Bibliography **151**

Chapter 1

Introduction

1.1 Standard Model and its limitations

The Standard Model (SM) [1–3] is the most successful theory in physics that describes the electromagnetic, weak and strong interactions in one coherent frame. It provides a description for the interactions between different particles in particle physics. Gravitational interactions are not included in the SM and they are described in general relativity. All confirmed observations up to the presently experimentally accessible energies of 14 TeV are fully described in this model. But this SM theory has its own limitation i.e. it falls short of being a complete theory of fundamental interactions. It leaves open questions on some phenomena that can be described within the SM but are left without deeper explanation. Examples are the number of particle generations, the origin of parity violation in weak interactions, the accelerating expansion of the universe (described by dark energy) or the dominance of matter over antimatter in the universe. In order to search for potential explanations and to find New Physics beyond the present SM, experimental tests are mainly conducted at two different and complementary frontiers.

1. There is the direct production of new particles at collider experiments performed at the highest available energies for e.g. the discovery of the Higgs boson at the Large Hadron Collider (LHC) experiments [4, 5] or the direct observation of new, yet unobserved effects on new particles at any energy.

2. There is the high precision determination of quantities that are well known in the SM and that are well calculable. Examples are at low energies are precise measurements of Atomic Parity Violation (APV) [6–8] and searches for permanent Electric Dipole Moments (EDMs) [9–11]. The high precision experiments [12] are sensitive to new particles with examples of masses beyond the reach of present accelerators. A deviation of the measured values

for which sufficiently accurate predictions can be calculated within the SM would be an indication of physics beyond the SM. This work concerns an experiment to measure Atomic Parity Violation.

The concept of fundamental global symmetries and the conservation laws associated with them have significantly contributed to modern physics theories. Symmetries are mainly associated with transformations of a system. A system is said to be symmetric, if a transformed system is completely indistinguishable from the original one [13] even after the transformations have occurred. Symmetries can be continuous or discrete depending on the eigenvalues of their quantum mechanical operators. Discrete symmetries are represented by operators with discrete eigenvalues. Examples are Charge conjugation (C), Time Reversal (T) and Parity (P) where the eigen values are $+1$ or -1. Parity symmetry which is also known as mirror symmetry or symmetry under spatial reflections, is represented here by the operator $\hat{P}$. Parity is said to be conserved only, if the Hamiltonian of any interaction $\hat{H}$ commutes with $\hat{P}$, else it is violated. Parity has been observed to be violated in atomic transitions. This implies that space reflection symmetry is broken by the existing weak interactions in atoms. In 1956, it was suggested by T. D. Lee and C. N. Yang [14] to search for Parity violation (P-violation). Shortly thereafter the first experimental observation of P-violation occurred in the β-decay of ^{60}Co by C. S. Wu and her collaborators [15].

1.2 Electroweak interaction

Atomic Parity Violation [16–21] experiments contribute to scrutinizing the electroweak sector of physics in an area accessible with accelerator experiments. The research on P-violation in atoms started with a search for optical rotation of the plane of linear polarisation of light passing through a gaseous vapour [22]. Such optical rotation experiments investigate the breaking of the mirror symmetry in absorption or emission of circularly polarised light. It appears that the optical rotation effects are enhanced in high Z atoms with an approximate dependence on Z^3, where Z is the nuclear charge of the atoms investigated [17, 23]. Optical experiments confirm that the long range electromagnetic and the short range weak interactions can be described in one coherent picture, the electroweak SM. The unification of the electromagnetic and the weak forces into one single electroweak interaction has been a major step towards our present understanding of fundamental forces [1–3, 16]. This unification gives rise to an interference of the exchange of Z^0 bosons and photons γ between electrons and quarks. The latter are contained

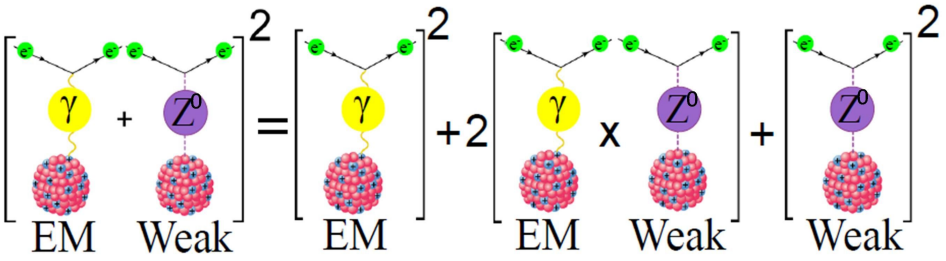

FIGURE 1.1: Electroweak unification via the exchange of a Z^0 boson and a photon γ between an electron and the nucleons that form the atomic nucleus. The amplitudes of the interaction processes of both the possible forces need to be added to arrive at the probability of the combined process. Modified from [24].

in the nucleons forming the atomic nucleus (see Fig. 1.1 for a graphical representation). The electroweak interaction in an atom is quantitatively determined by the electric charge and the weak nuclear charge Q_{weak} [17]. This quantity plays a similar role in electroweak interactions as the electric charge in Coulomb interaction. The accuracy to which Q_{weak} can be determined is limited by the quantitative understanding of atomic theory. Q_{weak} enables the extraction of a Standard Model parameter, the weak mixing (Weinberg) angle ($\sin^2\theta_W$) [25]. Electroweak theory yields

$$Q_{weak}(Z,N) = -N + (1 - 4sin^2\theta_W)Z, \tag{1.1}$$

where N is the number of neutrons and Z is the number of protons in an atomic nucleus, $\sin^2\theta_W$ connects the electric charge, e with the coupling constant of the weak interaction, g_W through the relation

$$sin^2\theta_W = \frac{e^2}{g_W^2}. \tag{1.2}$$

Fig. 1.2 displays the Weinberg angle ($\sin^2\theta_W$) at different momentum scales at which experiments have been conducted. The SM predicted running of this quantity is represented by the black solid line. Due to the radiative corrections the value of $\sin^2\theta_W$ decreases by about 3 % [16, 25], from its value at the lowest momentum transfer up to the momentum transfer from where $W^{\pm}$ bosons are produced. The value again increases at higher momentum values because of the interaction of the electrically charged vector bosons with each other. High energy experiments at SLAC and at CERN [26] have determined the Weinberg angle at the Z-pole by colliding electron and positron beams. Because of the high achieved accuracy the solid line in Fig. 1.2 has been fixed at this momentum scale. The SLAC E158 collaboration [27] measured the parity-violating asymmetry with a fixed target electron-electron (Møller) scattering, and the NuTeV [32] collaboration extracted

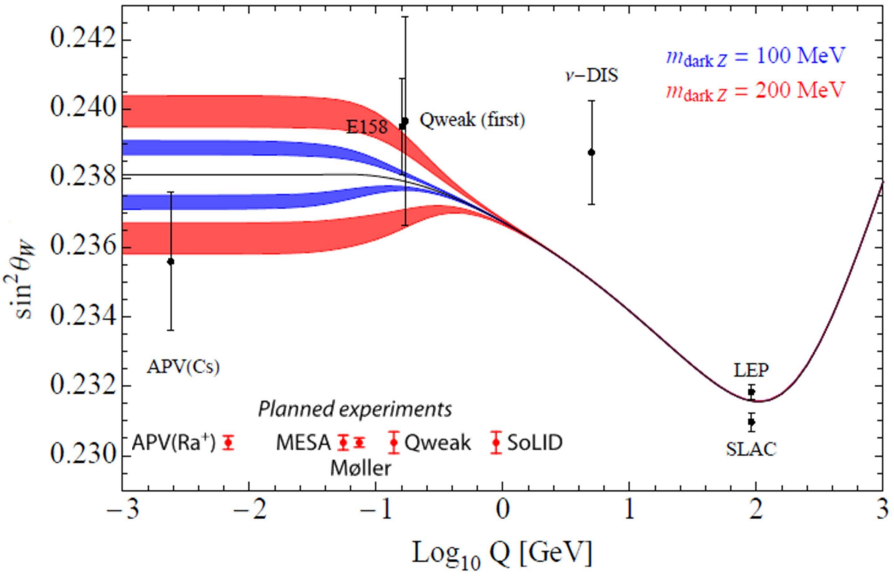

FIGURE 1.2: Running of Weinberg angle $\sin^2\theta_W$, the Standard Model parameter as a function of momentum scale in experiments. The black solid line represents the behaviour of $\sin^2\theta_W$ in SM. Its value has been fixed at the Z-pole at 91.2 GeV. APV(Cs) is the best high precision atomic experiment as of now. We are concerned with measurements towards APV(Ra^+) [28]. APV experiments are sensitive to dark Z-bosons [29–31]. Possible modifications of the running of $\sin^2\theta_W$ is indicated for two mass values of a dark Z-boson. The red and blue bands are sensitive to dark Z-boson of 200 MeV and 100 MeV, respectively. Taken from [31].

the $\sin^2\theta_W$ by measuring the ratios of neutral to charged current cross sections in deep inelastic scattering for both neutrinos and antineutrinos. The Qweak experiment was designed to measure the proton's weak charge in elastic electron-proton scattering. A best known precise experiment done at low energy range is the APV experiment in Cs [33–39]. As of now, these are the various experiments that have been performed at different momentum scales.

The main aim of this work is preparing a measurement of APV in a single trapped Ba^+ and Ra^+ ion with improved accuracy. Such an experiment is motivated in particular through the theoretical prediction, that APV is particularly sensitive to dark Z bosons [29–31] with masses below 100 MeV. This is important for the determination of dark matter which constitutes about 22 % of energy-matter in the universe. These APV measurements may unveil "Dark Parity Violation" arising due to this very light, weakly coupled dark Z boson from the dark matter sector. Depending on the mass of this dark Z boson, the weak coupling effects can shift the value of the Weinberg angle and can modify the curve predicted by the SM. APV experiments set the present limits for such dark Z bosons [29–31]. The modern day collider experiments are blind to these new forces as the masses of these dark force carriers and the cross-sections for the relevant processes are extremely small to be detected [4, 5].

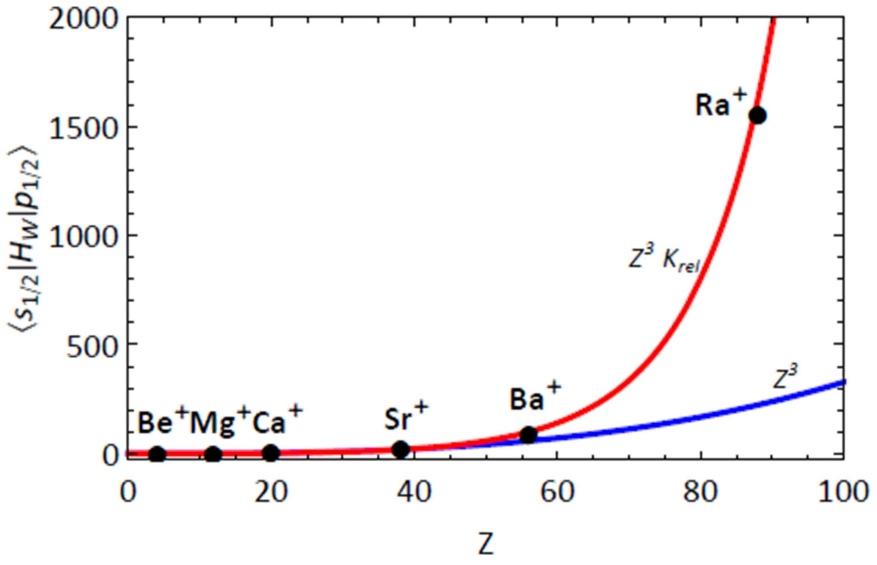

FIGURE 1.3: The scaling of the weak interaction matrix elements for atoms with atomic number Z. The blue line shows the scaling of the weak matrix element with the Z^3. The red line shows that the weak matrix element scales significantly stronger than Z^3 due to a relativistic factor K_{rel}. Adapted from [41].

Precise APV experiments require sufficient understanding of the heavy atomic systems like Fr, Ra, Ba and Cs. Precise calculations show that the electroweak effects in atoms scale stronger than with the cube of the atomic number Z [17] (see Fig. 1.3). In earlier experiments with Cs, the accuracy of the calculated atomic wavefunctions was the one major limitation in the extraction of the Weinberg angle. This work concerns single heavy alkaline earth metal ions like Ra^+ and Ba^+, because a single ion experiment on these systems are predicted to yield better precision in comparison to atoms due to its relatively simple electronic configuration [40].

1.3 APV measurement: determination of weak charge and Weinberg angle

In experiments measuring weak interactions in atoms using the ns $^2S_{1/2}$–(n-1)d $^2D_{3/2}$ transition in heavy alkaline earth ions such as Ba^+ and Ra^+, the interference of the electric quadrupole transition (electromagnetic) and an electric dipole forbidden transition (weak interaction) can be exploited. The electromagnetic interaction is dominant and can be measured experimentally very accurately. The weak interaction is rather weak i.e. some 18 orders of magnitude weaker and cannot be measured directly. The interference of the electric quadrupole transition and the

electric dipole transition is only some 9 orders of magnitude weaker and can, therefore, be measured with sufficient accuracy. From this interference, the parameter known as weak charge Q_{weak} can be deduced. In atoms electric dipole transitions between states of the same parity are forbidden. However, dipole transitions are enabled by a weak admixture of states of opposite parity to one or both of them. The amplitude $E1_{APV}$ for a dipole transition can be measured in experiments and it depends on the weak charge Q_{weak} as well as on a constant k that is determined by the atomic wavefunctions of the involved states [41]. We have the relation

$$Q_{weak} = \frac{E1_{APV}}{k}. \tag{1.3}$$

For Ba^+ the constant k in Eqn. 1.3 can be reliably calculated from the known atomic wavefunctions [41]. For Ra^+, first the validity of the calculated wavefunctions needed to be verified with precise laser spectroscopy of Ra^+ [42, 43]. Calculated atomic wavefunctions of Ra^+ were recently tested [24, 44] and with these the parameter k can be determined [41]. For this purpose, spectroscopy on Ra^+ has been performed in the recent past, e.g., through measuring the hyperfine structure of the $6d\,^2D_{3/2}$ state [45] (see Fig. 1.4), the lifetime of the $6d\,^2D_{5/2}$ state

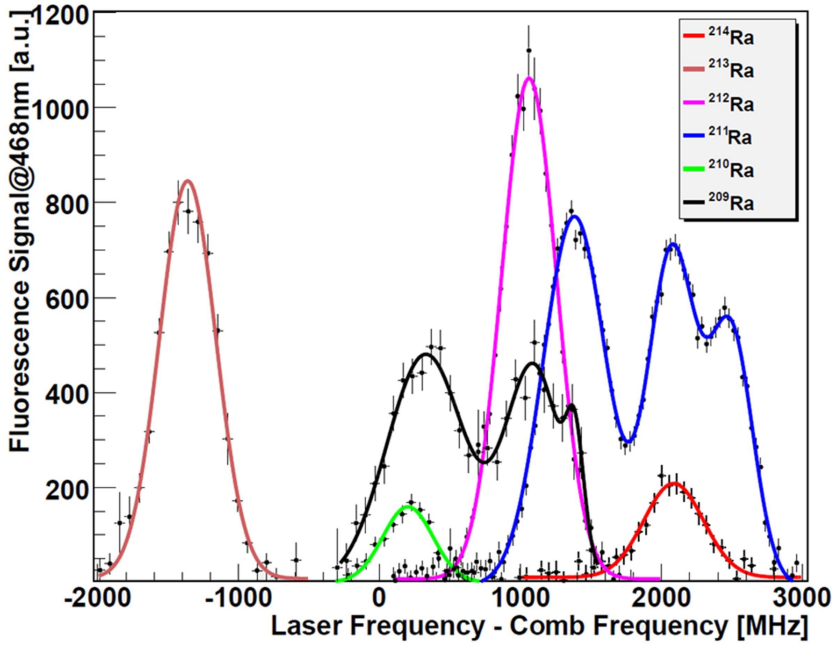

FIGURE 1.4: Fluorescence spectrum for the $6d\,^2D_{3/2}$ state of different isotopes of $^{209-214}Ra^+$ ions. The odd isotopes have hyperfine structures on it while there are no hyperfine structures for the even isotopes of Ra^+ ions. The measurements were performed with Ra^+ ions trapped in a Paul trap. (From [24, 44]).

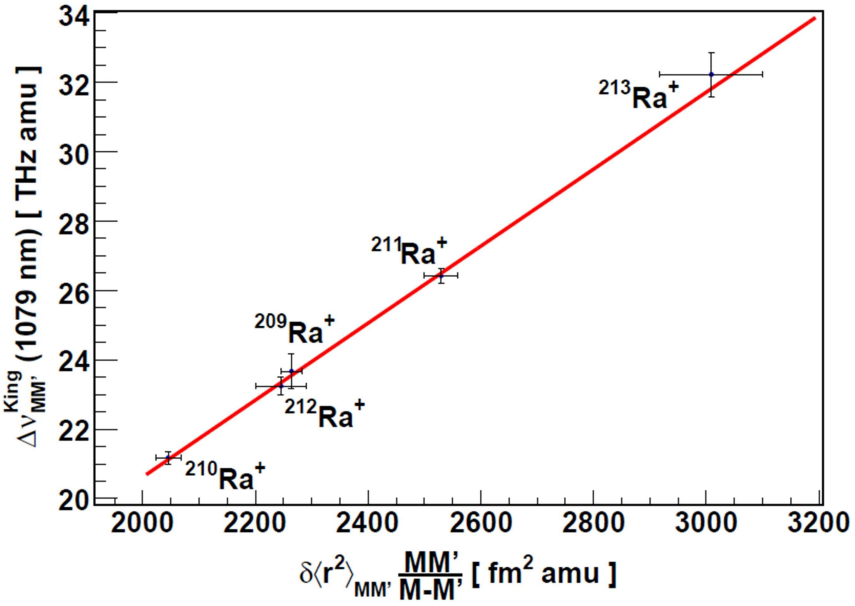

FIGURE 1.5: Isotopic shifts on the $6d\,^2D_{3/2}$–$7p\,^2P_{1/2}$ transition for different isotopes of $^{209-214}Ra^+$ ions. The measurements were performed with ions trapped in a Paul trap. (From [24, 44]).

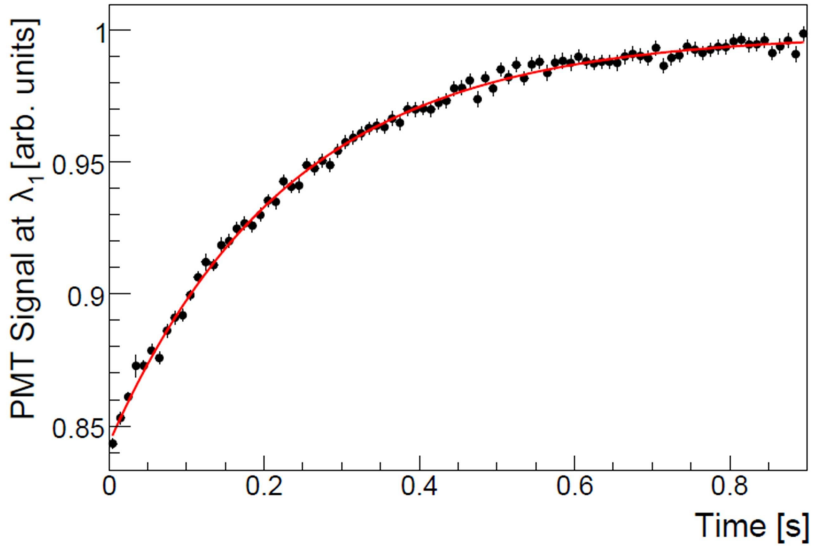

FIGURE 1.6: Lifetime measurements of the $6d\,^2D_{5/2}$ state in $^{212}Ra^+$ ions done at a neon buffer gas pressure of 4×10^{-5}mbar. The solid line represents the recovery time needed for ions to re-enter the fluorescence cycle and an exponential function is fitted to the data. The measurements were performed with ions trapped in a Paul trap. (From [24, 44]).

[42, 43] (see Fig. 1.6) and the isotope shift in the $6d\,^2D_{3/2}$–$7p\,^2P_{1/2}$ transitions in $^{209-214}Ra^+$ ions [46] (see Fig. 1.5).

The hyperfine structure measurements test the atomic wavefunctions at the origin. The isotope shifts probe the size and shape of the atomic nuclei. Lifetime

measurements of metastable states provide information on the matrix elements of quadrupole transitions (E2) which are essential for an APV experiment. The experiments agree at percent level with respect to the atomic theory calculations [24, 47]. This implies that the value of k is known to few percent level of accuracy [24, 44] and hence atomic theory is understood at this level of accuracy for Ra^+. Further theoretical calculations in this direction are still in progress in order to achieve sub % level accuracy, which will be needed to extract $\sin^2\theta_W$ at a competitive level. Further measurements for better accuracy on the hyperfine structure splitting and isotope shifts started recently at CERN/ISOLDE [48].

The magnitude of Q_{weak} connects to the Weinberg angle θ_W through the expression (see also Eqn. 1.1.)

$$Q_{weak} = -N + (1 - 4sin^2\theta_W)Z, \tag{1.4}$$

where N is the number of neutrons and Z is the number of protons in the atomic nucleus. Once Q_{weak} will be determined experimentally from $E1_{APV}$ and k, Eqn. 1.4 provides for extracting $\sin^2\theta_W$.

1.4 Single ion: trapping, laser cooling and spectroscopy

The presently achievable precision in an APV experiment is limited by experimental sensitivity, systematics and atomic structure uncertainties. An experiment with a single trapped and laser cooled heavy ion like Ba^+ and Ra^+ [49–51] has potential as the best solution to overcome the present precision limit.

The concept of ion trapping was first described by W. Paul [52]. It has been applied to many different problems in physics for e.g. precision RF spectroscopy, crystallization of an ion cloud plasma at mK temperatures, quantum mechanical studies of the interaction of a single ion with the radiation field and many more examples. The main advantage of this technique is to study the behaviour of the individual, stable, well controllable and isolated quantum systems for long periods (i.e. several hours) devoid of perturbations. Therefore, trapped ions are favourable for precision measurements, optical and microwave transition measurements especially with applications to frequency standards, quantum information processing and also have applications in condensed matter physics like the study of phase transitions in ion Coulomb crystals.

Single trapped heavy Ba^+ and Ra^+ ions can be laser cooled to make them well-suited systems for precision APV measurements because of their long coherence times, good quantum control and efficient search for systematic effects. These systems enable measurement of their properties with extremely high accuracy.

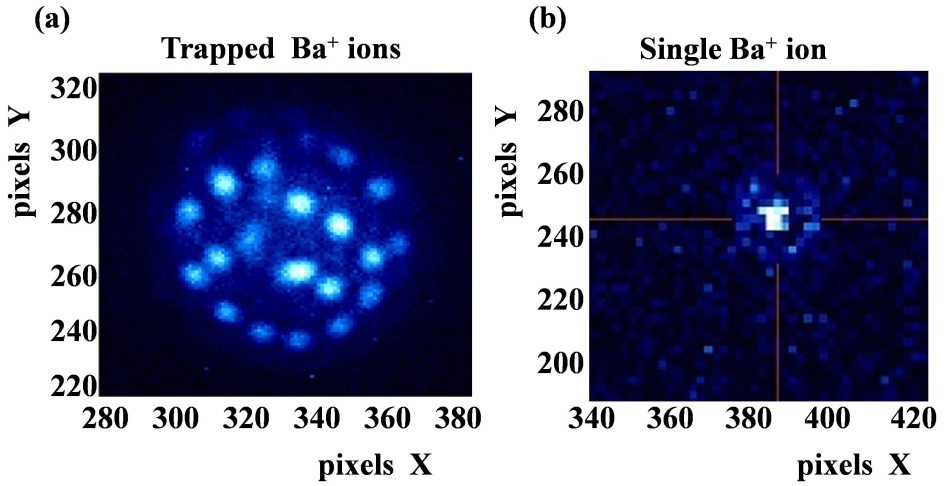

FIGURE 1.7: Trapped crystal of many Ba^+ ions (a) and one single trapped, laser cooled Ba^+ ion (b). Here a 1×1 pixel corresponds to $1\times1\,\mu m^2$. Precision laser spectroscopy on these trapped ions is a crucial prerequisite for the measurement of Atomic Parity Violation.

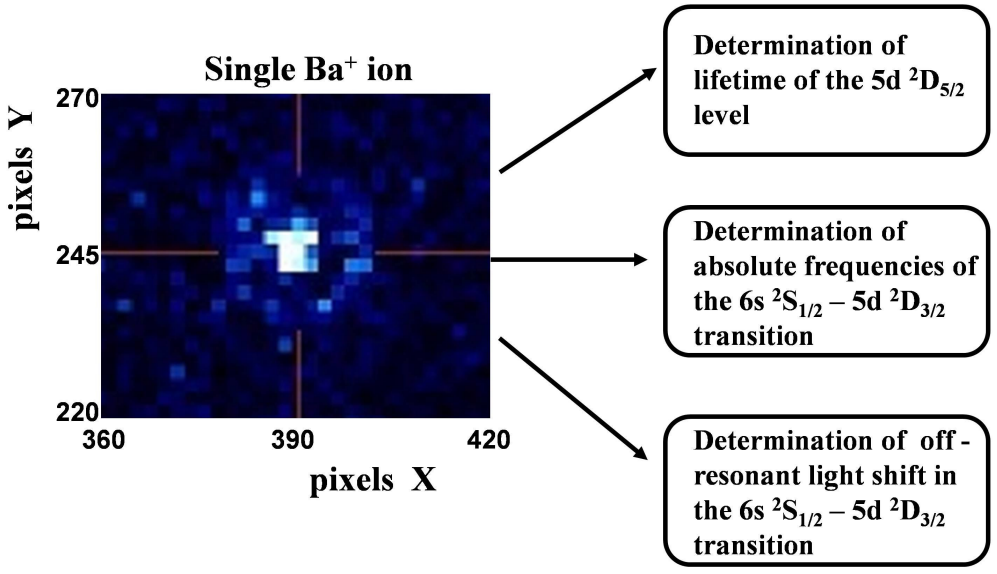

FIGURE 1.8: Schematics of high-resolution spectroscopic studies performed on a single trapped Ba^+ ion. Here a 1×1 pixel corresponds to $1\times1\,\mu m^2$. The ring around the Ba^+ ion arises from the diffraction limited optics in the detection path. These are precursor measurements for a Ra^+ ion experiment aimed towards a measurement of APV.

The availability of different isotopes provides for minimization of atomic structure uncertainties. The simple nature of such a laser cooled single ion system, extremely low collision rates with background gas and the small spatial region over which fields must be carefully controlled makes the analysis and control of systematic

errors tractable. Fig. 1.7 shows an example of trapped Ba^+ ions in a Paul trap.

Single ion spectroscopy, especially the high-resolution spectroscopy of the low-lying levels, is employed to search for all possible systematic effects. The high resolution spectroscopic studies with single trapped Ba^+ ion like the determination of the lifetime of the metastable states, absolute frequency determination of transitions between low lying levels to a 100 kHz level accuracy and energy level shifts in the presence of the on-resonant and off-resonant external laser fields are within the scope of this thesis (see Fig. 1.8). These studies are essential prerequisites for progress towards an APV experiment with a single trapped Ra^+ ion.

Chapter 2

Parity violation in heavy alkaline earth ions: Ba^+ and Ra^+

The theoretical concept of the measurement of weak interaction effects in alkaline earth metal ions such as Ba^+ and Ra^+ is the main topic of this chapter. The choice of Ra^+ as a suitable candidate for APV is motivated. In order to measure weak interaction effects, verification of the atomic wavefunctions to sub-% precision is required. The absolute frequencies of relevant optical transitions are compiled. The behaviour of their energy levels in external electric fields is described. Such knowledge is required for a determination of the weak mixing (Weinberg) angle from atomic spectroscopy on alkaline earth ions. In this chapter, we compile the known and relevant information for Ba^+ and Ra^+ ions.

2.1 Properties of Ba^+ and Ra^+

Singly ionized Ba^+ and Ra^+ can be trapped in e.g. a Paul trap. The transitions between the low-lying states of these ions are conveniently accessible with light from the present state-of-the-art laser systems. The behaviour of a single ion system in the presence of laser fields with different power, frequencies, and polarisations, magnetic fields, trapping voltages etc. are essential to understand the underlying physics of trapping, laser cooling and precise measurements. The measurements include the lifetime of the metastable state, and absolute frequencies and light shifts in $5d\,^2D_{3/2} - 6p\,^2P_{1/2}$ transitions in alkaline earth elements. For an alkaline earth metal system like Ba^+ and Ra^+, the frequencies of cooling and repump transitions are in the visible regime, where lasers to produce the necessary light are available, and reliable stabilization and locking techniques exist for the laser systems.

Ba^+

The Ba^+ ion is a Group-2 S-block heavy alkaline earth ion in the Mendeleev periodic table. The Ba atom has an atomic number $Z = 56$ and the ground state electronic configuration is $[Xe]\,6s^2$. A large number of stable isotopes is available with ^{138}Ba, being the most abundant isotope (71.7%). The Ba^+ ion was the first single ion observed in a Paul trap by Toschek, Dehmelt and coworkers [53] in 1977. Karlsson et al. [54] obtained the first spectroscopic data for ^{138}Ba. Fourier Transform Spectroscopy of ^{138}Ba has been used to analyze the optical spectra for Ba and Ba^+. A frequency uncertainty of about a few 10 MHz was reported in their measurements. A recent compilation of spectroscopic data for Ba^+ was published in 2004 [55] with typical uncertainties for the transitions that can be exploited for laser cooling such as $6s\,^2S_{1/2}$–$6p\,^2P_{1/2}$ and $5d\,^2D_{3/2}$–$6p\,^2P_{1/2}$ given as $0.01\,cm^{-1}$, corresponding to 300 MHz.

Ra^+

The Ra^+ ion -like Ba^+- is a Group-2 S-block heavy alkaline earth ion in the Mendeleev periodic table. The radium atom has an atomic number $Z = 88$ and the ground state electronic configuration is $[Rn]\,7s^2$. It is the only element with radioactive isotopes in the group. Its physical and chemical properties closely resemble its lighter congener Barium. There is a large range of Radium isotopes ranging from $(202 \geq A \leq 234)$ of which all are unstable. Among these, the longest lived, stable and the most common isotope is ^{226}Ra with a half-life of 1600 years. At accelerator facilities such as ISOLDE at CERN [56–58] and AGOR TRIμP at KVI [59] various Ra isotopes have been produced and precision laser spectroscopy [42, 44–47] has been employed on these isotopes. The main advantage for an APV measurement with Ra^+ is the availability of several isotopes. The ISOLDE collaboration at CERN [56, 60] used the isotopes $^{208-232}Ra$ to measure the hyperfine structures and isotope shifts (see [57, 58]). This can be exploited to verify the atomic structure calculations [24, 45–47]. For precision laser spectroscopy, the isotopes $^{209-214}Ra^+$ have been produced in online experiments where a lead beam $^{204/206}Pb$ collides with a rotating carbon wheel target (^{12}C) [59, 61]. The isotope $^{223}Ra^+$ can be obtained from the radioactive source $^{227}Ac(\tau_{1/2} = 21.8$ days) via the decay channel $^{227}Ac \rightarrow \beta^- + {}^{227}Th \rightarrow {}^{223}Ra + \alpha$ [62]. An offline radioactive source ^{229}Th ($\tau_{1/2} = 7932$ years) can be employed for the extraction of $^{225}Ra^+$ via the decay chain $^{229}Th \rightarrow {}^{225}Ra + \alpha$.

The wavelengths and branching ratios of the low-lying optical transitions which are relevant for the single ion trapping experiment for Ba^+ and Ra^+ are listed in Table 2.1 and 2.2 respectively.

TABLE 2.1: Optical transitions in $^{138}Ba^+$ ion for low lying levels. Wavelength data compiled from [55]. Possible light sources are listed in order to drive the respective transitions.

Transitions	$6s\,^2S_{1/2}$–$6p\,^2P_{1/2}$	$6s\,^2S_{1/2}$–$6p\,^2P_{3/2}$	$5d\,^2D_{3/2}$–$6p\,^2P_{1/2}$	$5d\,^2D_{3/2}$–$6p\,^2P_{3/2}$	$5d\,^2D_{5/2}$–$6p\,^2P_{3/2}$
Wavelengths (nm)	493.54539 [55]	455.53098 [55]	649.86932 [55]	585.52973 [55]	614.34129 [55]
Branching ratios	0.756(12) [63]	0.756(46) [64]	0.244(12) [63]	0.0290(15) [64]	0.2150(64) [64]
Einstein-A Coefficients (s^{-1})	$9.53(12)\times10^7$	$1.11(3)\times10^8$	$3.10(4)\times10^8$	$6.00(16)\times10^6$	$4.12(10)\times10^7$
Lasers used	SHG Ti:Sapphire	LED455 Thorlabs	Dye laser Coherent699	Toptica590nm laser	LED617 Thorlabs

TABLE 2.2: Optical transitions in $^{226}Ra^+$ ion for low lying levels. Wavelength data compiled from [58]. Possible light sources are listed in order to drive the respective transitions.

Transitions	$7s\,^2S_{1/2}$–$7p\,^2P_{1/2}$	$7s\,^2S_{1/2}$–$7p\,^2P_{3/2}$	$6d\,^2D_{3/2}$–$7p\,^2P_{1/2}$	$6d\,^2D_{3/2}$–$7p\,^2P_{3/2}$	$6d\,^2D_{5/2}$–$7p\,^2P_{3/2}$
Wavelengths (nm)	468.31266	381.52027	1079.14454 [65]	708.00115 [58]	802.1980 [58]
Branching ratios	0.909 [66]	0.878 [66]	0.091 [66]	0.016 [66]	0.106 [66]
Einstein-A Coefficients (s^{-1})	$9.3(1)\times10^7$	$1.19(2)\times10^8$	$3.34(4)\times10^7$	$4.70(9)\times10^6$	$3.53(7)\times10^7$
Lasers used	Laser diode Nichia	Laser diode Nichia	Laser diode Toptica	-	Laser diode Qphotonics

Choice of single trapped Ba^+ and Ra^+ ion

There are four reasons to choose single trapped alkaline earth metal ions like Ba^+ and Ra^+ in UHV to perform precise measurements. Being a monovalent heavy alkaline earth ion, it has a rather simple electronic configuration (see Fig. 2.1). This allows for precise measurements in which the atomic wavefunctions can be thoroughly tested. Being a heavier nucleus, it has a large number of constituent particles which makes the electron correlations and relativistic effects important. Its large number of nucleons makes it an attractive candidate for an atomic APV experiment. A single ion can be trapped and localized to the motional ground state which permits long perturbation-free interrogation times. Thus, it can be placed inside the tight focus of a laser beam.

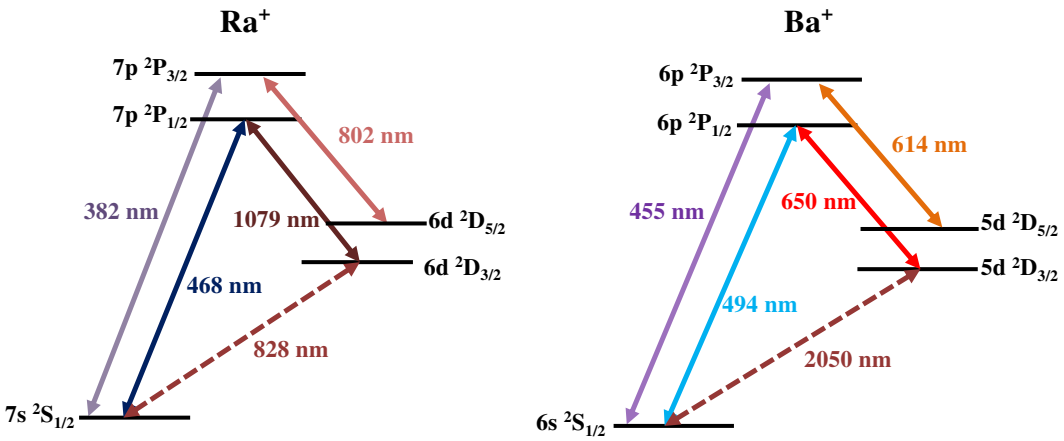

FIGURE 2.1: Energy level scheme for Ra^+ and Ba^+ for the lowest lying S, P and D states. Ra^+ and Ba^+ have a Λ-level configuration. Laser light exciting the $ns\,^2S_{1/2}$–$np\,^2P_{1/2}$ transition is known as the "pump laser light" while the laser light exciting the $(n\text{-}1)d\,^2D_{3/2}$–$np\,^2P_{1/2}$ transition is known as the "repump laser light".

2.2 Parity violation in Ba^+ and Ra^+

In atomic or ionic systems, the interference of Z^0 bosons and photons exchanged between the atomic electrons and the quarks in the atomic nucleus leads to a short range parity violating component in the interaction potential between the electrons and the nucleus. In case of heavy ions like Ba^+ and Ra^+, the strength of this weak parity violating component can be calculated with atomic theory taking into account the nuclear spin independent Hamiltonian for the weak interaction which is given by [6]. As these ionic systems possess different degenerate energy

levels with well-defined parities such a weak parity violating component arises due to the mixing of these opposite parity states. APV experiments are responsible for measuring such mixing of the opposite parity states like the s and p states. Effects due to the presence of new particles can also appear as corrections to these parity violating observables. In this case, however, the Standard Model effects are very small since, compared to atomic scale energies, the masses of the weak boson are very large. The relative sizes of these new effects are given by a ratio of their masses to the already very high energy weak scale. Again considering coupling constants of similar order.

$$\frac{\langle f|H_{new}|i\rangle}{\langle f|H_W|i\rangle} \propto \left(\frac{m_W}{m_{new}}\right)^2 \approx \left(\frac{100\,GeV}{1\,TeV}\right)^2 \approx 10^{-2} \tag{2.1}$$

Such a % level accurate measurement of the parity violation effects are sensitive to the indirect search for new particles.

Determination of $\mathbf{E1}_{APV}$

The transition amplitude $E1_{APV}$ is the allowed electric dipole transition part induced by Atomic Parity Violation. It is determined by measuring light shifts in the $ns\,^2S_{1/2}$–$(n\text{-}1)d\,^2D_{3/2}$ transition [40] where n = 6 for Ba^+ and n = 7 for Ra^+. Fig. 2.2 displays the energy level scheme of the Ra^+ ion where E2 represents the quadrupole transition which can be induced in an experiment. Here $E1_{APV}$ describes a dipole forbidden transition and it enables a measurement of the parity violating component in this transition. In the presence of magnetic fields, the Zeeman magnetic sublevels are separated by a frequency ω_0.

Fig. 2.2 illustrates the light shifts of the m = +1/2 and m = -1/2 Zeeman magnetic sublevels of the $7s\,^2S_{1/2}$ state in Ra^+ for the simultaneous application of the light fields driving the E2 and $E1_{APV}$ transition. Such a light shift is observable in the change of the Larmor precession frequency. For a single Ra^+ ion with zero nuclear spin, the splitting between the m = +1/2 and m = -1/2 sublevels of the $7s\,^2S_{1/2}$ ground state in a magnetic field B is about $\Delta\omega_{zeeman} = 0.23\,\frac{MHz}{mT}$ [67].

For APV precision experiments, the ion needs to be first localized within a fraction of one optical wavelength. For this, in our experiment, a single ion is first trapped and confined in a hyperbolic Paul trap and then laser cooled to temperatures below 100 μK. This brings about the confinement of the ion to within a few μm. In order to measure the light shift, the ion has to be further confined to a space smaller than one optical wavelength. This can be achieved by using cavities.

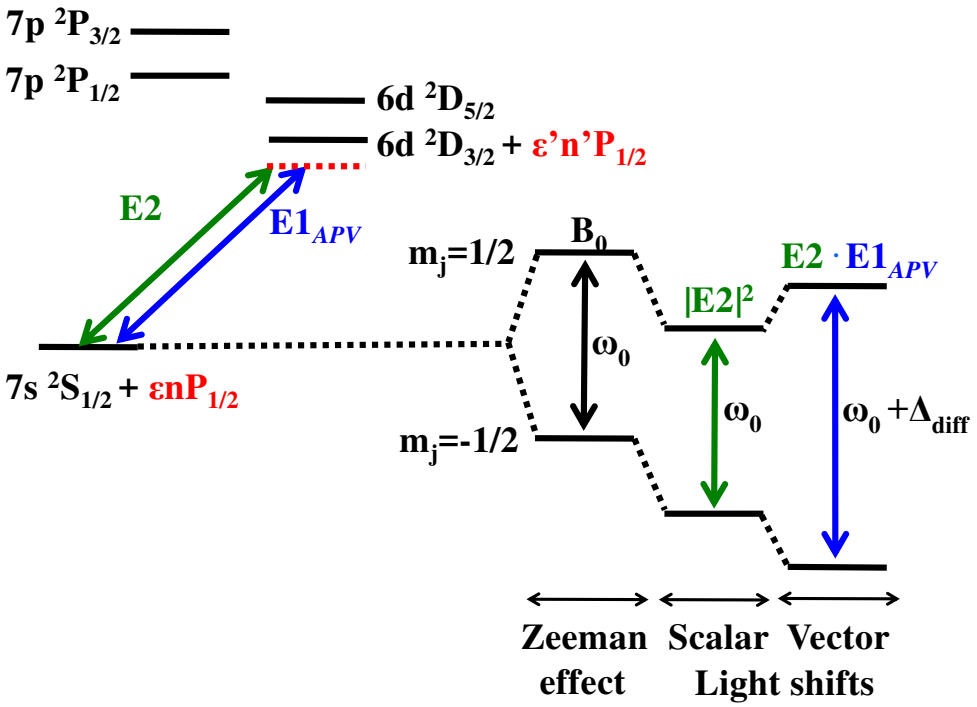

FIGURE 2.2: Scalar and vector light shifts of the magnetic sublevels in the Ra^+ ion in the presence of the field driving the E2 transition and the interference of the $E1_{APV}$ and E2 field [24].

Fig. 2.3 sketches a picture of one ion positioned in standing light fields created within two pairs of cavity mirrors that are arranged with their axes perpendicular to each other. The two cavities serve for creating standing wave fields for laser light during the $7s\,^2S_{1/2}$–$6d\,^2D_{3/2}$ transition in such a way that the ion is localized at the antinode of the standing wave where $E1_{APV}$ is maximum and at the node of the other standing wave where E2 is maximum. The cavity-controlled standing waves provide full control of the phase and amplitude of the light.

2.3 Ra^+: suitable candidate for APV measurements

Atomic systems such as Thallium (Tl) [68, 69], Lead (Pb) [70, 71] and Bismuth (Bi) [72] have been employed in order to observe and study the Weinberg angle, $sin^2\theta_W$ [6]. The biggest challenge of finding the value of the Weinberg angle in the experiments with heavier elements i.e. systems with more than one valence electron is the accuracy to which the atomic wavefunctions can be calculated for such systems. This challenge is significantly reduced for systems with one valence electron system. The atomic wavefunctions and the constant k (see Eqn. 1.3) can be accurately calculated [11, 73, 74]. Recent theoretical values for k in alkaline earth elements are compiled in Table 2.3.

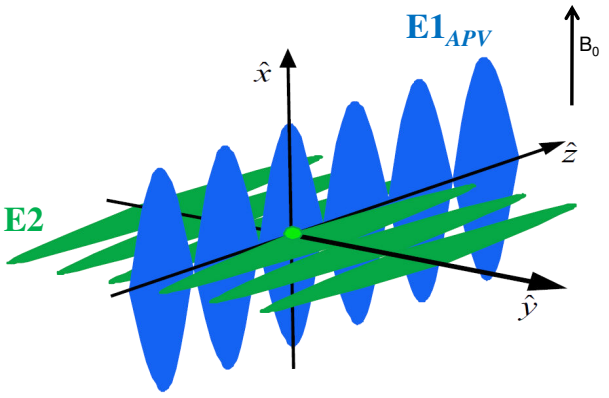

FIGURE 2.3: For the APV experiment, the ion is localized in two standing light fields which are perpendicular to each other. The two light fields drive the quadrupole and the dipole forbidden transitions in the ion respectively [40].

TABLE 2.3: Compilation of matrix elements for electric dipole forbidden transitions for heavy alkaline earth metal ions.

Atom/Ion	APV Transition	$k[\times 10^{-11}$ iea$_0$Q$_W$/N a.u.]	Reference
^{133}Cs	$\langle 6s\|\mathrm{E1}_{APV}\|5d\rangle$	3.62(14)	[75]
^{133}Cs	$\langle 6s\|\mathrm{E1}_{APV}\|7s\rangle$	0.8906(26)	[76, 77]
^{137}Ba$^+$	$\langle 6s\|\mathrm{E1}_{APV}\|5d\rangle$	2.46(2)	[21, 78]
^{223}Fr	$\langle 7s\|\mathrm{E1}_{APV}\|6d\rangle$	57.1(2.3)	[75]
^{223}Fr	$\langle 7s\|\mathrm{E1}_{APV}\|8s\rangle$	15.41(17)	[79–81]
^{210}Fr	$\langle 7s\|\mathrm{E1}_{APV}\|8s\rangle$	14.02(15)	[79–81]
^{226}Ra$^+$	$\langle 7s\|\mathrm{E1}_{APV}\|6d\rangle$	46.4(5)	[82]

It appears that Ra^+ is a promising system for a precise measurement of APV because of its large k value. Another advantage of Ra^+, which is a heavy element, is it can be confined comparatively to a smaller trapping volume than Ba^+ because the Lamb Dicke parameter η, which quantifies the possible localization and is inversely proportional to the square root of the ion mass (see Eqn. 2.2). We have

$$\eta = k\sqrt{\frac{\hbar}{2m\omega_{trap}}}, \tag{2.2}$$

where ω_{trap} is the trapping frequency, k is the constant as explained in Section 1.3. This is related to the Jaynes-Cummings interaction Hamiltonian which contains a term proportional to η when a laser light field couples to the motion of the ion in the trapping potential with their electronic levels. This results further in the reduction of the systematic uncertainties arising from stray fields. Atomic

Francium is another well-suited system to measure $\sin^2\theta_W$ in atomic systems. It is exploited by the experimental groups at Vancouver and Legnaro [78, 83–85]. One of the main challenges is that it is produced by nuclear reactions and the short lifetime and possible production rates can limit the APV measurements.

Theory calculations

The short range parity violating component in the interaction potential between the electrons and the nucleus mainly arise from the interference of Z_0 bosons and photons exchanged between the atomic electrons and the quarks in the atomic nucleus. The Hamiltonian for the weak interaction in heavy atoms is related to the Q_{weak} by the following relation:

$$H_W = Q_{weak} \times \frac{G_F}{\sqrt{8}}\gamma_5\rho_n(r), \tag{2.3}$$

where G_F is the Fermi constant, γ_5 is the Dirac matrix, $\rho_n(r)$ is the neutron density in the nucleus and Q_{weak} is the weak charge as mentioned in Eqn. 1.3 [6]. The overlap of the s and p atomic wave functions with the nucleus yields a proportionality to Z^2 in the matrix elements for the Hamiltonian of the weak interaction between electrons and nucleons in an atom. An additional factor of Z comes from the number of neutrons in a nucleus which itself is proportional to a good approximation to the number of protons in a nucleus. The total enhancement is therefore to good approximation proportional to Z^3. The matrix element for the weak interaction can be written as

$$\langle ns_{1/2}|H_W|n'p_{1/2}\rangle \propto Z^2 Q_{weak} K(Z,R), \tag{2.4}$$

where *K(Z, R)* is a relativistic factor that depends on the charge (Z) and the radius (R) of the atomic nucleus. In heavy atoms like Ra^+ ions, the relativistic factor produces an effect such that the APV signal increases faster than Z^3 (see Fig. 1.3) which describes the weak interaction matrix elements as a function of the nuclear charge for singly charged alkaline earth ions. The effect in Ra^+ and Fr is larger compared to the lighter elements. Calculations of the matrix elements reveal that the APV effect in Ra^+ is 20 times larger than in Ba^+ [21, 86]. Ions of heavy alkaline earth atoms, the APV effect in Ra^+ is 50 times larger than in Cs [16, 17]. It is 18 times larger than in Fr [46, 75]. Weak interactions include mixing of opposite parity states. The modified wavefunctions ($|nS_{1/2}\rangle$) can be calculated with a perturbation method. For Ra^+, due to the LS coupling the mixing of the state $7s\,^2S_{1/2}$ with the $7s\,^2P_{1/2}$ state results in the formation of a new atomic state.

This is given by the following relation:

$$|7\bar{S}_{1/2}\rangle = |7S_{1/2}\rangle + \epsilon|nP_{1/2}\rangle, \tag{2.5}$$

$$|7\bar{S}_{1/2}\rangle = |7S_{1/2}\rangle + \sum |nP_{1/2}\rangle \frac{\langle nP_{1/2}|H_W|7S_{1/2}\rangle}{E_{7S_{1/2}} - E_{nP_{1/2}}}, \tag{2.6}$$

The magnitude of the mixing is maximum for the S and P states. The mixing of the $6d\,^2D_{3/2}$ with the $6d\,^2P_{3/2}$ states in LS coupling is described by

$$|6\bar{D}_{3/2}\rangle = |6D_{3/2}\rangle + \epsilon'|nP_{3/2}\rangle, \tag{2.7}$$

$$|6\bar{D}_{3/2}\rangle = |6D_{3/2}\rangle + \sum |nP_{3/2}\rangle \frac{\langle nP_{3/2}|H_W|6D_{3/2}\rangle}{E_{6D_{3/2}} - E_{nP_{3/2}}}, \tag{2.8}$$

where H_W is given by Eqn. 2.3. With increasing principal quantum number, n, the differences between the level energies $E_{7S_{1/2}} - E_{nP_{1/2}}$ and $E_{6D_{3/2}} - E_{nP_{3/2}}$ also increase. In Ra^+, this mixing provides for a nonzero transition probability between the $7s\,^2S_{1/2}$ and $6d\,^2D_{3/2}$ states which would be forbidden in LS coupling as an electric dipole transition. The parity violating electric dipole amplitude $E1_{APV}$ is given by

$$E1_{APV} = \langle 7\bar{S}_{1/2}|D|6\bar{D}_{3/2}\rangle, \tag{2.9}$$

Substituting the values from Eqn. 2.6 and 2.8, we obtain $E1_{APV}$ [67].

2.4 Sensitivity to APV

2.4.1 Lifetime of the metastable $5d\,^2D_{5/2}$ state

The radiative lifetime of the excited metastable D states is an important quantity that provides for understanding the atomic level structure and in particular, to verify the atomic wavefunctions to percent level accuracy. Since these electric quadrupole transitions have extreme low transition probability, the measurement of these radiative lifetimes in ions requires isolation, free from disturbing collisions with other particles, at a time scale long compared to the lifetime. For this, a measurement of the lifetime of the metastable $5d\,^2D_{5/2}$ state in a single trapped Ba^+ ion in Ultra-High Vacuum (UHV) in the 10^{-11} mbar range has been performed [87].

In atoms or ions, the lifetime of an excited state is related to the absolute transition probability

$$\tau = \frac{1}{\sum_i A_{ik}} = \frac{\lambda^3}{\langle i|r|k\rangle^2}, \tag{2.10}$$

where i is the lower state and k is the higher state, A_{ik} is the spontaneous transition probability for electric quadrupole transitions which is given by

$$A_{ik} = \sum_i \frac{8\pi\omega^5}{3c^5h} |\langle\phi_i|Q|\phi_k\rangle|^2, \tag{2.11}$$

where Q is the electric quadrupole operator.

2.4.2 Absolute transition frequencies

Precise frequency measurements are an important tool for searching for APV in ionic systems. For such measurements, laser frequency stabilization to a few hundreds of kHz is the necessary prerequisite. These measurements are an important tool to study the systematic effects. The detailed explanation of the precise determination of absolute frequency for the cooling, repump and the clock transitions in a single trapped Ba^+ ion is discussed in Chapter 6 [88].

2.4.3 Light shifts in atoms

The light-matter interaction is the effect of the on-resonant and off-resonant laser fields on the atomic transition. In the presence of on-resonant laser light, the strong coupling of laser light with a single ion result in exchange of population between the two (i.e. ground and excited) states called Rabi oscillation. In the presence of an intense off-resonant laser field, there is no transfer of population between the two states but instead the laser polarises the ion resulting in a shift of the energy levels. This is known as light shift or AC Stark shift. There are two most important parameters that affect the magnitude of these light shifts.

1. Firstly, there is the detuning ($\delta = \omega_0 - \omega_L$) of the laser frequency with respect to the resonance of the transition, where ω_0 is the frequency of the atomic transition and ω_L is the frequency of the laser.

2. The strength of the coupling between the ion and the light field which is determined by the Rabi frequency Ω_{ge}.

In a two-level system and for large detunings compared to the power broadened linewidth, the light shift or the energy level shift is

$$\Delta E_{g,e} = \pm\hbar\frac{\Omega_{ge}^2}{4\delta}. \tag{2.12}$$

For particular ground and excited states $|g\rangle$ and $|e\rangle$, the AC stark shift is

$$\Delta E_{g,e} = \hbar\frac{\Omega_{ge}^2}{4\delta} = \frac{e^2}{4\hbar}\frac{|\langle g|\vec{E}.\vec{r}|e\rangle|^2}{\omega_0 - \omega_L}. \tag{2.13}$$

If the detuning of the light field with respect to the transition frequency is positive (δ>0, 'red detuned'), the excited and ground states shift up and down, respectively by equal amounts (see Fig. 2.4), respectively. In case of δ<0 (blue detuning), the excited and ground states shift down and up, respectively in energy. Light shifts, therefore, enable the determination of the atomic transition matrix elements.

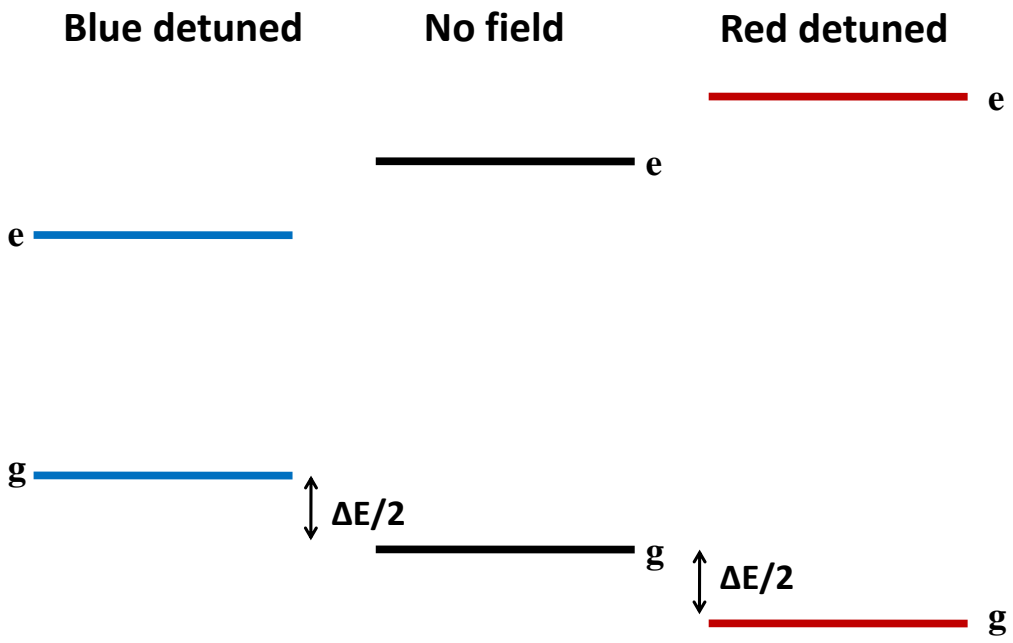

FIGURE 2.4: Energy level shift (light shift) for a two-level system e.g. between the ground and the excited state. The shift of both states during the red detuned and the blue detuned cases are shown.

However, light shifts also depend on the quantization axis and the polarisation of the light field. In the presence of an external intense light field i.e. light shifting laser light, energy level shifts appear in the magnetic sublevels (see Fig. 2.5):

1. Scalar light shift: In this case atomic energy levels shift by the same amount and in the same direction. For our case in Ba^+ and Ra^+, the S and D states shift by Δ_S^S and Δ_D^S. This shift depends on $|m_j|$ and it is observed in both Ba^+ and Ra^+.

2. Vector light shift: The vector light shift of a transition causes a frequency shift Δ_S^V and Δ_D^V where the levels shift in opposite direction depending on

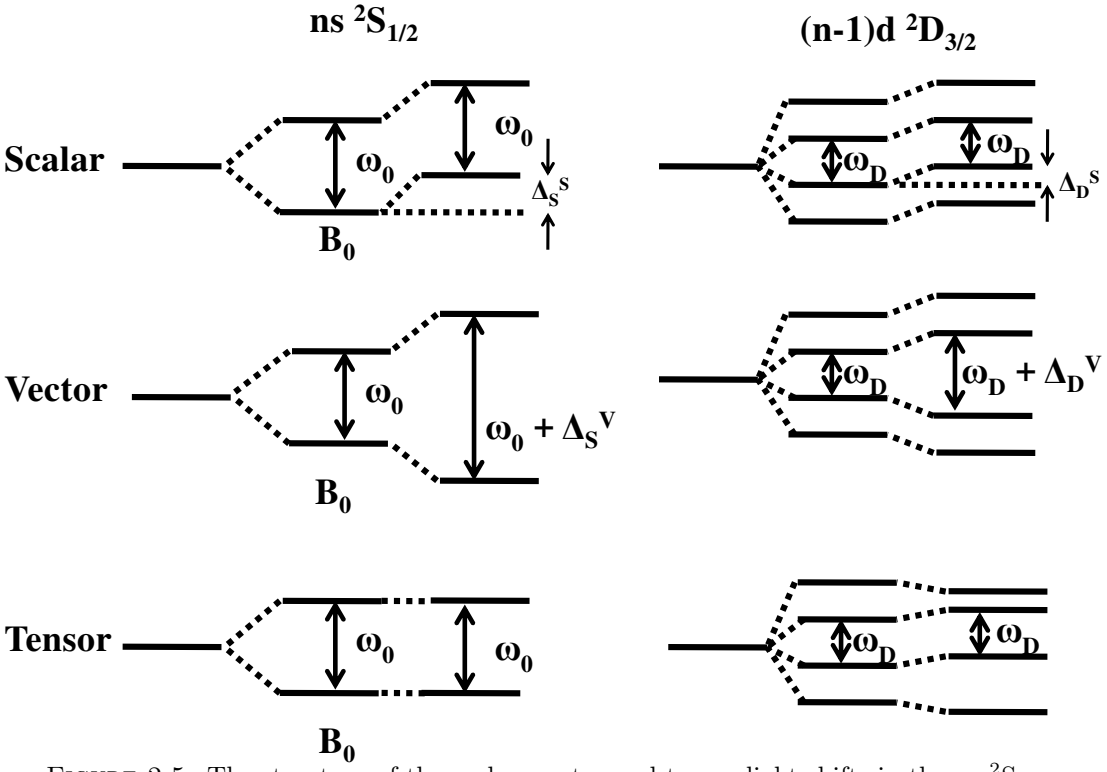

FIGURE 2.5: The structure of the scalar, vector and tensor light shifts in the ns $^2S_{1/2}$ and (n-1)d $^2D_{3/2}$ levels where n = 6 for Ba^+ and n = 7 for Ra^+. Here ω_0 and ω_D represents the splitting in the Zeeman sublevels of the ns $^2S_{1/2}$ and (n-1)d $^2D_{3/2}$ levels respectively. Modified from [89].

the sign of m_j, thus giving rise to additional level separation Δ_S^V in case of ns $^2S_{1/2}$ and Δ_D^V in case of (n-1)d $^2D_{1/2}$. This shift scales with m_j and is seen in case of (n-1)d $^2D_{3/2}$ states where Δ_D^V is an additional level separation in the presence of the interference of two light fields (see Fig. 2.5).

3. Tensor light shift: Unlike the scalar and vector light shifts, the tensor shifts are observed in the (n-1)d $^2D_{3/2}$ states (see Fig. 2.5). This shift is observed for $|m_j| > 1/2$.

TABLE 2.4: The scalar, vector and tensor light shift coefficients in the m = ± 1/2 splittings in the ns $^2S_{1/2}$ and (n-1) $^2D_{3/2}$. These coefficients are essential for doing a quantitative measurement of the light shifts. Adapted from [89].

Coefficients \ (j, j')	(1/2, 1/2)	(1/2, 3/2)	(3/2, 1/2)	(3/2, 3/2)	(3/2, 5/2)
Scalar $s(j, j')$	-1/6	-1/2	-1/12	-1/12	-1/12
Vector $v(j, j')$	-1/3	1/6	-1/12	-1/30	1/20
Tensor $t(j, j')$	0	0	1/12	-1/15	1/60

The scalar, vector and tensor light shift coefficients as calculated from the Clebsch-Gordon coefficients are summarized in Table 2.4. These coefficients are indispensable for the determination of the dipole matrix elements.

2.4.4 On resonance light shifts in Ra^+ and Ba^+.

Calculations of the AC Stark shift due to the standing wave fields on the $m = +1/2$ and $m = -1/2$ Zeeman sublevels of a single Ba^+ ion were conducted considering on-resonance light and small Zeeman splitting [40]. The two standing waves have a phase difference of $\pi/2$ which reverses the sign of the APV signal. This condition is fulfilled by choosing a particular configuration for these two independent fields [40].

$$E1_{APV} = \hat{x}E_0' cos kz \tag{2.14}$$

$$E2 = i\hat{z}E_0'' sin kz \tag{2.15}$$

The coupling strength of $E1_{APV}$ and E2 transitions with the electric fields E_0' and E_0'' is given by the Rabi frequencies.

$$\Omega_{APV}^{m,m'} = -\frac{1}{2\hbar}\sum \langle E1_{APV}^{m,m'}\rangle_i E_0'(0), \tag{2.16}$$

$$\Omega_{E2}^{m,m'} = -\frac{1}{2\hbar}\sum \langle E2^{m,m'}\rangle_{ij}\left[\frac{\partial E_0''(r)}{\partial x_j}\right], \tag{2.17}$$

where m, m' represent the magnetic quantum numbers of the two states and $\langle E1_{APV}^{m,m'}\rangle$ and $\langle E2^{m,m'}\rangle$ are the matrix elements for the dipole and quadrupole transitions, respectively. The light shift of the Zeeman split sublevels of a single ion is generated by the total field $\vec{E}(\vec{r})$ that has two independent components i.e. electric quadrupole and electric dipole forbidden components. The magnitude for each of the components in a single Ra^+ ion has been calculated by [40, 90] using the field in Eqn. 2.16 and 2.17

$$\Delta\omega_{APV} \propto \langle ns|E1_{APV}|(n-1)d\rangle E_0' \tag{2.18}$$

$$\Delta\omega_{APV} = (\pm)46.4 \times 10^{-11}\frac{ea_0}{2\hbar}E_0'' \tag{2.19}$$

$$\Delta\omega_{E2} \propto \langle ns|E2|(n-1)d\rangle E_0'' \tag{2.20}$$

$$\Delta\omega_{E2} = -2 \times 10^{-4}\frac{ea_0}{2\hbar}E_0''. \tag{2.21}$$

The quadrupole transition matrix element $\langle ns|E2|(n-1)d\rangle$ in Ra^+ and Ba^+ ions has been calculated using atomic theory [41]. The values for the $\langle ns|E1_{APV}|(n-1)d\rangle$ matrix element both for Ra^+ and Ba^+ are given in Table 2.5. The APV

effect (see Figs. 2.2 and 2.3) is optimized if the amplitude of the E_0' field increases, while the intensity of the E_0'' laser field is minimal. The light shift due to the quadrupole field is independent of m and the Larmor frequency does not change. For the dipole transition, the light shift depends on the magnetic quantum number, m. This produces a differential light shift between the two sublevels [40] (Δ_{diff} in Fig. 2.2). For a single Ra^+ ion and a single Ba^+ ion localized in a laser field of 100 mW focused to 10μm beam size the expected differential light shifts are [40, 91].

$$Ra^+ : \Delta_{diff} = (\Delta\omega_{APV}^{m=1/2} - \Delta\omega_{APV}^{m=-1/2})/2\pi \approx 4Hz \tag{2.22}$$

$$Ba^+ : \Delta_{diff} = (\Delta\omega_{APV}^{m=1/2} - \Delta\omega_{APV}^{m=-1/2})/2\pi \approx 0.4Hz \tag{2.23}$$

The measurement of the differential light shift can be performed with RF spectroscopy and the shelving technique [24, 89, 90, 92]. The possible accuracy of an APV effect in a single Ra^+ ion for one day of actual measurement time is [43]

$$\frac{S}{N} = \frac{E1_{APV}}{\partial E1_{APV}} \cong \Delta_{diff} f\sqrt{Nt\tau} \tag{2.24}$$

where N is the number of particles and $N = 1$, f is an efficiency factor determined by the experimental conditions, τ is the lifetime of the metastable $D_{3/2}$ state and t is the total measurement time. Table 2.5 gives the expected APV effects [40] for a single trapped Ba^+ and Ra^+ ions. A single Ra^+ has the potential for a more than

TABLE 2.5: Expected light shifts in single trapped Ba^+ and Ra^+ ion on resonance for 100 mW beam focussed to a 10μm diameter spot size at the ion at wavelength 2050 nm for Ba^+ and 828 nm for Ra^+.

Expected APV light shifts	Ba^+	Ra^+ [43]
Differential light shifts	0.4 Hz	4 Hz
Signal to Noise	200	180
Statistical accuracy	1.2 %	0.4 %

5-fold improvement in the measurement of the Weinberg angle within one day of measuring time. In order to achieve this desired precision, full understanding, and control over all systematic effects is indispensable.

2.5 Ba^+: predecessor to Ra^+ in APV measurements

Ra^+ isotopes exhibit a high sensitivity to the parity violating effects. However, all its isotopes are radioactive. Therefore, it is considered an efficient way of progressing by developing all tools and methods for an APV experiment with its stable chemical analogue Ba^+. It appears that only the wavelengths of optical

transitions are different and this facilitates a switch over in the final stage from Ba^+ to Ra^+. Stable Ba^+ is well-suited as a predecessor to radioactive Ra^+, because of its similar level scheme and chemical properties. The biggest challenges for the APV experiments on Ra^+ are the determination of the spectroscopic properties of radium like the transition wavelengths and line strengths and the laser cooling and trapping of heavy alkaline earth elements. At the latter part, Ba^+ comes into play. Once the properties are determined with Ba^+ the results can be transferred to Ra^+.

2.5.1 Concept of the experimental setup

The concept of the experimental setup includes the preparation of a single isolated ion for spectroscopy in a hyperbolic Paul trap, frequency stabilized lasers and data acquisition and analysis.

Hyperbolic Paul trap

For efficient localization of a Ba^+ ion, it is necessary to first trap and then laser cool the ion. The hyperbolic Paul trap [52, 93, 94] is the central instrument for the precise atomic physics measurements. Fig. 2.6 is a pictorial representation of the trap electrode assembly used in this experiment. We have a ring electrode and two electrically connected endcap electrodes. To these electrodes, a sinusoidal AC voltage $U(t) = V_o cos\Omega_{RF} t$, is applied (see Fig. 2.6(d)). The trap is housed in an ultra-high vacuum chamber at a residual gas pressure of typically 2×10^{-11} mbar which makes it a system that is essentially devoid of all kinds of external perturbations. Such a trapping assembly accounts for dynamical trapping conditions by creating a harmonic oscillating potential, Φ, with a central minimum. It is given by

$$\Phi = \frac{U_0 + V_0 cos\Omega_{RF} t}{2d^2}(2z^2 - x^2 - y^2), \tag{2.25}$$

where

$$d = \sqrt{\frac{1}{2}r_0^2 + z_0^2}. \tag{2.26}$$

Here U_0 is the DC potential, V_0 is the amplitude of the potential difference between the electrodes and Ω_{RF} is the rf frequency of the applied AC voltage. The Mathieu equations describe the equation of motion for a charged particle. We have for the particle coordinates

$$\frac{d^2u_j}{dt^2} + (a_j - q_j cos2T)u_j = 0 \tag{2.27}$$

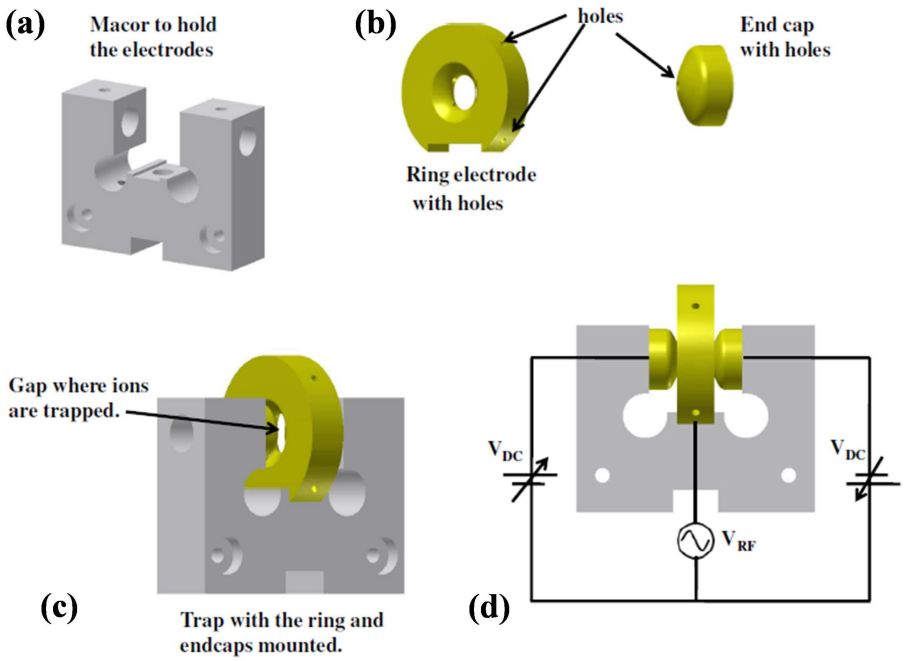

FIGURE 2.6: The ring and endcap electrodes of the Paul trap (b). These electrodes are mounted with the help of a Macor piece (a). Mounted trap with all electrodes(c). The ions are trapped using a rf field (d) in the gap created by the electrodes.

where $u_1 = x, u_2 = y, u_3 = z$, $T = \frac{1}{2}\Omega_{RF}t$ and a_j and q_j are the dimensionless stability parameters that determine the stable and unstable solutions of the Mathieu equations. We have

$$a_x = a_y = \frac{-4QU_0}{Md^2\Omega_{RF}^2} \quad a_z = \frac{8QU_0}{Md^2\Omega_{RF}^2} \tag{2.28}$$

$$q_x = q_y = \frac{2QV_0}{Md^2\Omega_{RF}^2} \quad q_z = \frac{-4QV_0}{Md^2\Omega_{RF}^2} \tag{2.29}$$

where M and Q are the mass and charge of the ion, respectively. The criterion for the stable confinement of this charged particle in the harmonic potential is determined by solving the equations of motion i.e. Eqn. 2.28 and 2.29. The solutions to the Mathieu equations can be expressed as a linear combination of harmonic functions

$$u_j(T) = A_j \sum c_{2n} cos[(\beta_j + 2n)T] + B_j \sum c_{2n} cos[(\beta_j + 2n)T], \tag{2.30}$$

where j=1,2,3. A_j, B_j are constants that depend on the initial conditions and β_j describe the stability parameter for the trap and $\beta_j \approx a_j + \frac{q_j^2}{2}$ where $a_j, q_j \ll 1$ for a particle in an oscillating field. In this case, the first order solution for the

Mathieu equation is

$$u_j \approx A[1 + \frac{q_j}{2} cos\Omega_{RF} t], \tag{2.31}$$

where $A = u_0 cos(2\pi\omega_j t + \phi)$. The particle shows a harmonic oscillation at frequency ω (macromotion) modulated by an oscillation at frequency Ω_{RF} (micromotion)

$$\omega_{j,RF} = \frac{1}{2}\beta_j \Omega_{RF}. \tag{2.32}$$

The secular frequency can be associated with the motion of the ion in a harmonic potential with frequency $\omega_{j,RF}$. In adiabatic approximation where the potential energy of the ions corresponds to the kinetic energy of the oscillation, the potential depth which generates the harmonic motion is

$$D_r = \frac{QV_0}{Mr_0^2\Omega_{RF}^2} = \frac{D_z}{2}, \tag{2.33}$$

for a hyperbolic Paul trap with $r_0^2 = 2z_0^2$. If a DC voltage (U_0) is applied to the end caps in a symmetric configuration, the potential depth of the trap changes and we have

$$D_z^{'} = D_z + \frac{U_0}{2}, \tag{2.34}$$

and

$$D_r^{'} = D_r - \frac{U_0}{2}. \tag{2.35}$$

Fig. 2.7 represents the Mathieu stability diagram [95] along with the lowest stability region for the hyperbolic 3D quadrupole Paul trap [52]. The maximum value q = 0.91 (for $U_0 = 0$) sets a boundary for the minimum mass/charge ratio of the particles that can be stored in a Paul trap. For high values of q, the orbits diverge and the ions are ejected from the trap (see Fig. 2.7). An additional DC potential (a $\neq 0$) allows to change this stability limit. This provides for a means to eject particles with e.g. heavier mass/charge ratios. The manipulation of the trap potentials across the stability region is a very powerful tool to avoid trapping of undesired ions. A detailed explanation of the properties of such a trap is given in Chapter 3.

Frequency stabilized lasers

For precision APV experiments with a single trapped Ba^+ and Ra^+ ion, lasers with stable light frequency are required i.e. the frequencies need to be controlled to a few tens of kHz level and with typical intensities of $100\,mW/cm^2$. Most of the transitions for Ba^+ and all for Ra^+ are accessible with light from semiconductor diode lasers (see Table 2.1 and 2.2). We use diode lasers in Littrow configuration where the antireflection coating of the diode and the external optics like a

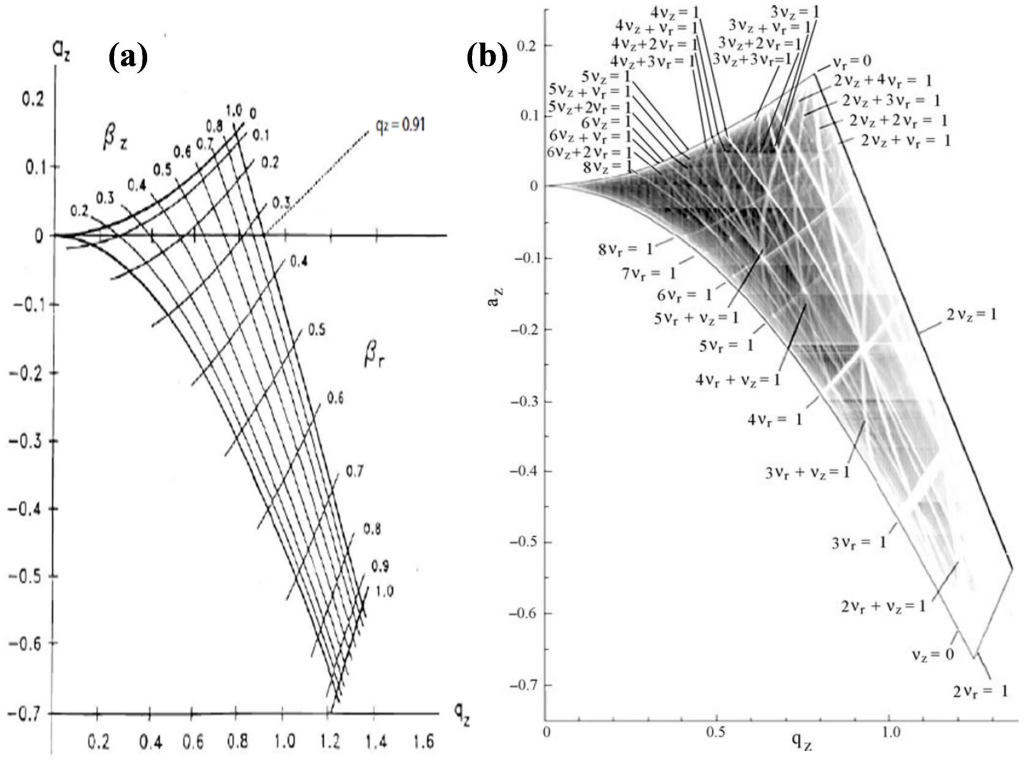

FIGURE 2.7: (a) Mathieu stability diagram in (a_z, q_z) space for a hyperbolic Paul trap. (b) An example of the same Mathieu stability diagram for a realized trap where the extra lines represent the different parametric resonances for different values of a and q where the stable trapping of ions is not possible [95].

collimating lens and a grating are used to provide a laser resonator. In this configuration, the first-order diffracted beam from the grating provides optical feedback to the diode thereby increasing the gain and hence results in lasing. Rotation of the diffraction grating is the primary means for tuning the laser output to the desired wavelength. These lasers are less expensive, compact, have long operation times and can be scanned over a frequency range of up to a few GHz. Frequency stability is maintained with saturation absorption spectroscopy to within 1 MHz or even better. For high-precision laser spectroscopy, the output light of such semiconductor lasers can be further narrowed down in frequency by additional optical elements such as high finesse cavities [96]. For Ba^+ level spectroscopy, the light from an external cavity diode laser at wavelength $\lambda_{1107} = 1107\,\text{nm}$ is frequency doubled to produce a beam at λ_{553}. Light from a laser diode at λ_{413} is employed for photoionization of Ba atoms to Ba^+ ions. A dye laser provides light at λ_{650} for repumping Ba^+ from the $5d\,^2D_{3/2}$ state to the $6p\,^2P_{1/2}$ state. The dye laser system has been chosen for its good long term frequency stability, its narrow laser linewidth (about 500 kHz) and its spectral purity in comparison to the external cavity diode lasers. For the cooling transition in Ba^+ at λ_{494} light, this frequency is generated by frequency doubling the light from a solid-state Ti:Sapphire laser at

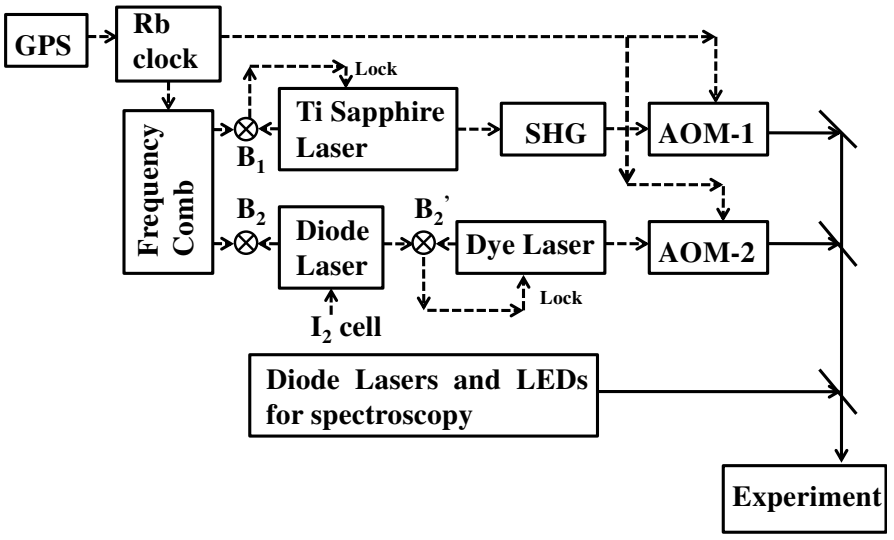

FIGURE 2.8: Schematic overview of the laser systems and their frequency locking for the experiment.

wavelength $\lambda_{987} = 987\,\text{nm}$. Further, a frequency comb is used as an optical ruler for the accurate measurement of these frequencies for precision spectroscopy. In addition to these lasers, light emitting diodes (LEDs) at λ_{455} and λ_{617} are used to drive the ion to and from the metastable D state. Fig. 2.8 gives a brief overview of their laser systems employed in the experiment. A detailed description of these stabilized laser systems, LEDs, and the frequency stabilizing techniques are given in Chapter 4.

Data acquisition and analysis

The experiment is controlled and the data are read out by the data acquisition system developed at KVI. A Voltage to Frequency Converter (VFC) module is used to transform all the signals from the photomultiplier tube (PMT), photodiodes(PD) and rf and dc voltages into frequencies. All these analog signals are further converted into digital ones by a scaler module. These digital signals are then further read by a VME with a frequency of 10 Hz. Several other parameters relating to this experiment like laser diagnostics, frequency comb, an electron multiplying CCD camera (EMCCD) and monitoring the wavelengths via the wavelength meters are all controlled by different individual computers. Further, a program named CADDIE (Control and Distributed Data-acquisition Integrated Environment) developed under the TRIμP program provides for an efficient communication between the computers (see Fig. 2.9). This program combines different

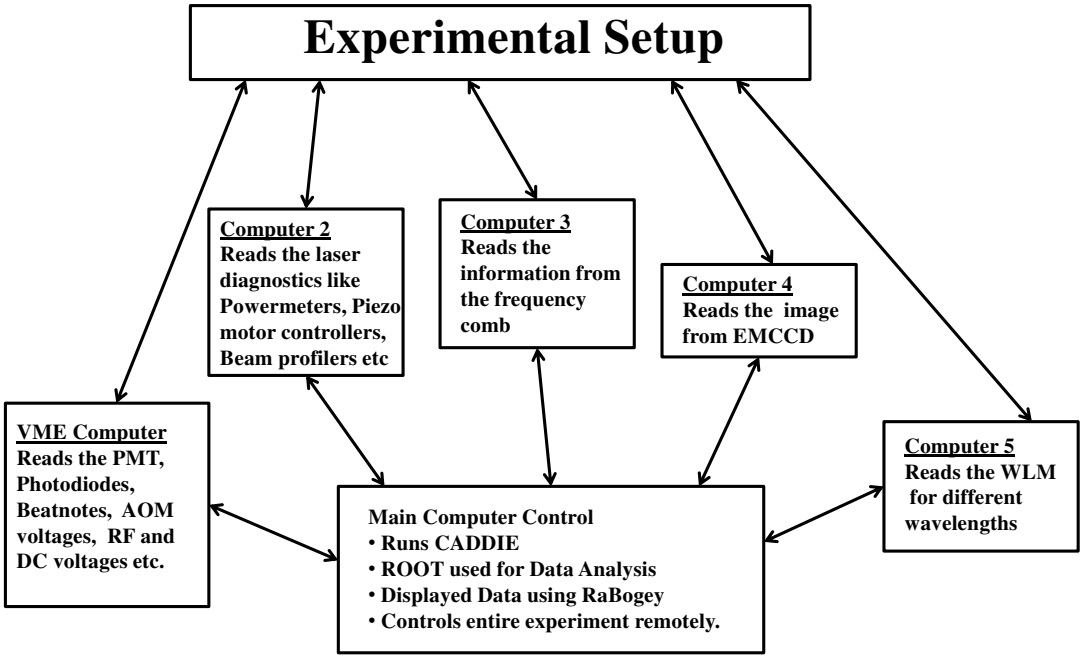

FIGURE 2.9: Schematics overview of the data acquisition (DAQ) system for the experiment. All computers run Caddie servers to send their data to the main computer. The data from different computers are handled by the main computer using ROOT.

data streams from a variety of sources into one synchronized data file with the experimental data. The data streams are made available for several uses at the same time.

The main computer runs the ROOT software developed at CERN [97, 98]. A ROOT based program called Bogey does the online analysis and monitors the crucial experimental parameters. A separate canvas is used to display the updated image from the EMCCD and the settings like exposure times, gain etc. are varied using the camera fit parameters. The updated photon-rf phase correlation signal providing information about the ion localization is displayed via canvas. Besides this, the laser beam shutters, power supplies for the oven and rf voltage levels are controlled by a digital output module (CAEN VF997) via the Bogey. Scripts are also written in ROOT for further analysis of the collected data.

2.6 Section Summary

Trapped and laser cooled heavy alkaline earth ions i.e. Ba^+ and Ra^+ are chosen here as the suitable candidates for APV. The measurement principle for APV in these atomic systems i.e. differential light shifts of the Zeeman sublevels in single

ions of Ba^+ and Ra^+ have been established. The concept of experimental setup has been accomplished. With well chosen light fields, the APV manifests itself as a difference in the light shift on resonance of the Zeeman sublevels in the ground state.

Chapter 3

Experimental tools for single ion spectroscopy

In our experiment, we investigate the heavy alkaline Ba^+ ion inside a hyperbolic Paul trap assembly. It is placed in Ultra-High Vacuum (UHV) in order to provide an environment with minimal disturbances for a single laser cooled Ba^+ ion. Rf and dc electric fields provide for control of the ion position at sub-μm scale. Photons scattered from the localized ion are detected both by an Electron Multiplying Charge Coupled Device (EMCCD) and a PhotoMultiplier (PMT). These detectors permit spatial and temporal detection of the trapped ion. The ions are created by photoionization of atoms in an atomic beam originating from an efficient UHV compatible oven.

3.1 Ultra-High Vacuum (UHV) system

Collisions of the trapped ion with the background residual gas in the vacuum system affect the lifetime of excited states of the trapped ions. They have an influence on the high-precision measurement of the lifetime of the excited atomic states. Therefore, the residual gas pressure in the chamber is kept below 10^{-10} mbar to reduce the influence of collisions. Such vacuum conditions are achieved by mounting the hyperbolic trap in an ultra-high vacuum compatible stainless steel (RVS 316LN) chamber. This material has been chosen to minimise the perturbations of the magnetic field environment. This chamber is rigidly mounted on to an optical table (see Fig. 3.1).

The operating pressure of a few 10^{-11} mbar in the chamber is achieved by various means. The surfaces of the chamber have been polished and glass ball treated

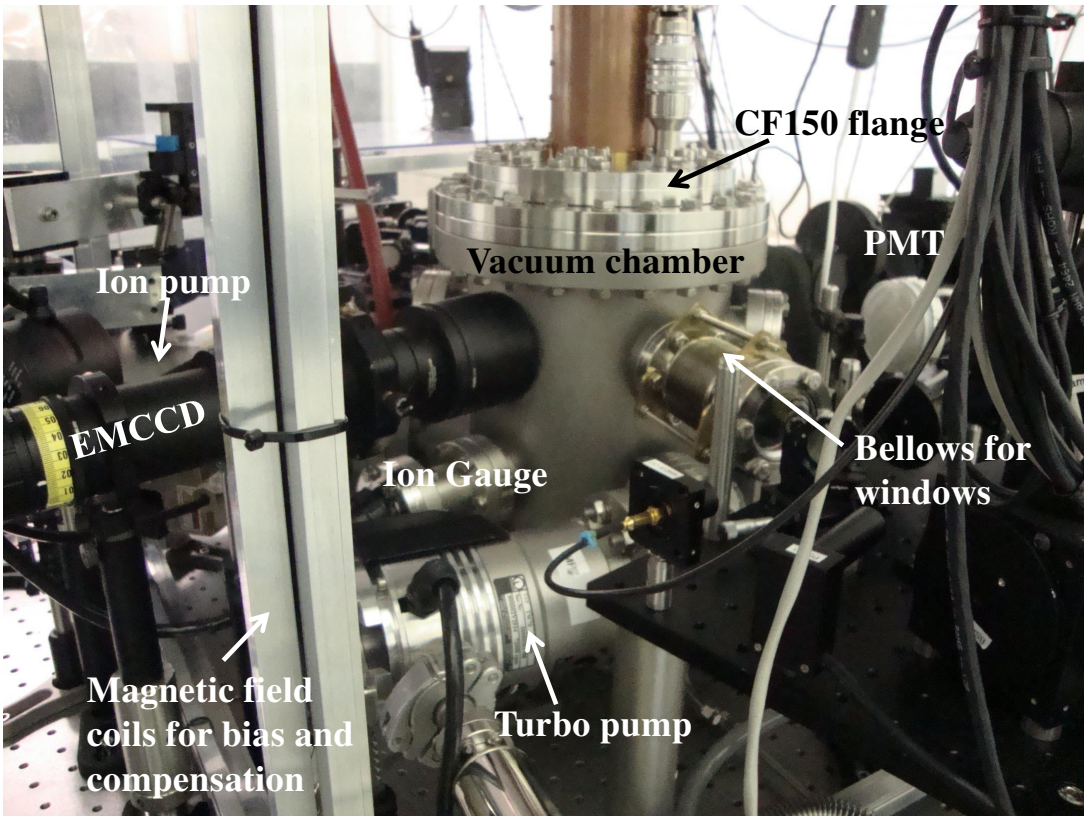

FIGURE 3.1: Ultra-High Vacuum chamber housing the rf Paul trap for Ba^+ ions in the experiment (photograph). The instrumentation is indicated by arrows.

(as specified by the manufacturer PINK). Then an oil-free scroll roughing pump (scroll Vacuum Pump from Scroll Meister) is used to reach a pressure down to several 10^{-3} mbar. A 70 l/s turbo pump (TURBOVAC TW70 H from Oerlikon Leybold Vacuum) reduces the pressure to several 10^{-8} mbar. During this phase of pumping down the chamber is heat treated at $\sim 150\,^{o}$C for about typically 3 days. Finally, a 75 l/s Ion Pump (TiTan from Gamma Vacuum) enables reaching a residual gas pressure below 10^{-10} mbar. Furthermore, a titanium sublimation pump (SUBLI-CON 51 from VACOM) is typically operated at a current of 40 A for 1 minute once a week to achieve a wall coating of the chamber that assists pumping to about 10^{-11} mbar. The central trapping setup inside the vacuum chamber is protected against the direct exposure to sublimated Ti atoms and a Ti coating by a mechanical baffle in the direct path.

The pressure is monitored with a Bayard Alpert ion gauge connected to an IGC100 Ion gauge controller (VACOM). This ion gauge is occasionally degassed to clean the ion gauge. During optical measurements with trapped ions, the gauge filament is turned off in order to avoid stray light and reduce the pressure even further. The ion pump controller is turned on only when the pressure in the chamber reaches to

about 10^{-7} mbar or below. At pressures below 10^{-10} mbar, we use the ion pump current for measuring the residual gas pressure.

Custom AR coated glass CF35 windows (see [67] for detailed specifications) are attached to flexible bellows that seal the ports where the laser beams at wavelengths λ_{494} and λ_{650} enter and leave the chamber. The windows (MVPZ40-DUVQ-AR468/493/802 from VACOM) have reflectivity of 0.12 %, 0.09 % and 0.32 % per surface at the operating wavelengths of 494 nm for Ba^+, 468 nm and 802 nm for Ra^+, respectively as specified by the manufacturer. The bellows allow avoiding the laser light interference by slightly tilting the windows against the beam axis. The other windows in the setup do not have bellows attached to them. Two sets of apertures act as a light baffle to avoid stray light from the laser beams. One set of these apertures is placed on the input window side of the vacuum chamber and another set before the exit window. Each set consists of 3 apertures with the outer two having an inner diameter of about 3 mm while the innermost one has a diameter of 2.5 mm. These apertures are coated with a UHV-compatible black paint (MLS-85-SB) [67] and the holes are provided with knife edges to prevent reflections. When the pressure in the chamber had reached less than several 10^{-8} mbar the atomic oven was turned on for the first time, in order to determine the outgassing rate of the heated oven and not to destroy the vacuum conditions when the pressure has reached the level of 10^{-11} mbar.

3.1.1 Maintaining good vacuum conditions

Baking of the vacuum system enables to attain a pressure of 10^{-11} mbar. For the purpose of baking, the top and bottom CF200 flanges of the chamber are connected with a stainless steel ring heaters that are wrapped around these flanges. This particular type of heaters is advantageous for baking the chamber for two particular reasons. Firstly, due to the presence of the necessary optics close to the chamber, there is a spatial limitation for the other kind of ceramic heaters that were available. Secondly, conduction of thermal energy works more efficiently than by convection that is used with ceramic heaters. These heaters are normally operated by a controller (built in-house) at a set temperature of about 160 °C to attain a steady temperature of about 140 °C (measured on the surface of the top flange of the chamber with a resistive thermometer). During this baking process, the heating of the ion pump is also turned on to clean the ion pump itself. During the baking, the whole chamber is wrapped throughout with aluminium foil.

Venting of UHV with dry nitrogen gas and liquid nitrogen cold traps

The occasionally necessary venting of the system is done with clean and dry N_2 gas of 99.99 % purity. A cold trap (see Fig. 3.2) in the gas line to the chamber at liquid nitrogen temperature collects condensable vapours in the venting system and in particular captures water vapour.

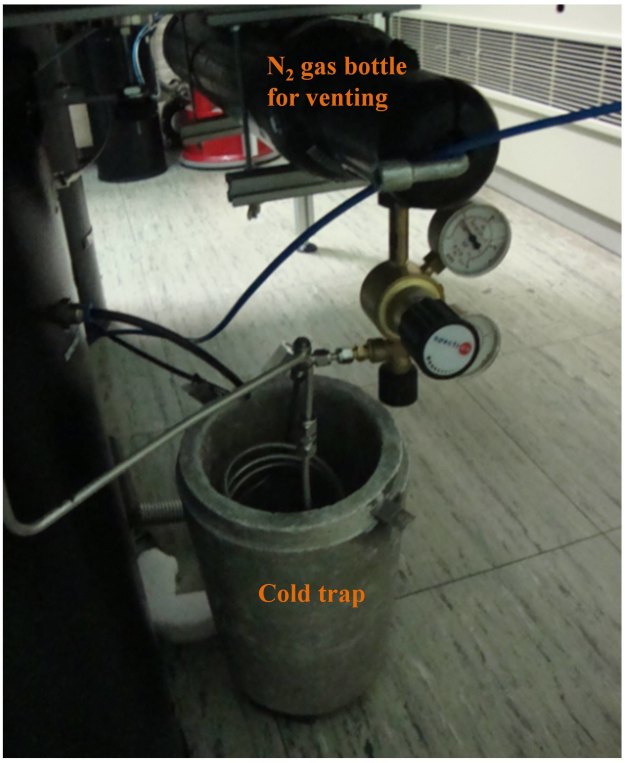

FIGURE 3.2: Cold trap along with the Nitrogen gas used during venting of the vacuum chamber. It is fixed under the optics table.

Cleaning of the ion pump

In the ion pump, there can be contaminations either due to the deposition of titanium coming from the filaments of the titanium sublimation pump or from when the pump is exposed to air especially when venting the chamber. These contaminations can be removed by running a discharge during which the valve to the roughing line is opened until the pressure in the chamber reaches about 10^{-2} mbar. At such a low pressure when the ion pump is turned on, it creates a plasma glow discharge. For a cleaned pump, at a residual gas pressure of about 10^{-11} mbar the ion pump current is $I_p = 24.5$ nA. The pump can maintain a pressure below 10^{-10} mbar for several months.

3.2 Hyperbolic Paul trap for optical spectroscopy

The hyperbolic trap (see Figs. 2.6 and 3.3) is mounted from the CF150 flange top of the UHV stainless steel chamber. The basic dimensions of the Paul trap are based on a prototype for storing different mass ions which had earlier been employed at the IBM Almaden Research Center, San Jose [99]. This trap consists of four 77.3 mm long OFHC (Oxygen free High Conductivity) Copper posts on which is mounted a Cu disc of diameter 95 mm and thickness 12 mm. This disc contains holes which are used to mount the trap electrodes parts. A MACOR® piece is used to hold the ring and the endcap electrodes assembly. A pictorial representation of the mounted electrodes are shown in Figs. 3.3 and 3.4. The ring has an inner diameter of 5 mm while the endcaps are separated by $\frac{5}{\sqrt{2}}$ =3.52 mm. The MACOR® spacer has graphite lines to provide for conductance to remove extra electrons that might have been deposited during the ion production process. For trapping of ions, the ring and endcap electrodes are further connected by a 2.5 mm diameter Cu wire to a feedthrough that sits in the center of the top CF150 flange.

The MACOR® is held in position by an L-shaped and hockey stick shaped Cu parts on both sides. The L-shaped part is used to hold the oven in position (labelled 10 in Fig. 3.3). The hockey stick shaped part (labelled 11 in Fig. 3.3) is employed to hold a best form lens of 40 mm focal length via a lens holder. The convex surface of the lens faces the trap and the flat surface points in the direction of the PMT to get a collimated beam. The lens holder is blackened throughout to avoid stray reflections. There is a 1 mm slit in the direction where the laser beams enter the trap which is also helpful for alignment of the beam through the trap. This slit is also blackened with UHV compatible black paint (MLS-85-SB) [67] to prevent any reflections. Every screw in the UHV environment has been prepared with the threaded part filed in such a way that they provide pumping through each part and sunken screws are usually used to remove any kind of sharp edges close to the electrodes of the trap setup.

The availability of extra optical ports is required for spectroscopic measurements. The endcap electrodes yield optical access for a laser beam through a 1 mm hole in their center. This feature has been exploited for performing light shift measurements (see Chapter 7). Further, this trap was modified to have 4 extra electrodes that can be employed to compensate for static stray fields and have better control of the ion motion. These extra electrodes were embedded in the ring electrode. They had 1.16 mm diameter and had 0.07 mm of electrical insulation of kapton around them.

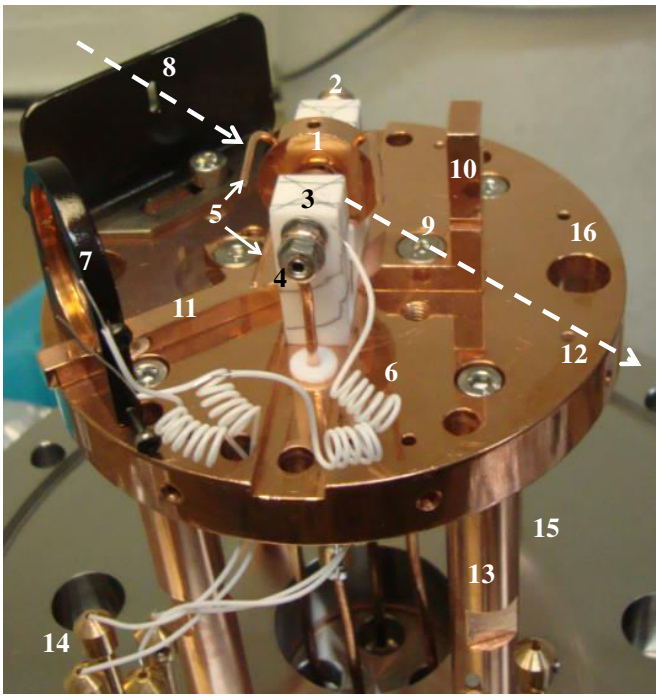

FIGURE 3.3: Photograph of a partially mounted trap assembly. 1) ring electrode, 2) two endcap electrodes, 3) Macor that holds the electrodes and black graphite markings, 4) holes of 1 mm diameter on the endcaps, 5) compensation electrodes, 6) Teflon cables connected to compensation electrodes, 7) lens holder, 8) slit through which laser beams enter, 9) sunken screw to prevent sharp edges, 10) L-shaped holder to mount the oven, 11) Hockey stick shaped Cu part, 12) dotted line with arrow pointing in the direction of the laser beams, 13) OFHC Cu posts, 14) feedthroughs for the 4 compensation electrodes, 15) CF150 flange, 16) Cu disc on which the whole setup is mounted. The dotted arrow points in the direction of the entry and exit of the laser beam through the trap.

Prior to assembling the copper parts, they are surface polished and cleaned in an ultrasonic bath with ethanol and thereafter with acetone. To prevent the oxidation of these copper parts, they were stored prior to their installation in the UHV experiment vacuum chamber in air tight desiccators with dry silica as desiccant.

3.2.1 Electric fields in a hyperbolic Paul trap

3.2.1.1 Rf trapping with resonators

In order to trap and localize ions, we need to create a pseudopotential well by applying a rf voltage to the electrodes. The rf voltage for trapping Ba^+ ions in a hyperbolic Paul trap is produced by the resonant electronic circuit as shown in

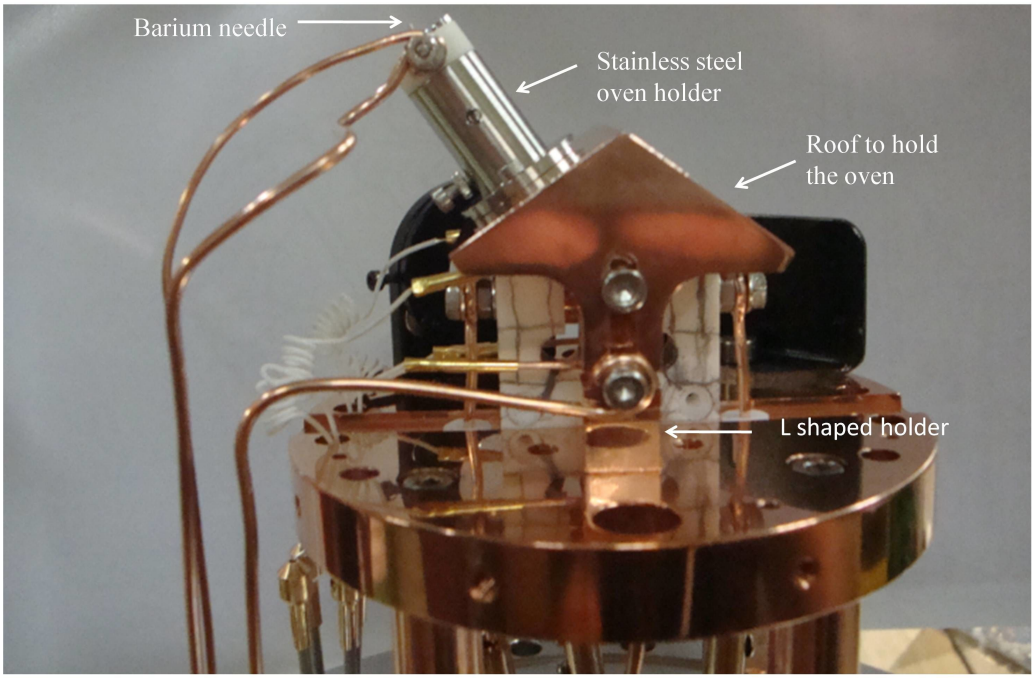

FIGURE 3.4: Mounted trap assembly together with the Ba atom oven. It shows the L-shaped holder that holds the oven rigidly in position. The teflon coated wires are used to connect the extra correction electrodes.

Fig. 3.5. The rf signal is generated from an HP33120A function generator. For pre-amplification of the output from the function generator a Mini-Circuits coaxial amplifier ZHL-1A-S (AMP1) is used and post-amplified with an RM-KL500-24 high power linear amplifier (AMP2) (see Fig. 3.5). A combination of two 50 Ω impedance low pass rf filters at 6 MHz (HPLP-06P00-C-300-N) and 11 MHz (HPLP-06P00-C-300-N) are installed to suppress higher harmonics in the trap potential. Further, this rf signal generated from the HP33120A function generator goes through a rf switching scheme (as shown in Section 3.2.1.2) which contains a series of a combiner, attenuator, and TTL switches which helps in changing the rf applied to the electrodes. A 20 dB attenuation rf probe connected to a URV35 rf millivolt meter is used to monitor the rf input in the LC circuit. The rf pickup is connected to an oscilloscope. The synthesizer frequency is tuned to the resonance of the LC circuit by this rf pickup signal and this is used to monitor the behaviour of the step-up transformer. The Q factor for this circuit is about 100. Table 3.1 shows a summary of the electrodes to which the rf is applied, the corresponding resonant frequencies, rf pickup and actual rf voltage used to trap ions. We use two 3 nF, 100 V and 10k Ω (not specified for high Q and 50 Hz) connected to two 10 MΩ , 2 kV resistor, and a 30 nF capacitor (specified for high Q and high frequency) are used to shunt the ground via a coaxial cable.

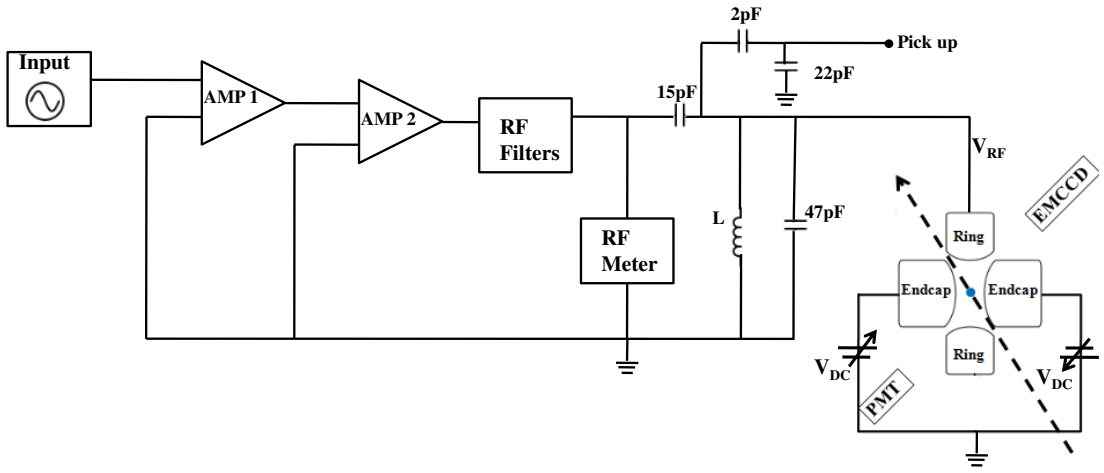

FIGURE 3.5: Circuit diagram for the rf supplied to the ring electrode. Here dc voltage can be applied to the individual endcap electrodes. The blue dot at the center of the electrodes represents a singly trapped Ba^+ ion. The dotted line shows the direction of the laser beam which overlaps with the ion.

TABLE 3.1: Calibration parameters for the different circuit schemes and resonator coils.

Resonator	Electrode to which high voltage is applied	Frequency [MHz]	rf pickup [Vp-p]	rf voltage [Volts]
1	Ring	5.446	1	230
1	End-caps	5.223	1	230
2	Ring	6.443	1	690
2	End-caps	6.246	1	690

Furthermore, when rf is applied to the ring and the endcaps are grounded the part connecting the 10 MΩ, 2 kV resistor, and 30 nF capacitor are also grounded so that an additional dc voltage can be applied on these endcaps. This coaxial cable (see Fig. 3.6 for a pictorial representation) is used to cover the huge antenna of high voltage. An 1800 pF high Q, 2 kV capacitor is used to have a balance of high rf voltage between the two end caps which makes it easier to trap ions. This circuit connection is used to prevent the ac leak from entering the dc voltage supply. Inside the chamber, this high rf voltage is normally provided by using a set screw type of connectors which provides for a good contact. On the outside of the chamber, these are connected to the barrel type or slip on connectors.

The higher harmonics on the rf resonant spectrum makes trapping very difficult. This can come from a blown up capacitor or a bad contact due to a layer of oxidation in the slip on connectors. This whole circuit is nicely covered by a

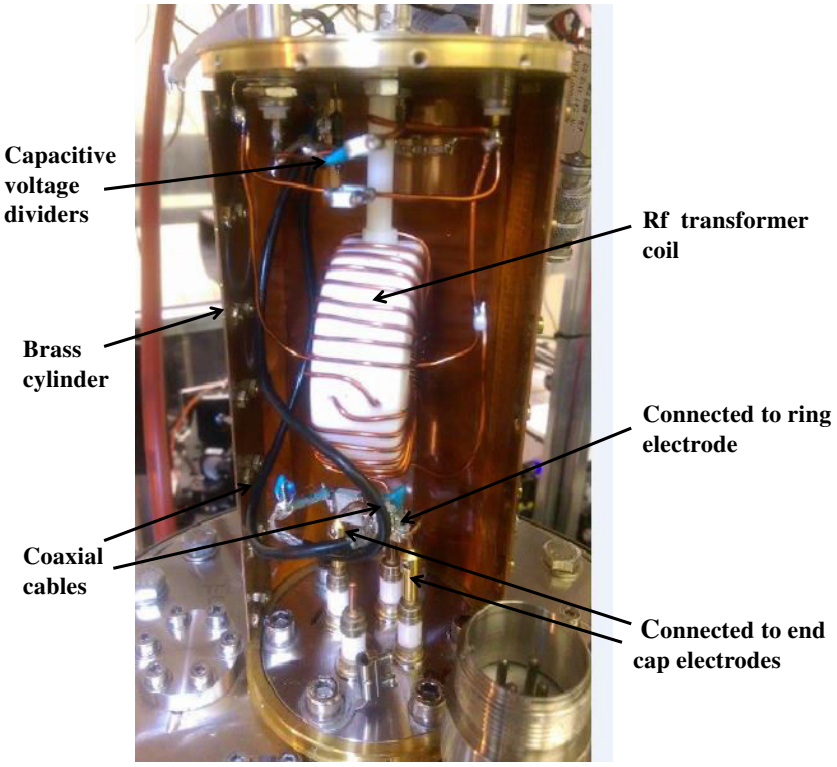

FIGURE 3.6: Photograph of transformer coil (center) that provides the trapping voltage to the electrodes. The connections to the HV DC feedthroughs connected to the endcap electrodes and the ring and capacitive voltage dividers for monitoring are visible. All the parts producing and monitoring the trapping voltages are protected inside a brass cylindrical shield.

kapton insulator and then by a brass cylinder so as to avoid sending rf to other sensitive electronics.

Balancing the voltage on the two endcaps

For trapping of ions with the rf applied to the endcaps, balancing of the voltages applied to the endcaps plays an important role, because that provides for putting the ion in the potential minima of the trap. This was done and it was concluded that there is about 350 V on each of the endcaps. This balancing helped in the better trapping of ions.

3.2.1.2 Adjusting the rf amplitude

Rf switching is an efficient method of loading few ions in the trap and cleaning it from undesired species. The switching mechanism provides a choice between four levels of the applied rf voltage. These four levels include the highest rf voltage,

constant voltage, lower voltage level and the dump level in which case the ions are lost/dumped (see Appendix B). The switch is controlled by 3 TTL level outputs via the data acquisition system (see Fig. 3.7).

3.2.2 Compensation of stray electric fields

A single Ba^+ ion confined in a hyperbolic trap is sensitive to stray charges that accumulate on the surface of the trap electrodes. The stray charges displace the ion from the trap center. The fields are readily build-up from charge depositions onto the trap electrodes during ion loading due to photoelectric charge creation from laser fields. Precise compensation of these stray electric fields is essential for our precision experiment.

Compensating micromotion means placing the ion at a position with a minimum amplitude of the rf quadrupole field. This is implemented by applying precise DC correction voltages to the individual trap electrodes. This can be further improved by dc voltages applied to the additional correction electrodes (see Fig. 3.3). The dc voltages can be adjusted such that the ion does not move when changing the rf voltage amplitude. Fig. C.1 of Appendix C shows the initial circuit diagram which provides for a dc potential being applied to the endcaps individually. The dc connections have been further modified by adding a circuit where a common

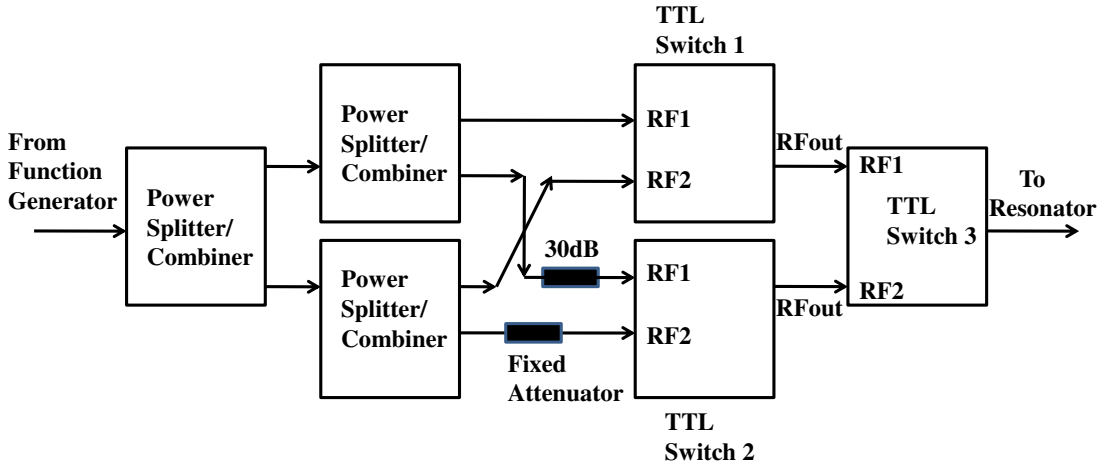

FIGURE 3.7: RF switching with fixed attenuation. This switching serves for the phase coherent changing of the trapping voltages for an efficient loading of ions into the trap. The power splitters/combiners are Minicircuits ZFRSC-42-S+ specified for 50 Ω and DC-4200 MHz.

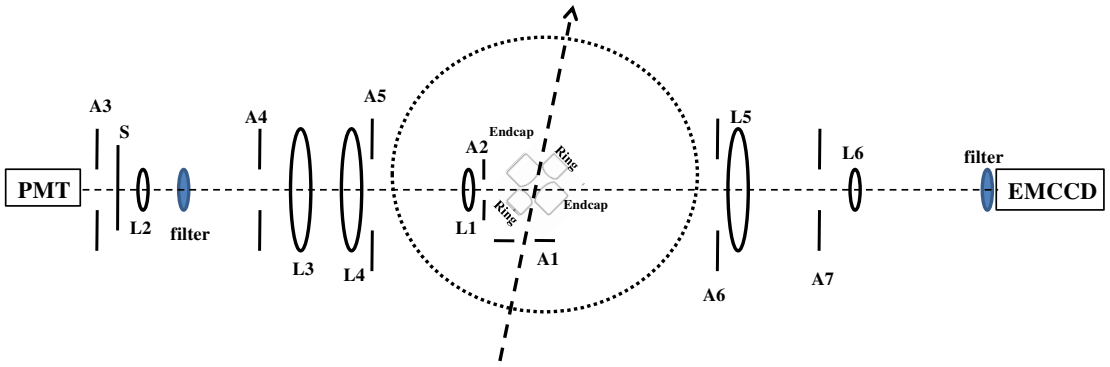

FIGURE 3.8: Detection optics used for both the PMT and EMCCD. This includes the optics required for the optimal imaging. The dotted arrow indicates the direction of the laser beams. The dotted circle represents the vacumm chamber. Inside chamber: A1 is a slit of 1 mm diameter, f_{L1}=40 mm and A2 is an aperture. PMT optics: f_{L2}=40 mm, f_{L3}=250 mm and f_{L4}=150 mm and A3, A4 and A5 are apertures. EMCCD optics: f_{L5}=100 mm and f_{L6}=40 mm and A6 and A7 are apertures.

dc potential can be applied to both endcaps simultaneously, independent of the applied dc potentials to each of the endcaps. The advantage of such a circuit is that the trap is more symmetric. As a consequence the lifetime of the ion in the trap is higher. Fig. C.2 of Appendix C gives the most advanced version of the circuit which is used for control of the ion position with mV resolution. This circuitry provides for more leverage in the applied voltages. With this an independent dc offset voltage of -20 V $< U_0 <$20 V can be applied between the individual endcaps and the ring electrode. This is also sufficient for positioning of the ion at the rf center of the trap with μm precision.

3.3 Fluorescence detection system

Laser-induced fluorescence from the different transitions in Ba^+ is detected from the ion using a Photomultiplier tube (PMT Hamamatsu H11123) and an electron multiplying CCD camera (Andor iXon EMCCD) mounted opposite to the PMT as viewed from the top (see Fig. 3.8). The time resolution of the optical signal from the ion(s) is determined by the PMT while the EMCCD camera provides for spatial resolution of the fluorescence signal. Fig. 3.8 gives the principle of the detection system together with all relevant optical elements. The apertures are aligned to suppress the stray light.

3.3.1 Cooled photomultiplier

The fluorescence from the ions is initially collected by a 40 mm best form lens (see Section 3.2). The collimated light signal is detected by the PMT (Hamamatshu H11123). Most of the scattered light reaching the PMT is reduced by blackened circular apertures. A 1 mm slit aperture close to and in the optical path before the trap (see Fig. 3.8) is employed to reduce stray light. The detection efficiency of the PMT system is given by the product of individual transmission $T_{windows}$, T_{optics}, $T_{apertures}$ and $T_{filters}$ of optical elements, the detection solid angle and the PMT quantum efficiency i.e.

$$\varepsilon = QE \times \Omega \times T_{windows} \times T_{optics} \times T_{apertures} \times T_{filters}. \tag{3.1}$$

The PMT Quantum Efficiency is about 0.1 and the solid angle subtended is Ω=0.05 steradian. The transmission through the windows, optics, apertures and filters accounts to 1 %, 0.88 %, 1 % and 0.45 %, respectively. An overall detection efficiency of 10^{-6} for the PMT system is estimated from these numbers. Since the scattering rate of a single cooled Ba^+ ion is about Γ=10^8 photons/s, we have a signal of $S = \Gamma \times \varepsilon = 10^2$ cnts/s.

The signal rate is comparable to the typical dark count rate of the PMT at room temperature. The thermal emission of the electrons from the photocathode of the PMT results in a dark count rate. This count rate can be further reduced by cooling the cathode of the PMT with a Peltier element. The temperature

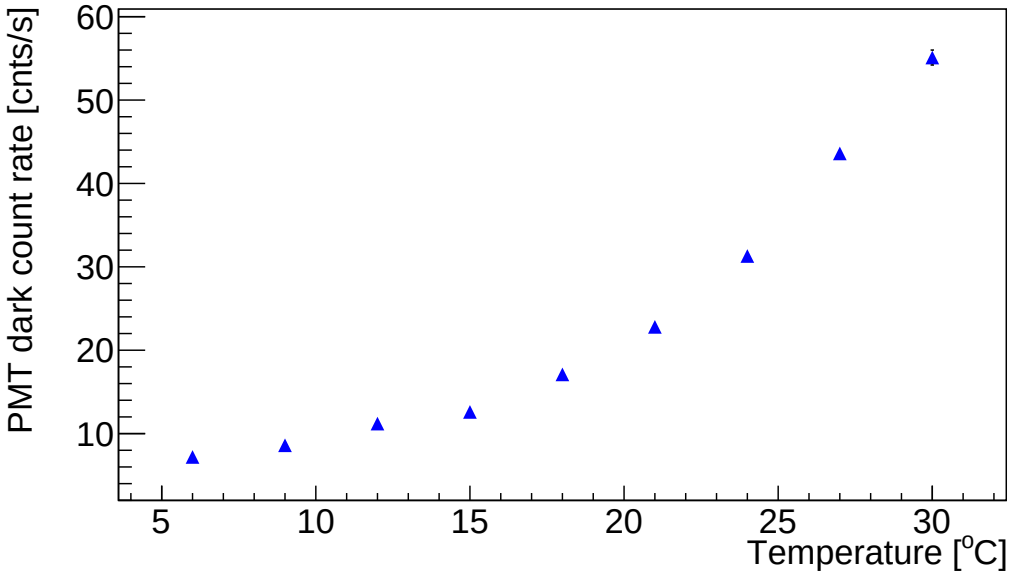

FIGURE 3.9: PMT thermal dark count rate as a function of its photocathode temperature. We operate at temperature 13 °C to avoid water condensation on the PMT.

can be measured with a PT100 temperature sensor. The dependence of the dark count rate as a function of the temperature of the cathode is displayed in Fig. 3.9. In this experiment, the operating temperature of the PMT cathode is set to T_{PMT}=13 °C. This value has been chosen to avoid water condensation on the PMT and its attached electronics. At this temperature, the PMT dark count rate has been reduced to about 10 cnts/s.

3.3.2 EMCCD

The image of a single ion is taken by an Andor iXon EMCCD detector with 512×512 pixels. The optical path in front of the pixel detector contains two lenses. A 2-inch diameter lens with 100 mm focal length close to a CF35 viewing port and outside of the vacuum chamber is used for collecting light from the ions. A 1-inch lens with 40 mm focal length is mounted on a translational mount which can be moved to adjust the focussing of the image. For finding the image of the ions, the big lens can be moved perpendicular to the optical axis using a 2D-translation stage. The image can be sharpened by adjusting the position of the 1-inch lens.

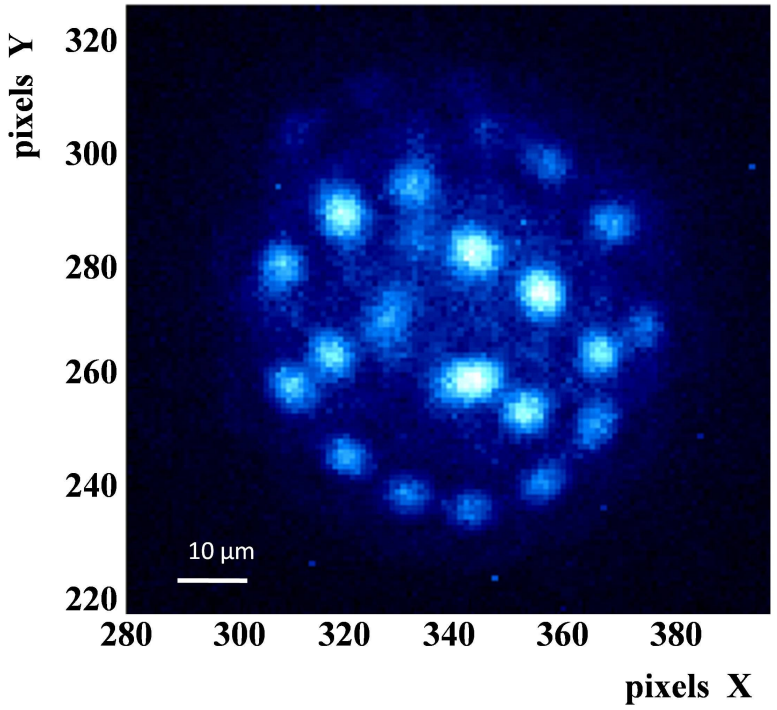

FIGURE 3.10: EMCCD camera image of many ions trapped and localized in the hyperbolic Paul trap. Some of the ions are aligned with the laser beam and are laser cooled while other ions are not optimally aligned. Here a 1×1 pixel corresponds to $1\times1\,\mu m^2$. The size of the image of an ion is proportional to the amplitude of its motion and gives an upper limit for its temperature. For a single laser-cooled ion this limit is of order $\leq$10 mK ($\approx$ 1 m/s); the Doppler limit for the Ba^+ cooling transition is 0.5 mK.

An 8-fold image magnification is achieved with the telescope as shown in Fig. 3.8. This camera also has an internal cooling system that reduces the image noise. The electron multiplication gain, the binning, the exposure time, selection of the region of interest (ROI) etc. can be further selected for each image. All this information regarding the trapped ions is recorded with the data acquisition system. As an example of the image of many trapped ions as taken with the EMCCD camera system (see Fig. 3.10).

3.4 UHV compatible effusive beam of Ba atoms

The source of atomic Ba for our ion trapping experiment is an evaporative oven to produce a Ba atom beam. It is required for fast heating, good collimation of the atomic beam and lowest possible outgassing rate. It consists of a thin-walled stainless steel hemostatic needle (Terumo Europe used for medical purposes) of 30 mm length × 0.9 mm inner diameter and a wall thickness of 0.2 mm (see Fig. 3.11). The total volume of this needle is about 10 mm^3 and holds approximately 10 mg of a finely grained mixture of Barium Carbonate ($BaCO_3$) and Zirconium (Zr) powder (SIGMA-ALDRICH) (isotopically pure 99 % $^{138}BaCO_3$ + Zr) [100]. Since $BaCO_3$ is a thermally stable metal carbonate, Zr acts as a catalyst and helps in the formation of Barium atoms when heated in a vacuum environment. The hollow needle is filled with the mixture and crimped at one end. The open end points to the center of the trap. A dc current of 4-8 A is used to resistively heat the needle. This dc current is provided from an ES015-10 Delta Elektronika power supply controlled via ethernet interface by the data acquisition system. The voltage drop across this needle is 0.8-0.9 V. The first operation of a newly filled needle (see Fig. 3.12) results in initial outgassing.

3.4.1 Optical detection of Ba atomic beam

Fig. 3.13 shows the energy levels of Barium atoms used for spectroscopy in the experiment. An external cavity diode laser at wavelength λ_{1107}=1107.5 nm is used for producing laser light at λ_{553} by frequency doubling it. This is used as diagnostic for the production of Barium atoms. The IR light is monitored by a wavelength meter (WLM) (WS6 IR from HighFinesse-Ångstrom). For scanning, the IR laser locked to the WLM, a ramp generator built in-house determines the amplitude and offset for the scan. A second laser diode at λ_{413} is employed for photoionization of Ba atoms to Ba^+ ions near the center of the trap. A second wavelength meter (WLM) (WS6 VIS from HighFinesse-Ångstrom) is used to monitor the light at wavelength λ_{413}.

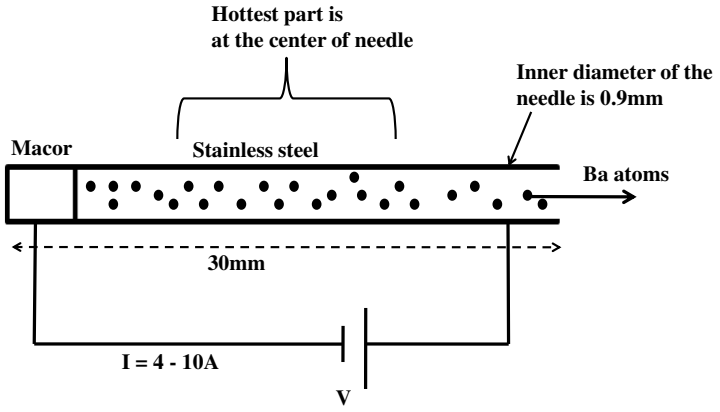

FIGURE 3.11: Schematics of the Ba needle oven. The length of the needle is 30 mm and have an inner diameter 0.9 mm. The voltage drop across the needle is 0.8-0.9 V and a current of 6 A is sufficient to reach a temperature of 600 °C.

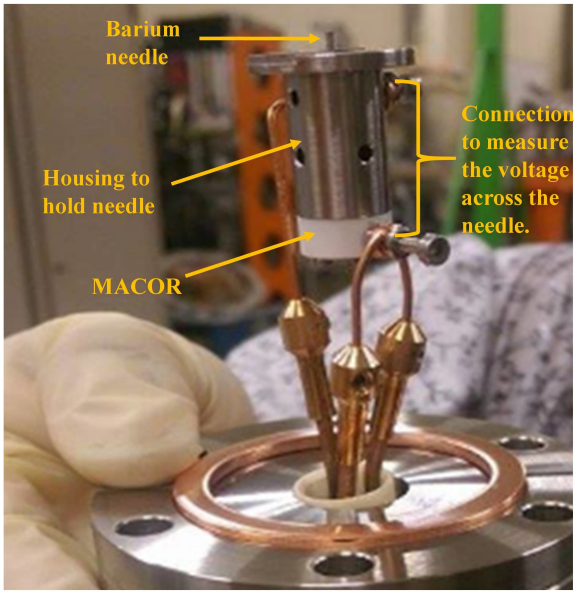

FIGURE 3.12: Ba oven on a CF35 flange. The needle is held by the stainless steel holder with a small part of it sticking out of the holder. A dc current is given to the needle across the two ends which measures the voltage drop across the needle.

The diagnostic test to confirm that there are Barium atoms being produced from this needle, we use IR laser diode operating at wavelength at $\lambda_{1107} = 1107.5$ nm (model LD-1120-0300-1 from Toptica) the light of which is frequency doubled and to produce light at λ_{553}. This IR laser is operated at 207 mA current and at 15.3 °C temperature and with a threshold current of about 45 mA. For the characteristic curve for such a diode, see Fig. D.1 of Appendix D.

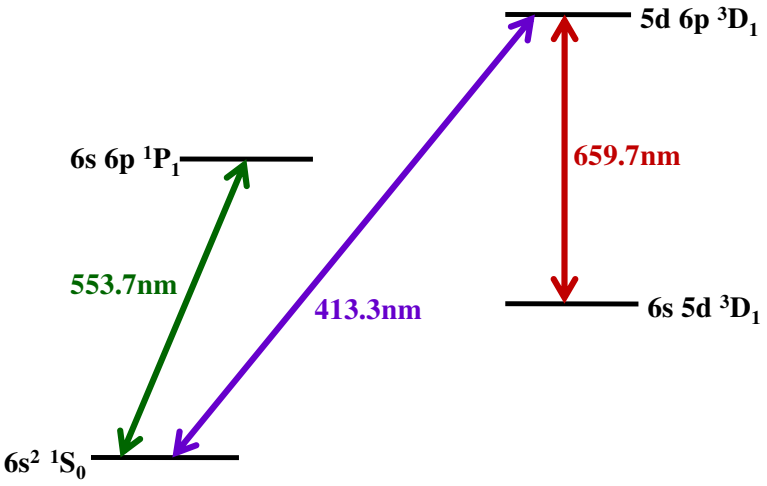

FIGURE 3.13: Level diagram for Ba atoms. The atomic transition $6s^2\,{}^1S_0$-$6s\,6p\,{}^1P_1$ at λ_{553} is for verification of the production of atoms.

Frequency doubling with a LBO crystal

In order to frequency double IR light at wavelength 1107.5 nm, an LBO crystal was heated to 91 °C to produce a 0.2 μW beam of green light in a diameter of 0.2 mm. The behaviour of the output power from this crystal for different applied voltages is shown in Fig. D.2 of Appendix D. Due to nonlinearity, such a crystal can emit light at a frequency different from the frequency of the absorbed light i.e. emits at twice the original frequency. The optical setup for the frequency doubling of laser light at λ_{553} is shown in Fig. 3.14.

We found that the resonance frequency for the confirmation of the production of the Barium atoms is at 1107.4000 nm in IR. The light at wavelength λ_{553} is used to drive the $6s^2\,{}^1S_0$–$6s\,6p\,{}^1P_1$ transition and is employed as diagnostic to confirm the production of Ba atoms. This resonance fluorescence is detected by using a filter (FB550-10 from THORLABS) with a central wavelength of 550 nm with a pass band of 10 nm in front of the detectors. Fig. 3.15 is the spectrum observed when two counter-propagating beams of light at λ_{553} were overlapped. Further, the production of atoms is confirmed from the change in the scattering rate and the increase in pressure with different currents applied to the oven (see Figs. 3.16 and 3.17, respectively).

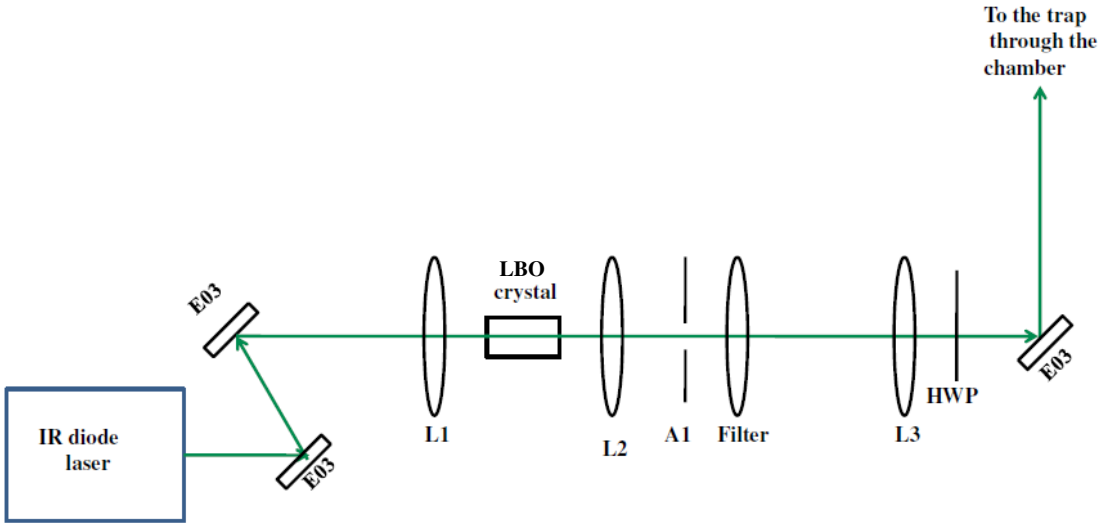

FIGURE 3.14: Optical layout for observation of Barium atoms. The IR diode laser beam at $\lambda_{1107} = 1107.5\,\text{nm}$ passed through a nonlinear frequency doubling crystal to produce frequency doubled light at λ_{553} which is an important diagnostic for verification of production of Barium atoms from the needle.

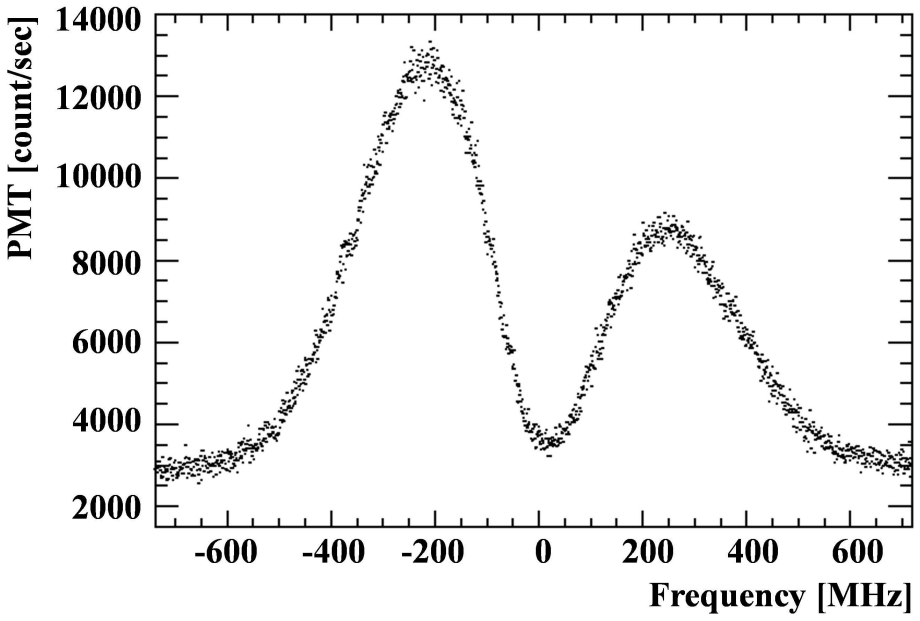

FIGURE 3.15: Doppler-free spectrum obtained from the overlap of two counter-propagating laser light beams at λ_{553}. Here the Doppler-free resonance transition is expected in the middle of the two peaks.

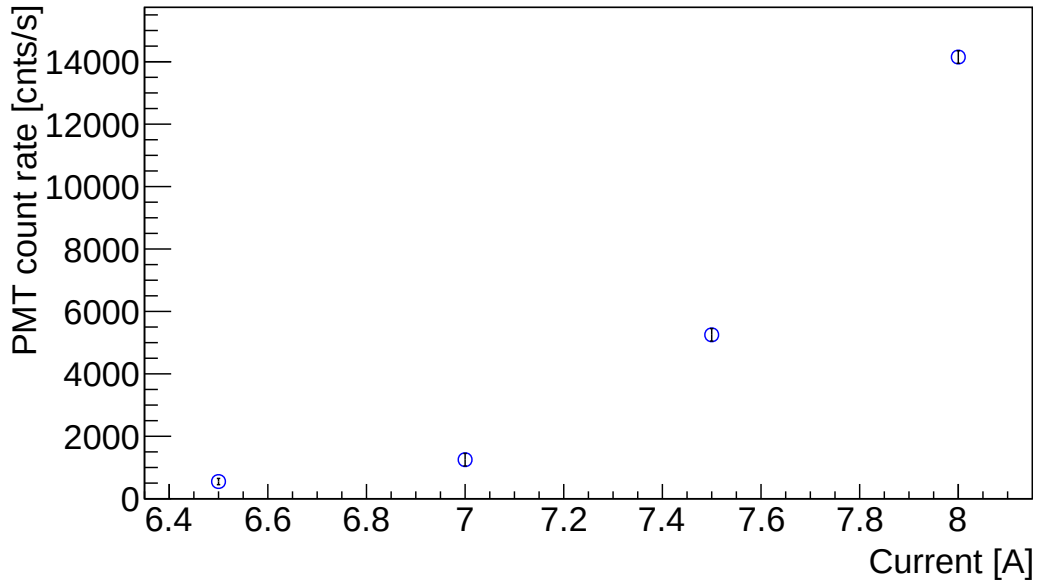

FIGURE 3.16: Change in the PMT count rate for different values of the current applied to the Ba oven. The uncertainties are about the same size as the symbols.

3.5 Formation of Ba^+ ions

After the production of Barium atoms, the next diagnostic step towards single Ba^+ ion precision spectroscopy is monitoring the formation of Ba^+ ions. Initially, an electron impact ionization [67] was employed for loading up to 10^6 ions in a few

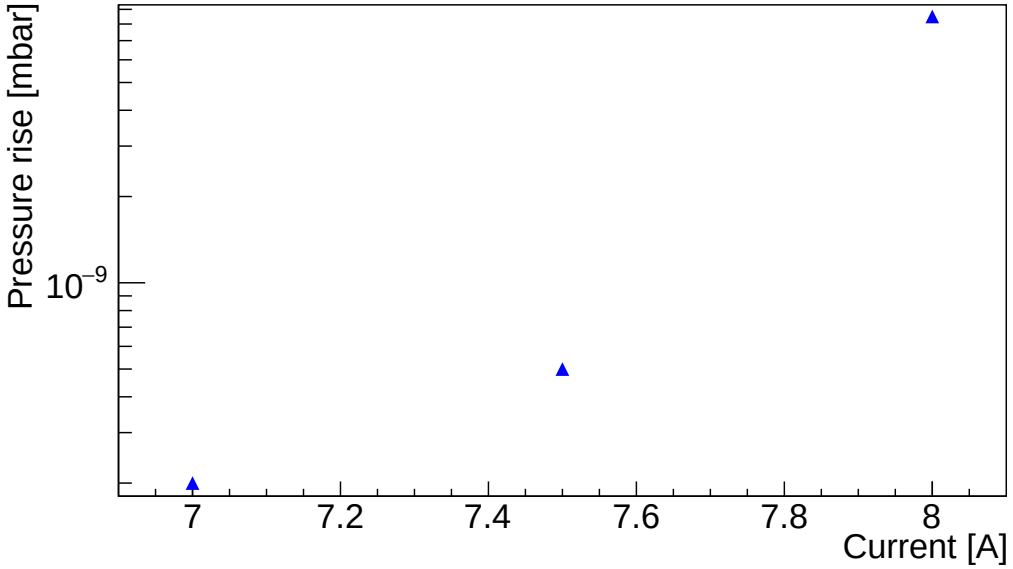

FIGURE 3.17: The logarithmic rise in the pressure for different currents applied through the tube in the Ba oven. The uncertainties are about the same size as the symbols. Here the flux of atoms from the oven for loading pressure remains below 2×10^{-10} mbar at a current of 7 A. This makes it suitable for such a UHV environment.

minutes time. However, the number of loaded ions could not be reasonably controlled with this technique. As a second approach, far off-resonant photoionization with a diode laser operating at λ_{413} was employed to produce a huge cloud of ions within about 5 sec of "on" timings. Finally, a two-step resonant photoionization process is employed to produce a small number of ions in a well-controlled way. This two-step resonant process of photoionization is shown in Fig. 3.18.

3.5.1 Photoionization using on-resonant diode laser at λ_{413}

Photoionization has a much higher efficiency than electron ionization in three respects. Firstly, the resonant two-step photoionization method accounts for isotope selective species [101] which helps in the clean loading of the ion trap. Secondly, it removes the possibility of deposition of the excess charge into the trap volume and on trap components that can disturb the trapping potential and hence could hamper precision spectroscopy. Thirdly, the typical loading rates are several orders of magnitude higher and therefore, the outgassing rate of the oven can be kept far lower.

For photoionization of Ba^+, an on-resonant laser (Blue-Violet Laser diode DL-5146-101S) at wavelength 405 nm was implemented. At operating current 79 mA and temperature 70 °C, the resonance wavelength of $\lambda_{413} = 413.3593$ nm was achieved to drive the $6s^2\,{}^1S_0$–$5d\,6p\,{}^3D_1$ transition.

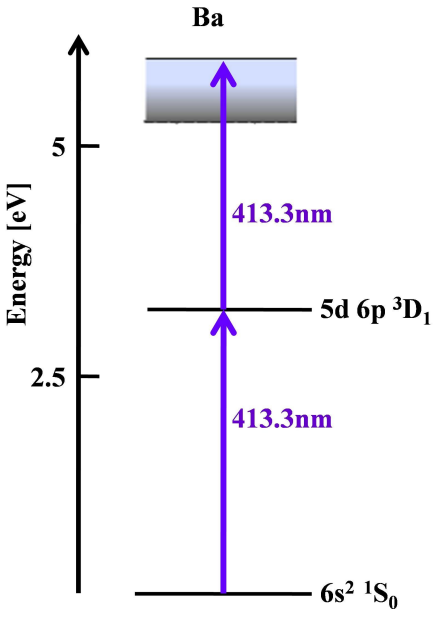

FIGURE 3.18: Two-step resonant photoionization scheme for Barium.

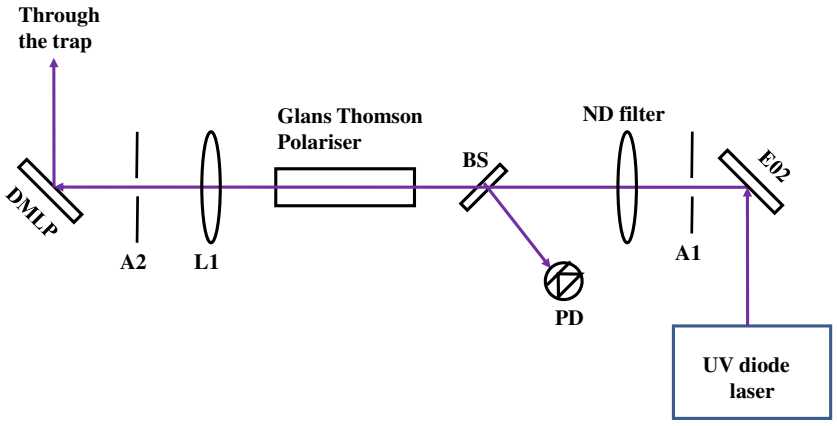

FIGURE 3.19: Optical setup for photoionization laser to produce Ba^+ from Ba atoms. The Glans Thomson polariser permits control of the power for ionization without changing the pointing of the beam. After the polariser the maximum power is 2.7 mW (as measured just after the lens L1), sufficient for producing ions.

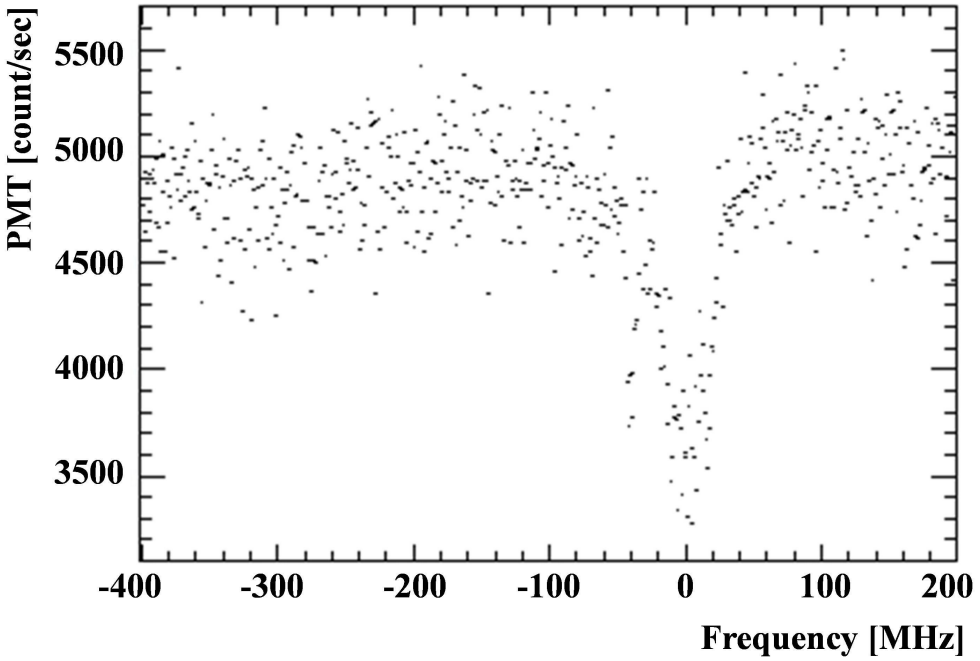

FIGURE 3.20: Atomic signal from $6s^2\,{}^1S_0$–$6s\,6p\,{}^1P_1$ transition at λ_{553} where the depletion in the signal is an indication of the atoms being ionized.

The concept of the optical setup for delivery of this laser through the trap is given in Fig. 3.19. After the polariser, the maximum power is 2.7 mW (as measured just after the lens L1) sufficient for producing ions. We use a filter (FB670-10 from THORLABS) with central wavelength 670 nm and a bandwidth of 10 nm in front of the detectors to collect fluorescence from the atomic beam. With the light at the $^1S_0$-$^1P_1$ transition on resonance, we scan the laser light driving the $^1S_0$-$^1D_1$ transition. On resonance, the light optically pumps the atoms to the $6s\,5d\,^3D_1$ state which reduces the fluorescence of light (see Fig. 3.20).

It was observed that the resonance wavelength at $\lambda_{413} = 413.3493$ nm differs by 17 GHz from the value of this transition at $\lambda_{413} = 413.3592$ nm. We attributed this to a readout problem of the particular WLM (WS6 IR from HighFinesse-Ångstrom) at this wavelength. With 0.2 mW of light at this wavelength, we get 1-2 ions in a time interval of 80-90 s. In this way we can control the amount of ions produced in the trap.

3.6 Magnetic field

For single Ba^+ ion precision spectroscopy, it was found that the presence of a magnetic field has an impact on the slope of the signal from the trapped ions. During such a precision experiment, care was taken that the magnetic field at the site of the trapped ion is cancelled and a homogeneous static magnetic field is applied by using a pair of Helmholtz coils. This field defines the quantization axis. Such a defined magnetic field of order 80 μT removes the degeneracy of the Zeeman and sufficiently splits the sublevels [102].

3.7 Section Summary

The setup of a Paul trap in a vacuum system at 10^{-11} mbar residual pressure provides the environment for creating, storing and performing spectroscopy on a single Ba^+ ion. The details of the Paul trap, the driving rf circuit, and the optical detection systems (cooled photomultiplier and EMCCD) are given. A UHV compatible source of a Ba atomic beam has been developed and its performance has been characterized with laser spectroscopy of atomic barium in the same setup. This enabled spectroscopy on the $6s^2\,^1S_0$–$5d\,6p\,^3D_1$ transition at wavelength λ_{413} which revealed a readout problem of the employed wavelengthmeter. The flux sufficient for loading ions into the trap is reached while the pressure rise in the vacuum system is below 10^{-10} mbar. With about 0.2 mW of the photoionization light, we get about one to few ions trapped. The good control of the amount of ions

produced in the trap, the excellent vacuum conditions and the optical detection system are the prerequisites for precise spectroscopic measurements in this thesis.

Chapter 4

Single Ba^+ spectroscopy and laser control system

For high precision single Ba^+ ion spectroscopy of the transitions between the lowest $6s\,^2S_{1/2}$, $6p\,^2P_{1/2}$, $6p\,^2P_{3/2}$ and $5d\,^2D_{5/2}$ states, the necessary laser light sources include a solid-state Ti : Sapphire laser, diode lasers and a dye laser for exciting the optical transitions (see Fig. 2.1 for energy level diagram of Ba^+). Frequency stabilization of these lasers to 100 kHz or better are indispensable in order to achieve high resolution spectra. The stabilization is implemented by exploiting absolute frequency references such as light from frequency comb, and saturated absorption spectra in molecular iodine (I_2). Laser light beam diagnostics and the indispensability of the laser light beam manipulation require the frequency doubling of Ti:Sapphire laser light in a non-linear crystal, implementation of frequency shifted beams by means of an Acousto-Optic Modulator (AOM) and switching between laser beams at different frequencies near wavelength λ_{650} for spectroscopy. Launching optics is set up for the delivery of the laser beams through the trap and monitoring the quality of the beams before and after the trap. In addition to these laser light beams, light of LEDs at wavelengths λ_{455} and λ_{617} is employed to achieve shelving into the $5d\,^2D_{5/2}$ state and deshelving from this state, respectively. A laser diode with light at wavelengths λ_{650} enables the induction of light shifts in the transitions. The schematics for the laser control system involving the frequency stabilization, beam manipulation and diagnostics and the launching optics is summarized in Fig. 4.1.

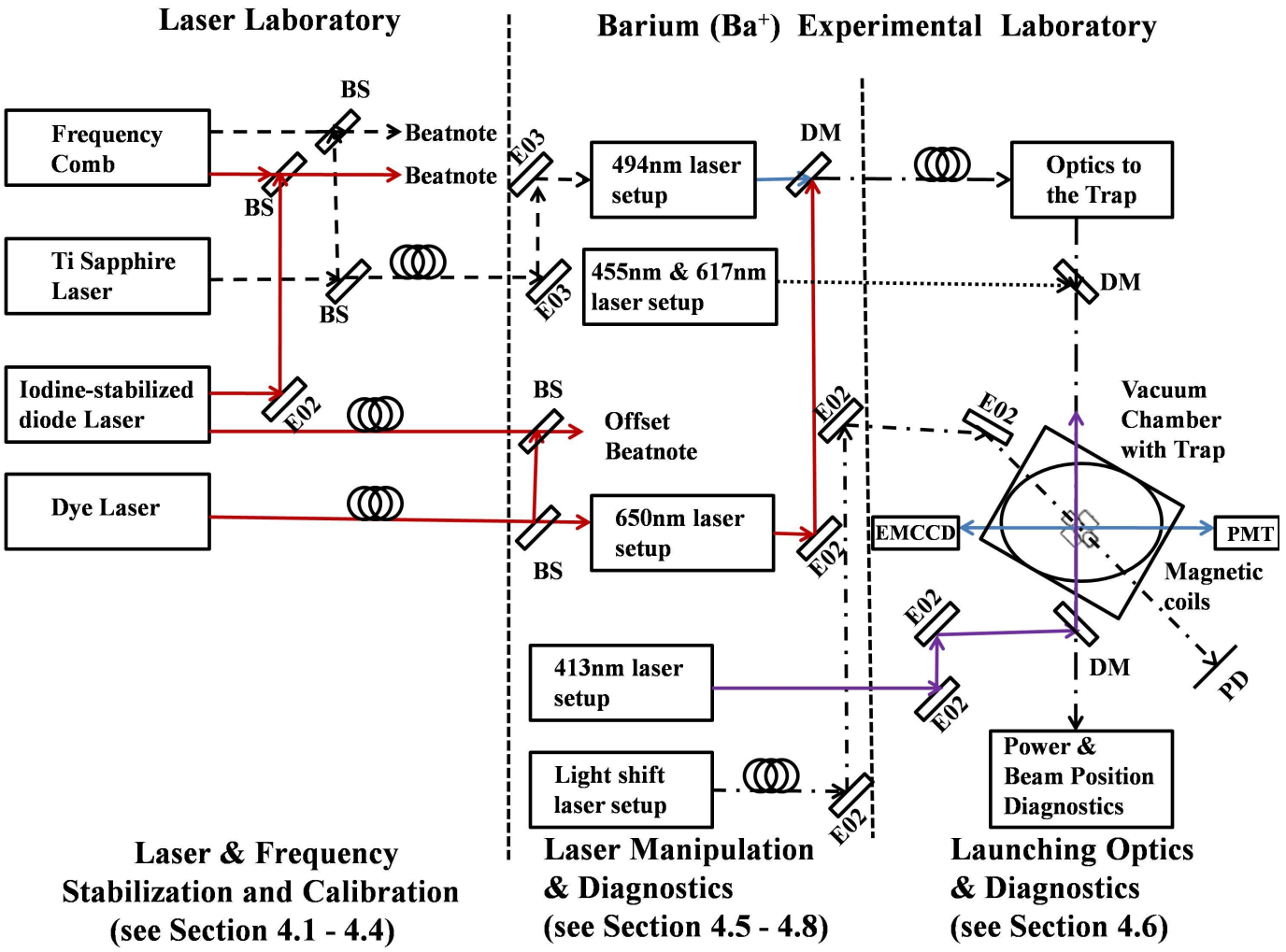

FIGURE 4.1: Schematics of the laser control systems involving the frequency stabilization, beam manipulation and diagnostics and the launching optics involved for the spectroscopy.

4.1 Optical frequency comb

A fiber-based femtosecond optical frequency comb (FC1500-250-WG from Menlo Systems) serves as a very precise optical ruler which is needed to measure the frequencies of the light from various laser devices. It gives precisely spaced optical frequencies that serve as reference lines over a spectrum ranging from extreme ultra-violet (UV) down to the mid-infra-red (IR). In such a system the accuracy of a reference frequency in the radiofrequency domain is transferred to the optical regime by the exploitation of the properties of a mode-locked laser [103, 104]. The latter is operated at a mode spacing of 245 MHz. The frequencies of light emerging from such a mode-locked laser are

$$\nu_m = m \times \nu_{comb,rep} + \nu_{comb,offset} \tag{4.1}$$

where m is the mode number and $\nu_{comb,offset}$ is the carrier envelope offset frequency, and $\nu_{comb,rep}$ is the synthesizer frequency used to achieve the mode locking or the repetition rate of the laser pulses. Fig. 4.2 shows an example of the long-term stability of the offset beat and the repetition rate of the frequency comb.

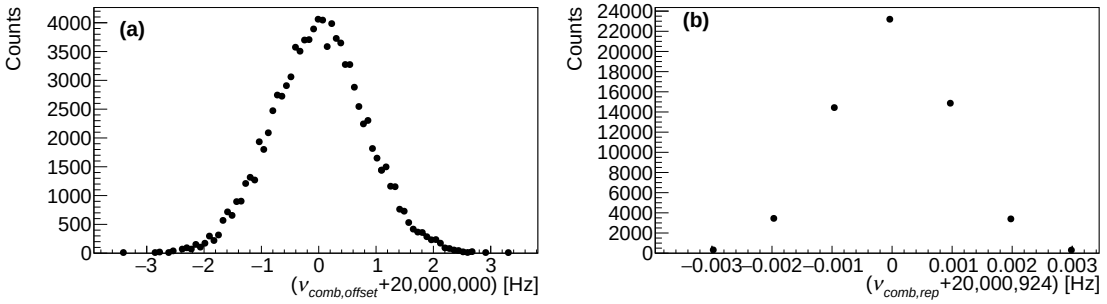

FIGURE 4.2: Example of long-term stability of the frequency comb offset (see (a)) and repetition rate (see (b)).

Further, the long-term frequency stability of the frequency comb in our experiment is provided by an SRS Rubidium frequency standard (FS725-10 MHz Rb Frequency Standard from Stanford Research Systems) which is phase-locked to an external 1 pps frequency reference GPS signal. This reference clock system provides a TTL output signal at 10 MHz. It has an exceptionally low phase noise. The SRS Rubidium (Rb) standard serves as the timebase for precision frequency measurements. This standard has an intrinsic short-term frequency stability of better than 10^{-11} in 1 s and less than 10^{-12} in 100 s. Because of its low phase noise (<-130 dBc/Hz at 10 Hz) and its frequency accuracy output signal at 10 MHz frequency, it is also used as the reference source for all rf synthesizers used in the experiment.

4.2 Ti:Sapphire laser

The Ti:Sapphire laser (Coherent MBR-110) has a bow-tie cavity. Its light has a linewidth of about 500 kHz. The laser delivers about 300-310 mW at an operating wavelength of $\lambda_{987} = 987$ nm. The Ti:Sapphire laser is optically pumped by the light from a diode pump solid state laser within an output pump power of 7.5 W which is supplied by the Coherent Verdi-V10 operating at wavelength 532 nm.

4.2.1 Beat note signal between the Ti:Sapphire laser and frequency comb

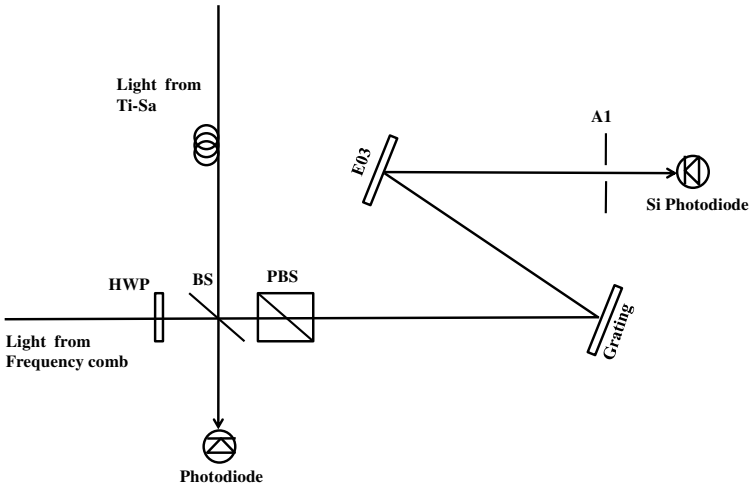

FIGURE 4.3: Optical setup for obtaining a beat note between light from the Ti:Sapphire (Ti:Sa) laser at wavelength $\lambda_{987} = 987$ nm and light from the frequency comb. PBS is the Polarising Beam Splitter while HWP are the Half-Wave Plates used for the optimisation of the beat note signal.

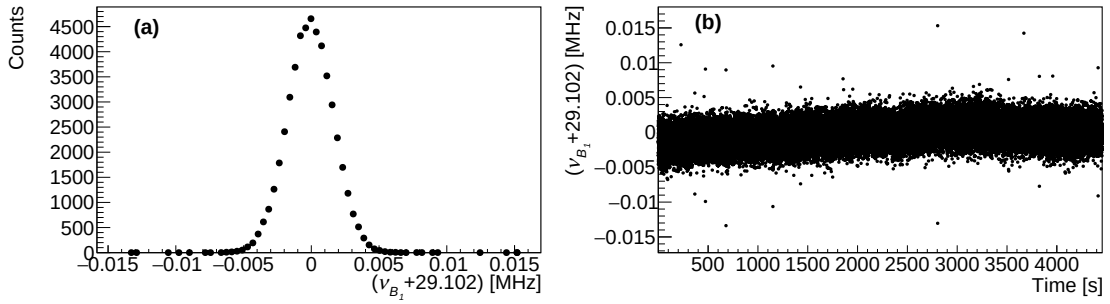

FIGURE 4.4: An example of a beat note signal for the Ti:Sapphire laser with the frequency comb. The frequency stability of this beat note is better than 10 kHz over typically hours.

In order to stabilize the Ti:Sapphire laser to better than 100 kHz, a beat note between the light from this laser and light from the frequency comb is obtained at

a wavelength $\lambda_{987} = 987\,\text{nm}$ by overlapping the two laser beams on a Si photodiode. The optical setup for obtaining this beat note is shown in the Fig. 4.3.

This beat note is an excellent diagnostic for measuring and monitoring the stability of the Ti:Sapphire laser in terms of frequency. The frequency of the light from the Ti:Sapphire stays within $\pm 5\,\text{kHz}$ (see Fig. 4.4) over hours.

4.3 Diode laser stabilized to iodine

For obtaining light at the frequency of the $6p\,^2P_{1/2}$–$5d\,^2D_{5/2}$ transition in Ba^+, an external cavity diode laser (HL6366DG/67DG) arranged in Littrow configuration with a linewidth of order 2 MHz is used at an operating wavelength λ_{650}. The laser is typically operated at 153 mA and its temperature is maintained at 40.2 °C.

Since the natural linewidth of the principal resonance line in Ba^+ is of order 10 MHz, the uncertainty of the laser frequency should be significantly less than this value. For this purpose, the laser is stabilized to an accuracy well below 1 MHz over periods of several hours by means of a secondary frequency reference line in molecular iodine (I_2). Frequency stabilization is necessary to account for thermal drifts.

The frequency stabilization has three stages:

1. Short-term frequency stability is achieved by saturation absorption signals in I_2. Through this, the diode laser light frequency is locked to a transition in molecular iodine. With frequency-modulated saturated absorption spectroscopy, a Doppler free signal is obtained from I_2 and the hyperfine structure in the molecule can be resolved (as explained in Section 4.3.1).

2. The light of the iodine-stabilized diode laser serves as a reference for the frequency of the dye laser (see Section 4.4) in the experiment. A frequency-offset locking technique (see Section 4.5) is implemented as a diagnostic for observing the frequency stability of the dye laser light which is employed for spectroscopy of the $6p\,^2P_{1/2}$–$5d\,^2D_{5/2}$ transition in Ba^+.

3. The long-term frequency stability of the iodine-stabilized diode laser is determined accurately by means of a beat note between light from this laser and light from the frequency comb.

4.3.1 Saturated absorption spectroscopy in iodine

Molecular iodine I_2 in a vapour cell provides for an inexpensive, stable and reliable frequency reference. Such references have been exploited for frequency stabilization of lasers [105–110], because the heavy diatomic molecule, I_2 exhibits a dense spectrum of rotational and vibrational transitions in the range from green to near-IR. Each of these transitions consists of either 15 or 21 hyperfine lines. The hyperfine B–X spectrum of molecular I_2 which extends from 500 nm to 900 nm has been the subject for the spectroscopic measurements in the Ba^+ ion. The details of diatomic molecular spectra and the nomenclature for such systems are given in reference [111].

The best performing vapour-cell frequency standards employ molecular I_2 in large diameter ($\sim$ 10 cm) and long ($\sim$ 1 m) vapour cells [112–117]. The iodine vapour cell that is used for the spectroscopic measurements has a diameter of $\sim$ 12 cm and a length of $\sim$ 70 cm. Fig. 4.5 shows the entire optical setup for spectroscopy

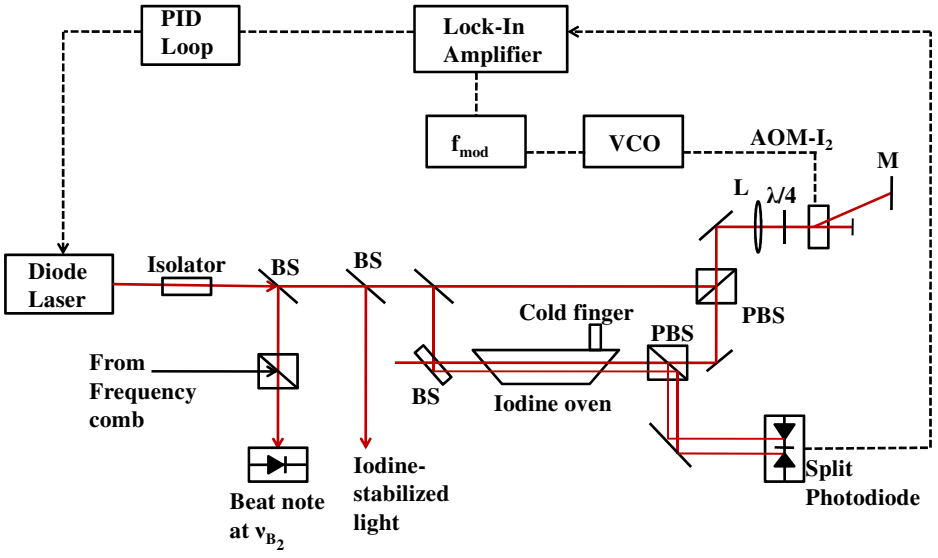

FIGURE 4.5: Optical setup of the saturation absorption spectroscopy in molecular iodine. It is used for frequency stabilization of the repump transition in Ba^+

together with the schematics of the feedback system for frequency locking i.e. the double pass AOM, RF amplifier, and Voltage Controlled Oscillator (VCO) (ZOS-100+, 12 V) [100] . To generate the signal in Doppler-free saturation absorption spectroscopy with counter-propagating beams, the pump laser is frequency modulated by using an Acousto-Optical Modulator(AOM) driven by an RF power amplifier (ZHL-1-2W) . This creates different orders of diffraction of which the first order is used as the modulated frequency. The probe is coherently demodulated to obtain the error signal. Besides improved optical isolation, intensity noise

suppression and fast frequency modulation, this double pass AOM helps to reduce the unwanted amplitude modulation.

The frequency-modulated signal [118] for the saturation spectroscopy is obtained from the VCO operated at a frequency range of the 80 MHz AOM by applying a voltage of a certain amplitude between 100 mV and 800 mV and an offset voltage using a waveform generator (HP 3314A). The typical modulation frequency and modulation depth are further controlled by this waveform generator. Here the waveform generator acts as a local oscillator that feeds the frequency modulated signal from the VCO to a 1-100 kHz lock-in amplifier (Scitech). The low noise split photodiode (PD) signal together with the modulated signal are fed to the lock-in amplifier which is further used to produce the error signal.

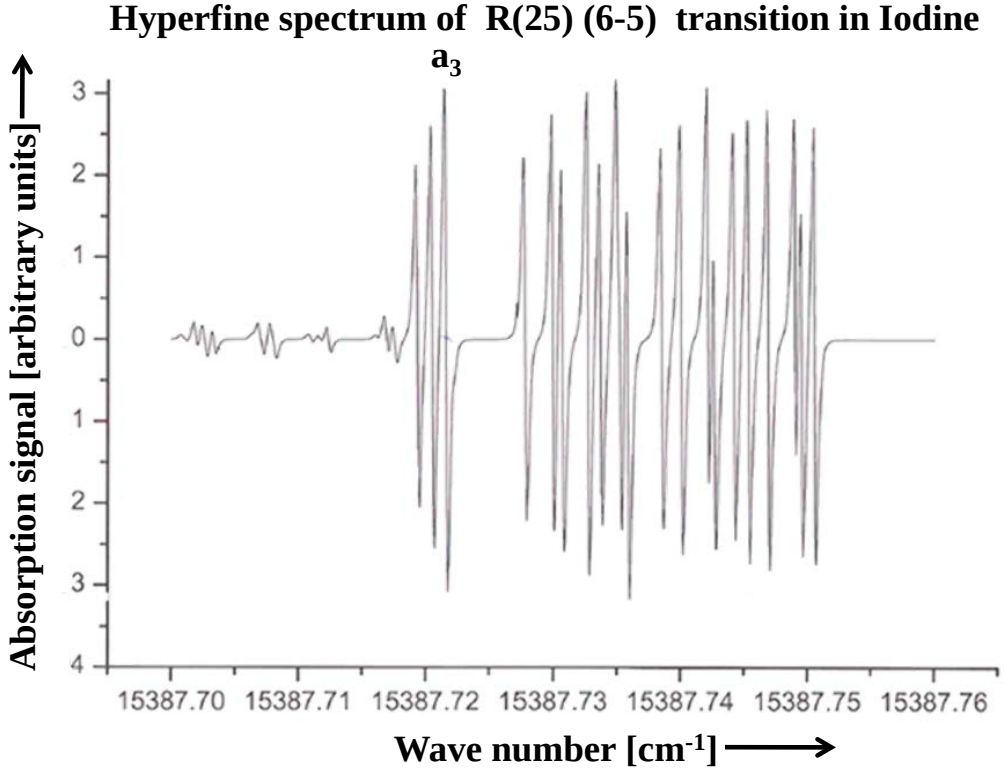

FIGURE 4.6: Calculated Doppler-free saturated absorption spectrum of the entire 21 lines using the IodineSpec software from Toptica Photonics. The line marked 'a3' is used for frequency locking at wavelength λ_{650} to drive the repump transition in Ba^+ [119].

This derivative-like signal after the lock-in amplifier is given to a servo/PID loop that has two paths to the diode laser. One is the signal that is fed back to the piezo of the diode laser. The piezo path consists of a proportional gain and an integrator gain, which is used to stabilize the frequency to the zero crossing of the derivative signal (see Fig. 4.7). The other is to the injection current of the

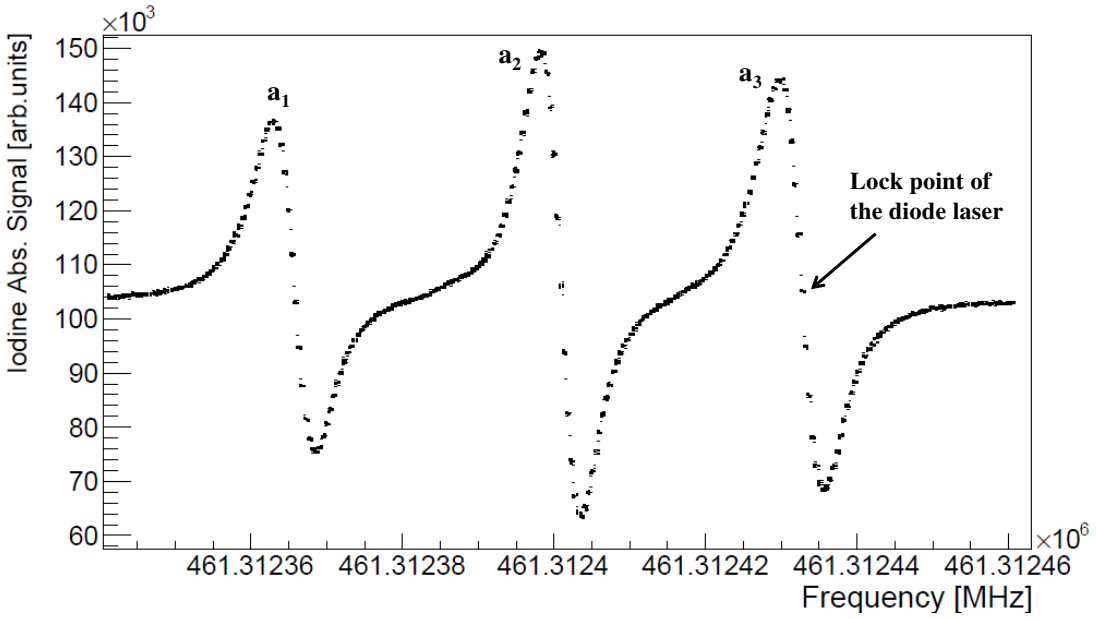

FIGURE 4.7: An example of measured 3 individual lines out of 21 in the hyperfine spectrum of the R(25)(6-5) transition in I_2 molecules. The line marked 'a3' is about 485 MHz above the repump transition in Ba^+. The diode laser light is frequency locked to the zero-crossing of the first derivative signal as marked in the figure.

laser diode. For the wavelength at λ_{650}, the nearest rovibrational transition in I_2 is the R(25)(6-5) transition [119]. It has a total of 21 lines (see Fig. 4.6). The line marked 'a3' in Fig. 4.7 is the nearest single component to the repump transition in Ba^+. This line is at wavenumber $\tilde{\nu} = 15387.7216\,\mathrm{cm}^{-1}$ (see Fig. 4.6) as per the IodineSpec software from Toptica Photonics [109, 110]. The frequency of the line is about 485 MHz above the frequency of the transition in Ba^+.

For frequency stabilization, the I_2 oven is maintained at a temperature 67 °C and the cold finger of the I_2 cell at 25 °C corresponding to a vapour pressure of 0.41 mbar. Typical operating parameters for generating the frequency-modulated signal are ν_{AOM-I_2} of 73.063 MHz and a modulation depth of 4 MHz. This is achieved by driving the VCO with an offset voltage of 3.89 V, a typical modulation frequency of 21.725 kHz and 500 mV amplitude. The sensitivity of the lock-in amplifier used is set to 1 mV with a time constant of 100 μsec. These settings enable us to get the first derivative signal of the Lorentzian absorption signal in iodine used for locking the diode laser and is sufficient for the spectroscopy in Ba^+.

4.3.2 Beat note signal between the diode laser and frequency comb

A beat note between the diode laser (HL6366DG/67DG) light taken via a single mode optical fiber from the diode laser and the light from the frequency comb

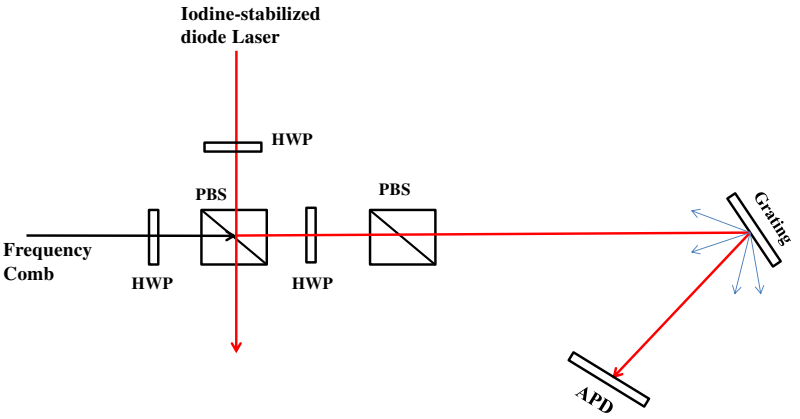

FIGURE 4.8: Optics diagram for the beat note created between the iodine-stabilized diode laser and the frequency comb. HWP represents the Half-Wave Plates which are used to optimise the power in the beat note. Linear polarisers and half-wave plates control the polarisation of the light. The Avalanche Photodiode(APD) is used for detection of this beat note. All the optics are set inside a Menlo System Beat note unit.

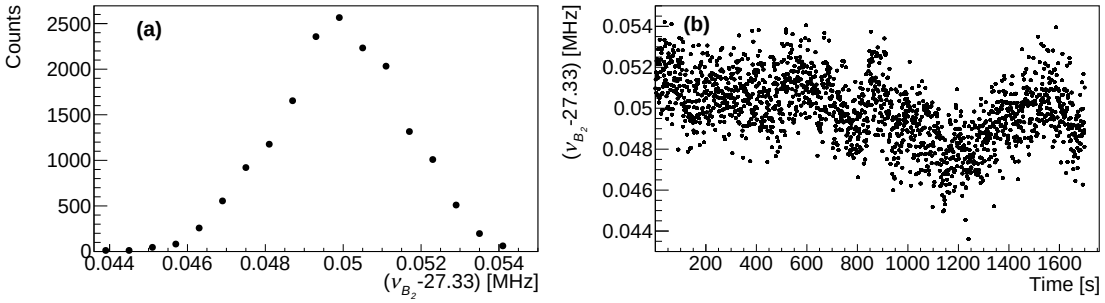

FIGURE 4.9: Example of the beat note signal for the iodine-stabilized diode laser with the frequency comb. The beat note stays within 5 kHz.

is created. Fig. 4.8 demonstrates the optical setup for the creation of beat note between the two laser light beams on the p/n junctions of an Avalanche Photodiode (APD). This beat note serves as a diagnostics to observe the short-term stability of this iodine-stabilized diode laser. The stability of this beat note is within ±80–90 kHz (see Fig. 4.9) over hours.

4.4 Dye laser stabilized to diode laser

A Coherent CR-699 ring dye laser (Coherent Inc. Palo Alto, USA) with a DCM (4-(dicyanomethylene)-2-methyl-6-(p-dimethylamino styryl)-4H-pyran) dye is used. The main concentration of the dye solution for optimum performance includes 1 gm of DCM dye dissolved in 0.6 liter of benzyl alcohol added to 1 liter of ethylene glycol. This is operated at 80 °C for about 2 hrs. This dye is then circulated

by a dye circulator RD-2000 (Radiant Dyes Laser and Accessories GmbH, Wermelskirchen, Germany) maintained at 7.6 bar pressure in the dye circulator. This laser together with the dye circulator is further cooled by a mini chiller. This laser with a linewidth of 500 kHz delivers about 80-100 mW at an operating wavelength of λ_{650} with a pump power of 1.8 W supplied from a diode pump solid state laser

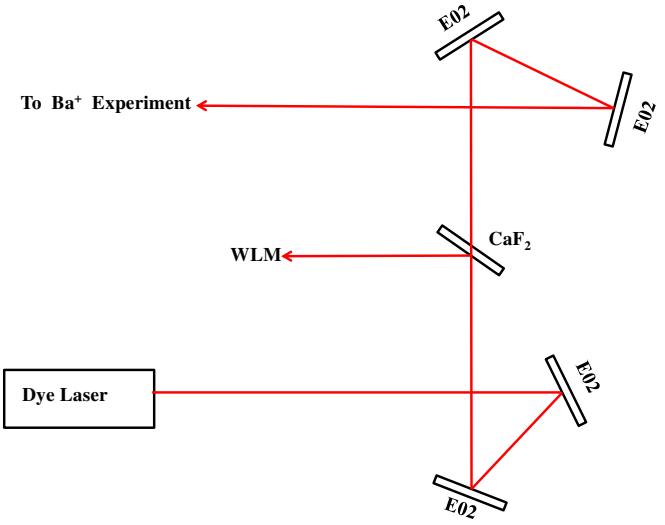

FIGURE 4.10: Schematic setup for the delivery of the light at wavelength 650 nm to the Ba^+ experiment and to the wavelength meter (WLM).

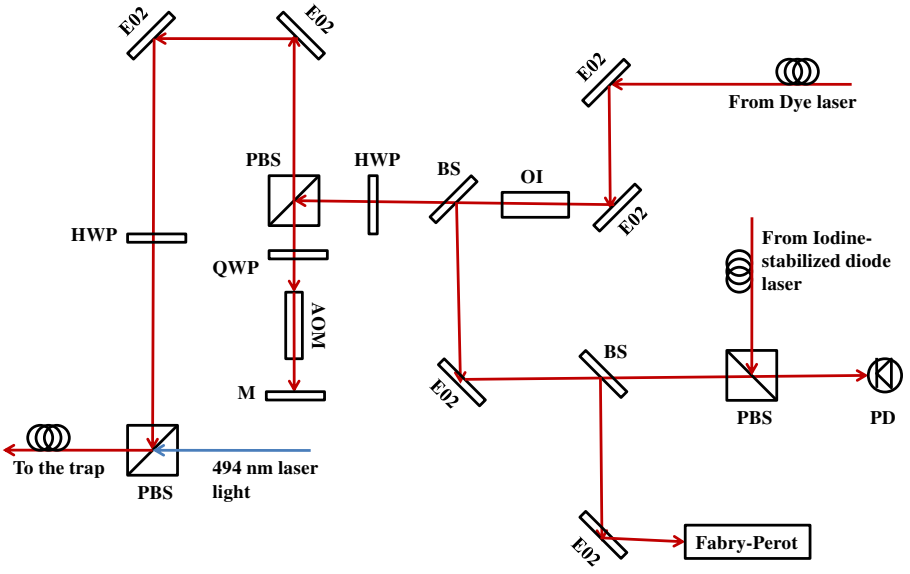

FIGURE 4.11: Optical schematic diagram for the delivery of the light at 650 nm through the trap. It shows the optics involved to get this light through the trap. The mirror M after the AOM is a curved mirror which enables the light to pass through it twice in order to shift the frequency of the light in a controlled manner.

(Coherent Verdi-V10 operating at 532 nm). This light is later transferred to the Ba^+ experiment (as shown in Fig. 4.10). The coarse tuning of the wavelength uses a WLM (WS6 VIS from HighFinesse-Ångstrom). The calibrated WLM is about ∼500 MHz. Fig. 4.11 shows the entire optical setup starting from the overlap of the light from the dye laser and iodine-stabilized diode laser and the transfer of this stabilized light from the dye laser through the trap.

4.5 Frequency-offset locking between iodine-stabilized diode laser and dye laser

This efficient method of frequency offset locking is used to transfer the short-term stability of the iodine-stabilized diode laser to the dye laser. The stability of the dye laser is then used for doing the spectroscopy with Ba^+. The frequency offset locking between these two lasers is done in 3 steps :

1. Detection of the beat note between the two lasers: The two beams from the iodine-stabilized diode laser and dye laser are overlapped using a beam splitter and the overlapped signal is collected on a silicon visible photodiode (built in-house) as shown in Fig. 4.12. This photodiode has a high bandwidth and

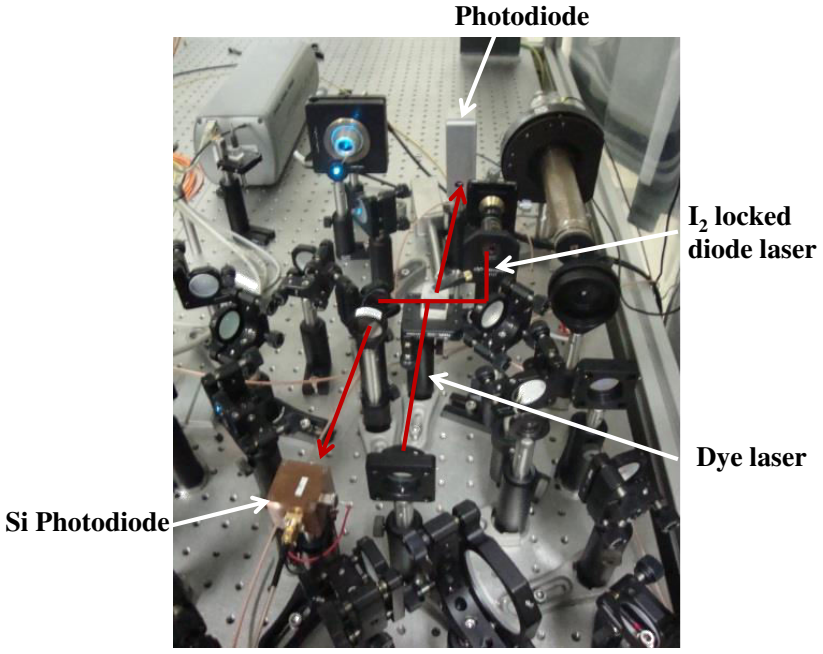

FIGURE 4.12: Photograph of the optical setup for beat note created between two red lasers. The arrows show the direction of the red beam.

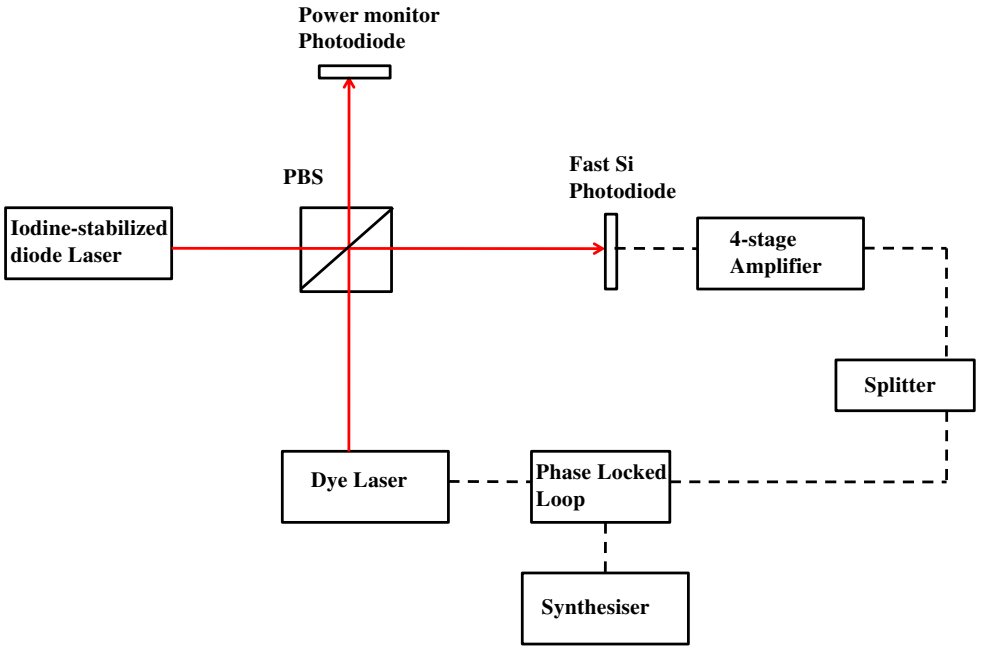

FIGURE 4.13: Schematic diagram of the optical setup to produce a beat note signal between the light of two red laser beams and the obtained signal used for the frequency offset locking.

can detect frequency differences up to 2.5 GHz. The signal from the photodiode is a low power level signal typically -60 dBm which was further amplified by using four 50Ω $ZX60-4016E+$ amplifiers specified for a bandwidth of 20 MHz to 4 GHz and a gain of about 20 dB each. This photodiode signal is then monitored with a 1 GHz Spectrum Analyser (HM5510). This detected about 2.1 mV of the signal. The optical diagram is shown in Fig. 4.13.

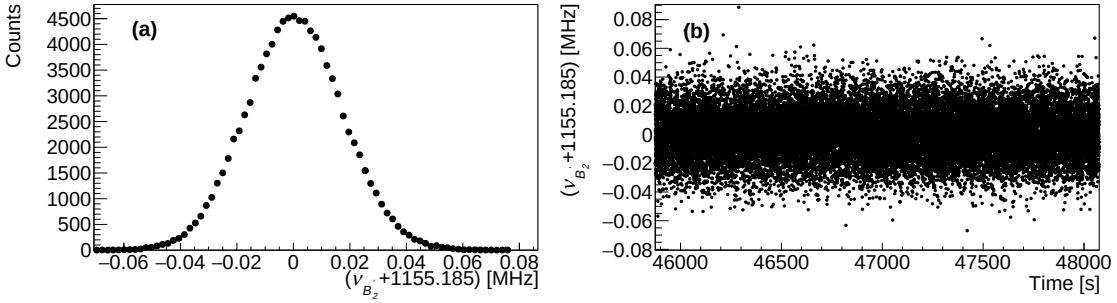

FIGURE 4.14: Example of offset beat note signal created between the light from the iodine-stabilized diode laser and the dye laser. The Full Width Half Maximum (FWHM) of this beat note is 40 kHz.

2. Comparison of the beat note with the reference frequency : A phase locked loop (PLL) circuit (AD4007) [120] compares the beat note frequency with the 16th harmonic of a reference frequency from an rf synthesizer. This produces

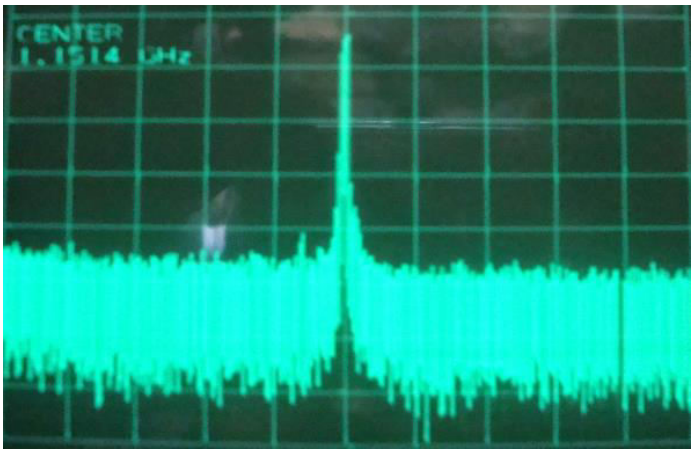

FIGURE 4.15: Photograph of the offset beat note signal between the light from the dye laser and the iodine-stabilized diode laser obtained on a spectrum analyser. The center frequency is at 1.1514 GHz and span is 500 MHz.

a very stable frequency with a low drift. This PLL produces an error signal as a function of the frequency difference between the measured beat note signal and the reference signal.

3. This error signal is then fed back to the laser via a PID control that helps stabilizing the frequency difference. The beat note stability (see Fig. 4.14) can be well monitored using this locking technique. In this configuration the beat note stays within ±50 kHz provided the S/N in this beat note is 45 dB as shown in Fig. 4.15.

Long Term thermal drifts: The laser drifts over time in terms of power due to temperature changes and other influences. These drifts are very slow, i.e. on a timescale of hours. The graphs show the stability in the power by splitting off a fraction of the light after the optical fiber which delivers the light to the trap

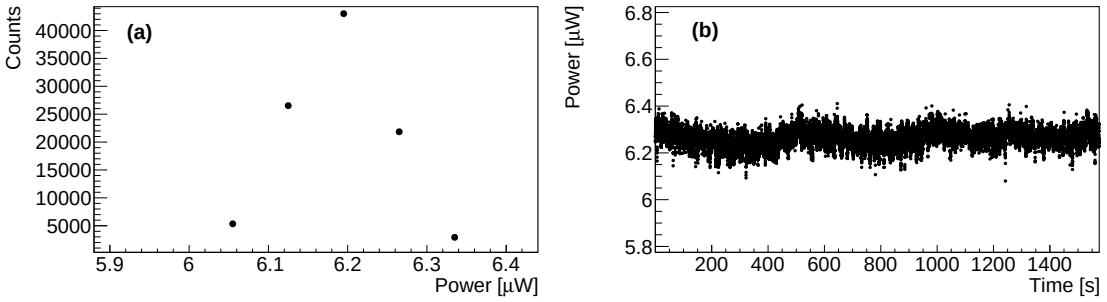

FIGURE 4.16: An example of the power of the light at λ_{650} being constant within 0.4 μW (FWHM) over longer periods of time. This is the observed reading in the power meter.

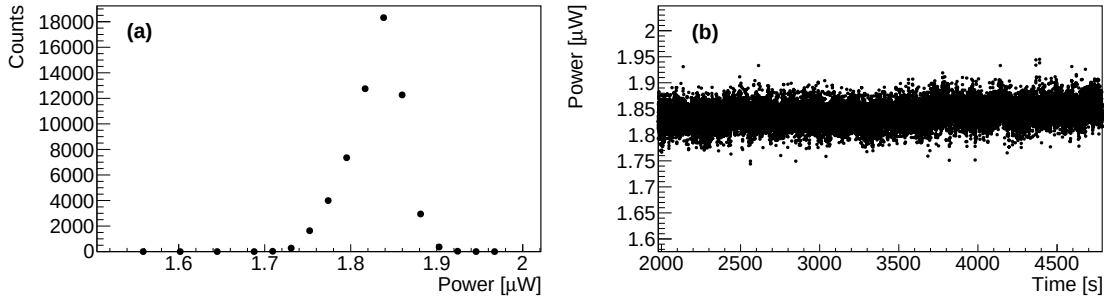

FIGURE 4.17: An example of the power of the light at λ_{494} being constant within $0.07\,\mu$W (FWHM) or better than 5% over longer periods of time. This is the observed reading in the power meter.

(see Figs. 4.16 and 4.17). The power at the position of the ion is 7.5(5) times the reading of the power meter for λ_{494} and 3.5(5) for λ_{650}.

4.6 Beam diagnostics and manipulation

4.6.1 Frequency doubling of Ti:Sapphire laser light

The light from the Ti:Sapphire Laser at a wavelength of $\lambda_{987} = 987\,\text{nm}$ and with 100 mW power is brought to the experiment (i.e. to Ba-Lab) via a single-mode optical fiber (see Fig. 4.18). This is focused to a MgO-doped PPLN second harmonic generation crystal (Covesion MSHG976-0.5-xx) inside of a linear enhancement cavity. The optimal quasi-phase matching condition is reached by heating and stabilizing the crystal to 156.8 °C with a temperature controller (Covesion). The frequency doubling occurs in both propagation directions of the light inside the optical cavity. This produces two counterpropagating laser beams at λ_{494} with about 5 mW power each. This is sufficient for the experiments on single Ba^+ ions. A fraction of this light is sent to a Fabry-Perot spectrum analyzer installed to monitor the modes of the laser. An Acousto-Optic Modulator is used to shift the light frequency and also for stabilization the power of the laser light at λ_{494}. A signal generator HP8657B provides an RF frequency for the AOM. The first order diffracted beam from this AOM is coupled to the trapping setup via a single-mode optical fiber. The intensity of this beam depends on the RF power applied to the AOM. The laser intensity is controlled with a photodiode (SM1PD1A) after passing through the vacuum chamber that enters the trapping setup (see Fig. 4.20). The signal of the photodiode (PD) is locked to a reference voltage with a PID controller. A ZLW-2 mixer from Mini-Circuits combines the output of the PID controller with the AOM RF power such that the diffracted beam intensity is corrected. The laser light at λ_{494} is actively stabilized in frequency. The operating center frequency of the AOM is given by $\nu_{AOM-1} = 198.9\,\text{MHz}$.

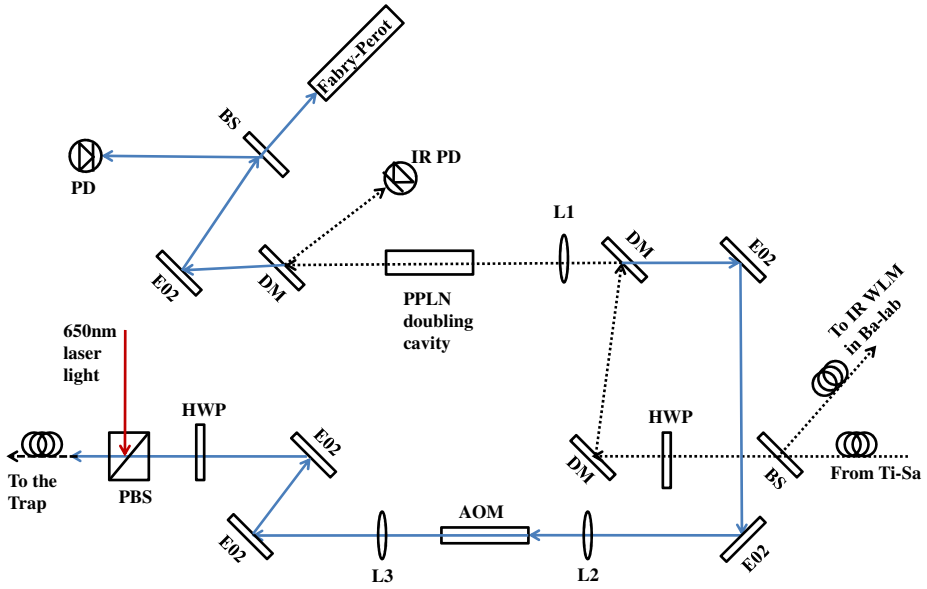

FIGURE 4.18: Optics diagram shows the frequency doubling of laser light at wavelength $\lambda_{987} = 987\,\text{nm}$ from Ti-Sa. The PPLN crystal is responsible for the second harmonic generation and for producing the light at λ_{494} for driving the cooling transition in Ba^+.

4.6.2 Dye laser light through the trap

The light from the dye laser at a wavelength of λ_{650} and 35 mW of laser power is transported to the experiment (in BaLab) via a single-mode optical fiber of 50 m length (see Fig. 4.11). After this single mode fiber, 13 mW of laser power can be delivered to the experiment. Before passing through the chamber and the trap, this red laser light (i.e. after the single mode fiber) is then passed through a double pass AOM operated at a center frequency of 350 MHz which helps to get rid of the alignment problems and helps for a better frequency stabilization. A signal generator provides a rf frequency for this AOM. The first order diffracted beam from this AOM is then coupled to the trapping setup using the same single-mode optical fiber as is used for light at λ_{494}. The intensity of this beam depends on the rf power applied to AOM. Before going through the chamber and the trap, there is 100 μW power of red light which is sufficient for laser spectroscopy and diagnostics. Later this red light is passed through a frequency switching scheme (as explained in Section 4.6.3) for high-resolution spectroscopy. Further, a fraction of this red light is sent to a Fabry-Perot interferometer installed to investigate the modes of the laser.

4.6.3 Frequency switching of dye laser for cooling and spectroscopy

This technique of switching of the dye laser light for cooling and spectroscopy is necessary during the high-resolution spectroscopy of the Ba^+ ion. In this technique, the spectrum of the ion is probed for a small interval of time while cooling it for most of the time by maintaining a constant temperature of the ion at optimized frequency detunings. This is achieved by changing the repump 650 nm frequency between two values using an RF switch (Mini-Circuits ZASW-2-50) that selects the frequency ν_{AOM-2} of the Acousto-Optical Modulator AOM-2 between frequencies ν^1_{AOM-2} that probes the atomic transition while ν^2_{AOM-2} cools the ion as shown in Fig. 4.19. A function generator is used to control the switching frequency between

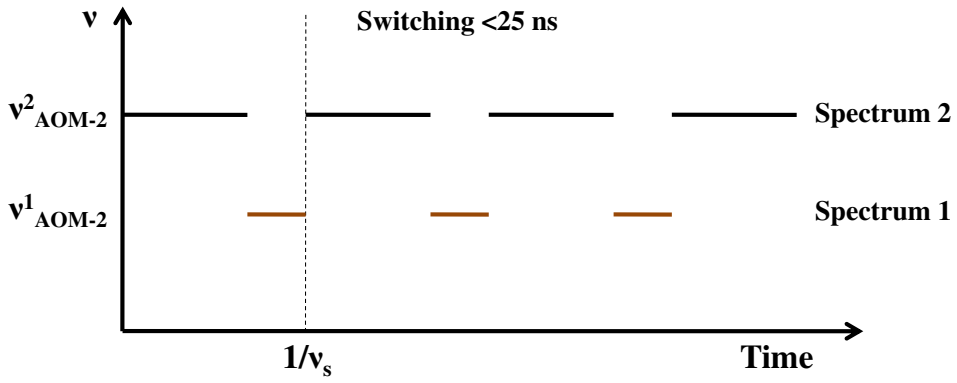

FIGURE 4.19: Schematic diagram for switching between two laser light frequencies to provide for sufficient optical cooling and for spectroscopy of Ba^+ in short interleaved intervals.

1 kHz to 300 kHz using a square pulse signal. The duty cycle can be varied between 10 % and 90 % for both these frequencies ν^1_{AOM-2} and ν^2_{AOM-2}. The PMT signals for either of these frequencies are recorded separately. The PMT output signal is gated with the signal that switches between these two synthesizer frequencies to the AOM-2 and this helps to assign PMT pulses to the synthesizer active at the moment.

4.6.4 Delivery of light to the center of trap

The delivery of the light beams through the trap involves the fibers for transport of light, mirrors for alignment of the beams through the trap, photodiodes, and power meters to record the amount of light and beam profilers to record the beam characteristics through the trap.

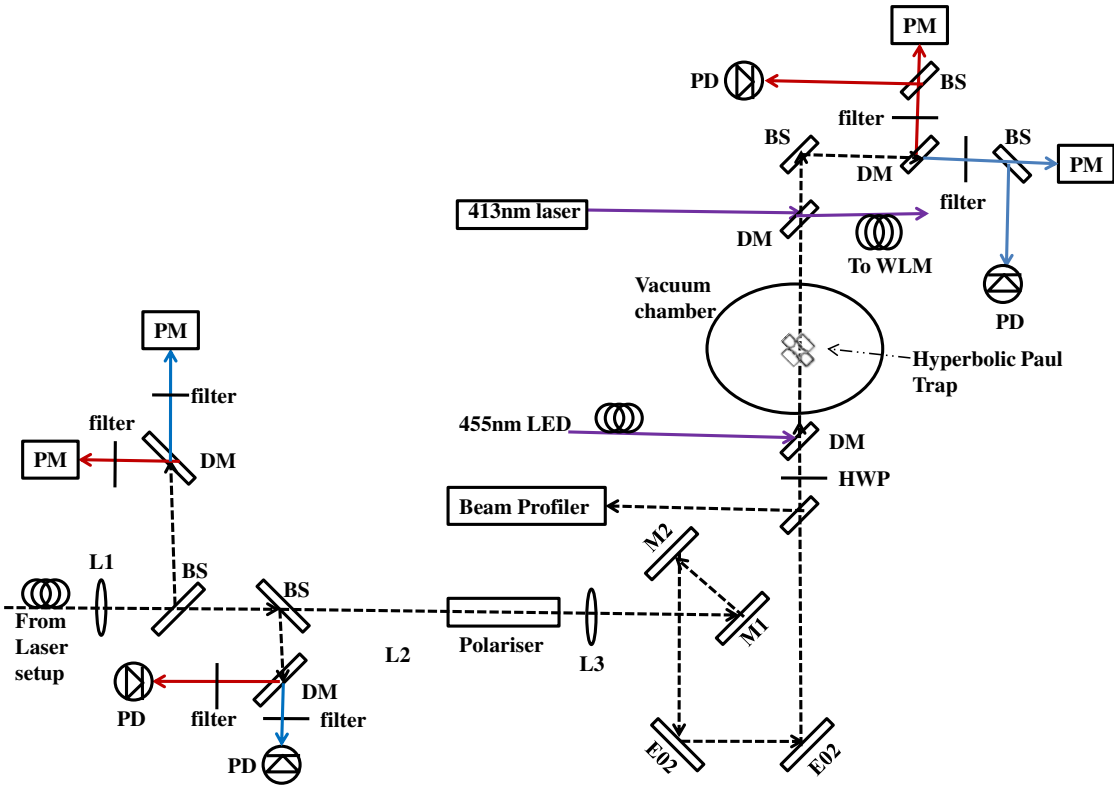

FIGURE 4.20: Optical diagram for the diagnostics of all the laser systems employed in the experiment.

1. Single and multimode optical fibers: The single-mode optical fibers enable us to transfer the light at different wavelengths through the trap. This is needed to get a clean gaussian beam at the site of the trapped ion. The multimode fibers help to monitor the different wavelengths using the WLM and also for transferring the light from the shelving and deshelving LEDs through the trap (see Section 4.7).

2. Piezo-controlled silver mirrors and dichroic mirrors: The mirrors M1 and M2 (see Fig. 4.20) are silver mirrors that are mounted on piezo driven mirror mounts (Agilis AG-UC2-UC8 series from Newport). This gives the advantage of the movement of the beams in precise steps of few tens of nanometers for measurements that are sensitive to these movements. They are more robust and have a predictable performance. The dichroic mirrors (DM) used are wavelength selective thus allowing only certain wavelengths to pass through. Besides, the broadband dielectric mirrors (E02-THORLABS) are used to align the beam through the trap. Filters are used to selectively transmit light for a particular range of wavelengths.

3. Beam splitters, photodiodes, power meters and position sensing devices: Beam splitters are utilized to divide a part of the beam to the photodiodes

(PD) and the other part onto the power meters (PM) as shown in Fig. 4.20. Photodiodes (PD) are used to monitor the power for each of the wavelengths used for the Ba^+ spectroscopy. Power meters have been installed before and after the trap to monitor the power of both the λ_{494} and λ_{650} laser light delivered through the trap. These are a good diagnostic to account for the optimal alignment of the laser beams through the trap. Besides these, position sensitive devices are also installed to give information about the position of the beams through the trap.

4. Beam profilers: There are two beam profilers for monitoring the beam positions through the trap. The beam profiler (BC106-VIS CCD Camera Beam profiler from THORLABS) as shown in Fig. 4.20 gives information about the beam characteristics for both the laser light at λ_{494} and λ_{650} before going through the trap. This is helpful to monitor the movement of the beam position in small steps using the piezo controlled mirrors. This acts as an important tool to align the laser beams through the trap electrodes with a minimum of scattered light. Perfect alignment of these beams through the electrodes ensures that the background is least i.e. 80 cnts/sec on the PMT for 1 μW of blue light at the power meter. Another beam profiler i.e. BP109-UV Scanning Slit Optical Beam Profilers from THORLABS is used for monitoring the beam properties of the light shift laser used for measuring light shifts (see Fig. 4.23). Both these beam profilers are mounted in such a position that the beam characteristics at this position are approximately the same as at the site of the ion.

4.7 Shelving and deshelving LEDs

The other transition from ground state $6s\,^2S_{1/2}$–$6p\,^2P_{3/2}$ in Ba^+ at λ_{455} is employed for shelving into the $5d\,^2D_{5/2}$ state (see Chapter 5). Light from a light emitting diode (LED) (Fiber-Coupled LED M455F1 specified for 1000 mA, 9.5 mW from Thorlabs) is employed to drive this transition. Fig. 4.21 shows the optical setup for the delivery of the LED light at λ_{455} through the trap. The long-term stability in terms of power of about 4-5 % is shown in Fig. 4.22.

Deshelving via the transition $5d^2D_{5/2}$–$6p^2P_{3/2}$ in Ba^+ is possible with light at λ_{614}. A high power light emitting diode (LED) (Mounted LED M617L3 with center wavelength at 617 nm and specified for 1000 mA, 600 mW from Thorlabs) is employed to drive this transition. Fig. 4.21 shows the optical setup for delivery of this LED light at λ_{455} through the trap. This light is further used to move the

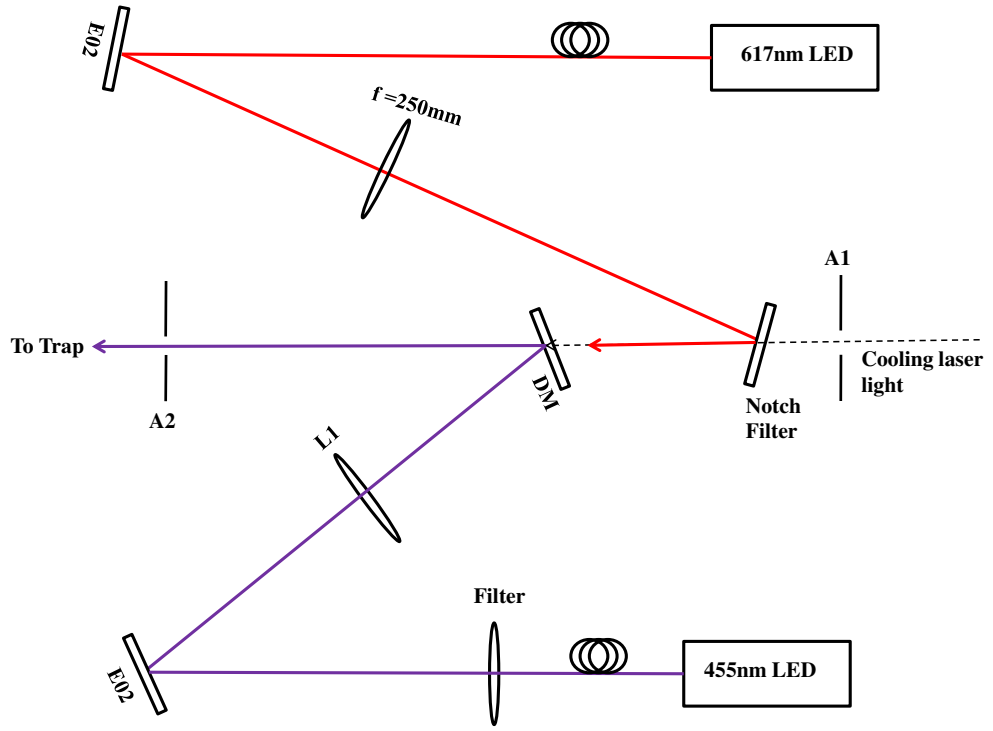

FIGURE 4.21: Schematic diagram for introducing a laser light beam at λ_{455} and λ_{617} for shelving and deshelving, respectively through the trap.

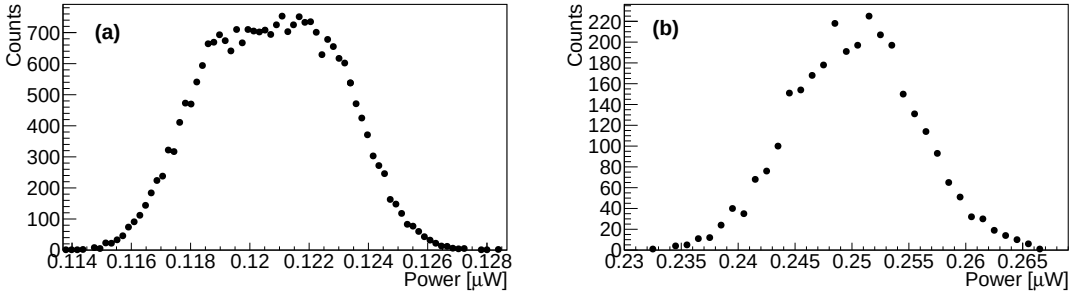

FIGURE 4.22: An example of the long term stability of the power of the LED. The output power is changed by 3-5 % over several hours of continuous data taking.

ion from the $5d\,^2D_{5/2}$ to the $6p\,^2P_{3/2}$ state during the lifetime measurements of the $5d\,^2D_{5/2}$ state.

4.8 Light shift laser

A central hole in the endcaps of the Paul trap permits optical access along the symmetry axis of the trap. This is at an angle of 54.7 ° to the cooling beams and

is exploited for light shift measurements as reported in Chapter 7. Here two laser sources are available:

1. An intense high-power solid state laser from Toptica Photonics (DL-RPA-SHG PRO) at an operating wavelength λ_{590} and with 2 W power.
2. An external-cavity tunable diode laser (HL6366DG from THORLABS) arranged in Littrow configuration with an operating wavelength λ_{650} for the $5d\,^2D_{3/2}$–$6p\,^2P_{1/2}$ transition.

The latter one is close within ±0.1 nm. It provides a power of up to 35 mW with the temperature maintained at 40.1 °C and an operating current of 162 mA. The wavelength of the light sources is monitored by a WLM.

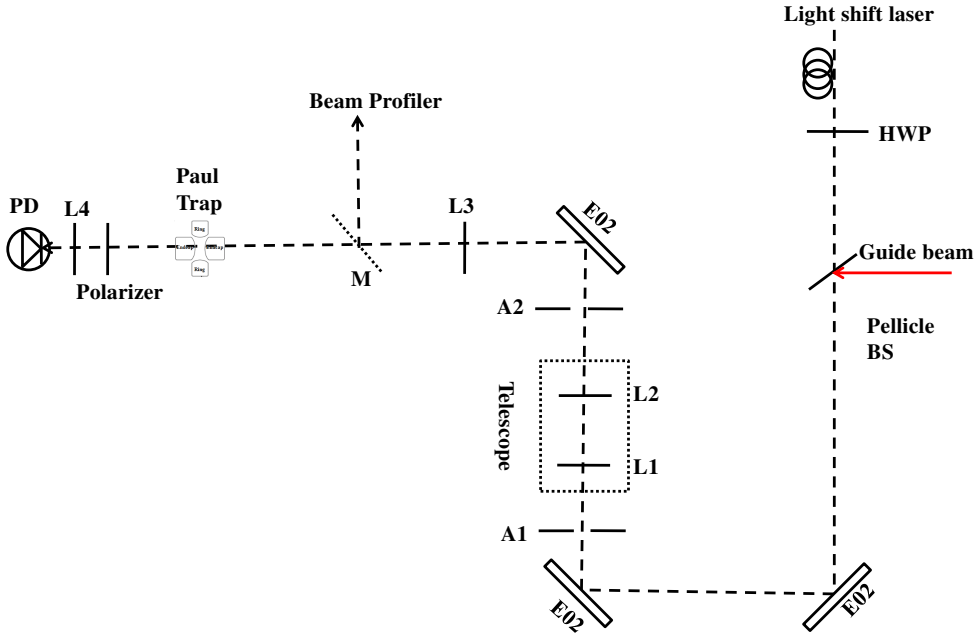

FIGURE 4.23: Optical setup diagram for delivery of the light shift laser through the trap. E02 is a piezo controlled mirror (Agilis AG-UC2-UC8 series from Newport). M is a flip-in mirror in the beam path to deflect the beam to the beam profiler which is placed at the virtual trap position.

Overlap of the light shift laser beam with the ion

This laser light is brought to the setup via a fiber coupled to produce a Gaussian beam at the site of the ion. An additional guide beam of resonant frequency with the transition in the ion confirms the presence of the ion in the trap. The first

approach to overlap the beam with the ion to better than $\sim$150 μm can be done with the beam profiler (BP109-UV Scanning Slit Optical Beam Profilers from THORLABS) (see Fig. 4.23). This beam profiler gives information on the shape, size and overlap of both beams. It was assured that there is maximum overlap of the peaks for both beams for this measurement.

The accurate control of the position of the beam at the site of the ion is relevant for measuring light shifts. The optical elements in the beam path have been chosen in such a way that the beam displacement is the least at the site of the ion. This is because these optical elements have non-parallel surfaces that can affect the beam position at the site of the ion. The last steering mirrors can be controlled by a piezo actuator $\sim$1 μm step size. The polarisation of the light is controlled by a waveplate. It is quantitatively analyzed by the combination of a rotatable polariser and a photodiode behind the trap.

4.9 Section Summary

The complete system for the generation of the required light sources including diagnostics for power and frequency stabilization has been implemented into the experimental setup. The optical setup serves for delivering the cooling laser light beams through the trap center of the electrodes. The frequency stabilization of the cooling lasers is achieved to relative order $\frac{\Delta\nu}{\nu} \approx 10^{-11}$. Beam diagnostic and manipulation techniques have been implemented for each of these laser systems. With the complete control of frequency and beam positions, we can load one to few ions. The laser cooling beams have typically a diameter of 120 μm and powers of 7.5(5) μW for λ_{494} and 3.5(5) μW for λ_{650} delivered to the trap center. Under these conditions, the ions are laser cooled to form crystals. At resonance, a typical PMT count rate of 2500 cnts/s per ion with a background of 80–100 cnts/s is observed. Lasers for Ba^+ ion production and LEDs for driving the shelving and deshelving transitions have been implemented. Lasers with light at λ_{590} and λ_{650} have been setup to induce light shifts and to provide for measuring them.

Chapter 5

Precise determination of lifetime of $5d\,^2D_{5/2}$ state in Ba^+

5.1 Introduction

The lifetime of the long-lived metastable $5d\,^2D_{5/2}$ state provides information on the atomic structure and permits the extraction of details of the atomic wavefunctions of the involved states. Measurements of the lifetime of the $5d\,^2D_{5/2}$ state have been previously implemented both in single and multiple trapped ions [121]. The stable trapping conditions which can be achieved in rf Paul traps offer the unique possibility to determine experimentally this lifetime of about half a minute. The radiative lifetime of the metastable $5d\,^2D_{5/2}$ state in Ba^+ is due to the electric quadrupole transition to the ground state. It is related to this matrix element by the following relation:

$$\tau_{D_{5/2}} = \frac{3h\epsilon_o c^5}{2\omega^5} \frac{1}{\langle 6s\,^2S_{1/2}|Q|5d\,^2D_{5/2}\rangle^2} \tag{5.1}$$

where Q is the quadrupole transition operator, $6s\,^2S_{1/2}$ and $5d\,^2D_{5/2}$ are the ground and metastable states, respectively.

Such measurements are sensitive to small changes in the performance of the experiment on long time scales. For a statistical accuracy of 4-5 %, 500 jumps are required. This yields a run time of 8-10 hrs for each individual measurement. Extremely good vacuum and laser stability in terms of power and frequency (as discussed in Chapters 3 and 4, respectively) enables such a measurement.

The lifetime of the metastable $5d\,^2D_{5/2}$ state in trapped Ba^+ ion(s) is measured by the electron shelving technique. The present status of the systematic lifetime measurements and their sensitivity to experimental parameters for single and multiple trapped ions are presented and summarized.

5.2 Electron shelving technique

The Ba^+ ion is an effective three-level lambda (Λ) system, in which one of the ground states is long-lived. The excitation to the $5d\,^2D_{5/2}$ state results in "quantum jumps" between dark and bright states which was first demonstrated by Nagourney et al. [122]. The technique is ideally suited for a precise determination of lifetimes with few laser cooled ions. In Subsection 5.2.1, we show a sufficiently large signal-to-noise ratio to count the ions in the bright state.

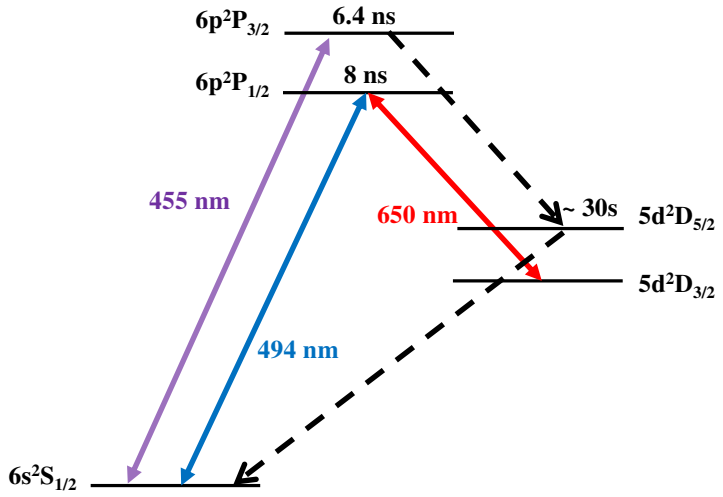

FIGURE 5.1: Implementation of shelving for the low-lying energy levels for Barium (Ba^+) ion. The long-lived metastable state is the $5d\,^2D_{5/2}$. The bold lines show the laser excitation of the laser cooling cycle. Light from the LED at λ_{455} excites the ion to the $6p\,^2P_{3/2}$ state which occasionally decays to the $5d\,^2D_{5/2}$. The rate of the decay to the $6s\,^2S_{1/2}$ state yields the lifetime of the $5d\,^2D_{5/2}$ state as indicated by the dotted lines.

5.2.1 Application to single trapped ion

Light of two laser beams at λ_{494} and λ_{650} with the detuning of δ_{494} = -48.4 MHz and δ_{650} = -1.2 MHz, drive the ion in a closed laser cooling cycle of $6s\,^2S_{1/2}$, $6p\,^2P_{1/2}$ and $5d\,^2D_{3/2}$ state (see Fig. 5.1). Observing the fluorescence from the $6p\,^2P_{1/2}$–$6s\,^2S_{1/2}$ transition implies that the ion is in the cooling cycle ("not shelved" or

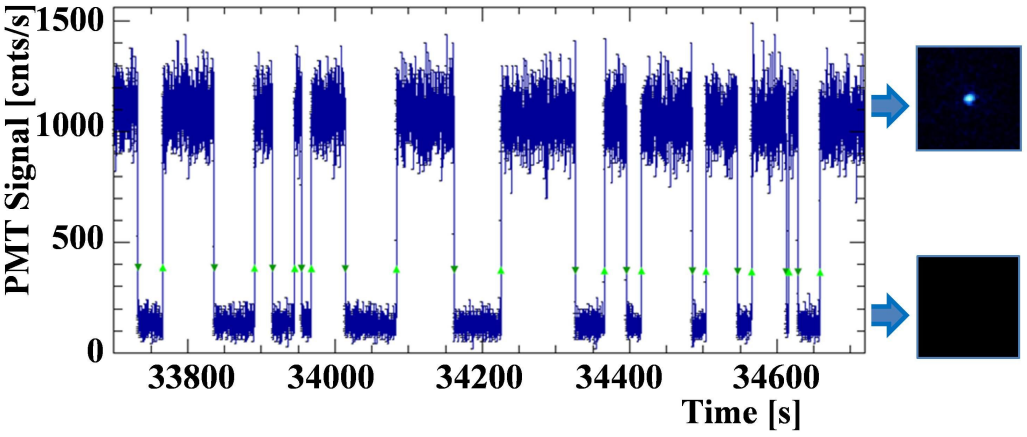

FIGURE 5.2: An example of shelving in a single trapped ion. Left: PMT trace of the 494 nm fluorescence from the $6p\,^2P_{1/2}$ state as a function of time shows quantum jumps observed in single Ba^+ ion. The low fluorescence level indicates that the ion is definitely in the metastable $5d\,^2D_{5/2}$ or shelved state. The green points represent the threshold count rate taken into account during data analysis. They show a clear discrimination between the dark and bright states. Right: EMCCD image of the ion in the unshelved state (top) and shelved state (bottom).

bright state). The high power LED which emits light around λ_{455} (Section 4.7) drives the ion to the $5d\,^2D_{5/2}$ state via exciting the $6s\,^2S_{1/2}$–$6p\,^2P_{3/2}$ transition. The fluorescence from the cooling cycle ceases. This marks the starting point of a shelving period. The period ends with the $5d\,^2D_{5/2}$–$6s\,^2S_{1/2}$ quadrupole transition. Fig. 5.2 displays an example of the photon rate recorded by the PMT versus time

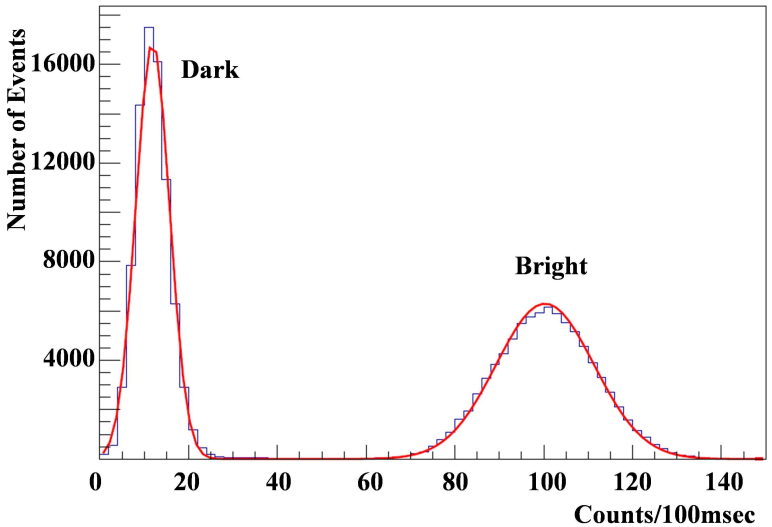

FIGURE 5.3: An example of the mean of the PMT fluorescence rates of the ion both in the shelved and unshelved state. Highest fluorescence rate indicates that the ion is "not shelved" into the $5d\,^2D_{5/2}$ state. Lowest fluorescence rate indicates that the ion is in the "shelved" or $5d\,^2D_{5/2}$ state. This procedure is applied to a larger dataset of 128 periods. This is for 100 ms counting interval.

for single Ba^+ ion. The highest PMT photon count rate of 1000 cnts/s indicates that the ion is in the cooling cycle. The lowest count rate of 100 cnts/s is due to the scattered light and dark count rate of the PMT. These "off/on" and "on/off" transitions in the fluorescence correspond to quantum jumps between the $5d\,^2D_{5/2}$ and $6s\,^2S_{1/2}$ states.

For quantum jumps analysis in single trapped Ba^+ ion, the average count/100 ms for the bright and the dark state results in a clear discrimination of these two levels (Section 5.3). The threshold for this particular sample of quantum jumps in a single ion is set to be at 400 counts/s. With this threshold, the length of the shelved and unshelved periods are determined and the probability distribution of intervals is plotted (see Fig. 5.3). There are two exponentials determined each for the unshelved and shelved period (see Fig. 5.4). These shelved and unshelved states directly give the $5d\,^2D_{5/2}$ state lifetime, $\tau_{D_{5/2}}$ and the shelving time τ_S. The distributions are in good agreement with an expected exponential decay.

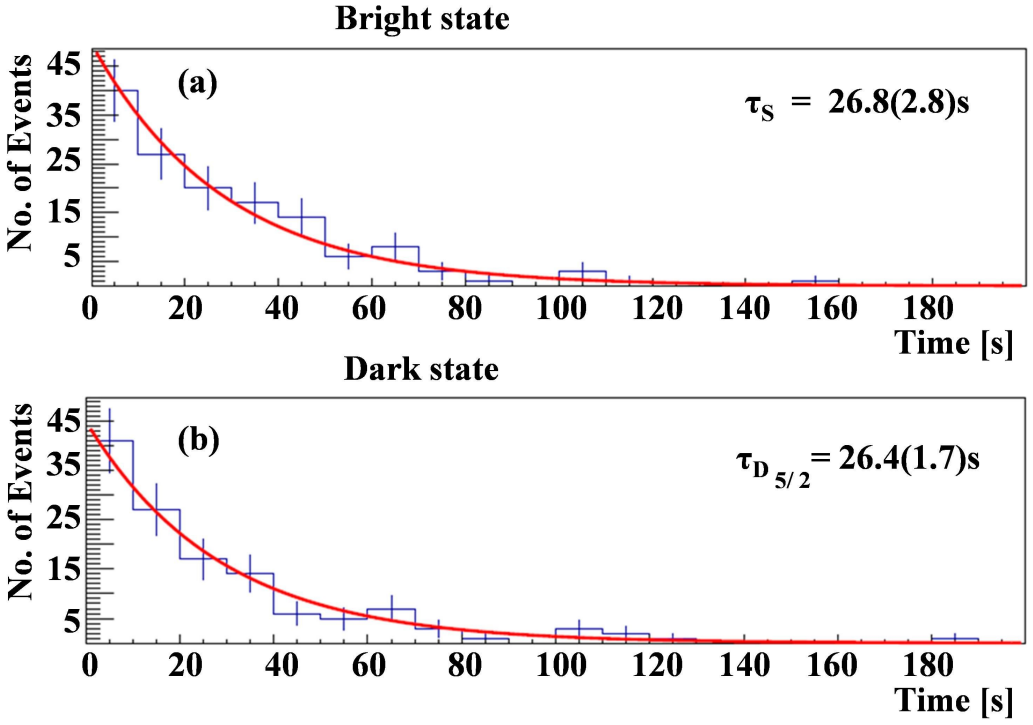

FIGURE 5.4: An example of a histogram for a "2 h" measurement time that represents the distribution of dwell times in the unshelved and shelved state for "on" and "off" times, respectively. An exponential is fitted to both the experimentally obtained histograms. This gives the lifetime of the trapped ion in both the shelved and unshelved states. (a) represents the lifetime of the unshelved/bright state with about 141 entries and mean lifetime of $\tau_S = 26.8(2.8)$ s while (b) represents the lifetime of the shelved/dark state with about 128 entries and mean lifetime of $\tau_{D_{5/2}} = 26.4(1.7)$ s.

5.2.2 Application to multiple trapped ions

The method works for several ions as long as the signal-to-noise is sufficient to discriminate between the different number of "bright ions". Figs. 5.5 and 5.6 shows an example of quantum jumps in a crystal of 3 ions. The highest photon count rate of 3300 cnts/s represents 3 "bright" ions. The count rate of 2300 cnts/s implies that 1 out of 3 ions is in the "shelved or dark" state, while 1200 cnts/s is

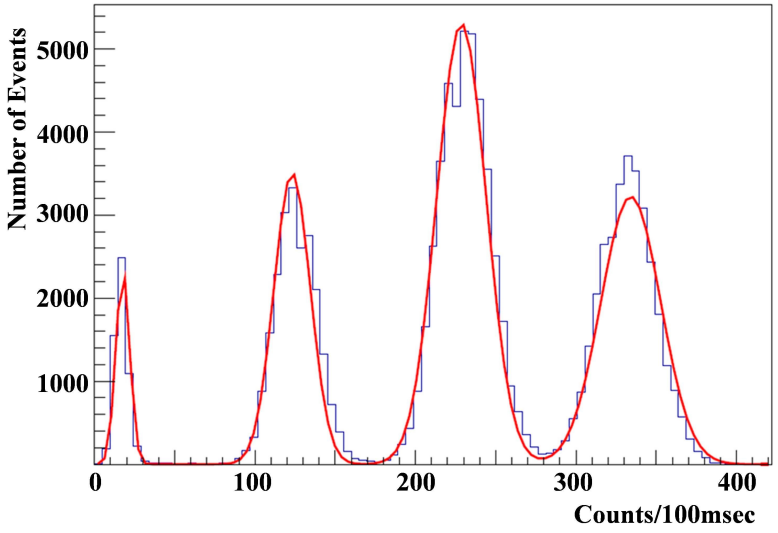

FIGURE 5.5: Mean of the PMT fluorescence rates of the ion both in the shelved and unshelved state. Highest fluorescence rate indicates that all the ions are "not shelved" into the $5d\,^2D_{5/2}$ state. Lowest fluorescence rate indicates that all the ions are in the "shelved" or $5d\,^2D_{5/2}$ state. The measurement is taken for 100 ms counting interval.

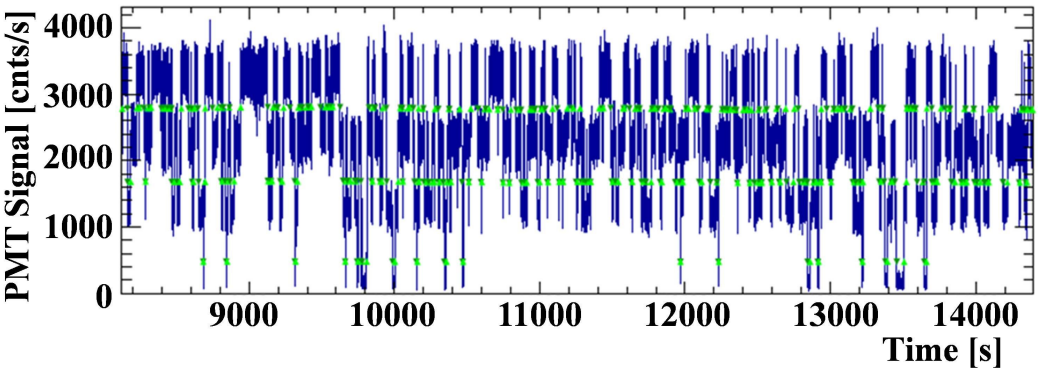

FIGURE 5.6: An example of shelving in 3 ions. PMT trace of the 494 nm fluorescence from the $6p\,^2P_{1/2}$ state shows quantum jumps observed in a crystal of 3 Ba^+ ions. The highest fluorescence level indicates that all the ions are not in the shelved state. The lowest fluorescence level indicates that all the ions are in the metastable $5d\,^2D_{5/2}$ or shelved state. The arrows represent the threshold count rate taken into account during data analysis. They show a clear discrimination between the dark and bright states.

when 2 out of 3 ions are shelved. A count rate of 200 cnts/s represents that all of 3 ions are shelved into the $5d\,^2D_{5/2}$ state.

Fig. 5.7 shows a zoomed image of the different levels of photon count rate for a crystal of 3 ions together with the images of the ions. The position of the bright ions in the images doesn't change, it implies that the dark ions are still trapped and sympathetically cooled.

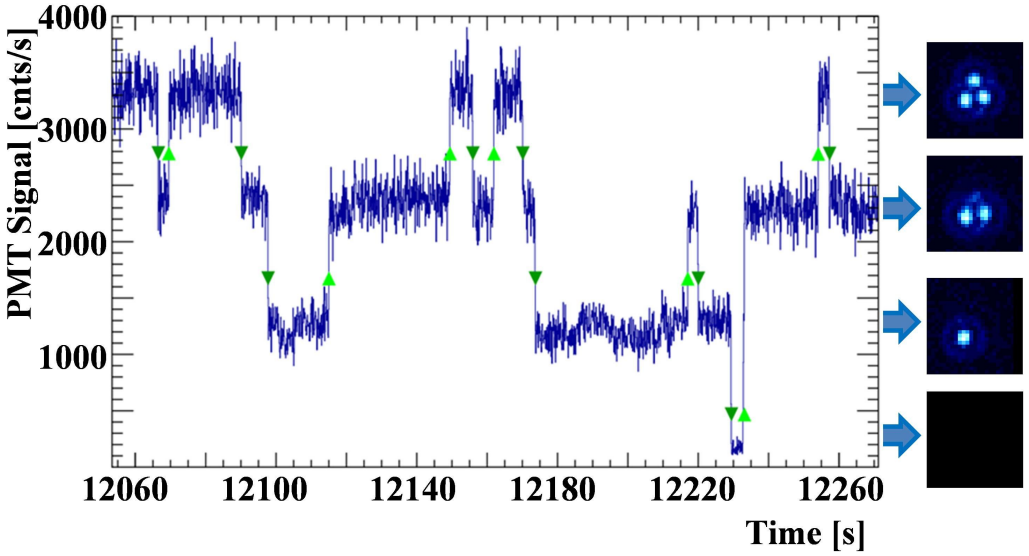

FIGURE 5.7: Zoomed image of a section of the PMT trace of the 494 nm fluorescence from the $6p\,^2P_{1/2}$ state shows quantum jumps observed in a 3-ion crystal of Ba^+ ions as shown in Fig. 5.6. The green arrows represent the threshold count rate taken into account during data analysis. The position of the bright ions indicates that all 3 ions are still in the crystal.

The threshold for quantum jumps analysis with 3 different number of "bright" ions is represented by four levels of fluorescence (see Fig. 5.5). The thresholds for this particular sample of quantum jumps for each ion in a 3-ion crystal is about 500, 1700 and 2800 counts/sec. The periods for the time intervals with a different number of bright ions result in this case in four exponential distributions. The maximum likelihood estimate is used to determine the exponential lifetimes, i.e. taking the mean of the interval lengths. Here the lifetime of the state is given by $\tau_i^{-1} = i\tau_{D_{5/2}}^{-1} + (n-i)\tau_s^{-1}$ where i out of n ions are shelved. Fig. 5.8 indicates that an exponential function can be fitted to each of the histograms as expected. Depending on the determining parameters for the threshold, the value of the threshold in the fluorescence rate can change.

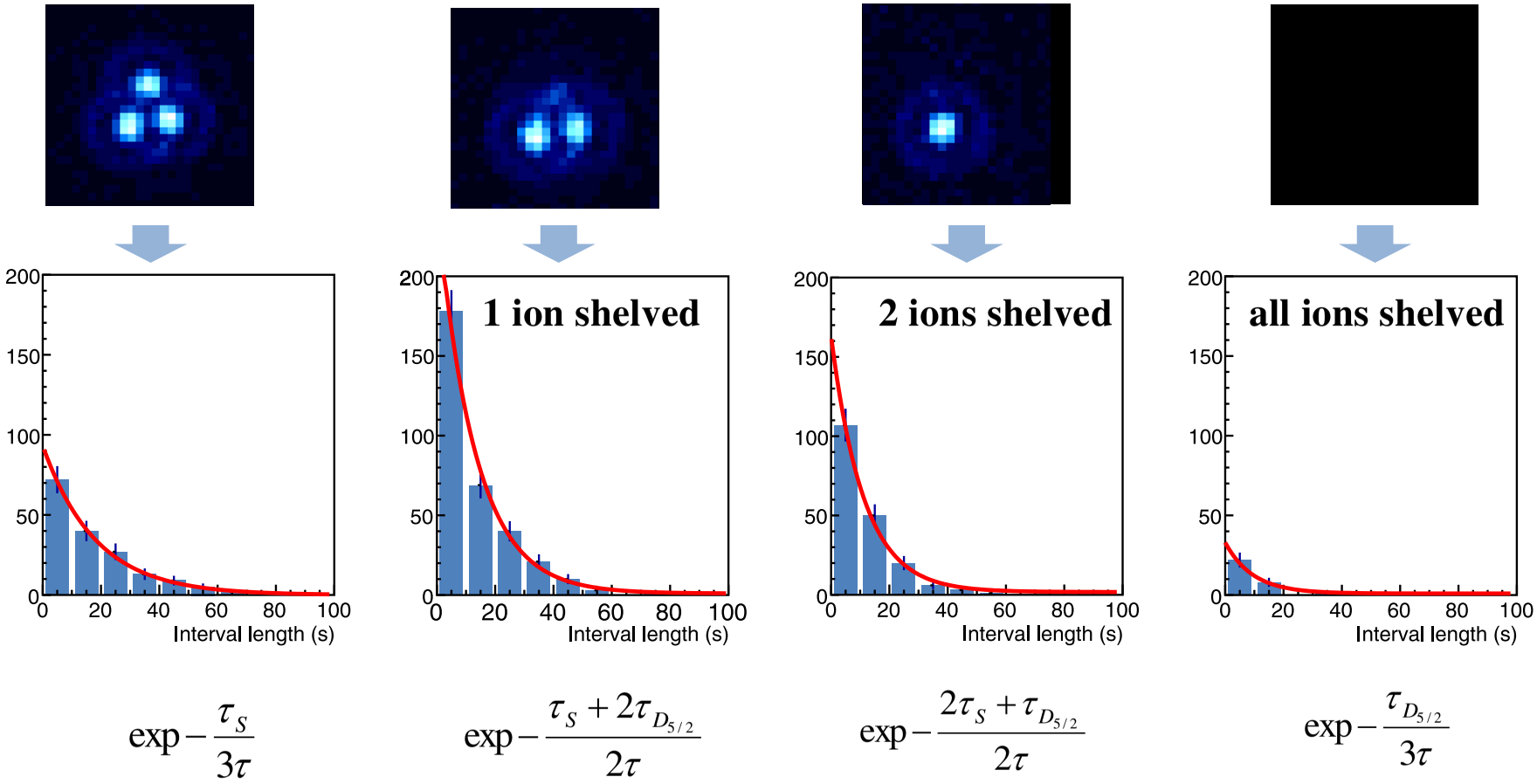

FIGURE 5.8: Histograms represent the distribution of dwell times in the unshelved and shelved state for "on" and "off" times, respectively. These histograms depict the cases when a different number of ion(s) are shelved and when all ions are unshelved. An exponential is fitted to each of these four experimentally obtained histograms. The time constants depend only on the τ_S and the lifetime of the $5d\,^2D_{5/2}$ state yielding a $\tau_{D_{5/2}} = 27.1(2.5)$ s and $\tau_S = 50.7(4.2)$ s.

5.3 Quantum jumps analysis

Large sets of data have been analyzed and an automatic procedure to determine thresholds have been developed. The different threshold levels create a probability distribution for the number of bright ions. Data has been taken under a large variety of experimental conditions. These data sets are analyzed for correlations with the experimental parameters. The data selection criteria includes the stability of frequencies and intensities and these are synchronously measured with the data. Since we record all the data, we can impose cuts on the data sets of ± 0.5 MHz on the frequency around the desired value and $\pm 5\,\%$ on the intensities of the laser lights (see Chapter 4).

Distribution of collected statistics for different experimental parameters

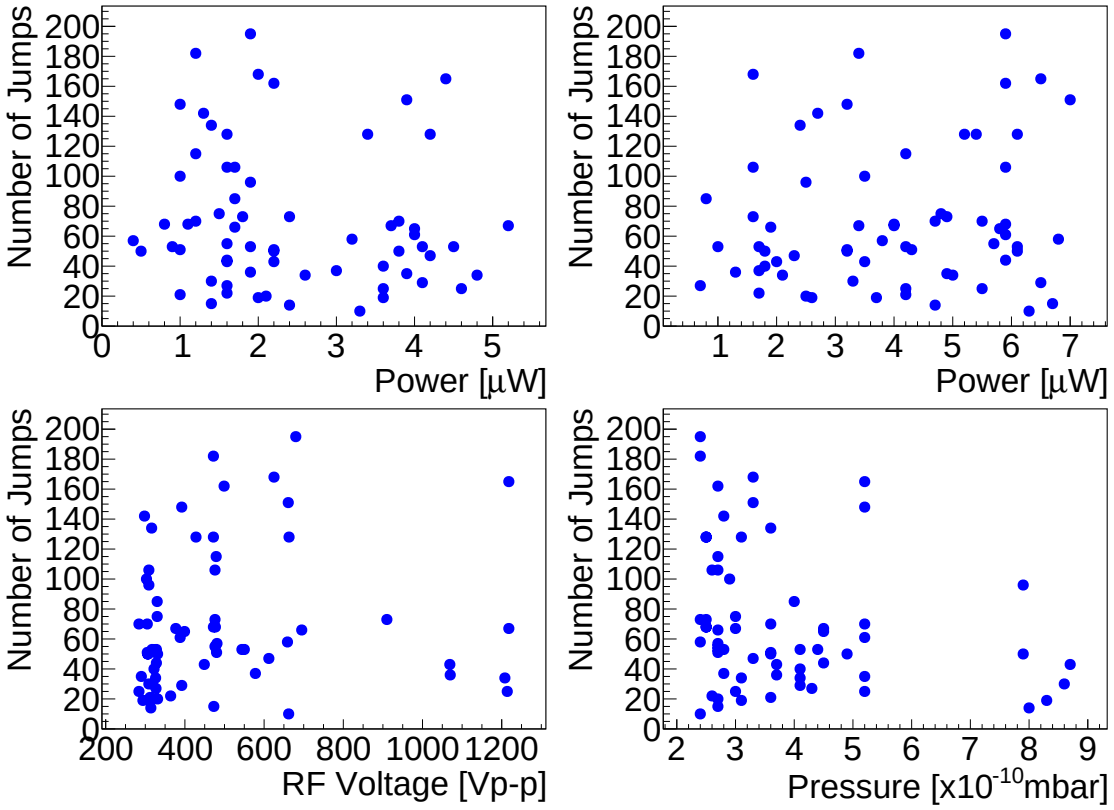

FIGURE 5.9: Variation of a number of jumps for different cooling, repump laser intensities, rf voltages and residual gas pressure conditions. The full datasets are listed in Tables G.1, G.2, G.3 and G.4, respectively in Appendix G.

From the measured data sets, the distribution of the statistics collected for the number of jumps was investigated. The data sets with different number of quantum jumps have been plotted for different critical parameters as shown in the graphs

here. These measurements show that these experimental parameters do not have a significant effect on the number of quantum jumps.

5.4 Sensitivity of lifetime to experimental parameters

Lifetime measurements of metastable long-lived states are sensitive to variations in experimental parameters over periods of several hours. We have collected sets of measurements. Data sets with similar parameters have been compiled leading to 200 measurements which contain between 50-250 quantum jumps. In the search for a dependence on experimental parameters, the data set has been regrouped according to a single selected parameter. The analysis exhibits no significant dependence on any of these parameters which allows us to determine the lifetime as a weighted average of all data sets.

Rf voltage amplitude

The amplitude of the rf potential on the trap electrodes determines the strength of the trapping potential and the effective volume of the trap. Furthermore, the different values select different $\frac{Q}{M}$ ratios for stable trapping which can affect the type of unwanted ions in the trap. Another effect is the different amount of heating due to the driven micromotion which could cause heating up of the ion into a higher motional state during the dark periods. The change in the trap potentials changes

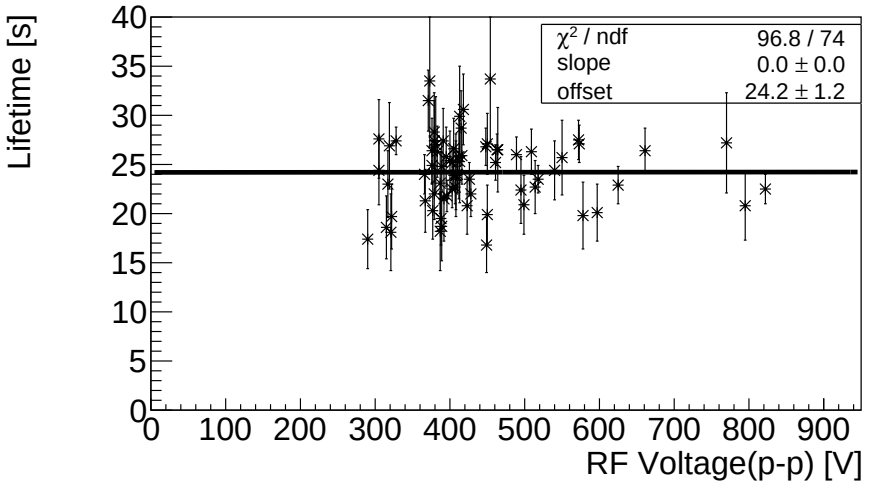

FIGURE 5.10: The experimentally determined lifetime of the $5d\,^2D_{5/2}$ state with respect to the RF amplitudes of the trapping field. Here the pressure is distributed over the whole range in the experiment and the pressure have not been applied in these measurements. A linear dependence has been fitted with a slope of 0.000(3) s/V and an offset of 24.2(1.2) s with a χ^2 of 96.8 for 74 d.o.f. The full dataset is listed in Table F.1 in Appendix F.

the micromotion and the effective trapping potentials. No dependence can be deduced from the data (see Fig. 5.10).

Laser intensities of the cooling lasers and the shelving LED light

The lifetime of this state was also measured for different cooling and repump laser intensities (see Fig. 5.11). The individual lifetime measurements do not depend on the employed light level for the laser cooling. A small weak dependence on the intensity of the LED (see Fig. 5.12) can be extracted for a dataset collected at a residual gas pressure of 8×10^{-11}mbar.

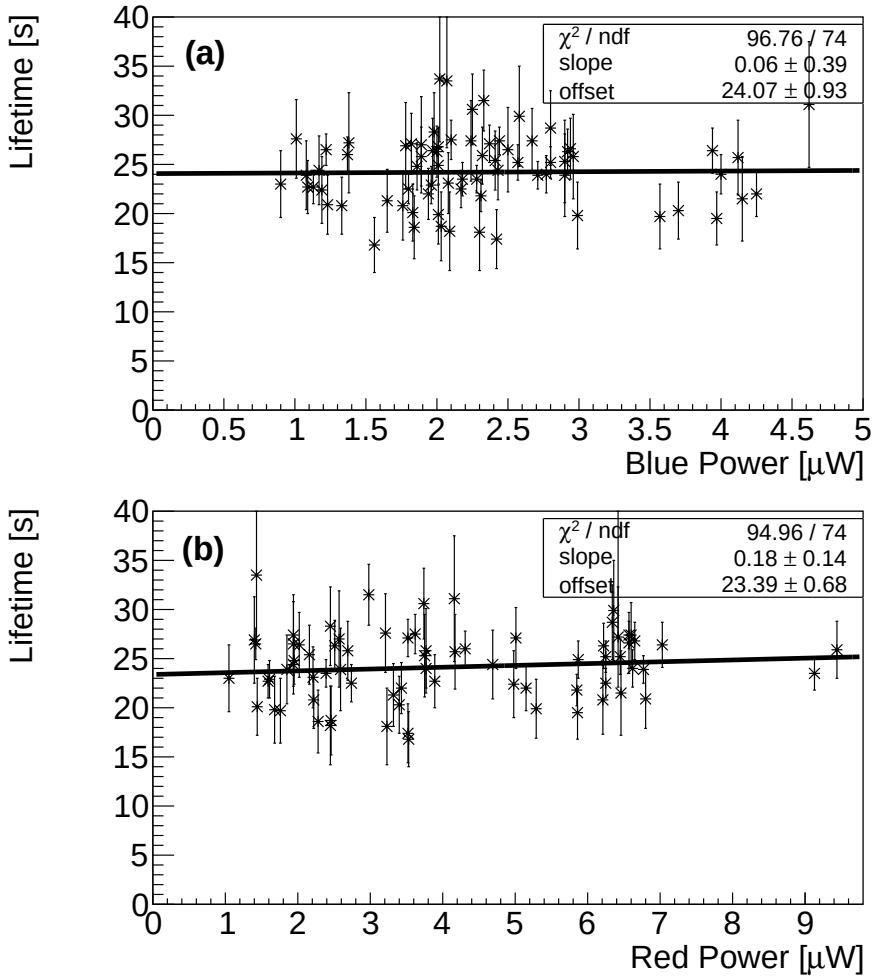

FIGURE 5.11: Variation of the lifetime of the $5d\,^2D_{5/2}$ state with respect to the cooling and repump laser intensities, respectively. 1μW of blue (see (a)) and red power (see (b)) corresponds to $7.5(5)\,\mu$W and $3.5(5)\,\mu$W, respectively delivered to the trap center. Here the pressure is distributed over the whole range in the experiment and the pressure corrections have not been applied in these measurements. For the blue power, a linear dependence has been fitted with a slope of $0.06(39)\,\mathrm{s}/\mu\mathrm{W}$ and an offset of $24.1(9)\,\mathrm{s}$ with a χ^2 of 96.76 for 74 d.o.f. For the red power, a linear dependence has been fitted with a slope of $0.18(14)\,\mathrm{s}/\mu\mathrm{W}$ and an offset of $23.4(7)\,\mathrm{s}$ with a χ^2 of 94.96 for 74 d.o.f. The full data sets are listed in Table F.1 in Appendix F.

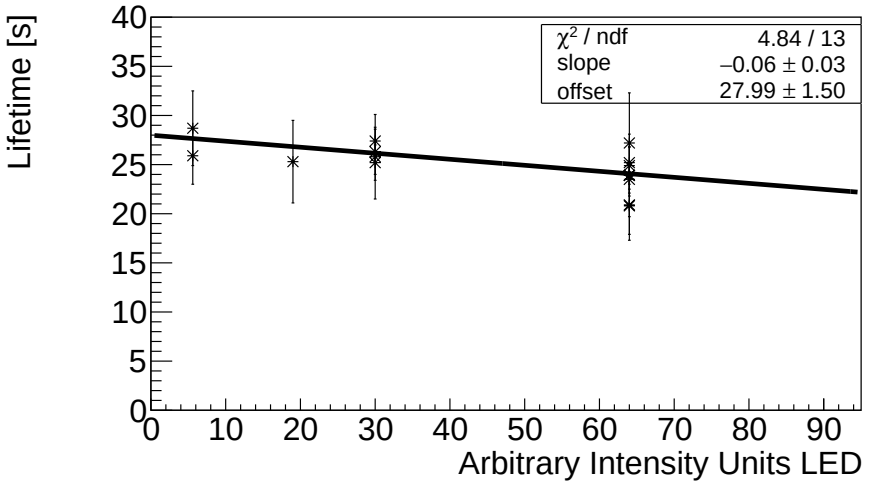

FIGURE 5.12: Measured lifetime of the $5d\,^2D_{5/2}$ state for different intensities of the shelving LED. Here the power dependence is plotted for a dataset with a residual gas pressure of 8×10^{-11}mbar. A linear dependence has been fitted with a negative slope of 0.06(3) s/AIUL and an offset of 28.0(1.5) s with a χ^2 of 4.84 for 13 d.o.f. Here AIUL stands for Arbitrary Intensity Units LED. The full data set is given in Table F.1 in Appendix F.

Different pressure conditions

The measurements for a single Ba^+ ion are sorted for different pressure conditions. We deliberately had changed the pressure condition by reducing the pumping speed on the large vacuum vessel which contains the trap. This leads to addition or extraction of particles to the trap which can affect the measured lifetime of the ion. The pressure range is from $(5\times10^{-11}$–$8.8\times10^{-10})$ mbar as determined from the

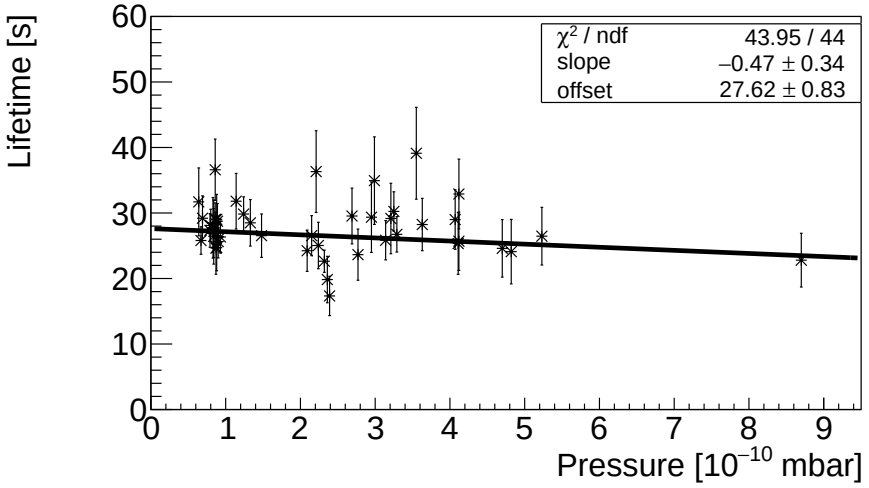

FIGURE 5.13: Corrected lifetime of the $5d\,^2D_{5/2}$ state for the different pressure conditions in a single trapped Ba^+ ion. Here the power dependence on LED has been taken into account. A linear dependence has been fitted with a negative slope of $0.47(34)\,s/10^{-10}$ mbar and an offset of 27.62(83) s with a χ^2 of 43.95 for 44 d.o.f. The full dataset is listed in Table F.1 in Appendix F.

current of the ion pump. The lowest pressures are as low as the best conditions under which the lifetime of the D-state in Ba^+ ions has been determined. At pressure $>10^{-10}$ mbar, a reduction of the lifetime has been observed. All the data for different pressures (see Fig. 5.13) have been corrected for the dependence on the shelving LED power.

5.5 Lifetime of $5d\,^2D_{5/2}$ state with multiple ions

An alternate method of using light at wavelength λ_{585} was used to provide shelving. The lifetime $\tau_{D_{5/2}}$ is determined by pulsed driving of the transition $5d\,^2D_{3/2}$–$6p\,^2P_{3/2}$ for shelving and observing the subsequent decay to the $6s\,^2S_{1/2}$ state by the recovery of the fluorescence signal to the level before the pulsed shelving (see Fig. 5.14). The recovery of the dark ions to the bright state gives the lifetime of $5d\,^2D_{5/2}$ state. This decay time is measured by trapping many ions and about

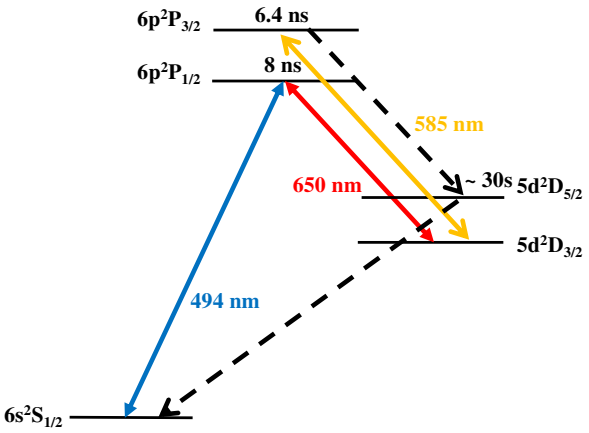

FIGURE 5.14: Alternate shelving scheme in Barium (Ba^+) ion with laser light at wavelength 585nm. The long-lived metastable state is the $5d\,^2D_{5/2}$. The bold lines show the laser excitation using the 494 nm and 650 nm transitions. The laser light at λ_{585} excites the ion to the $6p\,^2P_{3/2}$ state while the subsequent decay to the $5d\,^2D_{5/2}$ and finally to $6s\,^2S_{1/2}$ state is indicated by the dotted lines.

7nW of the light at λ_{585} set to 1 s "on" and 120 s "off" to shelve the ion. The ions shelve with less than 1 s. This "n" is found to be exponential and measured to be (26.1±2.4) s at a pressure of 2×10^{-11} mbar. This was tested with a crystal of 8 ions and also with a huge cloud of many ions with detuning of lasers not being sufficient for cooling so that they don't form crystals. The main advantage of this measurement is that the systematics in this type of measurement is very different from the method employed by using quantum jumps and the main disadvantage is that the control parameters are very difficult in this case.

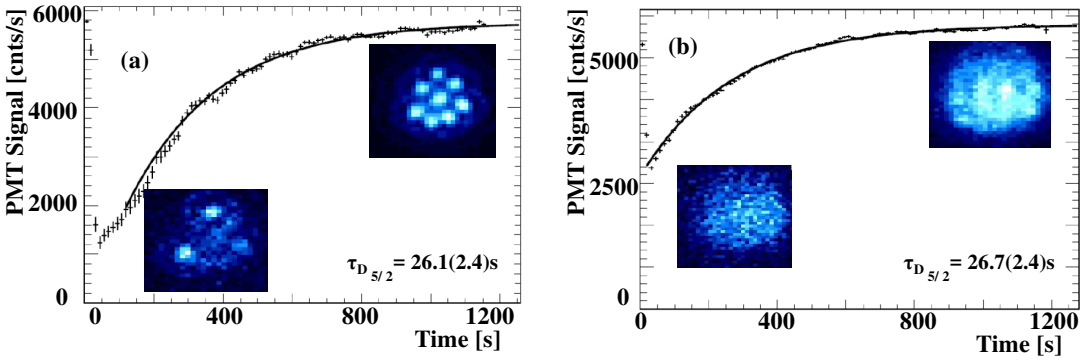

FIGURE 5.15: (a) Recovery of the dark ions into the bright state for a crystal of 8 ions. (b)Recovery of the dark ions into the bright state for a huge cloud of ions that has not crystallised. This exponential shows the spontaneous decay of the shelved ions into the bright state. This measurement is taken for one set of data points.

5.6 Results

In order to measure the lifetime $\tau_{D_{5/2}}$, different data sets were taken under in part significantly different conditions to enable observing and correcting for systematic errors. The lifetime $\tau_{D_{5/2}}$ is obtained for each data sample from the corresponding fit parameters. This was done to search for effects between the decay time of the different number of ions. Collisions with background gas can reduce the lifetime of the metastable state. In order to extrapolate the absolute value for the lifetime towards zero pressure, the lifetime $\tau_{D_{5/2}}$ was measured at different background pressures (see Fig. 5.13). A range of pressures between (0.5×10^{-11} and 8.8×10^{-10}) mbar have been explored. The Table 5.1 below is a compilation of the measurements done with single, multiple ions and a cloud of ions. Systematic checks potentially arising from laser intensities, rf voltages for trap and effects from the operating conditions of the ion pump have been taken into account (see Section 5.4).

TABLE 5.1: Measured lifetime of the $5d\,^2D_{5/2}$ state in single, multiple Ba^+ ions and with a large cloud. There is no significant difference between each of these cases. The values represent the average lifetime data after the pressure dependence has been corrected.

# of ions	$\tau_{D_{5/2}}$ [s]	Light source	Transition driven
Single ion	27.6(0.8)	455 nm LED	$6s\,^2S_{1/2}$–$6p\,^2P_{3/2}$
Eight ions	26.1(2.4)	585 nm laser	$5d\,^2D_{3/2}$–$6p\,^2P_{3/2}$
Cloud	26.7(2.4)	585 nm laser	$5d\,^2D_{3/2}$–$6p\,^2P_{3/2}$

5.7 Section Summary

TABLE 5.2: Compilation of the published values for theoretical calculations and measurements of the lifetime of the $5d\,^2D_{5/2}$ state in Ba^+ in vacuum. * represents a corrected theoretical value of [131]. This shows that within 15 years the reported lifetime has dropped by 20 %. @ are the values measured in this experiment. All the values include the corrections for known systematic shifts.

Theory			Experiments		
$\tau_{D_{5/2}}$ [s]	Year	Reference	$\tau_{D_{5/2}}$ [s]	Year	Reference
			27.6(0.8)	2016	This work
29.8(3)	2012	[127, 128]	26.7(1.7)@	2015	[87]
30.3(4)	2010	[134]	31.2(0.9)	2014	[126]
30.3(4)	2008	[130]	32.0(2.9)	2007	[125, 135]
31.6	2007	[125]	32.3	1997	[136]
30.8	2007*	[132]	34.5(3.5)	1990	[123]
30.3	2001	[75]	32(5)	1986	[122]
37.2	1991	[131]	47(16)	1980	[124]

The lifetime of the metastable $5d\,^2D_{5/2}$ state in Ba^+ has been determined earlier in different experiments [122–126]. Calculations are presently performed by different independent theory groups [75, 127–133]. All measurements to date as well as the calculated values for the lifetime of the $5d\,^2D_{5/2}$ state in Ba^+ has been compiled in Table 5.2. The result here of $\tau_{D_{5/2}} = 27.6(8)\,s$ is below and within 2.5 standard deviations of the latest theory value $\tau_{D_{5/2}} = 29.8(3)\,s$ [128] and within 3 standard deviations of the latest independent measurement of $\tau_{D_{5/2}} = 31.2(9)\,s$ [126]. From the lifetime measured in the case of multiple ions, the conclusion drawn is that

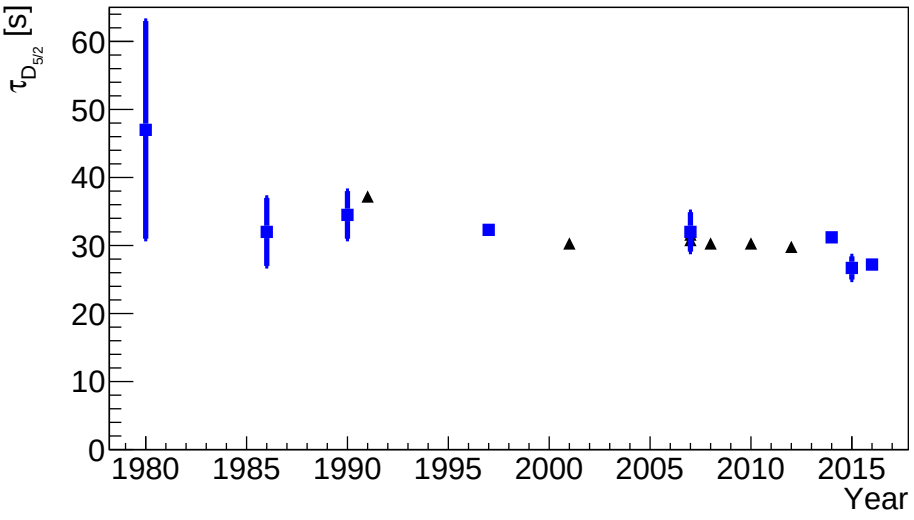

FIGURE 5.16: This figure shows the state-of-art for the lifetime measurements for the $5d\,^2D_{5/2}$ state in Ba^+. Squares represent the experimental measurements and triangles represent the calculations performed in recent years (see Table 5.2).

the shelving rate depends on the number of ions. The lifetime of the $5d\,^2D_{5/2}$ state measured with trapped multiple ions and with ion clouds is consistent with the measurements for a single ion in the trap. No significant correlation between lifetime $\tau_{D_{5/2}}$ and the number of ions is observed. Fig. 5.16 displays the time evolution of the different measurements and calculated values for the lifetime of the $5d\,^2D_{5/2}$ state of single Ba^+ ion.

Chapter 6

Single ion dynamics and determination of transition frequencies[1]

A good understanding of single ion dynamics and the effects on optical line shapes of the transitions is indispensable to investigate light-ion interactions. The coherent coupling by two light fields between three of the lowest levels determine the spectrum and is thus required in order to extract the transition frequencies in a single trapped Ba^+ ion. This is implemented by solving the Optical Bloch Equation (OBE) for the system including the magnetic sublevels.

Efficient trapping conditions and laser stabilities in terms of power and frequency (as discussed in Chapter 4) enables measurements to 100 kHz accuracy level. The optical frequency comb has been employed to measure the absolute transition frequencies with respect to the Cesium clock standard. Furthermore, the sensitivity of the resonances to various experimental conditions in a single trapped Ba^+ ion are summarized. The discussion in Section 6.3 and 6.4 follows the argumentation from the paper [88].

6.1 Line shape as result of laser cooling

A coherent coupling between the $6s\,^2S_{1/2}$ and $5d\,^2D_{3/2}$ levels in Ba^+ is observed when two laser fields are detuned by the same amount from their respective atomic resonances. Under these conditions, a two-photon process reduces the population

[1]The main contents of this chapter is also published under E. A. Dijck et al. (A. Mohanty) [88] and provides additional material.

of the $6p\,^2P_{1/2}$ level [137]. This coherence phenomenon is known as a Raman resonance. The dynamics of the population of all involved levels can be described by OBE [138–140]. The OBE are the equations of motions for the elements of the density matrix i.e. explicitly including both the coherences and populations which are represented by the off-diagonal and diagonal elements of the density matrix, respectively.

In the case of the laser cooled single Ba^+ ion, the Doppler shifts can be ignored when solving the OBE (see Eqn. 6.1). The Doppler-free spectrum is then calculated by solving the Liouville equation for the eight-level system (see Fig. 6.1). The Liouville equation describes the evolution of the density matrix which is expressed in terms of a commutator between the density matrix and the Hamiltonian, as well as additional terms that account for decay. It can be written as:

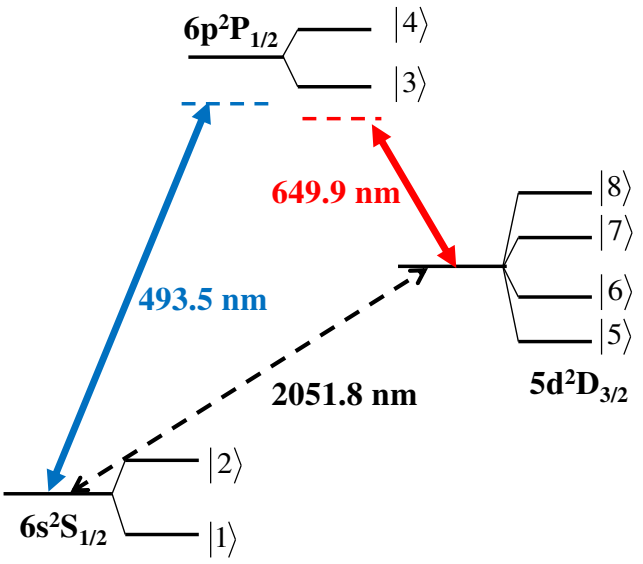

FIGURE 6.1: The relevant $^2S_{1/2}$, $^2P_{1/2}$ and $^2S_{1/2}$ levels for a Ba^+ ion along with their relevant m_j states and the investigated transition wavelengths.

$$\frac{d}{dt}\rho_{ij} = \frac{i}{\hbar}\sum_k (H_{ik}\rho_{kj} - \rho_{jk}H_{jk}) + R_{ij}(\rho), \tag{6.1}$$

where H is the Hamiltonian describing the interaction of the ion with two laser fields and R_{ij} is the damping matrix modelling relaxation and decoherence phenomena. The Hamiltonian that describes the coupling of the eight-level system (ordered according to level numbering in Fig. 6.1) to these two light fields in the

rotating wave approximation can be explicitly given by 8×8 matrix by

$$\mathrm{H}/\hbar = \begin{pmatrix} \Delta_1 - \omega_B & 0 & -\frac{2}{\sqrt{3}}\Omega_1 & 0 & 0 & 0 & 0 & 0 \\ 0 & \Delta_1 + \omega_B & 0 & \frac{2}{\sqrt{3}}\Omega_1 & 0 & 0 & 0 & 0 \\ -\frac{2}{\sqrt{3}}\Omega_1 & 0 & -\frac{1}{3}\omega_B & 0 & \frac{i}{\sqrt{2}}\Omega_2 & \frac{2}{\sqrt{6}}\Omega_2 & -\frac{i}{\sqrt{6}}\Omega_2 & 0 \\ 0 & \frac{2}{\sqrt{3}}\Omega_1 & 0 & \frac{1}{3}\omega_B & 0 & \frac{i}{\sqrt{6}}\Omega_2 & \frac{2}{\sqrt{6}}\Omega_2 & -\frac{i}{\sqrt{2}}\Omega_2 \\ 0 & 0 & -\frac{i}{\sqrt{2}}\Omega_2 & 0 & \Delta_2 - \frac{6}{5}\omega_B & 0 & 0 & 0 \\ 0 & 0 & \frac{2}{\sqrt{6}}\Omega_2 & -\frac{i}{\sqrt{6}}\Omega_2 & 0 & \Delta_2 - \frac{2}{5}\omega_B & 0 & 0 \\ 0 & 0 & \frac{i}{\sqrt{6}}\Omega_2 & \frac{2}{\sqrt{6}}\Omega_2 & 0 & 0 & \Delta_2 + \frac{2}{5}\omega_B & 0 \\ 0 & 0 & 0 & \frac{i}{\sqrt{2}}\Omega_2 & 0 & 0 & 0 & \Delta_2 + \frac{6}{5}\omega_B \end{pmatrix},$$

where $\omega_B = \mu_B|B|/\hbar$ is the Larmor frequency in a magnetic field $\vec{B}$, Δ_1 and Δ_2 are the detunings of two laser frequencies with respect to the unperturbed Ba^+ transitions and Ω_1 and Ω_2 are the corresponding Rabi frequencies depending on the amplitudes of the laser fields E_1 and E_2 as

$$\begin{aligned} \Omega_1 &= \frac{1}{2\hbar} E_1 \langle 6s\,^2S_{1/2}||er||6p\,^2P_{1/2}\rangle, \\ \Omega_2 &= \frac{1}{2\hbar} E_2 \langle 6p\,^2P_{1/2}||er||5d\,^2D_{3/2}\rangle. \end{aligned} \tag{6.2}$$

This is particular to a magnetic field $\vec{B}$ and polarisation of laser light. The relaxation matrix $\mathrm{R}(\rho)$ includes the spontaneous decay of the $6p\,^2P_{1/2}$ level and the decoherence effect due to finite laser linewidths. Here Γ_1= 14.7 MHz and Γ_2= 5.4 MHz are the partial decay rates of the $6p\,^2P_{1/2}$–$6s\,^2S_{1/2}$ and $6p\,^2P_{1/2}$–$5d\,^2D_{3/2}$ [141, 142] such that the total decay rate is Γ=Γ_1+Γ_2 with associated decoherence rate is $\gamma = \Gamma/2$. The linewidths of the two lasers are both taken to be equal to γ_l. Using $\gamma' = \gamma+\gamma_l$, the total relaxation matrix for a 8×8 matrix is

given by

$$
R= \begin{pmatrix}
\Gamma_1(\frac{1}{3}\rho_{33}+\frac{2}{3}\rho_{44}) & -\Gamma_1\frac{1}{3}\rho_{34} & -\gamma^{'}\rho_{13} & -\gamma^{'}\rho_{14} & -\gamma_l\rho_{15} & -\gamma_l\rho_{16} & -\gamma_l\rho_{17} & -\gamma_l\rho_{18} \\
-\Gamma_1\frac{1}{3}\rho_{43} & \Gamma_1(\frac{2}{3}\rho_{33}+\frac{1}{3}\rho_{44}) & -\gamma^{'}\rho_{23} & -\gamma^{'}\rho_{24} & -\gamma_l\rho_{25} & -\gamma_l\rho_{26} & -\gamma_l\rho_{27} & -\gamma_l\rho_{28} \\
-\gamma^{'}\rho_{31} & -\gamma^{'}\rho_{32} & -\Gamma\rho_{33} & -\Gamma\rho_{34} & -\gamma^{'}\rho_{35} & -\gamma^{'}\rho_{36} & -\gamma^{'}\rho_{37} & -\gamma^{'}\rho_{38} \\
-\gamma^{'}\rho_{41} & -\gamma^{'}\rho_{42} & -\Gamma\rho_{43} & -\Gamma\rho_{44} & -\gamma^{'}\rho_{45} & -\gamma^{'}\rho_{46} & -\gamma^{'}\rho_{47} & -\gamma^{'}\rho_{48} \\
-\gamma_l\rho_{51} & -\gamma_l\rho_{52} & -\gamma^{'}\rho_{53} & -\gamma^{'}\rho_{54} & -\Gamma_2\frac{1}{2}\rho_{33} & -\Gamma_2\frac{1}{2\sqrt{3}}\rho_{34} & 0 & 0 \\
-\gamma_l\rho_{61} & -\gamma_l\rho_{62} & -\gamma^{'}\rho_{63} & -\gamma^{'}\rho_{64} & -\Gamma_2\frac{1}{2\sqrt{3}}\rho_{43} & \Gamma_2(\frac{1}{3}\rho_{33}+\frac{1}{6}\rho_{44}) & \Gamma_2\frac{1}{3}\rho_{34} & 0 \\
-\gamma_l\rho_{71} & -\gamma_l\rho_{72} & -\gamma^{'}\rho_{73} & -\gamma^{'}\rho_{74} & 0 & \Gamma_2\frac{1}{3}\rho_{43} & \Gamma_2(\frac{1}{6}\rho_{33}+\frac{1}{3}\rho_{44}) & \Gamma_2\frac{1}{2\sqrt{3}}\rho_{34} \\
-\gamma_l\rho_{81} & -\gamma_l\rho_{82} & -\gamma^{'}\rho_{83} & -\gamma^{'}\rho_{84} & 0 & 0 & \Gamma_2\frac{1}{2\sqrt{3}}\rho_{43} & \Gamma_2\frac{1}{2}\rho_{44}
\end{pmatrix}
$$

The OBE takes into account the Zeeman split magnetic substates of the $6s\,^2S_{1/2}$, $6p\,^2P_{1/2}$ and $5d\,^2D_{3/2}$, the polarisation of the light and the magnetic field. The main parameters taken into account are frequencies, intensities, the linewidth of the transitions, magnetic field, and the polarisation of laser light with respect to direction of the magnetic field.

The OBE is solved numerically to determine the steady state solution for the density matrix ρ. The sum of the matrix elements $(\rho_{33}+\rho_{44})$ represents the population in the $6p\,^2P_{1/2}$ state and is thus proportional to the fluorescence rate at wavelength λ_{494nm} that is observed in the experiment. The detuning parameters Δ_1 and Δ_2,

$$\begin{aligned} \Delta_1 &= \nu_1 - \nu_{(6s\,^2S_{1/2}-5d\,^2D_{3/2})} - \nu_{(5d\,^2D_{3/2}-6p\,^2P_{1/2})} \\ \Delta_2 &= \nu_2 - \nu_{(5d\,^2D_{3/2}-6p\,^2P_{1/2})} \end{aligned} \tag{6.3}$$

relate the known laser frequencies ν_1 and ν_2 to the Ba^+ transition frequencies. The chosen parametrization minimizes the correlation between fit parameters.

6.2 Experimental determination

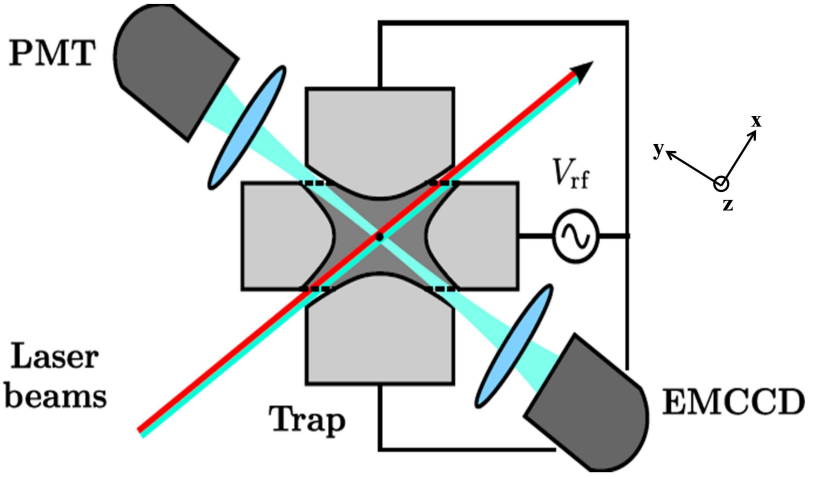

FIGURE 6.2: Schematic diagram of the hyperbolic Paul trap used for trapping Ba^+ ions. The inner diameter of the ring is 5 mm. Light scattered by ions is detected with a photomultiplier (PMT) and an electron-multiplying CCD camera (EMCCD). The coordinates are represented by x, y and z-axis.

6.2.1 Effects of micromotion

The equations above explicitly exclude the motion of the ion in the Paul trap i.e. the macromotion and micromotion. Its effect can be shown by increasing

the micromotion by a displacement of the ion from the trap center by an electric field (see Fig. 6.2). Fig. 6.3 shows the effect of micromotion on the spectrum of a single trapped Ba^+ ion when the frequency is scanned across the $6s\,^2S_{1/2}$–$6p\,^2P_{1/2}$ resonance. Fig. 6.3(a) and (b) show the distortions on the spectrum in the presence of micromotion and Fig. 6.3(c) and (d) represent the spectrum with minimized micromotion.

Photon-rf phase correlation

The photon-rf phase correlation is a light scattering technique used to study the dynamics of trapped Ba^+ ions. The technique is used to understand the localization and micromotion of the trapped ions. Here the arrival time of the fluorescence photons with respect to the phase of the rf voltage on the trap electrodes is recorded. A displacement of the ion from the trap center leads to a residual rf field seen by the ions. This results in a driven motion of the ions at the rf frequencies. Thus, the Doppler shift is modulated and the scattering rate changes accordingly. This fluorescence detection technique is a powerful tool to determine systematic effects that can affect the ion signal for e.g. alignment of the beams with the trapped ions, frequency instabilities or the presence of other ions in the trap.

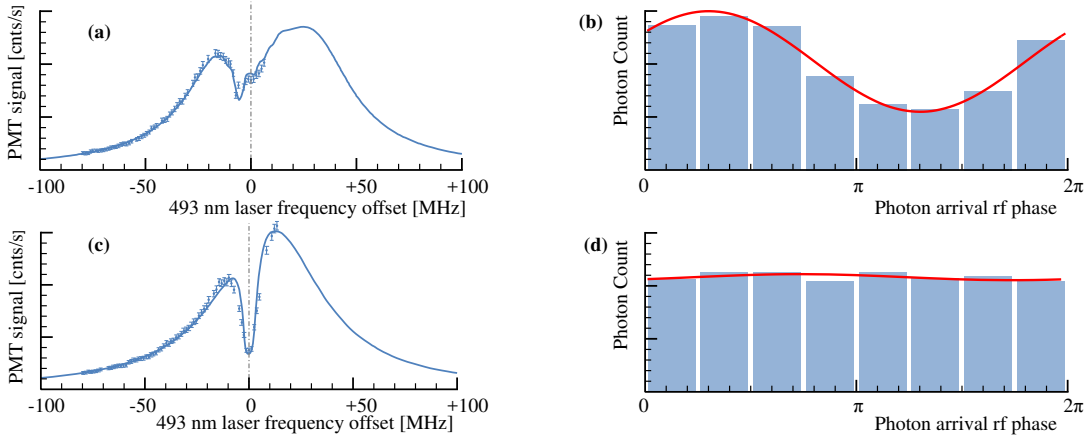

FIGURE 6.3: The Spectrum of $6s\,^2S_{1/2}$–$6p\,^2P_{1/2}$ transition in a single Ba^+ ion. (a) The Spectrum showing distortions in the presence of micromotion. (b) Photon correlation signal in the presence of micromotion. (c) Spectrum with minimized micromotion. (d) Photon correlation signal with minimized micromotion. The balancing of the dc field provided by the control voltages to the endcap electrodes minimizes the photon correlation.

6.2.2 Duty cycle and frequency switching

Keeping the ion cold implies longer cooling and short probing period. The double pass for frequency ν_{AOM-2} provides for stable power conditions and laser cooling at ν_{AOM-2}. The switching frequency ν_s (see Section 4.6.3) for the measurement was chosen to be 53.6 kHz and the duty cycle was set to 80 % for cooling and 20 % for spectroscopy. This implies that the ion is laser cooled for 14.9 μs, and the transition is probed thereafter for 3.7 μs. The spectrum recorded during the probe time is then analyzed according to the OBE model. The frequencies ν_1 and ν_2 (see Eqn. 6.3) depend on several experimental parameters (frequencies) which are set to appropriate values. These are listed in Table 6.1. For ν_1 and ν_2 we have

$$\nu_1 = 2 \times (\nu_{comb,offset} + m_1 \times \nu_{comb,rep} + \nu_{B_1}) + \nu_{AOM-1} \tag{6.4}$$

and

$$\nu_2 = \nu_{comb,offset} + m_2 \times \nu_{comb,rep} + \nu_{B_2} + \nu_{B_2'} + 2 \times \nu_{AOM-2}, \tag{6.5}$$

where $\nu_{comb,offset}$ and $\nu_{comb,rep}$ are the offset beat note and the repetition rate of the frequency comb, respectively, m_1 and m_2 are the mode numbers for the frequency comb, ν_{B_1} represents the beat note for the Ti:Sapphire light with the frequency comb, ν_{B_2} represents the beat note for the iodine-stabilized diode laser light with the frequency comb and $\nu_{B_2'}$ is the offset beat note between the light from the iodine-stabilized diode laser and the dye laser. Here ν_{AOM-1} and ν_{AOM-2} are the operating center frequencies of the AOM for light at wavelengths λ_{494} and λ_{650}, respectively.

TABLE 6.1: Intermediate frequencies to determine the laser frequencies in the trap (see also Fig. 4.1) according to Eqns. 6.4 and 6.5. During measurements the repetition rate of the comb $\nu_{comb,rep}$ has been varied in order to change ν_1.

Frequency	Value
$\nu_{comb,rep}$	250 000 233.5 Hz
$\nu_{comb,offset}$	-40 000 000.0 Hz
For light at wavelength λ_{494}	
m_1 (mode number)	1 214 851
ν_{B_1}	29.01(1) MHz
ν_{AOM-1}	198.90 MHz
For light at wavelength λ_{650}	
m_2 (mode number)	1 845 248
ν_{B_2}	-27.33(1) MHz
$\nu_{B_2'}$	-[1116.8(1)-1274.2(1)] MHz
ν_{AOM-2} (double pass)	348.00 MHz

6.3 Systematic study of Raman spectrum

Additional spectra have been recorded for different magnetic field settings, laser intensities, and laser polarisations to study systematic effects. The magnitude and direction of the magnetic field along with the direction of laser polarisation is a parameter required for the extraction of the fluorescence spectra. The magnetic field defines the quantization axis which is in the z-direction and both light fields are taken to propagate along the -y direction as shown in Fig. 6.2. For the

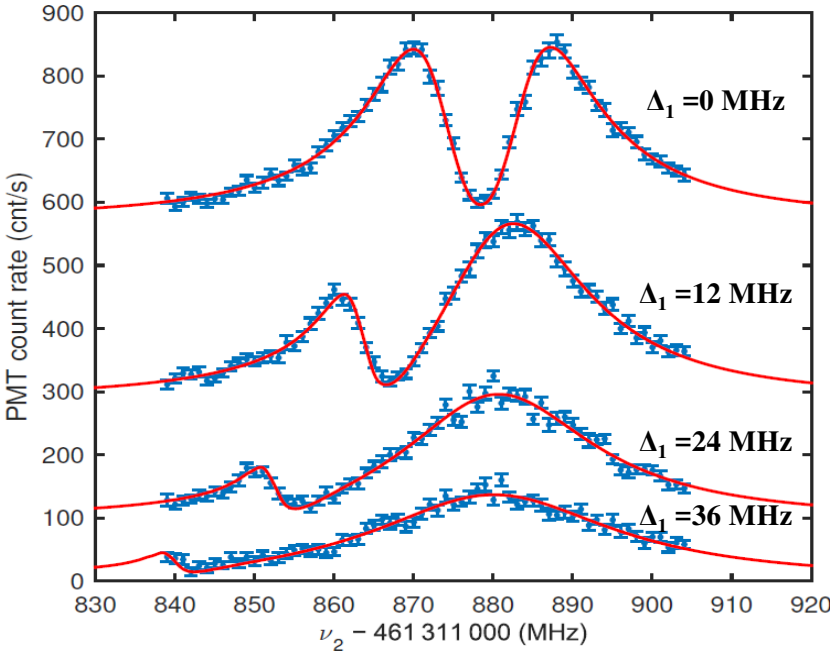

FIGURE 6.4: Raman spectra of the $5d\,^2D_{3/2}$–$6p\,^2P_{1/2}$ transition in a single Ba^+ ion recorded for different detunings Δ_1. Note that the baselines are shifted to show the spectra. Detuning Δ_1 is varied in steps of 12 MHz; intensities of the light fields are kept constant. Solid lines correspond to the result of fitting the OBE to the data.

measurements, the light at wavelength λ_{494} is linearly polarised, parallel to the magnetic field direction, and the light at wavelength λ_{650} is circularly polarised. Each of the spectra is obtained by scanning across the $5d\,^2D_{3/2}$–$6p\,^2P_{1/2}$ resonance. The red solid lines correspond to the result of fitting the OBE to the data. Fig. 6.4 shows spectra recorded with constant laser intensities and different detunings Δ_1. The red solid lines correspond to the result of fitting the OBE to the data.

An example of a spectrum is shown in Fig. 6.5 where both the light at wavelength λ_{494} and λ_{650} are about 85% linearly polarised at an angle of 75 ° to a magnetic field of 600 μT. In this more complex polarisation state, multiple dips in the fluorescence appear. The outermost features are due to coherences $|1\rangle\langle 8|$ and $|2\rangle\langle 5|$. The frequency difference between these outer dips can be employed as a calibration of the magnetic field strength (ω_B). Taking into account the polarisation of the

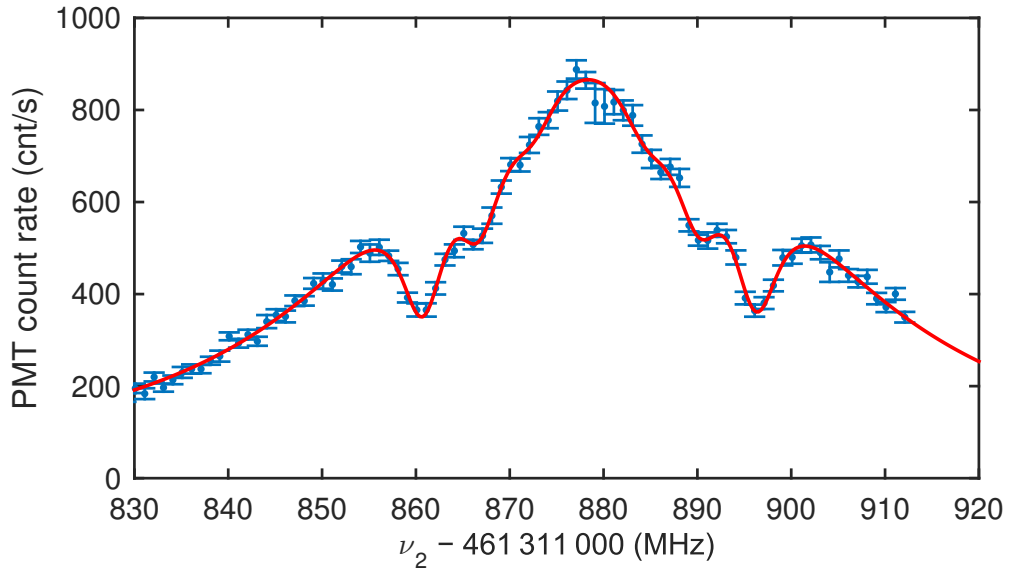

FIGURE 6.5: Spectra of the $5d\,^2D_{3/2}$–$6p\,^2P_{1/2}$ transition in a single Ba^+ ion. Both light fields are linearly polarised at an angle of 75 ° to the magnetic field direction, with about 15 % admixture of circularly polarised light. The solid line corresponds to the fit of the adjusted OBE, taking into account the polarisation of the laser light. Detuning $\Delta_1 \approx 0$ results in the symmetric line shape.

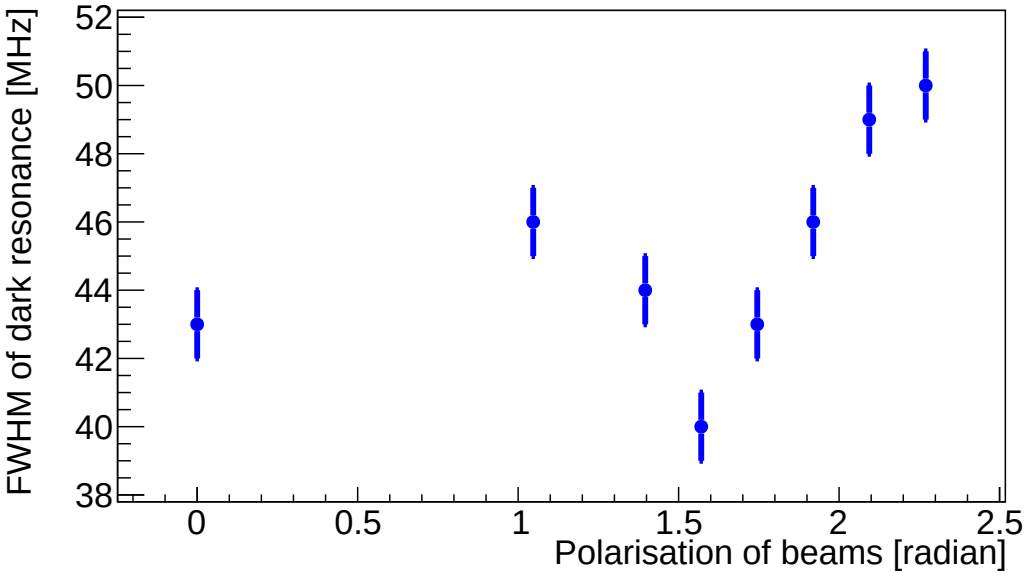

FIGURE 6.6: Variation of the Full Width Half Maximum (FWHM) of the Raman resonance spectrum (see Fig. 6.7) with respect to the polarisation of the laser at wavelength λ_{494}. The polarisation of the laser at λ_{650} is circularly polarised during the measurements. The magnetic field $\vec{B}$ was constant during this measurement.

laser light with respect to the magnetic field direction in the OBE, a solid line was fitted to the data.

Fig. 6.6 shows the variation of the Full Width Half Maximum (FWHM) of the dip of one set of Raman resonance spectra with respect to the polarisation of the

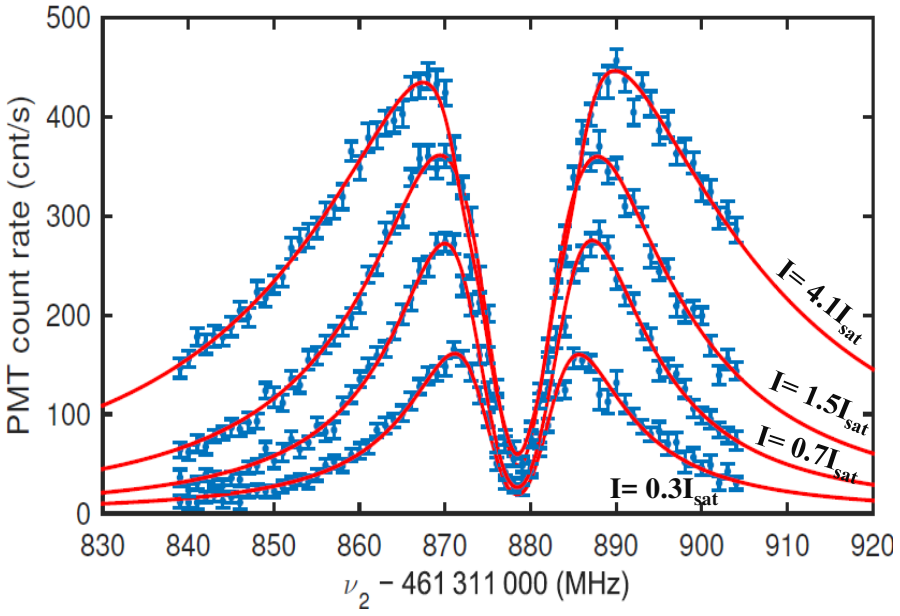

FIGURE 6.7: Spectra of the $5d\,^2D_{3/2}$–$6p\,^2P_{1/2}$ transition in a single Ba^+ ion recorded for different light intensities Ω_2, ranging from 0.3 to 4 times the saturation intensity. Frequency ν_1 is kept constant with $\Delta_1 \approx 0$. Solid lines correspond to the result of fitting the OBE to the data. The width of the spectra shows power broadening.

laser at wavelength λ_{494}. The laser light at λ_{650} is circularly polarised during the measurements. The measurement was carried out for a constant magnetic field $\vec{B}$. The magnetic field was chosen along the z-axis and the light at λ_{650} is circularly polarised. Fig. 6.7 shows a set of four spectra recorded with different intensities of the light at wavelength λ_{650}, corresponding to different Rabi frequencies Ω_2. The intensity ranged from 0.3 to 4 times the saturation intensity of the $5d\,^2D_{3/2}$–$6p\,^2P_{1/2}$ transition. The prominent features in the spectra, a dip in the fluorescence caused by the two-photon process at Δ_1=Δ_2 appears at $\Delta_1 \simeq \Delta_2 \simeq$0MHz . The polarisations of the two laser fields determine which coherences cause a fluorescence dip. For the measurements presented here the dominant contributions are from coherences $|1\rangle\langle 5|$ and $|2\rangle\langle 8|$ (see Fig. 6.1). In this case, the magnetic field magnitude is too small to resolve the two individual components here.

6.4 Results

The line shape is fitted to the individual spectrum by numerically calculating the steady state solution eight-level OBE (see Figs. 6.4, 6.5, and 6.7). Intensity-dependent light shift effects are included in the OBE and will drop out in the fitting procedure. However, a small mismatch in polarisation or magnetic field orientation between model and experiment can modify a transition amplitude component

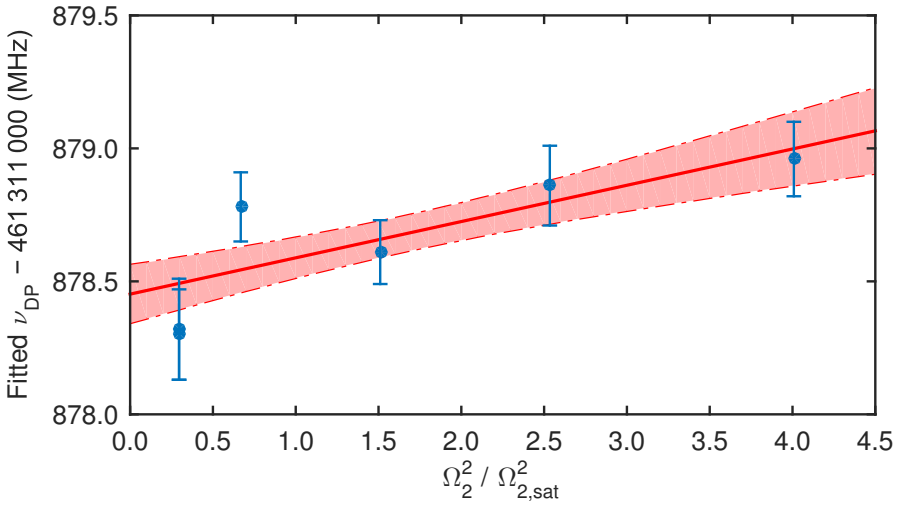

FIGURE 6.8: Extracted transition frequencies $\nu_{(5d\,^2D_{3/2}-6p\,^2P_{1/2})}$ as a function of laser intensity Ω_2 (given in terms of saturation intensity) for $\Delta_1 \approx 0$. The data shown include the spectra of Fig. 6.7. An intensity-dependent shift can be seen, which is attributed to a small mismatch between model and experiment in a transition amplitude component that causes a light shift. The solid line corresponds to a linear extrapolation to zero laser light intensity, with $1\,\sigma$ confidence bounds indicated.

resulting in a mismatch in the light shift. The atomic transition frequency is determined by extrapolating the fitted value to zero laser intensity (see Fig. 6.8). The weighted average of the $5d\,^2D_{3/2}$–$6p\,^2P_{1/2}$ and $6s\,^2S_{1/2}$–$5d\,^2D_{3/2}$ transition frequencies as well as their sum, the $6s\,^2S_{1/2}$–$6p\,^2P_{1/2}$ transition frequency, are given in Table 6.2. The results presented here are limited by statistics and the stability of the laser system.

TABLE 6.2: Transition Frequencies of the $5d\,^2D_{3/2}$–$6p\,^2P_{1/2}$ and $6s\,^2S_{1/2}$–$5d\,^2D_{3/2}$ transitions in Ba^+. Their sum yields the frequency of the $6s\,^2S_{1/2}$–$6p\,^2P_{1/2}$ transition.

Transition	Frequency (MHz)	Relative uncertainty
$\nu_{(5d\,^2D_{3/2}-6p\,^2P_{1/2})}$	461 311 878.5(1)	2×10^{-10}
$\nu_{(6s\,^2S_{1/2}-5d\,^2D_{3/2})}$	146 114 384.0(1)	6×10^{-10}
$\nu_{(6s\,^2S_{1/2}-6p\,^2P3/2)}$	607 426 262.5(2)	3×10^{-10}

6.5 Section Summary

The dynamics of a single trapped ion in the presence of laser cooling fields have been studied. Selecting suitable conditions permit performing precision spectroscopy of these laser cooling transitions which depend on laser detunings, magnetic fields, and laser polarisation. Prominent features are coherent two-photon Raman transitions. The analysis is provided in the framework of Optical Bloch

Equations (OBE), which takes all the parameters into account. The corresponding eight-level OBE was solved to describe the line shapes under the experimental conditions. We have identified and observed the impact of not fully reduced micromotion, laser polarisation, and magnetic field direction and the detuning of one of the two laser frequencies from the unperturbed values. All observed spectra are in excellent agreement with the results from the OBE. Selecting suitable parameters for polarisation and detuning we have determined the absolute transition frequencies of $6s\,^2S_{1/2}$–$6p\,^2P_{1/2}$, $5d\,^2D_{3/2}$–$6p\,^2P_{1/2}$, and $6s\,^2S_{1/2}$–$5d\,^2D_{3/2}$ transitions, which provides an improvement of almost 3 orders of magnitude over previous measurements of these transition frequencies in a single trapped ion compared to an accuracy of 10 MHz in the Fourier transform spectroscopy of large ion samples [54, 55].

Chapter 7

Light shifts in Ba^+

The presence of an electromagnetic field from intense laser radiation causes measurable modifications in atomic spectra. The light shift of a particular state requires the sum over all states (see Eqn. 2.13) and scales with the strength of the coupling to other states. The magnitude of light shifts depends inversely on the detuning of the frequency of the laser from resonant transitions. Furthermore, the polarisation with respect to the magnetic holding field breaks the symmetry between transitions between magnetic sublevels. The measurement of several different experimental parameters of the light shift contribution permits the determination of sets of matrix elements. Light shifts have been previously exploited in various different configurations in an attempt to determine atomic matrix elements for the Ba^+ system [43, 89, 92, 143]. Here, we exploited the λ-configuration of the laser cooling cycle in Ba^+. In Chapter 6 we have shown the excellent control of the experimental parameters e.g. laser frequency, polarisation, and magnetic field, which leads to a precise description of the spectra with contribution from all 8 Zeeman sublevels in the framework of OBE (see Eqn. 6.1).

The additional electromagnetic field is introduced by a laser beam which overlaps with the cooled ion. We observe in the presence of light at λ_{590}, i.e. 4.5(2) nm detuned from the nearest off-resonant $5d\,^2D_{3/2}$–$6p\,^2P_{3/2}$ transition in Ba^+, rapid optical shelving (see Section 7.2). Furthermore, near-resonant light to the $6p\,^2P_{1/2}$–$5d\,^2D_{3/2}$ transition with a detuning of less than 20 GHz (0.01 nm) shows polarisation and intensity dependent shifts of transitions between Zeeman sublevels.

7.1 Measuring light induced frequency shift

As a first step, we estimate the statistical sensitivity of a frequency shift determination of the transition frequencies for the case of a few ions in our trap. An

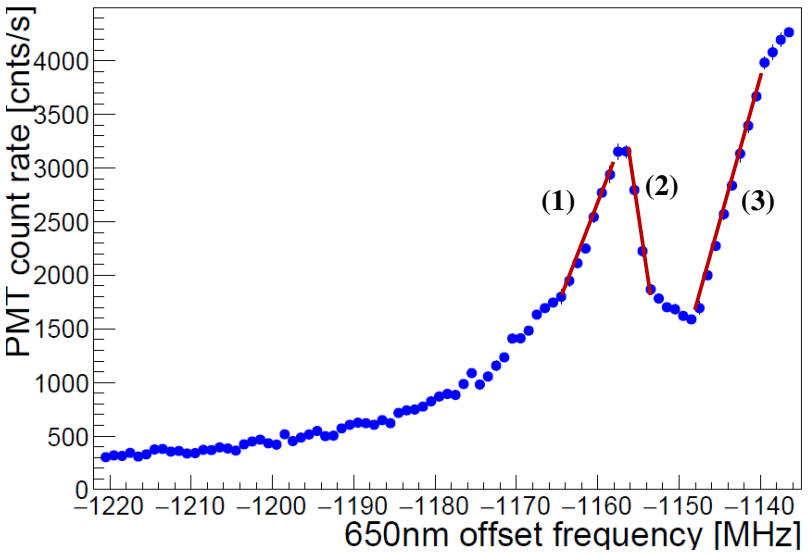

FIGURE 7.1: An example of the spectrum for a single trapped ion. The spectrum shows 3 different regions marked with straight lines. The frequency sensitivity of regions (2) and (3) are considered for different systematic checks. The region (1) is not taken into account as the linearity changes drastically which imply that the region is not a good choice to look for small light shifts.

example of a Raman resonance spectrum (see Fig. 7.1) is considered to perform the measurement. This spectrum shows three different regions of interest labelled as (1), (2) and (3). The region (2) and (3) are considered as they have a frequency sensitivity to the systematic changes like detuning from resonance, the intensities of the two lasers, a different number of ions etc. The change in count rate with light induced frequency shift, Δf_L is

$$\Delta R_L = \frac{dR}{df}\Delta f_L \tag{7.1}$$

or

$$\Delta f_L = \frac{df}{dR}\Delta R_L \tag{7.2}$$

where $\frac{df}{dR}$ is the slope of the spectrum. $\Delta R_L = R_d - R_L$ where R_L and R_d represents the count rate with and without the light shift laser. Further, we can make an estimate of the uncertainty of the determination of Δf_L. It is related to $\delta R_L = \sqrt{R_L + R_d}\cdot\sqrt{T}$ where T is the time spent at one detuning. The uncertainty in the frequency shift, Δf_L is given by the following equation:

$$\delta f_L = \frac{df}{dR}\delta R_L \tag{7.3}$$

The term $\frac{df}{dR}$ is determined for a set of experimental conditions like detunings δ_{494} from resonance for light at λ_{494} (see Fig. 7.2) and different intensities of light

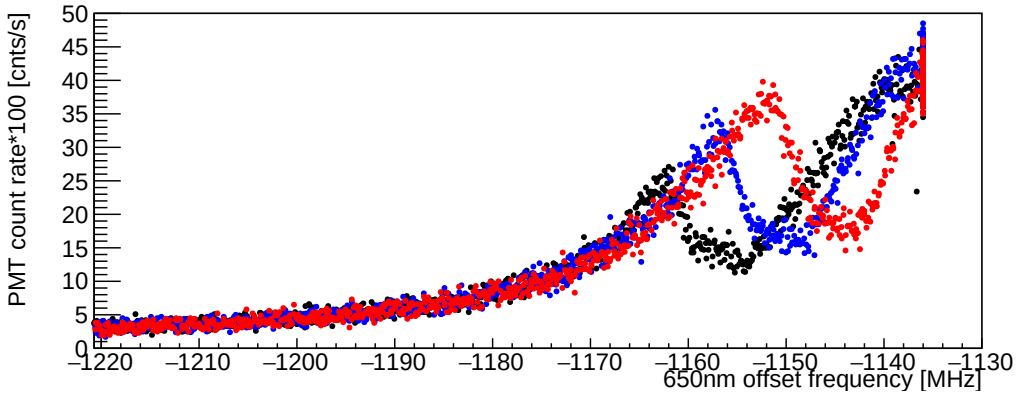

FIGURE 7.2: Spectra for different detunings δ_{494} of light at λ_{494}. The red points for detuning at δ_{494} = -8.4 MHz, the blue points are for detuning at δ_{494} = -14.4 MHz and the black points are for detuning at δ_{494} = -20.4 MHz from the resonance of the $6s\,^2S_{1/2}$–$6p\,^2P_{1/2}$ transition.

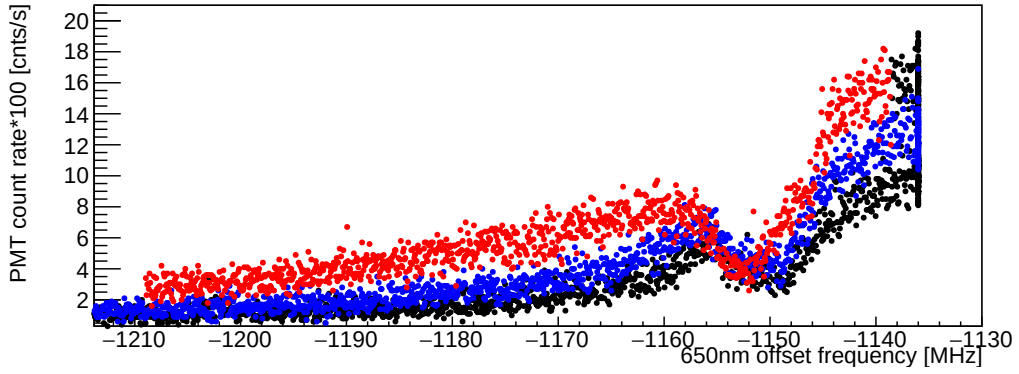

FIGURE 7.3: Spectra for different powers P_{650} of the λ_{650} light. The black points are for $P_{650} = 0.58\,\mu W$ or $\frac{I}{I_{sat}} = 13.6$, the blue points are for $P_{650} = 1.2\,\mu W$ or $\frac{I}{I_{sat}} = 28.04$ and the red points are for $P_{650} = 5.2\,\mu W$ or $\frac{I}{I_{sat}} = 121.6$. Here $I_{sat} = 2.5\,mW/cm^2$.

at λ_{650} (see Fig. 7.3). This analysis shows that a smaller detuning of the laser at wavelength λ_{494} from resonance increases the sensitivity. This is due to the larger photon scattering rate close to resonance (see Fig. 7.4(left)). Further, the intensity of the light at wavelength λ_{650} has only a small impact on the frequency sensitivity of the spectrum. The region (2) of Fig. 7.1 is about a factor of 2 more sensitive than region (3).

TABLE 7.1: Frequency sensitivity as determined from the slope of the different regions of the spectrum. This is employed for different detunings δ_{494} from resonance and different intensities of the light at λ_{650}. Here the P_{650} is the reading in the powermeters. This reading corresponds to an actual power of $P_{650} \times 3.5(5)\,\mu$W delivered to the trap center.

δ_{494} [MHz]	$\frac{I}{I_{sat}}$	$\frac{df}{dR}(10^{-5})$	R_L	δf_L for region (2) [MHz]
-20.4	4.3	5(1)	2000	-0.14(3)
-14.4	4.3	3.3(6)	2540	-0.17(3)
-8.4	4.3	1.7(4)	2970	-0.10(2)
δ_{494} [MHz]	$\frac{I}{I_{sat}}$	$\frac{df}{dR}(10^{-5})$	R_L	δf_L for region (3) [MHz]
-20.4	4.3	5(1)	2450	0.27(5)
-14.4	4.3	3.5(7)	2880	0.20(4)
-8.4	4.3	1.7(4)	2970	0.10(2)
$P_{650}[\mu W]$	$\frac{I}{I_{sat}}$	$\frac{df}{dR}(10^{-5})$	R_L	δf_L for region (2) [MHz]
0.58	13.6	53(10)	460	-0.49(9)
1.2	28.04	56(10)	560	-0.63(1)
5.2	121.6	33(6)	620	-0.41(8)
$P_{650}[\mu W]$	$\frac{I}{I_{sat}}$	$\frac{df}{dR}(10^{-5})$	R_L	δf_L for region (3) [MHz]
0.58	13.6	21(4)	620	0.26(5)
1.2	28.04	16(3)	700	0.23(5)
5.2	121.6	15(3)	880	0.27(5)

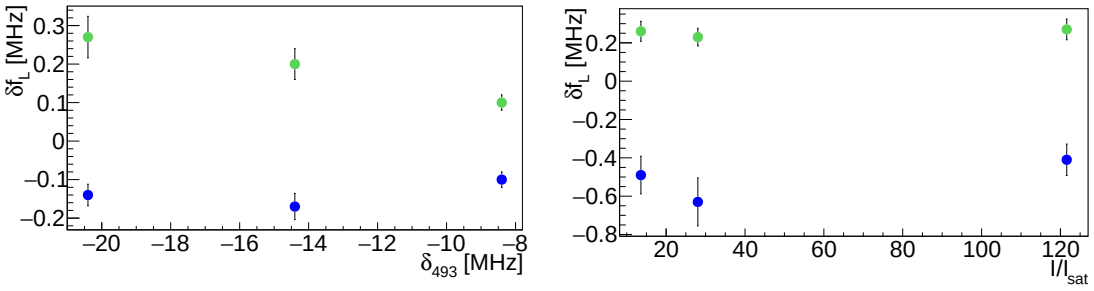

FIGURE 7.4: Measured frequency sensitivity for different detunings δ_{494} from resonance for the light at λ_{494} and different powers P_{650} of the λ_{650} light. The blue and green points represent the sensitivity for the region (2) and (3) respectively for the spectrum as shown in Fig. 7.1. The blue points represent negative sensitivities as compared to the positive sensitivities shown by the green points.

7.2 Shelving caused by light at wavelength 590 nm

The off-resonant light at λ_{590} with intensities of up to 4700(470) W/cm^2 is introduced into the trap via a small hole of 1 mm diameter in the endcap electrodes (see Section 4.8). This light causes an off-resonant driving of the $5d\,^2D_{3/2}$–$6p\,^2P_{3/2}$ transition which leads to shelving into the $5d\,^2D_{5/2}$ state (see Fig. 7.5). This is the dominant effect observed in the measurements. The same light also puts the ion into the $5d\,^2D_{3/2}$ and $6s\,^2S_{1/2}$ which is transferred back to the bright states. This leads to an intensity dependent shortening of the average time in the $5d\,^2D_{5/2}$ state. This shelving also prevents frequency measurements with longer integration times.

The optical setup is shown in Fig. 4.23 and the procedure of overlapping the laser beam with the ion are described. The overlap of both the guide beams and the

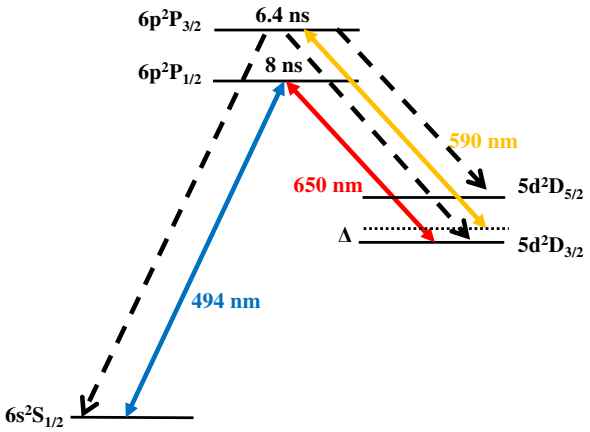

FIGURE 7.5: The additional laser at λ_{590} provides for an off-resonant coupling to the $6p\,^2P_{3/2}$ states. This light shelves the ion to the $5d\,^2D_{5/2}$ state (represented by dotted lines). This laser light is detuned by $\Delta = 4.5(2)$ nm from resonance of the $5d\,^2D_{3/2}$–$6p\,^2P_{3/2}$ transition and $\Delta = 24.3(2)$ nm from resonance of the $5d\,^2D_{5/2}$–$6p\,^2P_{3/2}$ transition. The $6p\,^2P_{3/2}$ state branches to the $5d\,^2D_{5/2}$, $5d\,^2D_{3/2}$ and $6s\,^2S_{1/2}$ states with 21.5 %, 2.9 % and 75.6 %, respectively.

TABLE 7.2: Branching ratios and wavelengths for the transitions from $6p\,^2P_{3/2}$ to $6s\,^2S_{1/2}$, $5d\,^2D_{3/2}$ and $5d\,^2D_{5/2}$. Detunings of the λ_{590} from the relevant transitions are described.

Transition	Wavelengths (nm) [55]	Detunings from λ_{590} (in nm)	Branching ratio [64]
$6p\,^2P_{3/2}$–$5d\,^2D_{5/2}$	585.52973	4.5(2)	0.2150(64)
$6p\,^2P_{3/2}$–$5d\,^2D_{3/2}$	614.34129	24.3(2)	0.0290(15)
$6p\,^2P_{3/2}$–$6s\,^2S_{1/2}$	455.53098		0.756(46)

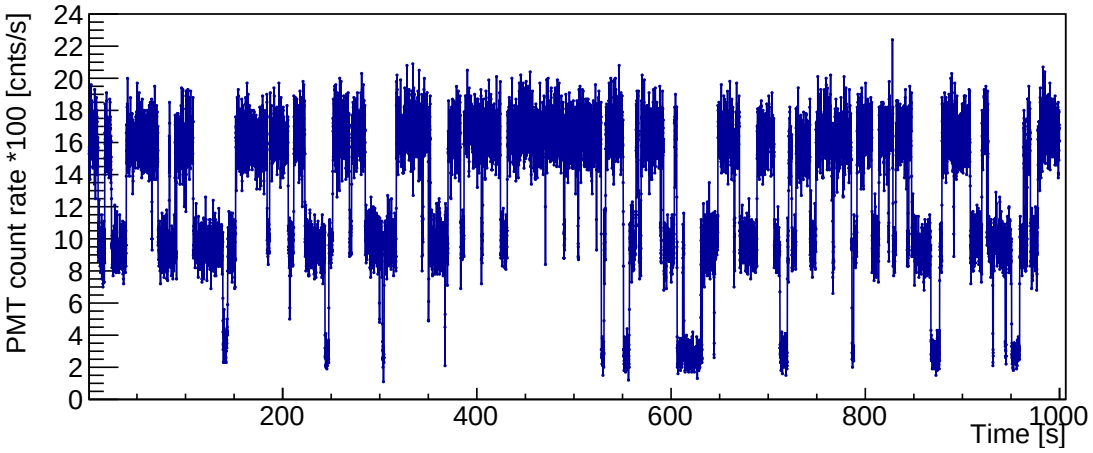

FIGURE 7.6: An example of shelving of 2 ions in the presence of an intense laser field at λ_{590}. The PMT trace of the 494 nm fluorescence from the $6p\,^2P_{1/2}$ state shows quantum jumps observed in a 2 Ba^+ ion crystal. The highest fluorescence level indicates that all the ions are not shelved. The lowest fluorescence level indicates that all the ions are in the metastable $5d\,^2D_{5/2}$ or shelved state. They show a clear discrimination between the dark and bright states.

beam at λ_{590} are maintained at 20 μm level accuracy. Fig. 7.6 shows an example of the shelving of ions to the $5d\,^2D_{5/2}$ state.

The shelving is observed by the reduction of fluorescence as it was described in the context with the $5d\,^2D_{5/2}$ lifetime measurement (see Chapter 5) and the data was analyzed accordingly. The analysis yields two parameters that are extracted i.e. the shelving rate r_S and the effective deshelving rate r_D for the $5d\,^2D_{5/2}$ level and plotted in Fig. 7.7. The measurement was repeated at different intensities I_{590} and number of trapped ions (see Table 7.3). In Chapter 5 we showed that the decay rate of the $5d\,^2D_{5/2}$ state does not depend on the number of trapped ions.

The laser induced rates are expected to depend linearly on the intensity I_{590} where the shelving rate approaches zero for no light while the deshelving rate is converging to the inverse of $5d\,^2D_{5/2}$ state lifetime ($\frac{1}{\tau_D}$). We model a linear behaviour of

TABLE 7.3: Measurements with different intensities I_{590} of light at λ_{590} and number of trapped ions. The shelving and deshelving rates for each of the intensities are compiled. *Table 5.1 from Chapter 5

Power (mW)	I_{590} (W/cm^2)	# of ions	r_S(s^{-1})	r_D(s^{-1})
300(30)	4700(470)	3	0.040(4)	0.14(2)
110(10)	2860(260)	2	0.020(2)	0.09(1)
0*	0	1-8	0	0.038(2)

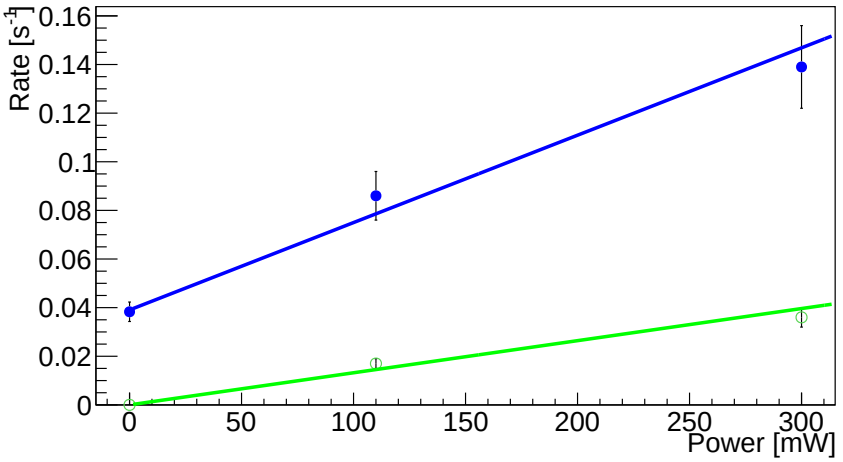

FIGURE 7.7: The shelving rate and the decay rate for the $5d\,^2D_{5/2}$ state for different powers of the light at λ_{590}. The blue points represent the decay/deshelving rate from the $5d\,^2D_{5/2}$ state and the slope of the deshelving curve is $0.36(5)\,W^{-1}s^{-1}$. The green points represent the shelving rate and the slope of the shelving curve is $0.13(1)\,W^{-1}s^{-1}$. This implies the ratio of shelving to deshelving, i.e. $\frac{r_S}{r_D} \simeq 0.37(5)$. Detunings for shelving and deshelving are Δ_S =4.5(2) nm, Δ_D =24.3(5) nm, respectively.

these rates on the intensity:

$$r_S = A\cdot B\cdot |\langle 5d\,^2D_{3/2}|e\cdot r|6p\,^2P_{3/2}\rangle|^2\cdot \frac{1}{\Delta_S^2}, \tag{7.4}$$

$$r_D = A\cdot (1-B)\cdot \sum_{i=5}^{8}\rho_{ii}\cdot |\langle 5d\,^2D_{5/2}|e\cdot r|6p\,^2P_{3/2}\rangle|^2\cdot \frac{1}{\Delta_D^2}, \tag{7.5}$$

where A comprises all common factors, B is the branching ratio (see Table 2.1 of Chapter 2), r_S and r_D are the shelving and deshelving rates, Δ_S and Δ_D are the detunings of light at λ_{590} from the $6p\,^2P_{3/2}$–$5d\,^2D_{5/2}$ and $6p\,^2P_{3/2}$–$5d\,^2D_{3/2}$ transition, respectively and $\Sigma_{i=5}^{8}\rho_{ii}$ is the probability of the ion to be in the $5d^2D_{3/2}$ state during the cooling cycle. Assuming that these are the major contribution to the rates, Eqn. 7.4 and Eqn. 7.5 can be combined to

$$\frac{1}{\sum_{i=5}^{8}\rho_{ii}}\cdot\frac{|\langle 5d^2D_{3/2}|e\cdot r|6p^2P_{3/2}\rangle|^2}{|\langle 5d^2D_{5/2}|e\cdot r|6p^2P_{3/2}\rangle|^2} = \frac{r_S}{r_D}\cdot\frac{\Delta_S^2}{\Delta_D^2}\cdot\frac{(1-B)}{B} \tag{7.6}$$

and

$$\frac{|\langle 5d^2D_{3/2}|e\cdot r|6p^2P_{3/2}\rangle|^2}{|\langle 5d^2D_{5/2}|e\cdot r|6p^2P_{3/2}\rangle|^2} = \frac{B_{6p\,^2P_{3/2}-5d\,^2D_{5/2}}}{B_{6p\,^2P_{3/2}-5d\,^2D_{3/2}}}\times\frac{\omega^3_{P_{3/2}-D_{3/2}}}{\omega^3_{P_{3/2}-D_{5/2}}} \tag{7.7}$$

where the experimental parameters are on the right-hand side of Eqn. 7.6. Here the ratio of squares of the matrix elements on the left-hand side of Eqn. 7.6 is determined from Eqn. 7.7 and put down in Table 7.4.

All values are compiled in Table 7.4 and the probability of the ion to be in the

TABLE 7.4: Determination of the ratio of squares of the matrix elements and the probability of the ion to be in the $5d^2D_{3/2}$ state during the cooling cycle from the shelving and the deshelving rates.

r_S	r_D	$\frac{r_S}{r_D}$	$\frac{r_S}{r_D}\cdot\frac{\Delta_S^2}{\Delta_D^2}\cdot\frac{(1-B)}{B}$	$\frac{\lvert\langle 5d^2D_{3/2}\lvert e\cdot r\rvert 6p^2P_{3/2}\rangle\rvert^2}{\lvert\langle 5d^2D_{5/2}\lvert e\cdot r\rvert 6p^2P_{3/2}\rangle\rvert^2}$	$\sum_{i=5}^{8}\rho_{ii}$
0.13(1)	0.36(5)	0.37(5)	0.22(4)	0.117(7)	0.5(1)

$5d\,^2D_{3/2}$ state during the cooling cycle is determined. This value is in good agreement with an estimate from the branching ratios as given in Table 7.2. An accurate determination to 1 % level accuracy requires the knowledge on the probability of ion to be in the $5d\,^2D_{3/2}$ state during the cooling cycle, intensity and detunings with a large statistics of at least 10,000 quantum jumps recorded over very long measurement times.

7.3 Light shift caused by near resonant light

Any off-resonant light causes shelving which changes the number of bright ions. A change in fluorescence rate can be caused by a change in the number of bright ions at random moments or light shifts. This ambiguity prevents the determination of frequency shifts in the observed spectra with long integration times to achieve high resolution as discussed in Section 7.1. A solution to this problem is the use of a near-resonant light to one of the laser cooling transitions in Ba^+. This reduces the off-resonant shelving dramatically.

We implement this with laser light near the $5d\,^2D_{3/2}$–$6p\,^2P_{1/2}$ transition with a detuning of ± 0.01 nm with intensities of up to $100\,W/cm^2$. Employing the same setup as for the frequency determination in Ba^+ in Chapter 6, the full spectrum with respect to the $5d^2D_{3/2}$–$6p^2P_{1/2}$ transition is measured in the presence of this additional light field. The induced light shifts of the $5d\,^2D_{3/2}$–$6p\,^2P_{1/2}$ transition and vector and tensor light shifts in the Zeeman sublevels for the $6s\,^2S_{1/2}$–$5d\,^2D_{3/2}$ transition in Ba^+ became observable.

7.3.1 Procedure to overlap laser beam with ion

The pointing stability and the spatial mode of the light shift laser beam at the site of the ion are important parameters in such an experiment. Thus, a measurement of the beam profile at the position of the ion is required. We employ the ion itself as a detector for the spatial overlap with the light shift laser beam. No additional

guide beam as for the case of a far-detuned laser field is necessary for this near-resonant light because the effect on the count rate can be made arbitrarily large.

The overlap procedure is a two-step process. A mode cleaned beam of power of 6-7 mW from a diode laser is focussed at the site of the ion. First, the light shift laser beam is deflected by a flip-in mirror before entering the trap region. A beam profiler is placed at a distance which corresponds to the virtual trap position in order to measure the beam properties at the site of the ion. A piezo-driven mirror mount (Agilis AG-UC2-UC8 series from Newport) permits the steering of the laser beam (see Fig. 4.23). The sensitivity of the piezo-driven mirror on the pointing at the virtual trap center was calibrated with the beam profiler to a μm precision. After this calibration, the flip-in mirror is retracted and the light shift is measured. Here the effect of the light shift resulted in a reduction of the scattering rate by up to 40 % (see Fig. 7.8). For a given position in y(x), the x(y) position was changed.

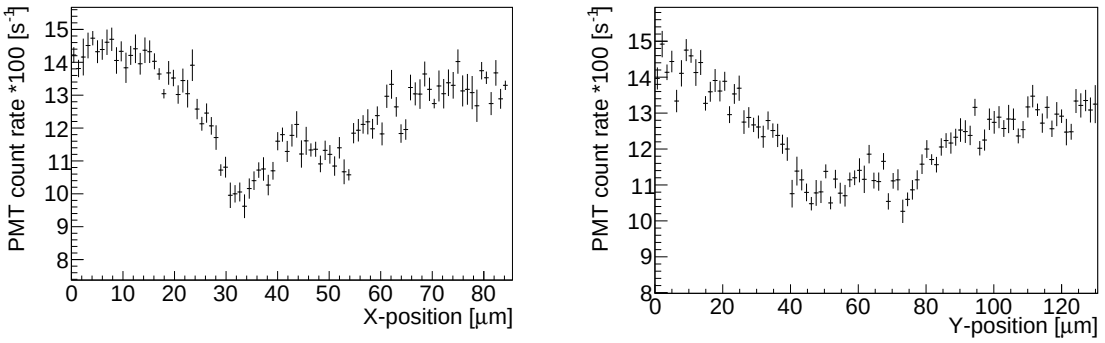

FIGURE 7.8: Variation of PMT scattering rate with respect to the movement of the beams in both the axes. It is an explanation of light shift effects with respect to the beam position. It gives the spatial mode of the diode laser which is $50(5) \times 35(5)\,\mu m^2$. This is the linear scan width calibrated with the beam profiler. This enables in the better determination of the beam profile with more statistics. The results are compared with the beam profiler.

The spectra reveal that the intensity profile of the light shift laser beam deviates from a gaussian profile. The FWHM of the profile is $35(5)\,\mu$m in x and $50(5)\,\mu$m in y, reflecting the astigmatic and elliptical profile of a diode laser. The estimated intensity at the position of the ion is about $110(13)\,W/cm^2$ for this elliptic beam. It was made sure that the light shift laser beam did not hit the edges of the electrodes by monitoring the gaussian beam after the trap.

A current change in the diode laser changes the position of the laser beam pointing by less than $5\,\mu$m. In addition, a possible change in the pointing due to the changes in the laser frequency was determined. A temperature change by $2\,K$ on the diode laser changes the wavelength by 0.1 nm. An improved beam profile measurement is required for systematic quantitative studies of light shifts. Furthermore the beam

profile of the laser can be improved by employing an optical fiber as a mode cleaner. With this an accurate estimate of the beam profile "in situ" can be achieved.

7.3.2 Specific light shift measurement

We employed the light at λ_{494} and λ_{650} at intensities $P_{494} = 21\,\mu W$ and $P_{650} = 13\,\mu W$, respectively for the laser cooling of the ion and the spectroscopy. The light at λ_{494} is maintained at a detuning of $\delta_{494} = $-1.2 MHz from resonance and is linearly polarised in vertical direction along the z-axis while the light at λ_{650} is circularly polarised. Here the light shift laser light is polarised in the horizontal direction. A magnetic field of $510\,\mu T$ in the z-direction (see Fig. 6.2) is employed for this measurement. The $5d\,^2D_{3/2}$–$6p\,^2P_{1/2}$ transition was scanned with and without the light shift laser with a scan speed of 1.45 MHz/s. A full set for one light shift laser detuning took 440 s. The detunings of the light shift laser light at wavelength λ_{650} was varied from -48(2) GHz to +31(2) GHz. A calculated spectrum under these experimental conditions for a detuning of Δ_{LS} = -18(2) GHz is displayed in Fig. 7.9.

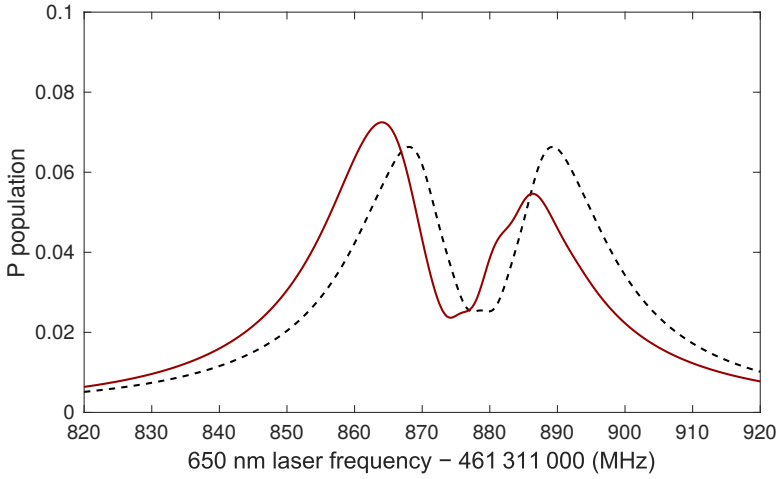

FIGURE 7.9: Calculated Raman dip spectrum for the $5d\,^2D_{3/2}$–$6p\,^2P_{1/2}$ transition in trapped Ba^+ ion. This is for a magnetic field of $510\,\mu T$ in the B_z direction. The dashed and the continuous curves represent the spectra in the absence and presence of the light shift laser light, respectively.

Fig. 7.10 shows the spectra for different detunings Δ_{LS} of the light shift laser. In each of these measurements, the blue and red spectra are in the absence and presence of light shift laser light, respectively. The scaling of the light shifts with the detunings of the light shift laser for the measurements is shown in Fig. 7.11. As per the simple approximation for the light shift at large detuning Δ_{LS}, the light shifts give a scaling which is inversely proportional to Δ_{LS}. The determined light shift = $0.16(3)\,\text{GHz}^2 \cdot \frac{1}{\Delta_{LS}}$ where Δ_{LS} is the detuning of the light shift laser

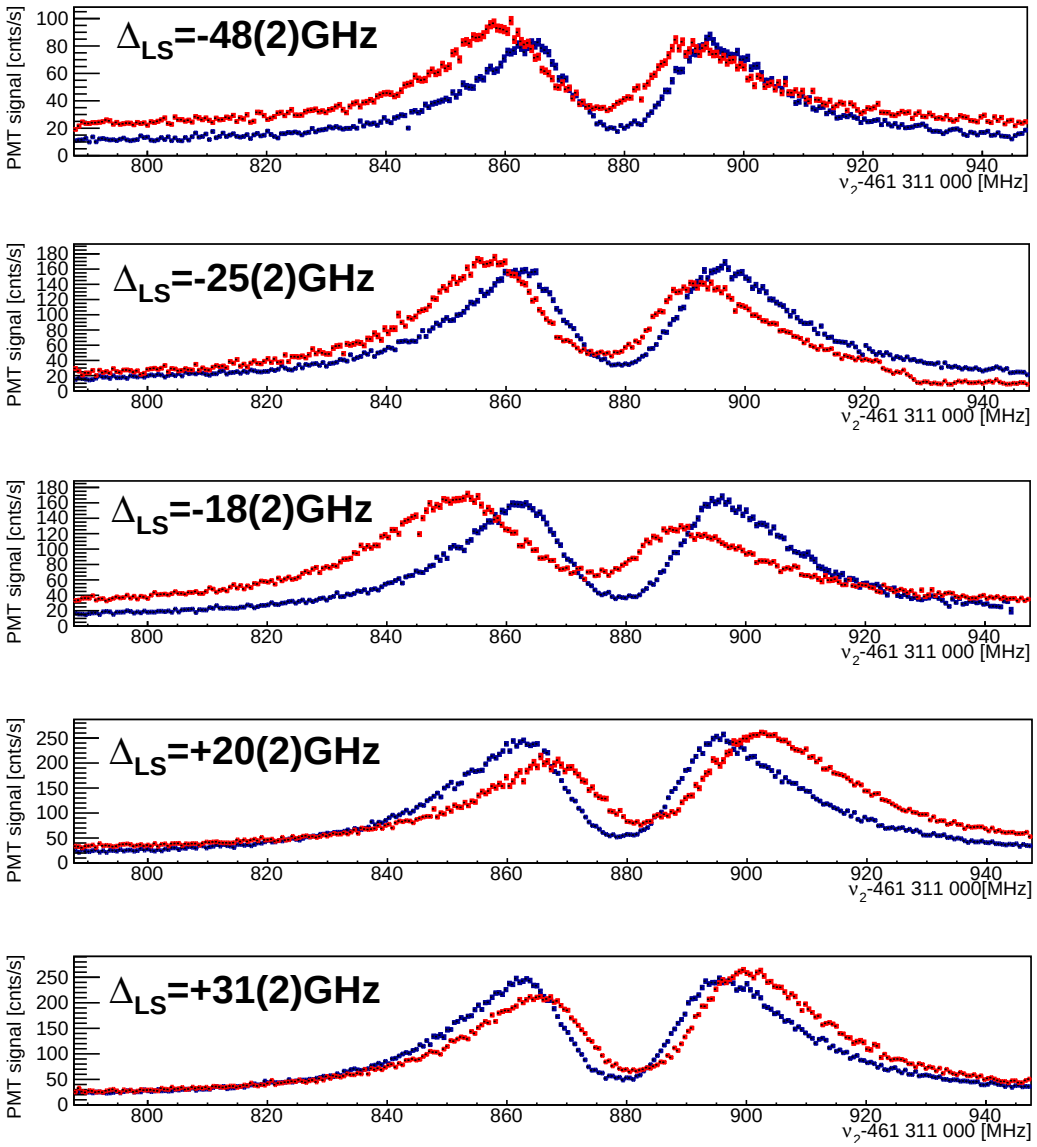

FIGURE 7.10: Measured Raman dip spectrum for the $5d\,^2D_{3/2}$–$6p\,^2P_{1/2}$ transition for a trapped Ba^+ ion. This is for a magnetic field of $510\,\mu T$ in the B_z direction. The blue and red spectra are taken in the absence and presence of light shift laser light, respectively. The detunings of the light shift laser light at wavelength λ_{650} was varied from -48(2) GHz to +31(2) GHz. Here the detunings are large compared to the power broadened linewidth.

from resonance. The deviations with respect to the detuning in our measurement are due to the polarisation with respect to the quantization axis i.e. magnetic field (see [144]) which is in agreement with the obtained data. These measurements are with a large blue power $P_{494} = 21\,\mu W$ and $\frac{I}{I_{sat}} = 12.2$ at the trap center. Under these conditions the Raman transitions between individual Zeeman states were not resolved.

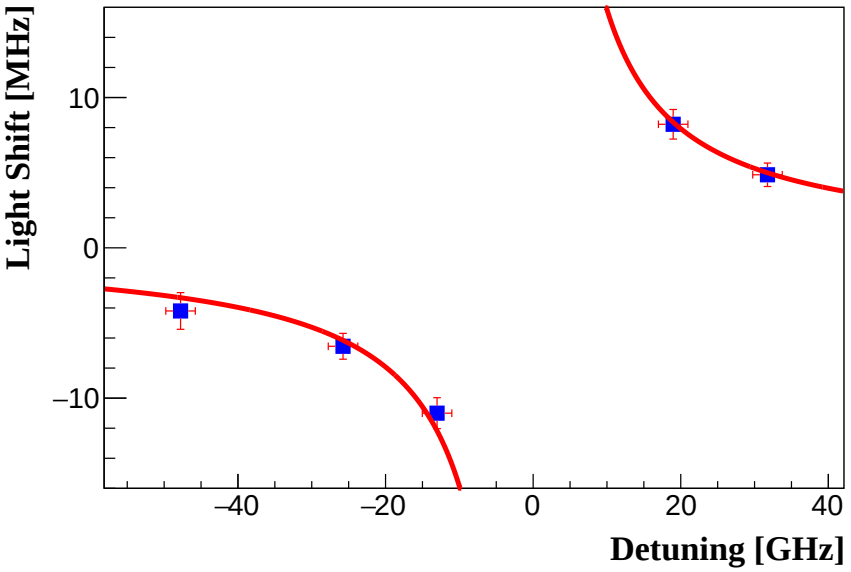

FIGURE 7.11: Scaling of light shifts for detuning from resonance of the light shift laser light. Here the determined light shift $= 0.16(3)\,\mathrm{GHz}^2 \cdot \frac{1}{\Delta_{LS}}$ where Δ_{LS} is the detuning of the light shift laser from resonance. There is in reasonable agreement with the estimated error bars.

7.3.3 Increased optical resolution of spectral features

The Raman transitions between individual Zeeman states are better resolved when the intensity I_{494} of the laser cooling light at λ_{494} was reduced to well below the

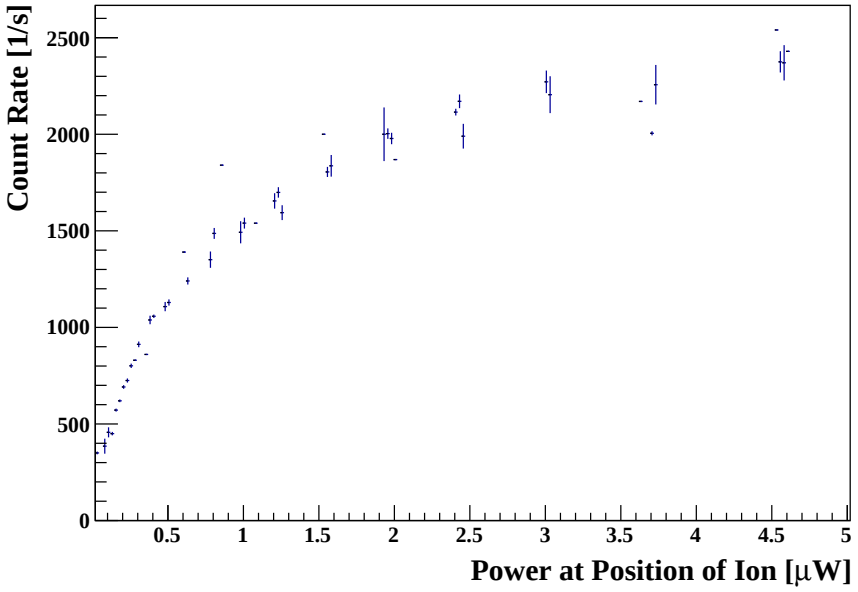

FIGURE 7.12: Fluorescence detected by the PMT for low power of the laser light at λ_{494} at a detuning δ_{494}. This indicates that saturation intensity is achieved with power of $1\,\mu$W.

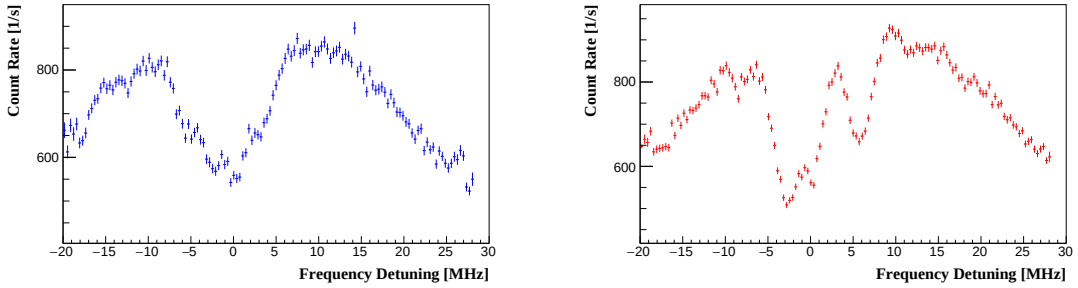

(A) Without light shift laser (B) With light shift laser

FIGURE 7.13: Measured spectra of the $5d\,^2D_{3/2}$–$6p\,^2P_{1/2}$ transition in a single Ba^+ ion in the absence (see (A)) and presence (see (B)) of light shift laser light. The light shift laser light is detuned by +31(2) GHz from resonance and is linearly polarised in the vertical direction. The magnetic field is constant at 510 μT in the B_z direction. The individual Zeeman components are better resolved in the presence of the light shift laser.

saturation intensity in the Ba^+ system. For the measurement, the scattering rate from the ion for a blue detuning δ_{494} = -1.2 MHz from resonance decreases at this intensity I_{494}. We determined that an incoming power of about 1 μW produces an intensity equal to the saturation intensity of the transition (see Fig. 7.12). As a compromise between signal rate and broadening effects, we have chosen about 1 μW of blue power. This lower power reduces the resolution of the Raman transitions to less than 2 MHz.

Under these conditions for laser intensities and the same polarisations for λ_{494}, λ_{650} and the light shift laser light with respect to the quantization axis, the spectra with and without the light shift laser light were recorded. The width of the frequency scan was reduced to the center of the transition including the Raman transition. The smaller linewidth is due to the lower intensity I_{494} which allows resolving of the individual components of the Raman transitions. Light shifts due to scalar, vector and tensor coefficients (see Chapter 2) can be well resolved. A quantitative analysis is possible if the experimental conditions are well controlled. This leads to the implementation of motorized rotation stages equipped with waveplates to control the polarisation.

For the measurements, the light at λ_{494} and λ_{650} is linearly polarised and circularly polarised, respectively, with the magnetic field of 400 μT in the B_x direction. The light shift laser light is linearly polarised in the vertical direction. A measurement of spectra for the different detunings Δ_{LS} of light shift laser light from resonance (see Fig. 7.14) was recorded. This measurement shows that the detunings of the light shift laser have an impact on the individual Zeeman components for each of the $6s\,^2S_{1/2}$–$5d\,^2D_{3/2}$ transitions, thereby leading to vector and tensor light shifts which shifts differently.

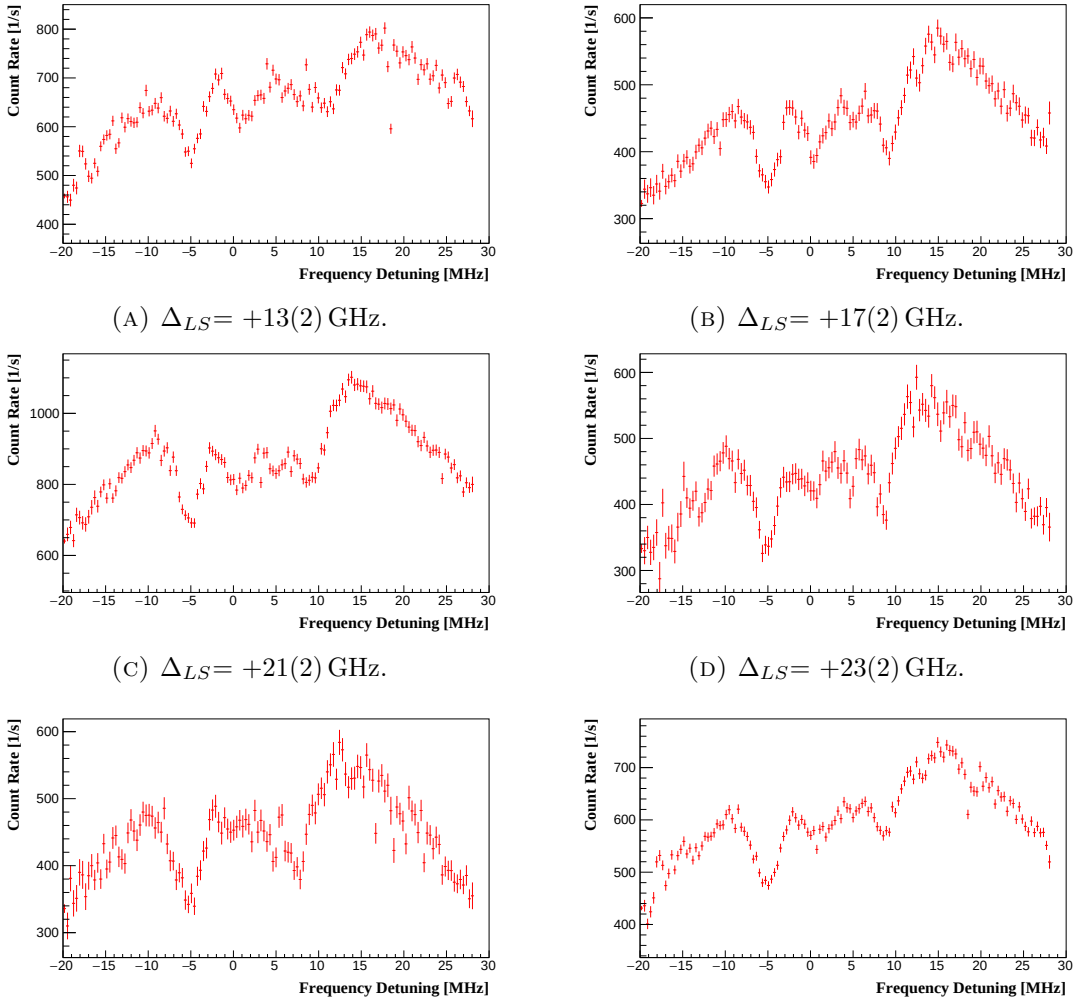

(A) Δ_{LS}= +13(2) GHz. (B) Δ_{LS}= +17(2) GHz.

(C) Δ_{LS}= +21(2) GHz. (D) Δ_{LS}= +23(2) GHz.

(E) Δ_{LS}= +31(2) GHz. (F) Δ_{LS}= +34(2)-+38(2) GHz.

FIGURE 7.14: Measured spectra for the resolved $6s\,^2S_{1/2}$–$5d\,^2D_{3/2}$ transitions in a single Ba^+ ion in the presence of the light shift laser (see (A)-(F)). The detunings of the light shift laser light at wavelength λ_{650} was varied from +13(2) GHz to +38(2) GHz and is linearly polarised in the vertical direction. The magnetic field is constant at 400 μT in the B_x direction. The individual Zeeman components are better resolved in the presence of the light shift laser light and varies with the detunings.

Another measurement was done for the Zeeman sublevels of the $6s\,^2S_{1/2}$–$5d\,^2D_{3/2}$ transition in a single Ba^+ ion for different orientations of the linearly polarised light shift laser light with the magnetic field along the B_z and B_x directions (see Fig. 7.15). For this measurement, the light at λ_{494} and λ_{650} are chosen to be linearly polarised vertically and circularly polarised, respectively. Figs. 7.15a and 7.15b represent the spectra in the absence of light shift laser light for a magnetic field of 510 μT in the B_z and 400 μT in the B_x direction, respectively. Figs. 7.15c, 7.15e, and 7.15g on the left column represent the spectra in the presence of light shift laser light which is linearly polarised at angles of 0°, 30° and 60° with respect to the magnetic field in the B_z direction. Figs. 7.15d, 7.15f, and 7.15h on the

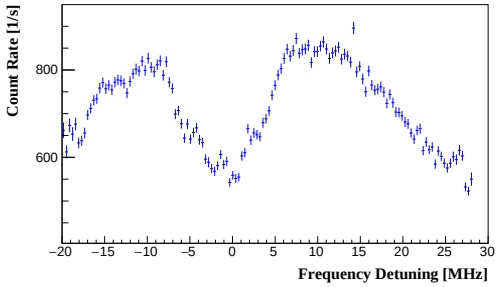

(A) Without light shift laser for 510 μT in B_z direction

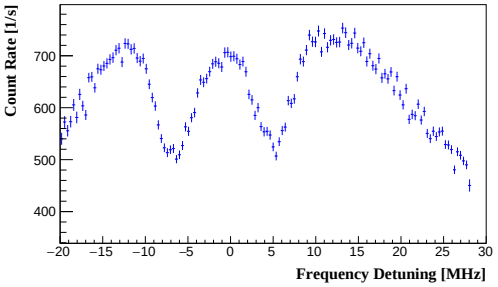

(B) Without light shift laser for 400 μT in B_x direction

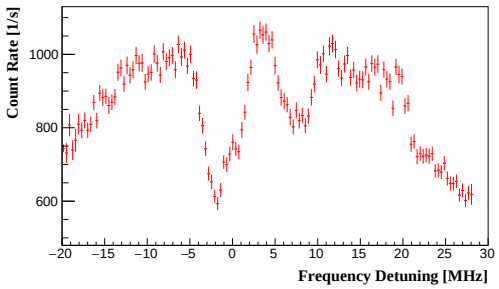

(C) At an angle of 0 ° in B_z.

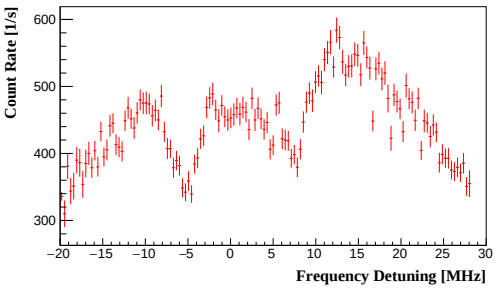

(D) At an angle of 0 ° in B_x.

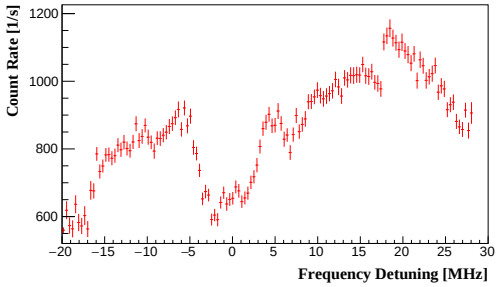

(E) At an angle of 30 ° in B_z.

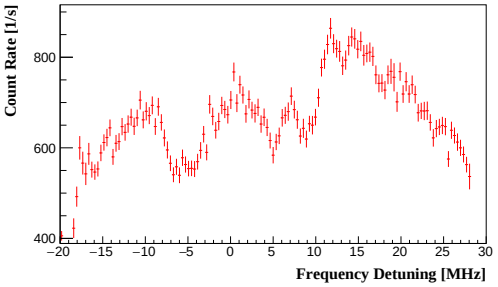

(F) At an angle of 30 ° in B_x.

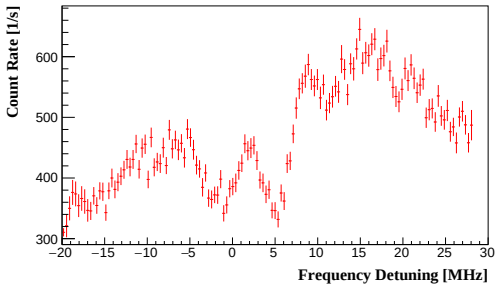

(G) At an angle of 60 ° in B_z.

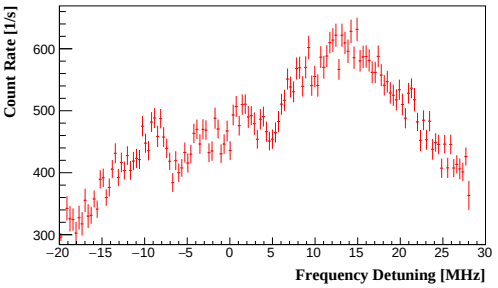

(H) At an angle of 60 ° in B_x.

FIGURE 7.15: Measured spectra of the $5d\,^2D_{3/2}$–$6p\,^2P_{1/2}$ transition in a single Ba^+ ion for magnetic fields in B_z and B_x (see (A) and (B)), respectively in absence of light shift laser light. The spectra for the well-resolved $6s\,^2S_{1/2}$–$5d\,^2D_{3/2}$ transitions (see (C)-(G)) in the presence of light shift laser are observed. Here, the light shift laser light is detuned by +31(2) GHz from resonance.

right column represent the spectra in the presence of light shift laser light which is linearly polarised at angles of 0 °, 30 ° and 60 ° with respect to the magnetic field in the B_x direction. These measurements show that the vector and tensor

light shifts of the individual Zeeman components shift differently for each case. Further quantification of the shifts in the individual Zeeman components requires better control of the spatial polarisation with respect to the magnetic field at the position of the ion.

7.4 Section Summary

The response of a trapped ion on an additional intense laser field has been studied for the condition of large and small detunings. The introduction of an off-resonant light at λ_{590} enables rapid shelving and deshelving rates of the ion. A linear behaviour of these rates on the light intensity has been observed. The different intensity dependence on the two rates is used to extract a value for the ratio between two matrix elements which is in agreement with other determinations. An improvement of such a measurement to 10^{-2} relative accuracy (% level) with an observation of more than 10,000 quantum jumps appears to be possible. A method for the determination of the intensity profile of a near-resonant laser has been developed. This is essential for a quantitative evaluation of light shifts since it depends on the local light intensity at the trap center.

The light shifts caused by a near-resonant light at λ_{650} was observed and determined to be $0.16(3)\,\mathrm{GHz}^2 \cdot \frac{1}{\Delta_{LS}}$. In this case effects from quantum jumps are suppressed. Under the condition of high laser intensity I_{494} for the laser cooling transition, the individual Raman transitions are not resolved. With low power of this light, the vector and tensor light shifts of the individual Zeeman components for different $6\mathrm{s}\,^2\mathrm{S}_{1/2}$–$5\mathrm{d}\,^2\mathrm{D}_{3/2}$ transitions are observed. This vector and tensor light shifts are determined by the spatial polarisation for the light fields with respect to the quantization axis at the position of the ion. Precise measurements for the determination of the spatial polarisation at the site of ion and a quantitative determination of the light shift parameter became feasible in this setup. This is a promising route towards determination of the relevant parameters for APV in a single trapped ion.

Chapter 8

Conclusion and Outlook

Trapped and laser cooled alkaline earth ionic systems like Ba^+ and Ra^+ are excellently suited for a precise measurement of Atomic Parity Violation (APV) because of the good calculability of atomic properties, the intrinsic sensitivity of these systems and the available technologies for laser cooled single ion high precision measurements. The experimental program on alkaline earth ions described in this thesis aims in particular, at the determination of the electroweak mixing angle ($\sin^2\theta_W$) at low momentum transfer. The precision to which $\sin^2\theta_W$ can be determined depends on the accuracy of the knowledge of the atomic structure of the respective ion and the ability to control the experimental conditions. This thesis discusses the available information on the atomic system Ba^+ and Ra^+ and provides experimental input for verifying recent improved calculations for the Ba^+ wavefunctions. The information on the lifetime of the long-lived $5d\,^2D_{5/2}$ state, level energies and light shifts in the presence of an additional laser field is provided with a focus on the experimental conditions and their influence on the measurements. Further, this information will be exploited in a next stage experiment on a single Ra^+ ion, where the weak effects are some 20 times larger.

A precise APV measurement with a single ion requires that the ion has to be localized to better than one optical wavelength. Under such conditions, a measurement of light shifts of order a few Hz of Zeeman sublevels of the $7s\,^2S_{1/2}$ ground state is a central part of the determination of the APV effect in a single trapped ion. This work comprises of the construction of a single Ba^+ ion experiment in this direction which includes the control of the number of ions produced, trapped and laser cooled in a Paul trap in a vacuum environment of below 10^{-10} mbar and the optical techniques implemented for the detection. This work also elucidates the frequency stabilization techniques for the employed laser systems. A frequency stability of 10^{-11} is achieved with these frequency stabilization techniques and the optical

frequency comb. These are the necessary prerequisites for the high precision spectroscopic measurements. The performance of these techniques in the setup has been characterized with single, multiple ions and ion clouds. The experimental setup is a crucial evolution towards parity measurement with a single trapped ion. The single laser cooled Ba^+ ion which is localized in the Paul trap to better than 1μm in all three spatial directions as derived from the diffraction limited imaging optics to an EMCCD camera forms the starting point for all discussed precision measurements.

Measurements of relevant atomic properties in Ba^+ have been performed with the setup. The lifetime $\tau_{D_{5/2}}$ of the metastable $5d\,^2D_{5/2}$ state is extensively studied both in single and multiple ions. The results are important to study the behaviour of trapped ions in the apparatus and this crucial measurement needs to be performed in Ra^+. The lifetime of the state is determined to be $\tau_{D_{5/2}} = 27.6(8)\,s$ for a single ion. This result is below and within 2.5 standard deviations and 3 standard deviations to the latest theoretical and experimental values, respectively. The measurements are thoroughly studied and dependence on experimental parameters have been investigated. Only a weak dependence on the residual gas pressure and the shelving LED intensity has been observed and have been taken into account in the analysis. This provides valuable information on the understanding of the intrinsic atomic structure and enables extraction of atomic wavefunctions of the involved states.

High-resolution frequency spectroscopy of the laser cooling transitions in Ba^+ with single and multiple trapped and laser cooled ions permits extracting the absolute frequencies of the $6s\,^2S_{1/2}$–$6p\,^2P_{1/2}$, $6s\,^2S_{1/2}$–$5d\,^2D_{3/2}$ and $6p\,^2P_{1/2}$–$5d\,^2D_{3/2}$ transitions with a single trapped Ba^+ ion. The uncertainty of the extracted frequencies has an accuracy better than 100 kHz. The crucial part in this achievement is the description of the spectrum with an 8-level Optical Bloch Equation (OBE), which includes detunings, intensities, and polarisation of the light field with respect to the quantization axis. The observed spectra are in excellent agreement with OBE. The presence of Raman resonance results in the most precise measurements for these transitions in Ba^+ with an improvement of more than a factor of 100 over previous determinations.

The achievement of quantum jump spectroscopy (Chapter 5) and understanding of the complex spectra (Chapter 6) are exploited towards the determination of the light shifts in the trapped Ba^+ system. Here the ion is optimally overlapped with the off-resonant light shift laser and it is found that the ion shelves to the metastable $5d\,^2D_{5/2}$ state. The shelving and deshelving rates have been determined for different laser light intensities at λ_{590}. The two rates are used to extract a value for the ratio between two matrix elements of the $5d\,^2D_{3/2}$–$6p\,^2P_{3/2}$ and

$5d\,^2D_{5/2}$–$6p\,^2P_{3/2}$ transitions which are in agreement with other determinations. An improvement of such a measurement to 10^{-2} relative accuracy (% level) with an observation of more than 10,000 quantum jumps appears to be possible. The light shift effect is observed for the first time in the $6p\,^2P_{1/2}$–$5d\,^2D_{3/2}$ transition in trapped Ba^+ ions using a near-resonant light at λ_{650} and has been determined to be $0.16(3)\,\mathrm{GHz}^2 \cdot \frac{1}{\Delta_{LS}}$. It is also shown that the optimal alignment of the light shift laser beam with the ion signal has a significant effect on the measurement. The systematic effects while measuring light shifts such as detunings, intensities, and polarisation of light shift laser with respect to the quantization axis (i.e. magnetic field) have been studied. The vector and tensor light shifts of the individual Zeeman components for different $6s\,^2S_{1/2}$–$5d\,^2D_{3/2}$ transitions are observed with low powers of light at λ_{494}. An extensive study of the vector and tensor light shifts in the context of the polarisation of the light shift laser light with respect to the quantization axis has been initiated by this work and is currently in progress. This is a major step towards light shift determination in the Zeeman sublevels of the ground state of a single ion and it is crucial for a precise determination of APV in the ion.

Further, for an APV experiment a measurement of light shifts produced by standing waves is necessary. The design and implementation of vacuum compatible high finesse cavities to produce and control these standing waves are in progress. An offline Ra^+ source is being setup where all the above high precision spectroscopic measurements will be employed towards determination of APV in a single Ra^+ ion. Refinement on theory is ongoing to enable the determination of the Weinberg angle ($\sin^2\theta_W$) from an APV experiment with higher accuracy than it was possible for Cs atoms. The extraction of $\sin^2\theta_W$ from the experiments with single ions at low energies at sub % level accuracy will provide a sensitive means to search for physics beyond the Standard Model such as, e.g., dark Z bosons [29–31]. Note, this single ion experiment will also establish the construction of a single ion clock [145] with a potential of 10^{-18} relative uncertainty.

Chapter 9

Nederlandse Samenvatting

Ionen van aardalkalimetalen zoals Ba^+ en Ra^+, gevangen in een elektrisch veld en lasergekoeld, zijn zeer geschikt voor het nauwkeurig meten van atomaire pariteitschending (*Atomic Parity Violation*, APV). De reden hiervoor is dat de atomaire eigenschappen van deze ionen goed te berekenen zijn, dat ze een hoge intrinsieke gevoeligheid hebben en dat de benodigde apparatuur voor precisie-experimenten met een enkel lasergekoeld ion beschikbaar is. Dit proefschrift beschrijft een programma van experimenten met aardalkalimetaal-ionen met als doel het meten van de Weinberg-hoek (of *electroweak mixing angle*, $\sin^2\theta_W$) bij lage impulsoverdracht. De nauwkeurigheid die bij het meten van $\sin^2\theta_W$ behaald kan worden wordt gelimiteerd door de precisie waarmee de atomaire structuur van de gebruikte atomaire systemen bekend is en hoe goed de experimentele omstandigheden beheerst kunnen worden. In dit proefschrift wordt eerst de beschikbare informatie over de atomaire systemen Ba^+ en Ra^+ behandeld en vervolgens nieuwe experimentele input geleverd om recent verbeterde berekeningen van de Ba^+-golffuncties mee te controleren. De experimenten met Ba^+-ionen omvatten metingen van de levensduur van de metastabiele toestand $5d\,^2D_{5/2}$, van energieniveaus en van *light shifts* ten gevolge van een extra lichtveld (optisch Stark-effect). Er wordt in het bijzonder aandacht besteed aan de experimentele condities en hun invloed op de metingen. Deze opgedane kennis van Ba^+ zal in de toekomst worden benut bij een volgende serie experimenten met een enkel Ra^+-ion, waarvan de gevoeligheid voor elektrozwakke effecten zo'n 20 maal groter is.

Voor een precisiemeting van APV met een enkel ion is het noodzakelijk dat het ion gelokaliseerd wordt tot op een afstand korter dan een optische golflengte. Vervolgens bestaat de meting uit het bepalen van light shifts van de grondtoestand $7s\,^2S_{1/2}$ in de orde van een paar Hz. Dit werk omvat hiertoe het opbouwen van een experimentele opstelling voor een enkel Ba^+-ion. Dit bestaat onder meer uit het ontwikkelen van methoden om het aantal ionen dat geproduceerd, gevangen

en lasergekoeld wordt in een Paul-val in een vacuüm van 10^{-11} mbar te controleren en het ontwikkelen van optische detectietechnieken om deze ionen zichtbaar te maken. Daarnaast is de frequentiestabilisatie van de benodigde lasersystemen van groot belang: door gebruik te maken van een optische frequentiekam wordt een relatieve frequentie-onzekerheid van 10^{-11} behaald. Al deze experimentele technieken vormen de voorwaarden voor precisie-spectroscopiemetingen en zijn gekarakteriseerd door middel van experimenten met een enkel ion, met meerdere ionen en met ionenwolken. De opgebouwde experimentele opstelling is een cruciale stap op weg naar het meten van pariteitschending in een enkel gevangen ion. Voor alle verder besproken precisiemetingen vormt een enkel lasergekoeld Ba^+-ion in een Paul-val dat tot op een afstand van minder dan $1\,\mu$m gelokaliseerd is in alledrie de ruimtelijke dimensies (geverifiëerd door een diffractie-gelimiteerd beeld op een EMCCD-camera) het startpunt.

Met behulp van de experimentele opstelling zijn verschillende relevante atomaire eigenschappen van Ba^+ gemeten. Ten eerste is de levensduur $\tau_{D_{5/2}}$ van de metastabiele toestand $5d\,^2D_{5/2}$ uitgebreid bestudeerd, zowel met een enkel ion als met meerdere ionen. De resultaten hiervan zijn belangrijk om het gedrag van de gevangen ionen te bestuderen en deze cruciale meting moet ook in Ra^+ uitgevoerd worden. De gemeten levensduur is $\tau_{D_{5/2}} = 27.6(8)\,$s met een enkel ion. Deze waarden liggen onder en binnen 2.5 standaard afwijkingen and 3 standaard afwijkingen lager dan de meest recente theoretische en experimentele resultaten, respectievelijk. De meetmethode is uitgebreid tegen het licht gehouden en afhankelijkheden van experimentele parameters zijn onderzocht. Er zijn geen significante correlaties met laserintensiteiten, laserfrequenties en sterkte van de ionenval gevonden. Er is rekening gehouden met een zwakke afhankekijkhoed van de druk en de intensiteit van en LED. Deze metingen verschaffen waardevolle informatie over de intrinsieke atomaire structuur en maken het mogelijk om de golffuncties van de betrokken energietoestanden te achterhalen.

Met behulp van spectroscopie met hoge resolutie met een enkel gevangen Ba^+-ion zijn de frequenties bepaald van de transities die voor het laserkoelen gebruikt worden, $6s\,^2S_{1/2}$–$6p\,^2P_{1/2}$, $6s\,^2S_{1/2}$–$5d\,^2D_{3/2}$ en $5d\,^2D_{3/2}$–$6p\,^2P_{1/2}$. De onzekerheid in de gemeten frequenties bedraagt minder dan 100 kHz. De cruciale stap om dit resultaat te bereiken is het beschrijven van de spectrums met behulp van optische Bloch-vergelijkingen voor de acht betrokken Zeeman-subniveaus. Deze vergelijkingen bevatten laserfrequenties, laserintensiteiten en laserpolarisatie ten opzichte van de kwantisatie-as. De gemeten spectrums komen goed overeen met de Bloch-vergelijkingen. Het analyseren van de Raman-resonanties in de spectrums maakt dit tot de meest nauwkeurige meting van deze transitiefrequenties in Ba^+,

waarbij de onzekerheid met meer dan een factor 100 verkleind is ten opzichte van de vorige meting.

De behaalde resultaten met kwantumsprong-spectroscopie (Hoofdstuk 5) en het begrip van complexe spectrums (Hoofdstuk 6) worden gebruikt bij het meten van light shifts in gevangen Ba^+-ionen. In een eerste experiment wordt de bundel van een niet-resonante *lightshift-laser* met een golflengte van 590 nm (nabij de transitie $5d\,^2D_{3/2}$–$6p\,^2P_{3/2}$) op de ionen gericht. Hierdoor worden de ionen *geshelved* in de metastabiele toestand $5d\,^2D_{5/2}$. De snelheid waarmee het *shelven* en *deshelven* plaatsvindt is gemeten bij verschillende laserintensiteiten. Met deze waarden is de ratio van de matrixelementen van de transities $5d\,^2D_{3/2}$–$6p\,^2P_{3/2}$ en $5d\,^2D_{5/2}$–$6p\,^2P_{3/2}$ bepaald en consistent bevonden met andere metingen. Het verbeteren van een dergelijke meting tot een relatieve nauwkeurigheid van 10^{-2} (%-niveau) lijkt mogelijk met het observeren van meer dan 10 000 kwantumsprongen. In een tweede experiment is een light shift direct waargenomen door de ionen te beschijnen met bijna-resonant laserlicht met een golflengte van 650 nm (nabij de transitie $6p\,^2P_{1/2}$–$5d\,^2D_{3/2}$). De gemeten magnitude van deze verschuiving is $0.16(3)\,\mathrm{GHz}^2/\Delta_{LS}$. Ook is gebleken dat de optische uitlijning van de lightshift-laser met respect tot de ionen een groot effect heeft op de meting. Systematische effecten zoals laserfrequenties, laserintensiteiten en de polarisatie van de lightshift-laser met respect tot de kwantisatie-as (het magneetveld) zijn bestudeerd. Vector- en tensor-lightshifts van de individuele Zeeman-componenten van de transitie $6s\,^2S_{1/2}$–$5d\,^2D_{3/2}$ zijn waargenomen wanneer de spectroscopie-laser met golflengte 494 nm een lage intensiteit heeft. Uit dit werk is een uitgebreide studie naar de vector- en tensor-lightshifts bij het variëren van de polarisatie van de lightshift-laser voortgekomen die op dit moment gaande is. Deze experiment vormen een belangrijke stap op weg naar het meten van light shifts in de Zeeman-subniveaus van de grondtoestand van een enkel ion en zijn daarmee cruciaal voor een nauwkeurige meting van APV in een ion.

Tenslotte is voor een APV-meting met light shifts ook een intens lichtveld nodig dat gerealiseerd kan worden met staande lichtgolven in een trilholte. Het ontwerpen en bouwen van een dergelijke trilholte met hoge finesse die geschikt is voor vacuüm is aan de gang. Eveneens is een *offline* Ra^+-bron (zonder gebruik van een versneller) in ontwikkeling. Alle eerdergenoemde spectroscopische technieken kunnen ook bij Ra^+ worden toegepast om toe te werken naar een APV-meting in een enkel Ra^+-ion. Er wordt daarnaast gewerkt aan het verfijnen van de atomaire theorie om het mogelijk te maken de Weinberg-hoek $\sin^2\theta_W$ in een APV-experiment te bepalen met een hogere nauwkeurigheid dan tot nu toe mogelijk was met Cs-atomen. Het bepalen van $\sin^2\theta_W$ tot sub-% nauwkeurigheid uit experimenten met een enkel ion bij lage energie zal een gevoelige manier zijn om te zoeken naar

deeltjes die niet in het Standaard Model beschreven worden, zoals de voorgestelde donkere Z-bosonen [29–31]. Merk tot slot op dat de in dit proefschrift beschreven experimentele opstelling voor een enkel ion ook kan worden ingezet om een optische atoomklok te bouwen [145] met een relatieve onzekerheid tot 10^{-18}.

Appendix A

Abbreviations

Symbol	Description
AC	**A**lternating **C**urrent
AIUL	**A**rbitrary **I**ntensity **U**nits **L**ED
AOM	**A**cousto-**O**ptic **M**odulator
APV	**A**tomic **P**arity **V**iolation
AR	**A**nti **R**eflection
Ba	**Ba**rium
$\mathbf{Ba}^+$	**Ba**rium ion
BaLab	**Ba**rium **Lab**oratory
CF150	**C**on**F**lat-150 flange
CF200	**C**on**F**lat-200 flange
C	**C**harge conjugation
CEO	**C**arrier **E**nvelope **O**ffset
Cu	**C**opper
DC	**D**irect **C**urrent
DM	**D**ichroic **M**irror
EDM	**E**lectric **D**ipole **M**oment
EMCCD	**E**lectron **M**ultiplying **C**harge **C**oupled **D**evice
FWHM	**F**ull **W**idth **H**alf **M**aximum
GPS	**G**lobal **P**ositioning **S**ystem
HWP	**H**alf **W**ave **P**lates
$\mathbf{I}_2$	molecular **I**odine
IR	**I**nfra**R**ed
λ_{413}	Wavelength of $6s^2\ {}^1S_0$–$5d\,6p\,{}^3D_1$ transition in atomic Barium
λ_{455}	Wavelength of $6s\,{}^2S_{1/2}$–$6p\,{}^2P_{3/2}$ transition in Ba^+
λ_{494}	Wavelength of $6s\,{}^2S_{1/2}$–$6p\,{}^2P_{1/2}$ transition in Ba^+
λ_{553}	Wavelength of $6s^2\ {}^1S_0$–$6s\,6p\,{}^1P_1$ transition in atomic Barium
λ_{585}	Wavelength of $5d\,{}^2D_{3/2}$–$6p\,{}^2P_{3/2}$ transition in Ba^+
λ_{614}	Wavelength of $6p\,{}^2P_{3/2}$–$5d\,{}^2D_{5/2}$ transition in Ba^+
λ_{650}	Wavelength of $5d\,{}^2D_{3/2}$–$6p\,{}^2P_{1/2}$ transition in Ba^+

Symbol	Description
LaserLab	**Laser Lab**oratory
LBO	Lithium Triborate $\mathbf{LiB_3O_5}$
LHC	**L**arge **H**adron **C**ollider
N	***N***umber of neutrons
ND filter	**N**eutral **D**ensity filter
OBE	**O**ptical **B**loch **E**quations
OFHC	**O**xygen **F**ree **H**igh **C**onductivity
P	**P**arity
PBS	**P**olarising **B**eam **S**plitter
PD	**P**hoto**D**iode
PID	**P**roportional **I**ntegration **D**ifferentiation
PMT	**P**hoto**M**ultiplier **T**ube
PPLN	**P**eriodically **P**oled **L**ithium **N**iobate
Ra	**Ra**dium
$\mathbf{Ra^+}$	**Ra**dium ion
Rb	**Rb**idium
RF	**R**adio **F**requency
SHG	**S**econd **H**armonic **G**eneration
SM	**S**tandard **M**odel
SRS	**S**tanford **R**earch **S**ystems
T	**T**ime reversal
TeV	**T**era **e**lectron **V**olt
Ti	**Ti**tanium
Ti:Sapphire	**Ti**tanium **Sapphire**
TTL	**T**ransistor-**T**ransistor **L**ogic
UHV	**U**ltra **H**igh **V**acuum
UV	**U**ltra **V**iolet
WLM	**W**ave**L**ength **M**eter
Z	Atomic Number/number of protons(from German: Atom***Z***ahl)
$\mathbf{Z^0}$	$\mathbf{Z^0}$ Bosons

Appendix B

Alternate method of rf-switching

For variable attenuation

Alternate method of rf-switching is used to load few ions in the trap via variable attenuation. The switching mechanism consists of four levels in the applied rf. These four levels include the highest, constant, lower and the dump level/lowest voltages in which case the ions are lost/dumped (see Table B.2). This is controlled by 3 TTL outputs via the data acquisition system. This changing power levels helps in selective loading of ions in the trap based on the masses. This is shown in Fig. B.1. The higher voltages help to get rid of the lighter ions while the lower voltages gets rid of the heavier ones as compared to Ba^+.

TABLE B.1: Truth Table for switching of the different rf voltages. This is particularly helpful at the time of loading of few ions. The switching levels can be changed to get a variable attenuation depending on the requirement.

Rf level	Switch 1	Switch 2	Switch 3	Switching level	rf voltage
1	0	0	0	highest	2100
2	1	0	0	constant	650
3	0	1	1	lower rf	410
4	1	1	1	lowest/Dump	140

For fixed attenuation

In order to have a more stable voltage the fixed voltage is used to do the lifetime measurements and the function generator that generates the rf signal was used to vary the fixed voltage as required for the measurements.

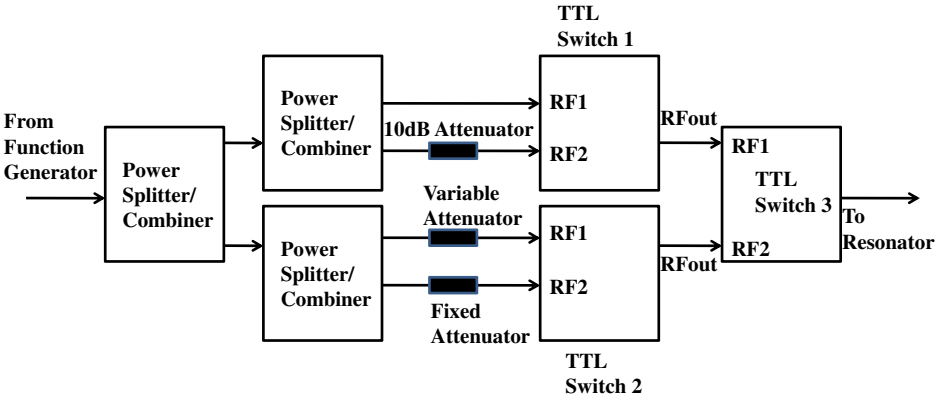

FIGURE B.1: RF Switching with variable attenuation. The switching is mainly used for an efficient loading of ions into the trap. The power splitters/combiners are Minicircuits ZFRSC-42-S+ specified for 50 Ω and DC-4200 MHz

TABLE B.2: Truth Table for switching of the different rf voltages. This is particularly helpful at the time of loading of few ions. This switching levels can be changed to get a variable attenuation depending on the requirement.

Rf level	Switch 1	Switch 2	Switch 3	Switching level	rf voltage [Vp-p]	Monitor voltage [V]
1	0	0	0	highest	4100	0.148
2	1	0	0	constant	1900	0.076
3	0	1	1	lower RF	1200	0.023
4	1	1	1	lowest/Dump	350	0.012

Stability of the RF Amplitude

The long term stability of the RF amplitude is a requisite for Ba^+ spectroscopy.

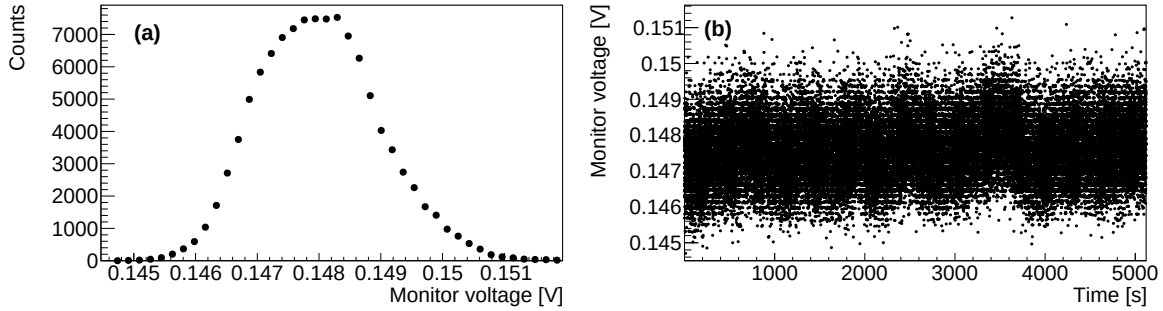

FIGURE B.2: The long term voltage stability for monitoring the rf voltage amplitude in the data acquisition. This monitor voltage (see Table B.2) is taken into account during precision measurements.

Appendix C

DC voltages to the endcaps

We have use DC voltages to localise the ion at the potential minima of the trap. Fig.C.1 shows the simple electronic circuit diagram for the DC voltages applied to the end caps. The only limitation of this circuit is the applied DC voltages was about $\pm 9\,\mathrm{V}$ and and was not able to change the DC voltages on both of them simultaneously. With this circuit, it was not possible to give a common offset between the two end cap electrodes. So, the electronic circuit for the DC voltages applied to the end caps are modified as shown in Fig. C.2 (next page). In this case, the voltages can be varied from $\pm 20\,\mathrm{V}$. This helps to apply DC voltages to the end caps individually as well as apply a common offset DC voltage between the two end caps. The electronics has a provision of applying DC voltages to the additional electrodes in future that will help in better localisation of ion at potential minima.

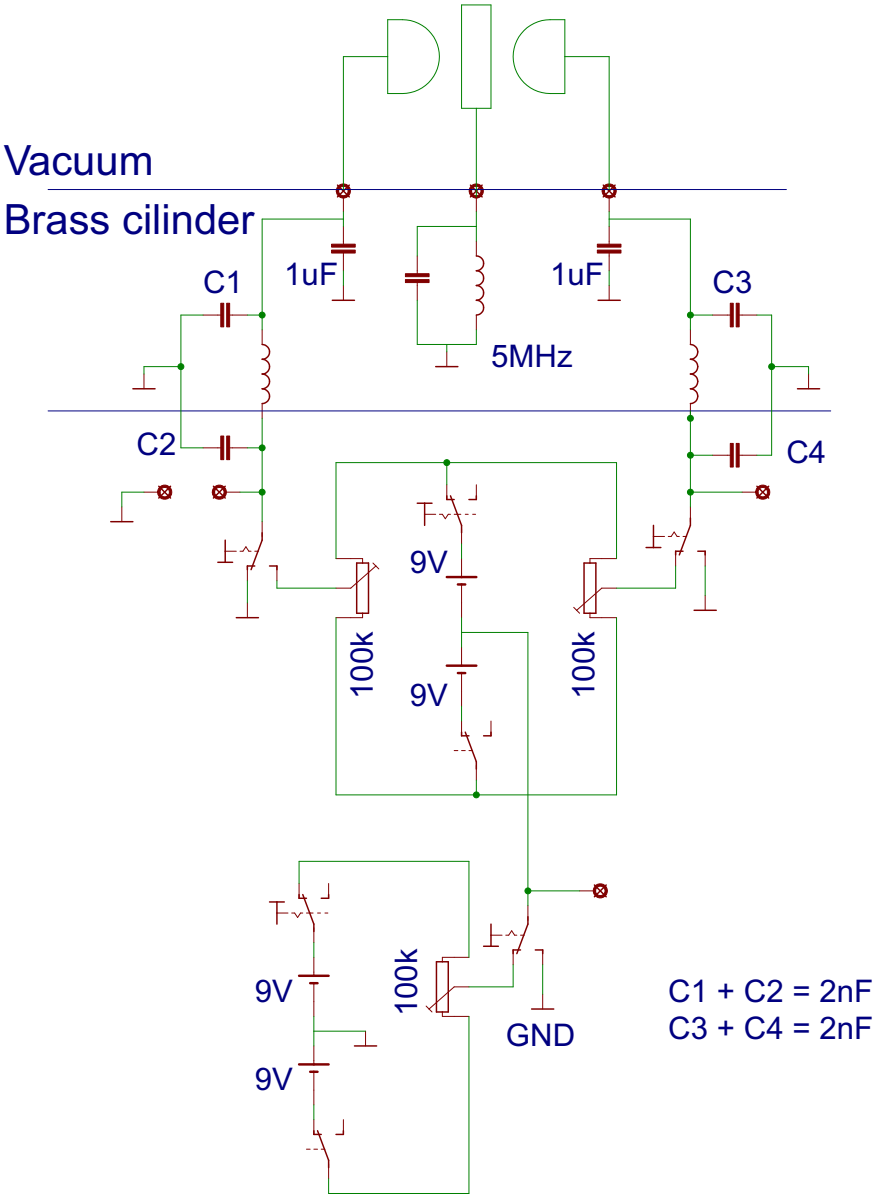

FIGURE C.1: Circuit diagram for the DC offset voltages given to the endcaps. The yellow and green connections are connected to each of the end caps and they help in applying voltages to each of them independently. The blue connection helps to the application of the voltages to both of them simultaneously. All credits for this goes to Leo Huismann.

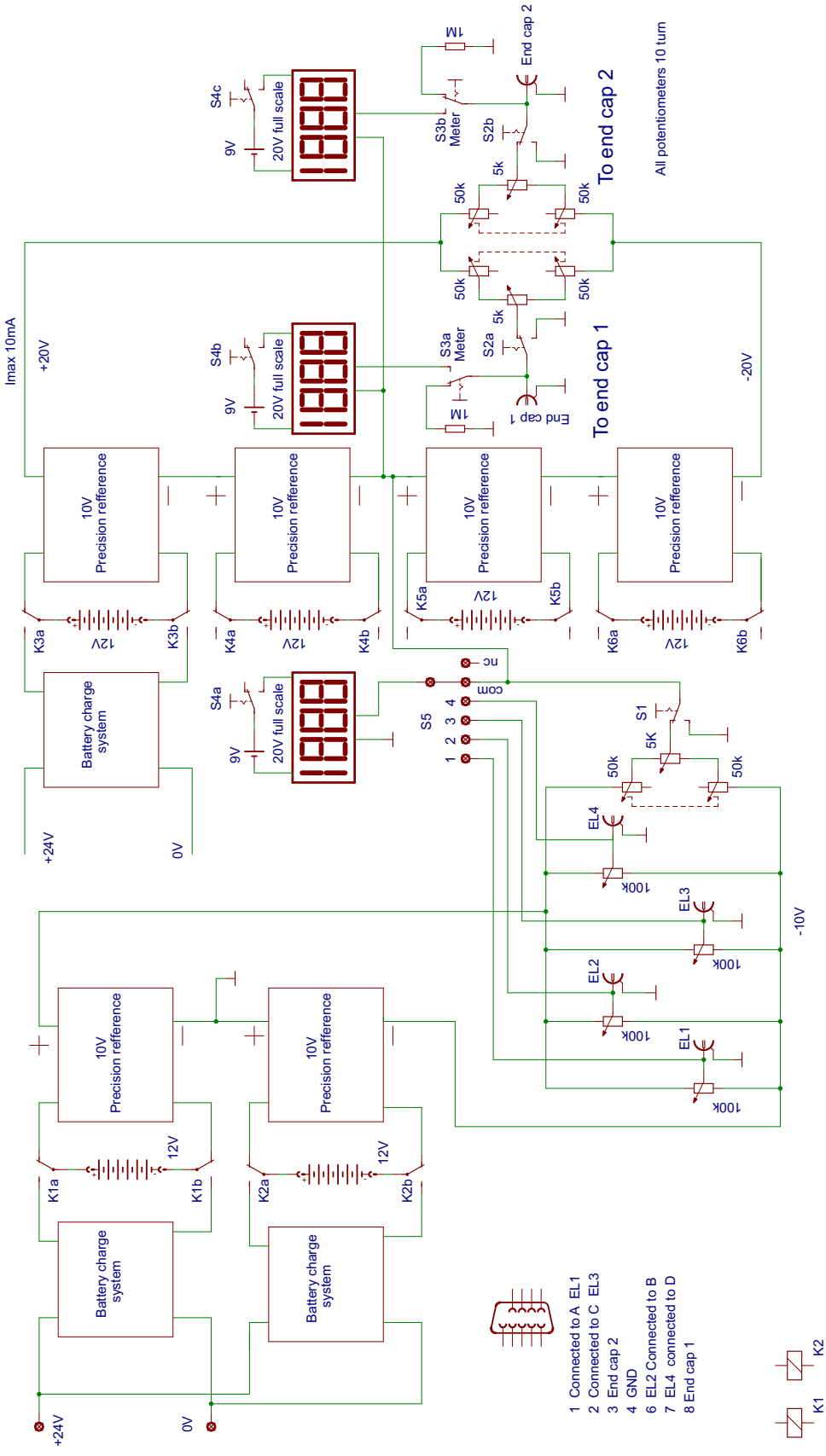

FIGURE C.2: Complicated circuit diagram for the DC offset voltages given to end caps. This can be varied from -20 V $<$ U_0 $<$20 V. The two digital meters on the right connected to end cap 1 and end cap 2 respectively monitors the DC voltage applied to each of them. The other digital meter on the left monitors the common DC voltage given to both of these two end caps. All credits for this goes to Leo Huismann.

Appendix D

Atomic spectroscopy of the $6s^2\ ^1S_0$–$6s\ 6p\ ^1P_1$ transition in barium

The graph below shows the characteristic curve for power vs current for the IR light at a wavelength 1107.5 nm (model LD-1120-0300-1 from Toptica) used for frequency doubling and the 553.7 nm light used for Barium atom spectroscopy as discussed in section 3.4.1 of Chapter 3.

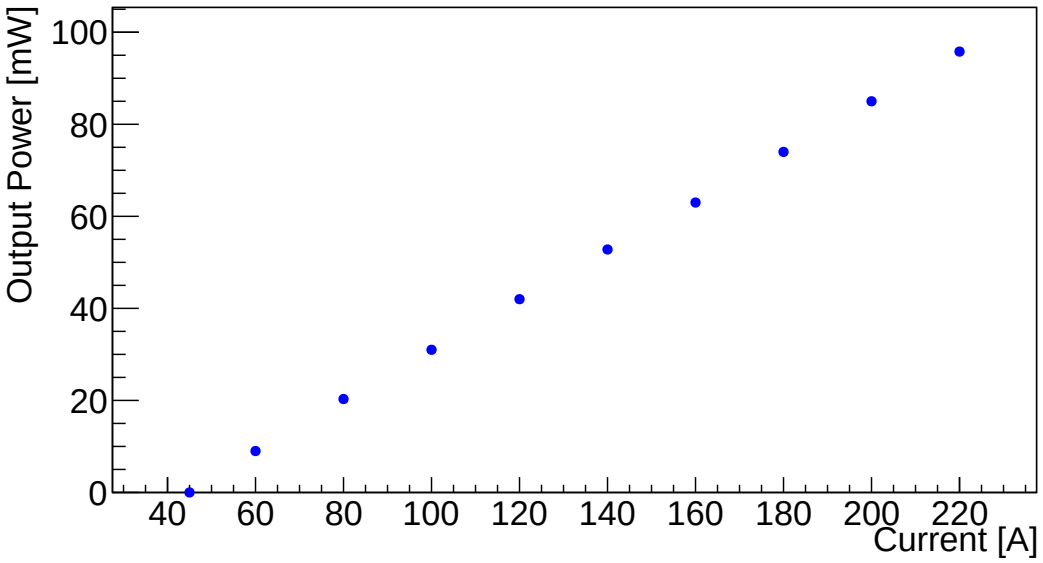

FIGURE D.1: Power vs current characteristic curve for the behaviour of the diode laser at a wavelength 1107.5 nm.

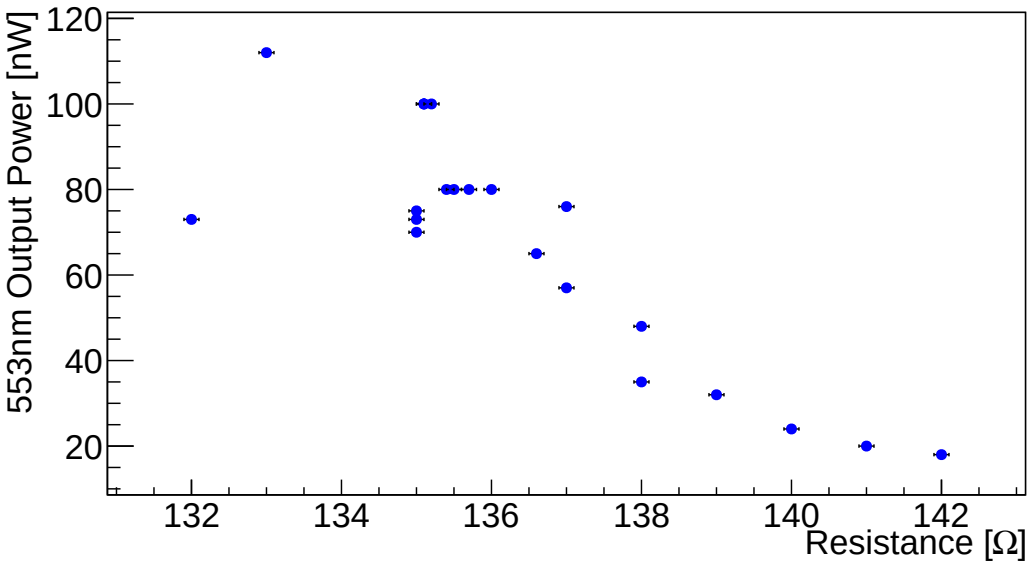

FIGURE D.2: Characteristic curve showing the output power from the crystal for different applied voltages to it. The optimal settings for detection of Barium atoms were at 91 °C and 135 Ω as per PT100. The crystal is a loan from Prof. Axel Görlitz from Universität of Düsseldorf.

$6s^2\ {}^1S_0$–6s 6p $^1P_1$ transition in barium at wavelength 553nm

The Doppler broadened spectrum for the transition at wavelength 553.7 nm was recorded for different oven currents (see Fig. D.3). Each of these spectrum represents the atomic flux which follows a Maxwell Boltzmann distribution. One such

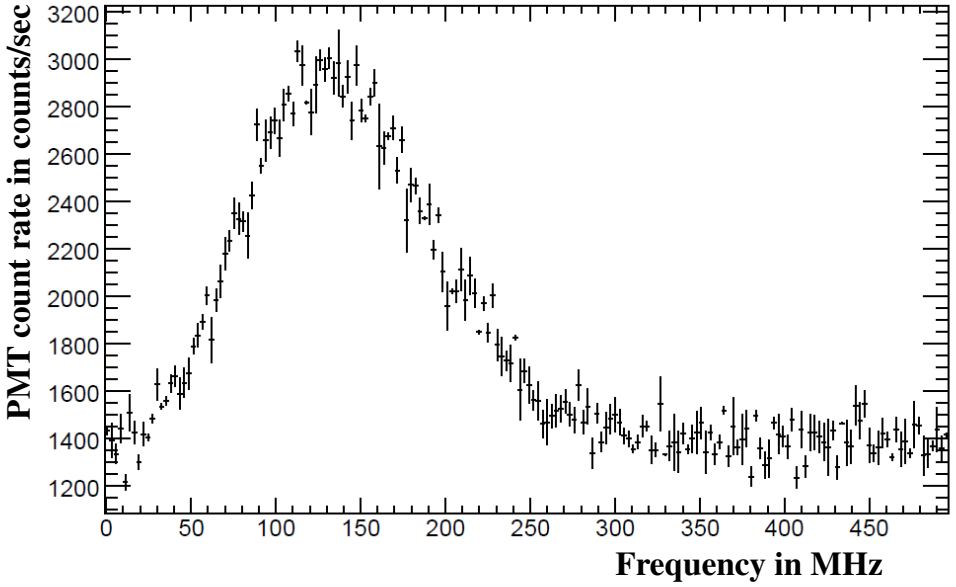

FIGURE D.3: Doppler broadened spectrum of the $6s^2\ {}^1S_0$–6s 6p $^1P_1$ transition in atomic barium obtained for one particular oven current, i.e 7 A. This follows a Maxwell Boltzmann distribution.

spectrum is shown above which has a FWHM of about 140±20 MHz with the atoms having a thermal velocity of about 77 m/s and the angle at which the oven produces the atoms crosses the 553 nm beam at about 12 °.

Appendix E

Laboratory Parameters

Below we list the typical parameters under which the experiments have been performed.

Pressure = 2.9×10^{-11} mbar
The Titanium sublimation pump is turned on once every week at 40 A for 1 min to maintain a good vacuum.

Wavelengths required

The different wavelengths as measured in various channels of WLM (WS6 VIS from HighFinesse-Ångstrom)
λ_{IR} = 987.0907 nm (T = 24.6 °C as measured in Channel 1)
λ_{Iodine} = 649.8685 nm (T = 24.6 °C as measured in Channel 3)
λ_{Dye} = 649.8699 nm (T = 24.6 °C as measured in Channel 5)
$\lambda_{Photoionisation}$ = 413.3493 nm (T = 24.6 °C as measured in Channel 15)
provided the wavelength changes with change in temperature of WLM.

Output Power required

Output light at 987 nm from the Ti:Sapphire laser = 300 mW
Output light at 650 nm from the Dye laser = 80-90 mW

Beam Position

Cooling Beam Position on the Beam Profiler (BC106-VIS CCD Camera Beam profiler from THORLABS)
X = 142μm (axis 1 of APT user)
Y = 52 μm (axis 2 of APT user)
For finer optimisation of the ion signal, the x and y axis of the mirror connected to Channel. 2 of the APT user. The beams always have these settings provided the translational mirrors are not touched manually. RF is set to 2.45 Vp-p in the scope.

Frequency comb and beatnote settings

Offset beatnote of the frequency comb = 20 MHz
Repetition rate of the frequency comb = 20000934 Hz
Beat note between the iodine-stabilized diode laser light with the frequency comb = 28.975 MHz
Beat note with light from Ti:Sapphire and frequency comb = 29.5 MHz
Offset beatnote between the light from the iodine-stabilized diode laser and the dye laser = -1151 MHz

Loading cycle for one ion

Loading of a single or few ions in the trap in a controlled way is one of the important and a reproducible parameter. This was done by following a cycle which is given as follows:

1. Red Laser = 20 s off, 70 s on
2. Blue Laser = 10 s on, 20 s off, 60 s on
3. Photoionisation laser = 45 s off, 3 s on, 42 s off with a wavelength set to 413.3493 nm (as in WLM)
4. RF level = 45 s at level 4; 5 s at level 3; 1 s at level 2; 30 s at level 1; 9 s at level 2
5. Ba oven at 6.5 A and 2.9 V = 50 s on, 40s off
6. Comb synthesiser = 20000654 Hz. At this setting, the blue laser is 186 MHz red detuned to laser cool the ions.

PMT (model: Hamamatshu H11123)

Dark count rate = 10 counts/s at a temperature of 13 °C
With 1 μW of blue, PMT count rate = 80 counts/s
PMT signal per ion = 800-1000 counts/s, provided optimally aligned with the cooling and repump beams.
At rf voltage of 2.45 Vp-p and DC voltage of 0.12 V on end cap1 and 0.02 V on end cap2 helps to localise the ion better and obtain a flat photon correlation signal as shown in Fig. 6.3(d).

EMCCD

The position of the ion signal on the EMCCD is at
X = 320 pixels
Y = 280 pixels
provided the RF is at 2.45 Vp-p (as in scope) and nobody has bumped into the camera optics.
The ion/ions are well localised at this position.

Magnetic Field Settings

The trap is located in the center of 3 pairs of coils. These coils provide a magnetic field of about 80μT per Ampere of current.
For operation, we have
Z-direction (Ch 1)= 1 mA ; 0.001 V
X-direction (Ch 2) = 2.201 A ; 4.695 V
Y-direction (Ch 3) = 301 mA; 0.609 V
The magnetic field along x-direction is perpendicular to the polarisation direction of the blue light field.

Cooling Beams and polarisation

Beam characteristics for the cooling and repump beams at the site of the trapped ion are as follows:
Beam waist for both beams = 60 μm
Light at wavelength λ_{650} is circularly polarised

Light at wavelength λ_{494} is linearly polarised in vertical direction and perpendicular to quantisation axis

Light at wavelength λ_{590}

Beam characteristics for the light at wavelength λ_{590} are as follows:
Operating wavelength = 590.06 nm
Beam waist = 100μm
Light at wavelength λ_{590} is linearly polarised at an angle of 45 ° to the blue light

Light at wavelength λ_{650}

Beam characteristics for a near off-resonant light at wavelength λ_{650} are as follows:
Beam waist = 45μm
Beam power at the site of the ion = 6-7 mW
Light at wavelength λ_{650} is linearly polarised

Appendix F

Lifetime vs parameters

TABLE F.1: Measured mean lifetime of the $5d\,^2D_{5/2}$ state in Ba^+ as a function of parameters such as blue and red powers, different setting for LED light at wavelength λ_{455}, rf voltages and the residual gas pressure as measured in the ion pump. The lifetime and its error are corrected for the shelving LED intensity dependence (see Fig. 5.12) using $\tau' = \tau_0 + 0.061 *$ LED Power. The corrected lifetime τ_0 have been plotted against pressure (see Fig. 5.13). Note some pressure readings are unreliable, so they are not given here.

Blue Power	Red Power	LED Setting	LED Power	RF voltage	Residual Gas Pressure	τ_0	τ'	Error	Corrected Error	Number of Ions
[μW]	[μW]		[AIUL]	[Vp-p]	[10^{-10} mbar]	[s]	[s]	[s]	[s]	
4.62	4.16	4.5	64	1214	2.99	31.1	35.0	6.4	6.7	1
3.94	7.03	4.5	64	661	3.25	26.4	30.3	2.3	3.0	1
4.12	4.17	4.5	64	550	2.69	25.7	29.6	3.8	4.2	1
3.97	5.86	5.5	117	388	5.23	19.5	26.7	2.7	4.3	1
4.15	6.46	4.5	64	392	4.11	21.5	25.4	4.3	4.7	1
3.70	3.40	6.0	135	377	2.95	20.3	28.5	2.9	4.9	1
4.25	5.15	4.5	64	428	3.14	22.0	25.9	2.3	3.0	1
2.99	1.68	4.5	64	578	2.77	19.8	23.7	3.4	3.9	1
1.96	1.61	4.5	64	625	3.29	22.9	26.8	1.9	2.7	1
1.83	1.44	6.0	135	597	3.21	20.1	28.3	2.9	4.9	1
1.17	4.69	4.5	64	305	3.63	24.4	28.3	3.5	4.0	1
1.01	3.21	6.5	192	305	3.55	27.6	39.3	4.0	6.9	1
1.84	2.28	5.0	100	315	4.70	18.6	24.7	3.2	4.3	1
2.30	3.23	5.0	100	321	4.82	18.1	24.2	3.9	4.9	1
1.56	3.53	5.0	100	449	8.70	16.8	22.9	2.8	4.0	1
3.57	1.76	5.0	100	322	4.12	19.7	25.8	3.3	4.4	1
1.78	1.40	5.0	100	319	4.12	26.9	33.0	4.4	5.3	1
0.90	1.05	5.0	100	317	4.07	23.0	29.1	3.4	4.5	1
1.13	1.59	–	–	407	2.32	22.7	–	1.7	1.7	1
1.33	2.22	4.0	33	423	–	20.8	22.8	2.9	3.1	1
1.22	1.42	4.0	33	463	2.41	26.5	28.5	1.6	1.9	3
2.10	3.62	3.0	22	572	2.19	27.5	28.8	2.0	2.1	2
2.37	3.52	3.0	22	573	2.22	27.1	28.4	1.9	2.0	2
2.42	3.52	–		290	2.39	17.4	–	3.0	3.0	1
4.00	3.77	2.5	11	366	2.21	24.0	24.7	2.0	2.0	4
2.41	2.16	3.0	22	400	2.15	25.4	26.7	3.0	3.1	1
1.08	1.85	3.0	22	408	2.24	23.9	25.2	3.5	3.6	1
2.08	2.21	3.0	22	387	2.09	23.1	24.4	3.1	3.2	1

Blue Power	Red Power	LED Setting	LED Power	RF voltage	Residual Gas Pressure	τ_0	τ'	Error	Corrected Error [s]	Number of Ions
[μW]	[μW]		[AIUL]	[Vp-p]	[10^{-10} mbar]	[s]	[s]			
1.86	1.95	6.5	192	389	2.21	24.8	36.5	2.4	6.1	1
1.97	2.02	3.0	22	376	2.15	26.4	27.7	3.3	3.4	3
2.24	1.94	3.0	22	379	2.21	27.4	28.7	4.1	4.2	2
2.00	2.51	3.0	22	383	2.29	26.3	27.6	2.6	2.7	2
2.09	2.45	3.0	22	387	2.34	18.2	19.5	4.0	4.1	2
2.03	2.46	3.0	22	389	2.36	18.7	20.0	3.5	3.6	1
2.17	2.74	5.0	100	403	1.33	22.5	28.6	1.9	3.5	1
1.89	2.69	5.0	100	395	1.14	25.8	32.0	3.0	4.2	1
1.89	2.57	4.5	64	381	–	27.0	31.0	4.9	5.2	2
1.98	2.45	4.5	64	379	–	28.3	32.2	4.0	4.4	2
2.07	1.43	3.5	30	373	–	33.5	35.3	6.8	6.9	2
1.94	3.43	4.0	33	379	–	22.0	24.0	2.6	2.8	1
1.65	3.32	3.0	22	367	–	21.3	22.6	3.2	3.3	1
2.33	2.98	4.5	64	371	–	31.5	35.4	3.1	3.6	1
2.90	2.59	4.5	64	408	0.83	23.9	27.8	4.2	4.6	1
2.90	3.75	3.0	22	413	0.84	25.3	26.6	4.2	4.3	1
2.96	3.77	3.5	30	412	0.84	25.8	27.6	4.3	4.4	1
2.25	3.74	5.0	100	418	0.86	30.6	36.7	3.6	4.6	1
2.32	9.44	2.0	10	416	0.81	25.9	26.5	2.9	2.9	2
2.18	9.13	4.5	64	426	0.79	23.5	27.4	1.7	2.5	1
2.01	5.87	4.5	64	376	0.89	24.9	28.8	1.9	2.7	1
2.31	5.85	4.5	64	396	0.90	21.8	25.7	1.6	2.5	1
2.80	6.25	4.5	64	403	0.86	25.2	29.1	1.6	2.5	1
2.71	6.77	4.5	64	405	0.86	23.9	27.8	1.4	2.3	1
2.80	6.34	2.0	10	415	0.88	28.7	29.3	3.8	3.8	1
2.57	6.45	3.5	30	461	0.83	25.2	27.0	1.8	2.0	3
2.92	6.22	3.5	30	509	0.80	26.3	28.1	2.3	2.5	1
2.67	6.60	3.5	30	391	0.69	27.4	29.2	3.3	3.4	1
2.44	6.57	3.5	30	328	0.71	27.4	29.2	1.4	1.6	2
2.58	6.36	3.5	30	413	0.64	29.9	31.7	5.1	5.2	1
2.94	6.57	3.5	30	405	0.66	26.6	28.4	3.1	3.2	2
2.77	6.62	3.5	30	410	0.67	24.0	25.8	1.9	2.1	1
2.28	2.39	4.5	64	518	–	23.5	27.4	1.4	2.3	1
2.43	1.94	4.5	64	540	–	24.4	28.3	3.0	3.5	1
2.50	1.94	4.5	64	464	–	26.5	30.4	4.3	4.7	1
1.19	4.98	4.5	64	495	1.47	22.4	26.3	3.4	3.9	2
1.09	3.89	4.5	64	514	1.48	22.7	26.6	2.7	3.3	1
1.37	4.31	4.5	64	489	1.24	26.0	29.9	1.8	2.6	1
1.23	6.80	4.5	64	499	0.88	20.9	24.8	3.0	3.5	1
1.38	6.42	4.5	64	770	0.89	27.2	31.1	5.1	5.4	2
1.80	6.25	4.5	64	822	0.93	22.5	26.4	1.5	2.4	1
1.76	6.21	4.5	64	795	0.87	20.8	24.7	3.5	4.0	1
2.02	6.42	5.0	100	454	1.01	33.7	39.8	6.4	7.0	4
2.01	6.65	5.0	100	448	0.98	26.8	32.9	1.9	3.5	3
2.54	5.73	5.0	100	445	0.93	43.0	49.1	15.7	16.0	3
2.67	5.69	5.0	100	446	0.94	47.8	53.9	11.2	11.6	2
2.01	5.29	5.0	100	450	0.96	19.9	26.0	3.0	4.2	2
1.82	5.01	5.0	100	450	0.99	27.1	33.2	3.1	4.2	2

Appendix G

Jumps vs parameters

TABLE G.1: Number of quantum jumps as a function of blue power for the lifetime of the $5d\,^2D_{5/2}$ state in Ba^+ (see Fig. 5.9).

Power [μW]	Number of Jumps	Power [μW]	Number of Jumps	Power [μW]	Number of Jumps
3.9	35	1.9	36	1.4	30
3.6	25	1.3	142	1.6	43
3.8	70	1.5	75	3.6	40
1.0	148	1.0	100	2.6	34
3.8	50	1.2	70	0.9	53
4.0	65	1.0	51	1.2	182
5.2	67	0.5	50	1.2	115
4.4	165	1.0	21	2.2	51
4.2	47	1.4	134	2.4	73
4.8	34	2.0	19	0.8	68
4.6	25	2.4	14	0.4	57
3.9	151	1.9	96	1.4	15
4.5	53	2.2	50	1.6	106
4.1	53	1.7	66	1.6	55
4.0	61	1.6	22	1.1	68
4.1	29	1.7	106	1.6	128
3.7	67	1.8	73	2.2	162
3.6	19	2.1	20	1.9	195
4.2	128	1.9	53	3.2	58
3.0	37	1.6	27	3.4	128
2.0	168	1.6	44	3.3	10
2.2	43	1.7	85	–	–

TABLE G.2: Number of quantum jumps as a function of red power for the lifetime of the $5d\,^2D_{5/2}$ state in Ba^+ (see Fig. 5.9).

Power [μW]	Number of Jumps	Power [μW]	Number of Jumps
4.9	35	2.5	96
5.5	25	3.2	50
5.5	70	1.9	66
3.2	148	1.7	22
6.1	50	1.6	106
5.8	65	1.6	73
4.0	67	2.5	20
6.5	165	1.7	53
2.3	47	0.7	27
5.0	34	5.9	44
4.2	25	0.8	85
7.0	151	3.3	30
6.1	53	3.5	43
4.2	53	1.8	40
5.9	61	2.1	34
6.5	29	1.0	53
3.4	67	3.4	182
2.6	19	4.2	115
5.2	128	4.3	51
1.7	37	4.9	73
1.6	168	4.0	68
2.0	43	3.8	57
1.3	36	6.7	15
2.7	142	5.9	106
4.8	75	5.7	55
3.5	100	5.9	68
4.7	70	5.4	128
3.2	51	5.9	162
1.8	50	5.9	195
4.2	21	6.8	58
2.4	134	6.1	128
3.7	19	6.3	10
4.7	14	–	–

TABLE G.3: Number of quantum jumps as a function of rf voltages for the lifetime of the $5d\,^2D_{5/2}$ state in Ba^+ (see Fig. 5.9).

rf voltage [Vp-p]	Number of Jumps	rf voltage [Vp-p]	Number of Jumps
290	35	314	14
284	25	309	96
284	70	306	50
392	148	695	66
399	65	364	22
1218	67	309	106
1218	165	910	73
612	47	331	20
1208	34	328	53
1214	25	327	27
661	151	328	44
544	53	330	85
550	53	309	30
388	61	449	43
392	29	322	40
377	67	326	34
294	19	317	53
428	128	472	182
578	37	479	115
625	168	480	51
1069	43	476	73
1070	36	477	68
298	142	476	106
330	75	476	55
303	100	472	68
305	70	472	128
305	51	499	162
307	50	680	195
312	21	659	58
316	134	663	128
310	19	–	–

TABLE G.4: Number of quantum jumps as a function of residual gas pressure for the lifetime of the $5d\,^2D_{5/2}$ state in Ba^+ (see Fig. 5.9).

Pressure $[10^{-10}\,\text{mbar}]$	Number of Jumps	Pressure $[10^{-10}\,\text{mbar}]$	Number of Jumps
1.4	35	1.0	36
1.4	25	0.76	142
1.4	70	0.81	75
1.4	148	0.97	70
1.3	50	0.95	51
1.2	65	0.77	66
1.2	67	0.67	106
1.4	165	0.70	20
0.87	47	1.8	53
0.83	34	1.1	27
0.80	25	1.3	44
0.87	151	3.8	30
0.74	53	1.3	43
0.72	53	1.1	40
1.4	61	1.0	34
1.1	29	1.1	53
0.79	67	0.6	68
0.84	19	0.56	195
0.84	128	0.54	58
0.74	37	0.6	128
0.88	168	0.59	10
1.0	43	–	–

Bibliography

[1] S. L. Glashow. *Partial symmetries of weak interactions.* Nucl. Phys. **22**, 579 (1961).

[2] S. Weinberg. *A model of leptons.* Phys. Rev. Lett. **19**, 1264 (1967).

[3] A. Salam. *Gauge unification of fundamental forces.* Rev. Mod. Phys. **52**, 525 (1980).

[4] S. Chatrchyan et al., CMS collaboration. *Observation of a new Boson at a Mass of 125 GeV with the CMS experiment at the LHC.* Phys. Lett. B **716**, 30-61 (2012).

[5] G. Aad et al., ATLAS collaboration. *Observation of a New Particle in the search for the Standard Model Higgs Boson with the ATLAS detector at the LHC.* Phys. Lett. B **716**, 1-29 (2012).

[6] J. S. M. Ginges and V. V. Flambaum. *Violations of Fundamental Symmetries in Atoms and Tests of Unification Theories of Elementary Particles.* Phys. Rep. **397**, 63-154 (2004).

[7] E. N. Fortson and L. L. Lewis. *Atomic Parity Nonconservation Experiments.* Phys. Rep. **113**, 289-344 (1984).

[8] E. D. Commins. *Atomic Parity Violation Experiments.* Phys. Scr. **36**, 468-475 (1987).

[9] K. Jungmann. *Searching for Electric Dipole Moments.* Ann. Phys. **525**, 550-564 (2013).

[10] T. Fukayama. *Searching for New Physics beyond the Standard Model in Electric Dipole Moment.* Int. J. Mod. Phys. A **27**, 1230015 (2012).

[11] V.A. Dzuba, V.V. Flambaum. *Parity violation and electric dipole moments in atoms and molecules.* Int. J. Mod. Phys. E **21**, 1230010 (2012).

[12] V. A. Dzuba, V. V. Flambaum. *Current trends in searches for new physics using measurements of parity violation and electric dipole moments in atoms and molecules.* arXiv:1009.4960

[13] M. Sozzi. *Discrete Symmetries and CP Violation: From Experiment to Theory.* Oxford University Press, Oxford (2008).

[14] T. D. Lee and C. N. Yang. *Parity nonconservation and a two-component theory of the neutrino.* Phys. Rev. **105**, 1671 (1957).

[15] C. S. Wu, E. Ambler, R. W. Hayward, D. D. Hoppes and R. P. Hudson. *Experimental test of Parity Conservation in a Beta Decay.* Phys. Rev. **105**, 1413-1415 (1957).

[16] S. G. Porsev, K. Beloy, and A. Derevianko. *Precision Determination of Electroweak Coupling from Atomic Parity Violation and Implications for Particle Physics.* Phys. Rev. Lett. **102**, 181601 (2009).

[17] M. A. Bouchiat and C. C. Bouchiat. *Weak Neutral Currents in Atomic Physics.* Phys. Lett. B **48**, 11-114 (1974).

[18] M. A. Bouchiat and C. Bouchiat. *Parity Violation in Atoms.* Rep. Prog. Phys. **60**, 1351–1396 (1997).

[19] J. Guéna, M. Lintz, and M. A. Bouchiat. *Atomic Parity Violation: Principles, Recent Results, Present Motivations.* Mod. Phys. Lett. A **20**, 375–389 (2005).

[20] A. Derevianko and S. G. Porsev. *Theoretical Overview of Atomic Parity Violation.* Eur. Phys. J. A **32**, 517–523 (2007).

[21] W. J. Marciano and J. L. Rosner. *Atomic Parity Violation as a probe of New Physics.* Phys. Rev. Lett. **68**, 898 (1992).

[22] Ya. B. Zel'dovich, Zh. Eksp. Theor. Fiz. **36**, 964 (1959).

[23] I. B. Khriplovich, Pis'ma Zh. Eksp. Theor. Fiz. **20**, 686 (1974).

[24] G. S. Giri. *Radium Ion Spectroscopy Towards Atomic Parity Violation in a Single Trapped Ion.* PhD thesis, University of Groningen (2011).

[25] J. Erler and M. R. Musolf. *Weak mixing angle at low energies.* Phys. Rev. D **72**, 073003 (2005).

[26] ALEPH Collaboration, DELPHI Collaboration, L3 Collaboration, OPAL Collaboration, SLD Collaboration, LEP Electroweak Working Group, et al. *Precision Electroweak Measurements on the Z-Resonance.* Phys. Rep. **427**, 257–454 (2006).

[27] P. L. Anthony, R. G. Arnold, C. Arroyo, K. Bega, J. Biesiada, P. E. Bosted, G. Bowe, J. Cahoon, R. Carr, G. D. Cates, J. P. Chen, E. Chudakov, M. Cooke, P. Decowski,A. Deur, W. Emam, R. Erickson, T. Fieguth, C. Field,

J. Gao, M. Gary, K. Gustafsson, R. S. Hicks, R. Holmes, E. W. Hughes, T. B. Humensky, G. M. Jones, L. J.Kaufman, L. Keller, Yu. G. Kolomensky, K. S. Kumar, P. LaViolette, D. Lhuillier, R. M. Lombard-Nelsen, Z. Marshall, P. Mastromarino, R. D. McKeown, R. Michaels, J. Niedziela, M. Olson, K. D. Paschke, G. A. Peterson, R. Pitthan, D. Relyea, S. E. Rock, O. Saxton, J. Singh, P. A. Souder, Z. M. Szalata, J. Turner, B. Tweedie, A. Vacheret, D. Walz, T. Weber, J. Weisend, M. Woods, and I. Younus. *Precision Measurement of the Weak Mixing Angle in Møller Scattering.* Phys. Rev. Lett. **95**, 081601 (2005).

[28] L. W. Wansbeek, B.K. Sahoo, R. G. E. Timmermans, K. Jungmann, B. P. Das, D. Mukherjee. *Atomic parity nonconservation in* Ra^+. Phys. Rev. A **78**, 050501(R) (2008).

[29] H. Davoudiasl, W. J. Marciano. *Running in Dark Sector.* Phys. Rev. D. **92**, 035008 (2015).

[30] H. Gharibnejad and A. Derevianko. *Dark forces and atomic electric dipole moments.* Phys. Rev. D. **91**, 035007 (2015).

[31] H. Davoudiasl, H-S. Lee, W. J. Marciano. *Muon g-2, rare kaon decays and parity violation from dark bosons.* Phys. Rev. D. **89**, 095006 (2014).

[32] G. P. Zeller, K. S. McFarland, T. Adams, A. Alton, S. Avvakumov, L. de Barbaro, P. de Barbaro, R. H. Bernstein, A. Bodek, T. Bolton, J. Brau, D. Buchholz, H. Budd,L. Bugel, J. Conrad, R. B. Drucker, B. T. Fleming, R. Frey, J. A. Formaggio, J. Goldman, M. Goncharov, D. A. Harris, R. A. Johnson, J. H. Kim, S. Koutsoliotas, M. J.Lamm, W. Marsh, D. Mason, J. McDonald, C. McNulty, D. Naples, P. Nienaber, A. Romosan, W. K. Sakumoto, H. Schellman, M. H. Shaevitz, P. Spentzouris, E. G. Stern, N. Suwonjandee, M. Tzanov, M. Vakili, A. Vaitaitis, U. K. Yang, J. Yu, and E. D. Zimmerman. *Precise Determination of Electroweak Parameters in Neutrino-Nucleon Scattering.* Phys. Rev. Lett. **88**, 091802 (2002).

[33] C. S. Wood, S. C. Bennett, D. Cho, B. P. Masterson, J. L. Roberts, C. E. Tanner, and C. E. Wieman. *Measurement of Parity Nonconservation and an Anapole Moment in Cesium.* Science **275**, 1759–1763 (1997).

[34] S. C. Bennett and C. E. Wieman. *Measurement of the 6S-7S Transition Polarizability in Atomic Cesium and an Improved Test of the Standard Model.* Phys. Rev. Lett. **82**, 2484–2487 (1999).

[35] S. G. Porsev, K. Beloy, and A. Derevianko. *Precision Determination of Weak Charge of* ^{133}*Cs from Atomic Parity Violation.* Phys. Rev. D **82**, 036008 (2010).

[36] V. A. Dzuba, J. C. Berengut, V. V. Flambaum, and B. Roberts. *Revisiting Parity Nonconservation in Cesium.* Phys. Rev. Lett. **109**, 203003 (2012).

[37] V. M. Shabaev, K. Pachucki, I. I. Tupitsyn, and V. A. Yerokhin. *QED Corrections to the Parity-Nonconserving 6s-7s Amplitude in ^{133}Cs.* Phys. Rev. Lett. **94**, 213002 (2005).

[38] M.A. Bouchiat, J. Guena, L. Hunter t and L. Pottier. *Observation of a parity violation in Cesium.* Phys. Lett. B **117**, 5 (1982).

[39] M. C. Noecker, B. P. Masterson, and C. E. Wiemann. *Precision Measurement of Parity Nonconservation in Atomic Cesium: A Low-Energy Test of the Electroweak Theory.* Phys. Rev. Lett. **61**, 3 (1988).

[40] N. Fortson. *Possibility of measuring Parity nonconservation with a single trapped atomic ion.* Phys. Rev. Lett. **70**, 2383 (1993).

[41] L. Wansbeek. *Atomic Parity Violation in a single radium ion.* PhD thesis, University of Groningen (2011).

[42] G. S. Giri et al. *Precision Spectroscopy of trapped radioactive radium ions.* Can. J. Phys. **89**, 69 (2011).

[43] T. W. Koerber, M. Schacht, W. Nagourney, and E. N. Fortson. *Radio Frequency Spectroscopy with a Trapped Ba^+ Ion: Recent Progress and Prospects for Measuring Parity Violation.* J. Phys. B **36**, 637–648 (2003).

[44] O. O. Versolato. *Laser spectroscopy of trapped Ra^+ ions: Towards a Single-Ion Optical clock.* PhD thesis, University of Groningen (2011).

[45] O. O. Versolato et al. *Laser Spectroscopy of trapped short-lived Ra^+ ions.* Phys. Rev. A **82**, 010501(R) (2010).

[46] O. O. Versolato et al. *Atomic parity violation in a single trapped Ra^+ ion.* Hyperfine Interact. **199**, 9–19 (2011).

[47] G. S. Giri et al. *Isotopic shifts of $6d^2D_{3/2}$-$7p^2P_{1/2}$ transition in trapped short-lived $^{209-214}Ra^+$.* Phys. Rev. A **84**, 020503(R) (2011).

[48] K. M. Lynch et. al. *Collinear resonance ionization spectroscopy of radium ions.* CERN-INTC-2014-043 / INTC-P-413 (2014).

[49] M. Nuñez Portela, J. E. van den Berg, H. Bekker, O. Böll, E. A. Dijck, G. S. Giri, S. Hoekstra, K. Jungmann, A. Mohanty, C. J. G. Onderwater, B. Santra, S. Schlesser, R. G. E. Timmermans, O. O. Versolato, L. W. Wansbeek, L. Willmann, H. W. Wilschut. *Towards a precise measurement of atomic parity violation in a single Ra^+ ion.* Hyperfine Interact. **214**, 157-162, (2013).

[50] M. Nuñez Portela, E. A. Dijck, A. Mohanty, H. Bekker, J.E. van den Berg, G.S. Giri, S. Hoekstra, C. J. G. Onderwater, S. Schlesser, R. G. E. Timmermans, O. O. Versolato,L. Willmann, H. W. Wilschut, K. Jungmann. *Ra^+ Ion Trapping: Toward an Atomic Parity Violation Measurement and an Optical Clock.* Appl. Phys. B **114**, 173-182 (2014).

[51] L. Willmann, K. Jungmann, C. J. G. Onderwater, R. G. E. Timmermans, H. W. Wilschut. *Trapped radioactive isotopes for fundamental symmetry investigations.* EXA 2011, 315-319 (2012).

[52] W. Paul. *Electromagnetic traps for charged and neutral particles.* Rev. Mod. Phys. **62**, 531 (1990).

[53] W. Neuhauser, M. Hohenstatt, P. E. Toschek, and H. Dehmelt. *Localized Visible Ba^+ Mono-Ion Oscillator.* Phys. Rev. A **22**, 1137–1140 (1980).

[54] H. Karlsson and U. Litzén. *Revised Ba I and Ba II Wavelengths and Energy Levels Derived by Fourier Transform Spectroscopy.* Phys. Scr. **60**, 321–328 (1999).

[55] J. J. Curry. *Compilation of Wavelengths, Energy Levels, and Transition Probabilities for Ba I and Ba II.* J. Phys. Chem. Ref. Data **33**, 725–746 (2004).

[56] K. Wendt, S.A. Ahmad, W. Klempt, R. Neugart, E.W. Otten, and H.H. Stroke. *On the Hyperfine Structure and Isotope Shift of Radium.* Zeitschrift für Physik Du Atoms, Molecules and Clusters, **4**, 227–241 (1987).

[57] E. Rasmussen. *Das Bogenspektrum des Radiums.* Z. Phys. **87**, 607–615 (1934).

[58] E. Rasmussen. *Serien im Funkenspektrum des Radiums. Ra II.* Z. Phys. **86**, 24–32 (1933).

[59] P. D. Shidling, G. S. Giri, D. J. van der Hoek, K. Jungmann, W. Kruithof, C. J. G. Onderwater, M. Sohani, O. O. Versolato, L. Willmann, and H. W. Wilschut. *Production of Short Lived Radioactive Beams of Radium.* Nucl. Instrum. Methods Phys. Res. Sect. A **606**, 305–309 (2009).

[60] W. Neu, R. Neugart, E. W. Otten, G. Passler, K. Wendt, B. Fricke, E. Arnold, H. J. Kluge, G. Ulm, and ISOLDE Collaboration. *Quadrupole Moments of Radium Isotopes from the $7p^2P_{3/2}$ Hyperfine Structure in Ra II.* Z. Phys. D **11**, 105–111 (1988).

[61] S. I. Purushothaman. *Superfluid Helium and Cryogenic Noble Gases as Stopping Media for Ion Catchers.* PhD thesis, University of Groningen (2008).

[62] B. Santra. *Precision Spectroscopy of Neutral Radium: Towards Searches for Permanent Electric Dipoles Moments.* PhD thesis, University of Groningen (2013).

[63] M. D. Davidson, L. C. Snoek, H. Volten, and A. Dönszelmann. *Oscillator Strengths and Branching Ratios of Transitions between Low-Lying Levels in the Barium II Spectrum.* Astron. Astrophys. **255**, 457 (1992).

[64] N. Kurz, M. R. Dietrich, Gang Shu, R. Bowler, J. Salacka, V. Mirgon, and B. B.Blinov. *Measurement of the Branching Ratio in the 6P3/2 Decay of Ba II with a Single Trapped Ion.* Phys. Rev. A **77**, 060501 (2008).

[65] J. E. Sansonetti, W. C. Martin, and S. L. Young. *Handbook of Basic Atomic Spectroscopic Data.* J. Phys. Chem. Ref. Data **34**, 1559–2260 (2005).

[66] B. K. Sahoo, B. P. Das, R. K. Chaudhuri, D. Mukherjee, R. G. E. Timmermans, and K. Jungmann. *Investigations of Ra^+ Properties to Test Possibilities for New Optical-Frequency Standards.* Phys. Rev. A **76**, 040504 (2007).

[67] M.Nunez Portela. *Single Ion Spectroscopy in Preparation of an Atomic Parity Violation Measurement in Ra^+.* PhD thesis, University of Groningen (2015).

[68] N. H. Edwards,S. J. Phipp, P. E. G. Baird, and S. Nakayama *Precise Measurement of Parity Nonconserving Optical Rotation in Atomic Thallium.* Phys. Rev. Lett. **74**, 2654 (1995).

[69] P. Vetter, D. M. Meekhof, P. K. Majumder, S. K. Lam- oreaux, and E. N. Fortson, *Precise Test of Electroweak Theory from a New Measurement of Parity Nonconservation in Atomic Thallium.* Phys. Rev. Lett. **74**, 2658 (1995).

[70] D. M. Meekhof, P. A. Vetter, P. K. Majumder, S. K. Lamoreaux, and E. N. Fortson, *Optical-rotation technique used for a high-precision measurement of parity nonconservation in Atomic Lead.* Phys. Rev. A **52**, 1895 (1995).

[71] S. J. Phipp, N. H. Edwards, P. E. G. Baird, and S. Nakayama, *A measurement of parity non-conserving optical rotation in Atomic Lead.* J. Phys. B **29**, 1861 (1996).

[72] M. D. Macpherson, K. P. Zetie, R. B. Warrington, D. N. Stacey, and J. P. Hoare, *Precise measurement of parity nonconserving optical rotation at 876 nm in Atomic Bismuth.* Phys. Rev. Lett. **67**, 2784 (1991).

[73] H. Gharibnejad, E. Eliav, M. S. Safronova, and A. Derevianko. *Resolving all-order Method Convergence Problems for Atomic Physics Applications.* Phys. Rev. A **83**, 052502 (2011).

[74] B. K. Sahoo, R. Chaudhuri, B. P. Das, and D. Mukherjee. *Relativistic Coupled-Cluster Theory of Atomic Parity Nonconservation: Application to* $^{137}Ba^{+}$. Phys. Rev. Lett. **96**, 163003 (2006).

[75] V. A. Dzuba, V. V. Flambaum, and J. S. M. Ginges. *Calculations of Parity-Nonconserving sd Amplitudes in Cs, Fr,* Ba^{+} *and* Ra^{+}. Phys. Rev. A **63**, 062101 (2001).

[76] S. G. Porsev, K. Beloy, and A. Derevianko, *Precision Determination of Electroweak Coupling from Atomic Parity Violation and Implications for Particle Physics.* Phys. Rev. Lett. **102**, 181601 (2009).

[77] B. K. Sahoo. *Ab initio Studies of Electron Correlation Effects in the Atomic Parity Violating Amplitudes in Cs and Fr.* J. Phys. B **43**, 085005 (2010).

[78] G. Stancari, S. N. Atutov, R. Calabrese, L. Corradi, A. Dainelli, C. de Mauro, A. Khanbekyan, E. Mariotti, P. Minguzzi, L. Moi, S. Sanguinetti, L. Tomassetti, and S. Veronesi. *Francium Sources and Traps for Fundamental Interaction Studies.* Euro. Phys. J. Special Topics **150**, 389–392 (2007).

[79] M. S. Safronova and W. R. Johnson *High-precision calculation of the parity-nonconserving amplitude in Francium.* Phys. Rev. A **62**, 022112 (2000).

[80] V.A.Dzuba, V.V.Flambaum, M.S.Safronova *Breit interaction and parity nonconservation in many-electron atoms.* Phys. Rev. A **73**, 022112 (2006).

[81] V.A.Dzuba, V.V.Flambaum, O.P. Sushkov, *Calculation of energy levels, E1 transition amplitudes, and parity violation in Francium.* Phys. Rev. A **51**, 3454 (1995).

[82] L. W. Wansbeek, B. K. Sahoo, R. G. E. Timmermans, K. Jungmann, B. P. Das, and D. Mukherjee. *Atomic Parity Nonconservation in* Ra^{+}. Phys. Rev. A **78**, 050501 (2008).

[83] E Gomez, S Aubin, R Collister, J A Behr, G Gwinner, L A Orozco, M R Pearson, M Tandecki, D Sheng, and J Zhang. *The FrPNC Experiment, weak interaction studies in Francium at TRIUMF.* J. Phys. Conference Series **387**, 2004 (2012).

[84] E. Gomez, L. A. Orozco, and G. D. Sprouse. *Spectroscopy with Trapped Francium : Advances and Perspectives for Weak Interaction Studies.* Rep. Prog. Phys. **69**, 79–118 (2006).

[85] S. N. Atutov, V. Biancalana, A. Burchianti, R. Calabrese, L. Corradi, A. Dainelli, V. Guidi, B. Mai, C. Marinelli, E. Mariotti, L. Moi, A. Rossi, E.

Scansani, G. Stancari, L. Tomassetti, and S. Veronesi. *The Legnaro Francium Magneto-Optical Trap.* Hyperfine Interact. **146**, 83-89 (2003).

[86] V. A. Dzuba and V. V. Flambaum. *Calculation of Nuclear-Spin-Dependent Parity Nonconservation in s-d transitions of Ba^+ , Yb^+ , and Ra^+ ions.* Phys. Rev. A **83**, 052513 (2011).

[87] Amita Mohanty, Elwin A. Dijck, Mayerlin Nuñez Portela, Nivedya Valappol, Andrew T. Grier, Thomas Meijknecht, Lorenz Willmann, Klaus Jungmann. *Lifetime measurement of the $5d^2D_{5/2}$ state in Ba^+.* Hyperfine Interact. **233**, 113 (2015).

[88] E. A. Dijck, M. Nuñez Portela, A. T. Grier, K. Jungmann, A. Mohanty, N. Valappol, and L. Willmann. *Determination of transition frequencies in a single $^{138}Ba^+$ ion.* Phys. Rev. A **91**, 060501(R) (2015).

[89] J. A. Sherman. *Single Barium Ion Spectroscopy: Light Shifts, Hyperfine Structure, and Progress on an Optical Frequency Standard and Atomic Parity Violation.* PhD thesis, University of Washington (2007).

[90] T. W. Koerber. *Measurement of Light Shift Ratios with a Single Trapped $^{138}Ba^+$ Ion, and Prospects for a Parity Violation Experiment.* PhD thesis, University of Washington (2003).

[91] M. Schacht. *Spin state detection and manipulation and parity violation in a single trapped ion.* arxiv:1308.2207.

[92] J. A. Sherman, A. Andalkar, W. Nagourney, and E. N. Fortson. *Measurement of Light Shifts at two Off-Resonant Wavelengths in a Single Trapped Ba^+ ion and the Determination of Atomic Dipole Matrix Elements.* Phys. Rev. A **78**, 052514 (2008).

[93] C. J. Foot. *Atomic Physics.* Oxford University Press, New York, first edition edition (2005).

[94] H. G. Dehmelt. *Radiofrequency Spectroscopy of Stored Ions I.* Adv. At. Mol. Phys. Academic Press, **3**, 1968.

[95] Günter Werth, Viorica N. Gheorghe, F. G. Major *Charged Particle Traps II: Applications.* Springer Series on Atomic, Optical, and Plasma Physics **54**, 3-34 (2009).

[96] N. Valappol. *Stable lasers for Optical clocks and Atomic parity violation measurement.* PhD thesis, University of Groningen, in preparation.

[97] R. Brun and F. Rademakers. *ROOT - An Object Oriented Data Analysis Framework.* Nucl. Instrum. Methods in Physics Research Section A: Accelerators, Spectrometers, Detectors and Associated Equipment **389**, 81–86 (1997). New Computing Techniques in Physics Research V.

[98] *https://root.cern.ch/*

[99] K. Jungmann, J. Hoffnagle, R. G. DeVoe, and R. G. Brewer. *Collective Oscillations of Stored Ions.* Phys. Rev. A **36**, 3451–3454 (1987).

[100] U. Dammalapati. *Metastable D-state spectroscopy and laser cooling of Barium.* PhD thesis, University of Groningen (2006).

[101] N. Kjaergaard, L. Hornekaer, A.M. Thommesen, Z. Videsen, M. Drewsen. *Isotope selective loading of an ion trap using resonance-enhanced two photonionisation.* Appl. Phys. B **71**, 207-210 (2000).

[102] D. J. Berkeland, M. G. Boshier. *Destabilization of dark states and optical spectroscopy in Zeeman-degenerate atomic systems.* Phys. Rev. A **65**, 033413 (2002).

[103] J. L. Hall. *Nobel Lecture: Defining and measuring optical frequencies.* Rev. Mod. Phys. **78**, 1279 (2006)

[104] T. W. Hänsch. *Nobel Lecture: Passion for precision.* Rev. Mod. Phys. **78**, 1297 (2006)

[105] U. Dammalapati, L. Willmann, J. Mulder, and K. Jungmann. KVI Annual Report, **38** (2002).

[106] C. S. Edwards, G. P. Barwood, P. Gill, F. Rodriguez-Llorente, and W. R. C. Rowley. *Frequency-stabilised diode lasers in the visible region using Doppler-free iodine spectra.* Opt. Comm. **132**, 94 (1996).

[107] I. Velchev, R. van Dierendonck, W. Hogervorst, and W. Ubachs, J. *A Dense Grid of Reference Iodine lines for optical Frequency Calibration in the range 571-596nm.* Mol. Spectrosc. **187**, 21 (1998).

[108] S. C. Xu, R. van Dierendonck, W. Hogervorst, and W. Ubachs, J. *A Dense Grid of Reference Iodine lines for optical Frequency Calibration in the range 595-655nm.* Mol. Spectrosc. **201**, 256 (2000).

[109] S. Kremser, B. Bodermann, H. Knöckel, and E. Tiemann. *Frequency stabilization of diode lasers to hyperfine transitions of the iodine molecule.* Opt. Comm. **110**, 708-716 (1994).

[110] H. Knöckel, S. Kremser, B. Bodermann, and E. Tiemann. *High Precision Measurements of Hyperfine Structures Near 790nm of I_2.* Z. Phys. D **37**, 43 (1996).

[111] G. Herzberg. *Spectra of Diatomic Molecules.* D. Van Nostrand Company, 1950.

[112] J. Ye et al. *Absolute Frequency Atlas of Molecular I_2 Lines at 532nm.* IEEE Trans. Instrum. Meas. **48**, 544-549 (1999).

[113] J. Ye, L.S. Ma and J.L. Hall. *Molecular Iodine Clock.* Phys. Rev. Lett. **87**, 270801 (2001).

[114] B. Argence, H. Halloin, O. Jeannin, P. Prat, O. Turazza, E. de Vismes, G. Auger, and E. Plagnol. *Molecular laser stabilization at low frequencies for the LISA mission.* Phys. Rev. D **81**, 082002, (2010).

[115] K. Nyholm et al. *Frequency Stabilization of a Diode-Pumped Nd:Yag Laser at 532nm to Iodine by Using Third-Harmonic Technique.* IEEE Trans. Inst. and Meas. **52**, 284-287 (2003).

[116] G. D. Rovera et al. *Absolute frequency meaurements of an I_2 stabilized Nd:YAG optical frequency standard.* Meas. Sci. Technol. **13**, 918-922 (2002).

[117] E. J. Zang et al. *Realization of Four-Pass I_2 Absorption Cell in 532nm Optical Frequency Standard.* IEEE Trans. Inst. Meas. **56**, 673-676 (2007).

[118] G.C. Bjorklund and M. D. Levenson *Frequency Modulation (FM) Spectroscopy.* Appl. Phys. B **32**, 145-152 (1983).

[119] S. Gerstenkorn and P. Luc. *Atlas du Spectre d'Absorption de la Molecule de d'Iode, Vol. 14000cm^{-1}-15600cm^{-1}.* (Laboratoire Aime Cotton, CNRS II, Orsay, 1980).

[120] R. H. L van Wooning, *Laser Frequency Offset Locking.* Brede Bachelor of Engineering (BBoE) thesis, KVI and Hanzehogeschool, Groningen, Netherlands (2008).

[121] C. J. S. Donald, D. M. Lucas, P. A. Barton, M. J. McDonnell, J. P. Stacey, D. A. Stevens, D. N. Stacey and A. M. Steane. *Search for correlation effects in linear chains of trapped Ca^+ ions.* Europhys. Lett. **51**, Number 4 (2000).

[122] W. Nagourney, J. Sandberg and H. Dehmelt. *Shelved Optical Electron Amplifier: Observation of Quantum jumps.* Phys. Rev. Lett. **56**, 2797-2799 (1986).

[123] A. A. Madej, J. D. Sankey. *Quantum Jumps and the Single trapped Barium Ion: determination of collisional Quenching Rates for the $5d^2D_{5/2}$ Level.* Phys. Rev. A. **41**, 2621-2630 (1990).

[124] F. Plumelle, M. Desaintfuscien, J.L. Duchene, and C. Audoin. *Laser Probing of Ions Confined in a Cylindrical Radiofrequency Trap.* Opt. Comm. **34**, 71-76 (1980).

[125] J. Gurell, E. Biémont, K. Blagoev, V. Fivet, P. Lundin, S. Mannervik, L. O. Norlin, P. Quinet, D. Rostohar, P. Royen, and P. Schef. *Laser-Probing Measurements and Calculations of Lifetimes of the $5d^2D_{3/2}$ and $5d^2D_{5/2}$ metastable Levels in Ba II.* Phys. Rev. A **75**, 052506 (2007).

[126] C. Auchter, T. W. Noel, M. R. Hoffman, S. R. Williams, and B. B. Blinov. *Measurement of the Branching Fractions and Lifetime of the $5d^2D_{5/2}$ Level of Ba^+.* Phys. Rev. A **90**, 060501(R) (2014).

[127] B. K. Sahoo, R. Chaudhuri, B. P. Das, and D. Mukherjee. *Relativistic Coupled-Cluster Theory of Atomic Parity Nonconservation: Application to $^{137}Ba^+$.* Phys. Rev. Lett. **96**, 163003 (2006).

[128] B. K. Sahoo and B. P. Das. *Ba^+ Quadrupole Polarizabilities: Theory versus Experiment.* Phys. Rev. A **86**, 022506 (2012).

[129] B. K Sahoo, Md. R. Islam, B. P. Das, R. K. Chaudhuri, D. Mukherjee. *Lifetimes of the metastable $^2D_{3/2,5/2}$ states in Ca^+, Sr^+ and Ba^+.* Phys. Rev. A **74**, 062504 (2006).

[130] E. Iskrenova-Tchoukova and M. S. Safronova. *Theoretical Study of Lifetimes and Polarizabilities in Ba^+.* Phys. Rev. A **78**, 012508 (2008).

[131] C. Guet and W. R. Johnson. *Relativistic Many-Body Calculations of TransitionRates for Ca^+, Sr^+ and Ba^+.* Phys. Rev. A **44**, 1531-1535 (1991).

[132] C. Guet and W. R. Johnson. *Erratum: Relativistic Many-Body Calculations of transition rates for Ca^+, Sr^+ and Ba^+.* Phys. Rev. A **76**, 039905(E) (2007).

[133] U.I. Safronova, M.S. Safronova. *Excitation energies, E1, M1, and E2 transition rates, and lifetimes in Ca^+, Sr^+, Cd^+, Ba^+, and Hg^+.* Can. J. Phys. **89**, 465-472 (2011).

[134] M. S. Safronova, Phys. Rev. A **81**, 052506 (2010).

[135] P. Royen, J. Gurell, P. Lundin, L. O. Norlin and S. Mannervik. *Monitoring the weak collisional excitation of a stored ion beam reveals the radiative decay rate of extremely long-lived metastable levels.* Phys. Rev. A **76**, 030502(R) (2007).

[136] N. Yu, W. Nagourney, and H. Dehmelt, Phys. Rev. Lett. **78**, 4898 (1997).

[137] I. Siemers, M. Schubert, R. Blatt, W. Neuhauser, and P. E. Toschek. *The "Trapped State" of a trapped ion-Line Shifts and Shape.* Europhys. Lett. **18**, 139 (1992)

[138] Y. Stalgies, I. Siemers, B. Appasamy, and P. E. Toschek. *Light shift and Fano resonances in a single cold ion.* J. Opt. Soc. Am. B **15**, 2505-2514 (1998)

[139] H. Oberst. *Resonance Fluorescence of Single Barium Ions.* Master's thesis, Universitat Innsbruck, Innsbruck (1999).

[140] T. Zanon-Willette, E. de Clercq, and E. Arimondo. *Ultrahigh-resolution spectroscopy with atomic or molecular dark resonances: Exact steady-state line shapes and asymptotic profiles in the adiabatic pulsed regime.* Phys. Rev. A **84**, 062502 (2011)

[141] P. Kuske, N. Kirchner, W. Wittmann, H. J. Andra, and D. Kaiser *Lifetime measurements by pulsed laser excitation of fast ion beams.* Phys. Lett. A **64**, 377 (1978).

[142] D. De Munshi, T. Dutta, R. Rebhi, and M. Mukherjee. *Precision measurement of branching fractions of* $^{138}Ba^{+}$*: Testing many body theories below one percent level.* Phys. Rev. A **91**, 040501(R) (2015).

[143] J. A. Sherman, T. W. Koerber, A. Markhotok, W. Nagourney, and E. N. Fortson. *Precision measurement of light shifts in a single trapped* Ba^{+} *ion.* Phys. Rev. Lett. **94**, 243001 (2005).

[144] F.Levi et al. *Precision test of the AC Stark shift in a rubidium vapour.* Phys. Rev. A **93**, 023433 (2016).

[145] E. A. Dijck. *A Single* Ra^{+} *Optical clock.* PhD Thesis, University of Groningen, in preparation.

List of Publications

Light shifts measured in trapped and laser cooled Ba^+ ions
Amita Mohanty, Elwin A. Dijck, Nivedya Valappol, Lorenz Willmann, Klaus Jungmann *in preparation*.

Consistency of $5d\,^2D_{5/2}$ state lifetime measurements for single and multiple laser cooled Ba^+ ions
Amita Mohanty, Elwin A. Dijck, Nivedya Valappol, M. Nuñez Portela, Lorenz Willmann, Klaus Jungmann *in preparation*.

Determination of the dipole matrix element ratio in multiple laser cooled $^{138}Ba^+$ ions
Amita Mohanty, Elwin A. Dijck, Nivedya Valappol, Thomas Meijknecht, Lorenz Willmann, Klaus Jungmann *in preparation*.

A UHV compatible effusive beam of Ba^+ ion source-For Atomic Parity Violation
Amita Mohanty, Elwin A. Dijck, Nivedya Valappol, Aswin, Lorenz Willmann, Klaus Jungmann *in preparation*

Lifetime measurement of the $5d\,^2D_{5/2}$ state in Ba^+
Amita Mohanty, Elwin A. Dijck, Mayerlin Nuñez Portela, Nivedya Valappol, Andrew T. Grier, Thomas Meijknecht, Lorenz Willmann, Klaus Jungmann
Hyperfine Interactions 233, 113 (2015).

Determination of transition frequencies in a single $^{138}Ba^+$ ion
E. A. Dijck, M. Nuñez Portela, A. T. Grier, K. Jungmann, **A. Mohanty**, N. Valappol, L. Willmann
Phys. Rev. A 91, 060501(R) (2015).

A gas cell for stopping, storing and polarizing radioactive particles
A. Sytema, J.E. van den Berg, O. Böll, D. Chernowitz, E.A. Dijck, J.O. Grasdijk, S. Hoekstra, K. Jungmann, S.C. Mathavan, C. Meinema, **A. Mohanty**, S.E. Müller, M. Nuñez Portela, C.J.G. Onderwater, C. Pijpker, L. Willmann, H.W. Wilschut
Nuclear Instruments and Methods in Physics Research: A 822, 77-81, (2016).

Ra^+ Ion Trapping: Toward an Atomic Parity Violation Measurement and an Optical Clock
M. Nuñez Portela, E. A. Dijck, **A. Mohanty**, H. Bekker, J.E. van den Berg, G.S. Giri, S. Hoekstra, C. J. G. Onderwater, S. Schlesser, R. G. E. Timmermans, O.

O. Versolato,L. Willmann, H. W. Wilschut, K. Jungmann
Applied Physics B 114 (1-2), 173-182, (2014).

Towards a precise measurement of atomic parity violation in a single Ra^+ ion
M. Nuñez Portela, J. E. van den Berg, H. Bekker, O. Böll, E. A. Dijck, G. S. Giri, S. Hoekstra, K. Jungmann, **A. Mohanty**, C. J. G. Onderwater, B. Santra, S. Schlesser, R. G. E. Timmermans, O. O. Versolato, L. W. Wansbeek, L. Willmann, H. W. Wilschut
Hyperfine Interactions 214 (1-3), 157-162, (2013).

Acknowledgements

I express my sincere gratitude to my promotor Prof. Klaus Jungmann and co-promotor Dr. Lorenz Willmann whose guidance and knowledgable support enabled the successful completion of my thesis. They have enriched my knowledge on physics and encouraged me to think and perform like an experimentalist. They are my best teachers with a unique scientific temperament which I always appreciate. Their discussions inspired me to carry out mindful experimental observations and draw conclusions from them. Besides being very educational, it was also very interesting and fun experience to work with both of them.

I am grateful to my reading committee members Prof. Ronnie Hoekstra (University of Groningen, The Netherlands), Prof. Wilfried Nörthershäuser (University of Darmstadt, Germany) and Prof. Nathal Severijns (University of Leuven, Belgium) for spending their valuable time on careful scrutinization of my thesis and for their useful feedback. My sincere thanks to the Foundation for Fundamental Research on Matter (FOM) under Programme 114 (TRIμP), FOM programme 125 (Broken Mirrors and Drifting Constants) and the Netherlands Organization for Scientific Research (NWO) for financially supporting this work.

I would like to appreciate the entire team Elwin, Nivedya, Mayerlin and Thomas for their productive discussions and immense contributions towards performing the experiment. Thanks to Elwin and Lorenz who always helped me with learning ROOT and analysis of the data. All credit goes to Elwin for helping me write the Dutch summary ("Nederlandse Samevatting") for the thesis. I would like to thank my professors Dr. Hans Wilschut, Dr. Rob Timmermans, Dr. Gerco Onderwater, Dr. Steven Hoekstra and Dr. Ronnie Hoekstra for all their valueable and educative discussions during the TRIμP (now called FIS) meetings. I always enjoyed the regular radium ion meetings which are a continuous source of knowledge and enabled the progress of the experiment. I would like to thank my KVI colleagues Corine, Joost, Auke, Sreekanth, Artem, Olivier, Kevin, Andrew, Keri, Joël, Martijn, Sietse, Paul, Aswin, Joeren, Harmjan, Bodhaditya, Soumya, Duurt, Wilbert, Hendrik, Sophie, Zahra for all their scientific help during the research work.

I appreciate the technical staff Leo, Oliver and Otto for all their support and assistance during my tenure of four years. A big thanks to Hilde who helped me with all the paperworks and approach the appropriate path in the university and with FOM. I would like to acknowledge the technical support from the electronics and mechanical workshop, the drawing office, vacuum and IT departments of KVI for their help and cooperation. Thanks to André, Dirk, Nanko, Rudolf and

Sandra from mechanical workshop for building the hyperbolic Paul traps and multiple mechanical pieces for this experiment and thanks to Imko for the technical drawings. I am also grateful to the KVI administration, financial department and personnel department for their administrative support.

I acknowledge my sincere thanks to Prof. Bhanu Pratap Das who made me aware of the experimental TRIμP (now named FIS) group and encouraged me to join this group here in Groningen, The Netherlands. I am thankful to all my professors during my masters who were always a source of encouragement. I would also like to thank all my friends Prachi, Preeti, Tapan, Minakshi, Narsi Reddy, Soumi and Niladri from my master days. Thanks to my best friend Prachi for the wonderful but rare physics discussions.

Last but not the least, credit goes to my parents and brother who were my biggest pillar of support during the PhD. They were my continuous source of inspiration and encouragement. I am also thankful to all my relatives and friends for their support and encouragement during these four years.

Amita Mohanty
September 2016